SHIBAURA INSTITUTE OF TECHNOLOGY

Graduate School of Engineering and Science

AGH UNIVERSITY OF SCIENCE AND TECHNOLOGY

Faculty of Energy and Fuels

DOCTORAL DISSERTATION

Perovskite-based oxygen storage materials

Alicja Klimkowicz

Supervisor: Prof. dr. Akito Takasaki

Supervisor: Dr hab. inż. Konrad Świerczek, prof. AGH

TOKYO, KRAKOW 2016

A heartfelt thanks to
Dr hab. inż. Konrad Świerczek, prof. AGH
for comprehensive support
and assistance during my scientific work.
It would not be like this, if it wasn't for you.

A heartfelt thanks to
Prof. dr. Akito Takasaki
for comprehensive support
and assistance during my scientific work.

Thanks also to all those who contributed to this work:
friends, family, coworkers, lab members
both in Poland and in Japan.
The list is long. Thank you.
Special thanks to Zuzanna Płoch.

The project was funded by the National Science Centre Poland (NCN) on the basis of the decision number DEC-2011/01/B/ST8/04046.
The author acknowledges financial support from JSPS-PAN Joint Research Project "Development of IGFC System with Oxygen and Hydrogen Storage Units".
The author acknowledges the Helmholtz-Zentrum Berlin for provision of neutron beamtime at beamline E9 of BAR II.

Table of contents

Summary

This thesis concerns determination of oxygen storage-related properties, as well as other basic physicochemical characteristics in a group of candidate oxygen storage materials (OSM), having perovskite-type crystal structure. Series of cation-ordered Mn-based oxides with a general formula of $BaLnMn_2O_{5+\delta}$ (Ln: Pr, Nd, Sm, Gd, Dy, Er and Y), Ln-site substituted $BaY_{1-x}Ln_xMn_2O_{5+\delta}$ (Ln: Pr, Sm, Gd), and doubly doped materials belonging to $Ba_{0.9}Sr_{0.1}Y_{1-x}Ln_xMn_2O_{5+\delta}$ group, and additionally, selected Co- and Fe-containing oxides were characterized in terms of their crystal structure in oxidized and reduced state, structural evolution on temperature and oxygen content. Thorough studies concerning their oxygen storage properties, with oxidation (in air) and reduction (in 5 vol.% H_2 in Ar) characteristics recorded as a function of temperature, kinetics of the oxidation/reduction determined from the isothermal studies, as well as reversible oxygen storage capacity (OSC), constitute a main part of the experimental work. Complementary research on microstructure and morphology, oxidation state of the manganese cations, as well as electrical conductivity and Seebeck coefficient dependence on temperature was also conducted for selected samples. An attempt to elucidate correlation between the chemical composition of the considered oxides and their physiochemical properties influencing oxygen storage performance have been conducted. The performed studies in this thesis allowed to select the best candidate materials, having high and reversible OSC, which surpass the currently commercialized compounds.

The main part of the thesis contains 11 chapters, with the initial chapter 1 presenting an introduction to currently, commercially used oxygen production and storage methods (cryogenic liquefaction, pressure and temperature driven adsorption, usage of membranes, oxygen tanks). Chapter 2 contains introduction to oxygen storage materials, description of the mechanism of incorporation and release of the oxygen into/from the oxides, with following information about four particular OSM systems. Selected applications of the oxygen storage materials (three-way catalytic converters, chemical looping processes, flameless combustion of hydrocarbons) are discussed in chapter 3.

Due to the fact that the considered in this thesis compounds exhibit perovskite-type crystal structure, either with or without cation ordering, the next chapter 4 shows a detailed information about structural properties of the parent ABO_3-type, as well as cation-ordered ($AA'B_2O_6$, $A_2BB'O_6$) perovskites, and $A_2B_2O_5$-type brownmillerites. Additional data

concerning oxygen nonstoichiometry, transport and magnetic properties of such oxides are also given.

Preparation methods of the materials and experimental techniques used for characterization of the synthesized compounds are described in chapter 5. The following techniques were utilized: X-ray diffraction (XRD) and neutron diffraction methods with Rietveld analysis of the data, performed at room temperature and at elevated temperatures, thermogravimetric (TG) analysis conducted as a function of temperature, with isothermal studies executed with a change of atmosphere between synthetic air and 5 vol.% H_2 in Ar, microstructural studies using scanning electron microscope (SEM), with additional measurements of the specific surface area by BET technique, X-ray photoelectron spectroscopy (XPS) studies, as well as electrical conductivity and Seebeck coefficient measurements. Parameters used for evaluation of OS properties were also described.

Research results obtained by author of this thesis are gathered in chapters 6-10. In chapter 6, an effect of introduction of different lanthanides into Ln site in $BaLnMn_2O_{5+\delta}$ (Ln: Pr, Nd, Sm, Gd, Dy and Y) on the physicochemical properties of the materials was evaluated. Detailed information about crystal structure of the oxidized $BaLnMn_2O_6$ ($\delta \approx 1$) and reduced $BaLnMn_2O_5$ ($\delta \approx 0$) is shown, indicating linear relationship between the unit cell volume and ionic radii of Ln in both, $BaLnMn_2O_6$ and $BaLnMn_2O_5$. Conducted structural measurements as a function of temperature, allowed to observe *in situ* transformations ongoing during the oxidation process of the initially reduced material. Precise neutron diffraction measurements conducted in Helmholtz Zentrum Berlin in atmosphere of 5 vol.% H_2 in Ar allowed for *in situ* observation of the reduction process and determination of the mechanism of the oxygen release. Furthermore, possibility of reduction under low vacuum environment (~ 100 Pa) at elevated temperatures of the oxidized samples was also researched. The performed XPS studies indicated presence of manganese cations having different oxidation states and modification of chemical environment of the elements, between the reduced and oxidized samples. Analysis of the microstructure of the obtained $BaLnMn_2O_{5+\delta}$ powders was performed, in order to have fully-characterized samples for the thermogravimetric studies.

Comprehensive characterization of all compounds was conducted in terms of their oxygen storage-related properties by means of the TG method. In all of the cases, close to theoretical value of the OSC was recorded during isothermal experiments performed at 500 °C with the atmosphere change between synthetic air and 5 vol.% H_2 in Ar gas mixture, corresponding to the change between almost fully oxidized $BaLnMn_2O_6$ and fully

reduced $BaLnMn_2O_5$. The recorded reversible capacities correlate well with a molar mass of the compounds, being the highest for $BaYMn_2O_{5+\delta}$ (3.71 wt.%) and the lowest for $BaDyMn_2O_{5+\delta}$ (3.16 wt.%). It was documented that for all of the materials the reduction process occurs much slower (on the order of several minutes) than the oxidation (seconds), and therefore limits the oxygen storage performance. This phenomena originates from the exothermic nature of the oxidation process. The recorded temperature dependence of the reduction time was interpreted on a basis of oxygen diffusion in a bulk, and as such, allowed to calculate the activation energy of the ionic transport. It was also found that materials with larger grains show deteriorated kinetics of the reduction process, due to the enlarged diffusion length in the bulk of the crystal. Furthermore, the relationship between Ln cation present in $BaLnMn_2O_{5+\delta}$ and the characteristic temperature of the oxidation process was shown. It should be emphasized that the recorded oxygen storage performance of majority of the considered $BaLnMn_2O_{5+\delta}$ surpasses that of the commercial materials.

Chapter 7 of this thesis presents comprehensive characterization of the physicochemical properties of novel $BaErMn_2O_{5+\delta}$ system ($BaErMn_2O_5$ and $BaErMn_2O_6$). The published by author paper concerning both of these oxides is the first literature report on the A-site cation-ordered $BaLnMn_2O_{5+\delta}$ with the smallest introduced Er^{3+} lanthanide cations. The presented characterization of the structural properties, oxygen storage performance, as well as data concerning dependence of the electrical conductivity and Seebeck coefficient on temperature allowed to significantly broaden knowledge about the $BaLnMn_2O_{5+\delta}$ system. The smallest change of unit cell volume between the reduced and oxidized Er-containing material was documented. Also, it was found that $BaErMn_2O_6$ shows much higher electrical conductivity than $BaErMn_2O_5$, which can be associated with delocalized Mn^{3+}/Mn^{4+} and localized Mn^{2+}/Mn^{3+} states, respectively.

An attempt to optimize oxygen storage performance in the compounds was conducted by a partial substitution of yttrium by different Ln in $BaY_{1-x}Ln_xMn_2O_{5+\delta}$ (Ln: Pr, Sm, Gd; x = 0.25, 0.5 and 0.75), as presented in chapter 8. Apart from the structural characterization, which revealed expected changes of the crystal symmetry, unit cell parameters and volume, with the increasing substitution amount in the series, investigations of the oxygen storage properties showed complex behavior, only partially correlated with the chemical composition. Among studied compounds, the best performance was registered for $BaY_{0.75}Pr_{0.25}Mn_2O_{5+\delta}$ sample, for which the reduction time at 500 °C during the 2nd cycle was only about 3.4 min, and improved to 2.6 min on the 50th cycle. Furthermore, no changes of the microstructure on cycling of this oxide were

measured, indicating excellent stability. Systematic studies of doubly substituted $Ba_{1-y}Sr_yY_{1-x}Ln_xMn_2O_{5+\delta}$ (Ln: Pr, Sm and Gd) materials were also performed, and the obtained results are gathered in chapter 9. A relatively narrow range of possible substitution of Ba^{2+} by Sr^{2+} cations was found, greatly limiting the anticipated improvement of the reversible OSC. Nevertheless, satisfactory oxygen storage performance was documented for $Ba_{0.9}Sr_{0.1}Y_{0.75}Sm_{0.25}Mn_2O_{5+\delta}$ oxide and an increase of the measured OSC for $Ba_{0.9}Sr_{0.1}YMn_2O_{5+\delta}$ material.

Possibility of a major improvement of OSC was explored in studies of properties of Fe- and Co-containing oxides, as presented in chapter 10. The selected materials with a general formula of: $La_{0.6}Sr_{0.4}Co_{0.8}Fe_{0.2}O_{3-\delta}$, $La_{0.5}Sr_{0.5}Co_{0.5}Fe_{0.5}O_{3-\delta}$, $Sm_{0.5}Sr_{0.5}Co_{0.5}Fe_{0.5}O_{3-\delta}$, $La_{0.5}Ba_{0.5}Co_{0.5}Fe_{0.5}O_{3-\delta}$, as well as $Sm_{0.5}Ba_{0.5}Co_{0.5}Fe_{0.5}O_{3-\delta}$ in reduced and oxidized forms were characterized in terms of their crystal structure. In the case of $Sm_{0.5}Ba_{0.5}Co_{0.5}Fe_{0.5}O_{3-\delta}$ sample, layered type of ordering of Sm^{3+} and Ba^{2+} cations was detected, similar to the one present in the studied Mn-containing oxides. Transition upon oxidation from brownmillerite-type to perovskite-type phase was detected by *in situ* XRD experiments for initially reduced $La_{0.6}Sr_{0.4}Co_{0.8}Fe_{0.2}O_{3-\delta}$, $La_{0.5}Sr_{0.5}Co_{0.5}Fe_{0.5}O_{3-\delta}$ and $Sm_{0.5}Sr_{0.5}Co_{0.5}Fe_{0.5}O_{3-\delta}$. The highest OSC (exceeding 4 wt.%) was measured for $La_{0.6}Sr_{0.4}Co_{0.8}Fe_{0.2}O_{3-\delta}$, while the fastest reduction speed at 500 °C (~ 2.3 min) was found for $La_{0.5}Sr_{0.5}Co_{0.5}Fe_{0.5}O_{3-\delta}$. The materials were also found to exhibit lower activation energy of the ionic transport. The compounds, however, were shown to suffer from insufficient stability in reducing conditions, especially at higher (≥ 500 °C) temperatures, limiting their possible application.

Conclusions based on the presented studies and given discussion are listed in chapter 11, with recommendations about future research on OSMs also included. In addition, the thesis contains four appendixes. The first one (A) is devoted to a highly-precise structural identification of selected $BaLnMn_2O_{5+\delta}$, which was performed by analysis of synchrotron data gathered at Argonne's Laboratory Advanced Photon Source (USA). Second appendix B contain additional information of neutron diffraction measurement setup and parameters of the structural refinements of the gathered data. Appendix C presents information about submitted patent proposal concerning improvement of OSMs by a high-energy milling process. Additional, selected results of flameless oxidation of methane with $BaYMn_2O_6$ used as the catalyst and oxygen carrier are included in Appendix D.

Tytuł pracy w języku polskim

Materiały o strukturze perowskitu do magazynowania tlenu

Streszczenie

Niniejsza praca dotyczy określenia właściwości związanych z magazynowaniem tlenu, jak również innych podstawowych właściwości fizykochemicznych dla grupy związków o strukturze typu perowskitu, będących potencjalnymi materiałami do magazynowania tlenu (ang. *oxygen storage materials*, OSM). Seria tlenków na bazie Mn, z obecnym uporządkowaniem kationowym, o ogólnym wzorze $BaLnMn_2O_{5+\delta}$ (Ln: Pr, Nd, Sm, Gd, Dy, Er i Y), materiałów częściowo podstawianych w podsieci Ln o składzie $BaY_{1-x}Ln_xMn_2O_{5+\delta}$ (Ln: Pr, Sm, Gd) oraz związków podwójnie domieszkowanych należących do grupy $Ba_{0,9}Sr_{0,1}Y_{1-x}Ln_xMn_2O_{5+\delta}$, a także wybranych tlenków zawierających Co i Fe została scharakteryzowana pod względem struktury krystalicznej w stanie utlenionym oraz zredukowanym, a także zmian strukturalnych zachodzących ze zmianą temperatury, jak również zawartości tlenu. Szczegółowe badania dotyczące właściwości magazynowania tlenu, z charakterystyką procesów utleniania (w powietrzu) i redukcji (w 5 %obj. H_2 w Ar), mierzoną w funkcji temperatury, kinetyką izotermicznego utleniania/redukcji, a także odwracalną pojemnością magazynowania tlenu (ang. *oxygen storage capacity*, OSC) stanowią główną część danych eksperymentalnych. Dla wybranych próbek przeprowadzono komplementarne badania mikrostruktury i morfologii przygotowanych materiałów, stopnia utlenienia kationów manganu, jak również pomiary zależności przewodnictwa elektrycznego i współczynnika Seebecka od temperatury. Podjęta została próba wyjaśnienia korelacji pomiędzy składem chemicznym rozważanych tlenków, a ich właściwościami fizykochemicznymi, wpływającymi na parametry związane z magazynowaniem tlenu. Przeprowadzone w pracy badania pozwoliły na wyłonienie najlepszych materiałów, które charakteryzują się wysoką, odwracalną pojemnością OSC, która przekracza wartości podawane dla obecnie stosowanych materiałów komercyjnych.

Główną część pracy stanowi 11 rozdziałów, wśród których we wprowadzającym rozdziale 1 zawarto informacje dotyczące komercyjnie wykorzystywanych metod produkcji i magazynowania tlenu (skraplanie kriogeniczne, adsorpcja zmiennociśnieniowa i zmiennotemperaturowa, zastosowanie membran, zbiorniki na tlen). Rozdział 2 zawiera wprowadzenie do materiałów magazynujących tlen, opis mechanizmu wbudowywania

i uwalniania tlenu do/z materiałów tlenkowych oraz informacje na temat czterech systemów OSM. Wybrane zastosowania materiałów służących do magazynowania tlenu (trójfunkcyjne konwertery katalityczne, procesy z pętlą chemiczną, bezpłomieniowe spalanie węglowodorów) zostały opisane w rozdziale 3.

Ze względu na fakt, że rozważane w niniejszej pracy związki wykazują strukturę krystaliczną typu perowskitu z obecnym uporządkowaniem kationów lub z jego brakiem, w kolejnym rozdziale 4 przedstawiono szczegółowe dane dotyczące właściwości strukturalnych związków podstawowych typu ABO_3, a także perowskitów z uporządkowaniem kationów ($AA'B_2O_6$, $A_2BB'O_6$) oraz materiałów typu brownmillerytu $A_2B_2O_5$. Podano również uzupełniające informacje dotyczące niestechiometrii tlenowej, właściwości transportowych i magnetycznych tych tlenków.

Sposoby otrzymywania materiałów oraz techniki eksperymentalne użyte do scharakteryzowania zsyntetyzowanych związków opisane są w rozdziale 5. Do badań wykorzystano: dyfrakcję promieni rentgenowskich (XRD) z analizą danych przy użyciu metody Rietvelda, pomiary wykonano w temperaturze pokojowej oraz w temperaturach podwyższonych, analizę termograwimetryczną (TG) przeprowadzoną w funkcji temperatury, wraz z izotermicznymi badaniami przy zmianie atmosfery pomiędzy powietrzem syntetycznym a mieszaniną 5 %obj. H_2 w Ar, analizę mikrostrukturalną z użyciem skaningowego mikroskopu elektronowego (SEM). Dodatkowo opisano wykonane badania powierzchni właściwej metodą BET, spektroskopię fotoelektronów (XPS), a także sposób pomiaru przewodnictwa elektrycznego i współczynnika Seebecka. Opisano również parametry użyte do oceny materiałów pod kontem magazynowania tlenu.

Wyniki badań uzyskane przez autorkę niniejszej pracy zebrane są w rozdziałach 6-10. W rozdziale 6, określono wpływ wprowadzenia wybranych lantanowców w pozycję Ln w strukturze $BaLnMn_2O_{5+\delta}$ (Ln: Pr, Nd, Sm, Gd, Dy i Y) na właściwości fizykochemiczne materiałów. Przedstawiono szczegółowe informacje na temat struktury krystalicznej utlenionych $BaLnMn_2O_6$ ($\delta \approx 1$) oraz zredukowanych $BaLnMn_2O_5$ ($\delta \approx 0$), które wskazują na liniową zależność pomiędzy wielkością komórki elementarnej i promieniem jonowym Ln dla obu serii, $BaLnMn_2O_6$ oraz $BaLnMn_2O_5$. Przeprowadzone w funkcji temperatury pomiary strukturalne *in situ* pozwoliły zaobserwować przemiany zachodzące w procesie utleniania zredukowanego uprzednio materiału. Dodatkowe precyzyjne badania dyfrakcji neutronów w ośrodku Helmholtz Zentrum Berlin wykonane w atmosferze redukcyjnej 5 %obj. H_2 w Ar pozwoliły na obserwacje *in situ* procesu redukcji oraz określenie mechanizmu oddawania. Ponadto, zbadano możliwość redukcji

utlenionych związków w warunkach niskiej próżni (~ 100 Pa) w podwyższonej temperaturze. Przeprowadzone badania XPS wskazały na obecność kationów manganu na różnym stopniu utlenienia oraz zmianę otoczenia chemicznego pierwiastków pomiędzy składami zredukowanymi oraz utlenionymi. Analizę mikrostruktury otrzymanych proszków $BaLnMn_2O_{5+\delta}$ przeprowadzono w celu uzyskania pełnej charakterystyki próbek do badań termograwimetrycznych.

Przeprowadzono wszechstronną charakterystykę wszystkich rozważanych związków w aspekcie ich właściwości związanych z magazynowaniem tlenu stosując metodę TG. We wszystkich przypadkach, podczas pomiarów w 500 °C przy zmianie atmosfery pomiędzy syntetycznym powietrzem a mieszaniną 5 %obj. H_2 w Ar odnotowano wartości OSC bliskie teoretycznym, odpowiadającym zmianie pomiędzy praktycznie całkowicie utlenionym $BaLnMn_2O_6$ oraz całkowicie zredukowanym $BaLnMn_2O_5$. Zmierzone wartości OSC dobrze korelują z masą molową związków. Dla $BaYMn_2O_{5+\delta}$ są one najwyższe (3,71 %wag.), natomiast dla $BaDyMn_2O_{5+\delta}$ najniższe (3,16 %wag.). Udokumentowano, że dla wszystkich badanych materiałów proces redukcji przebiega znacznie wolniej (rzędu kilku minut), w porównaniu do procesu utleniania (sekundy), a zatem ogranicza efektywność magazynowania tlenu. Zjawisko to może być tłumaczone egzotermiczną naturą procesu utleniania. Zmierzoną zależność czasu redukcji próbek od temperatury zinterpretowano w powiązaniu z dyfuzją tlenu wewnątrz ziaren, co umożliwiło obliczenie energii aktywacji transportu jonowego. Stwierdzono również, że materiały o większych ziarnach wykazują pogorszenie kinetyki procesu redukcji z powodu zwiększonej drogi dyfuzji objętościowej. Wykazano zależność pomiędzy rodzajem kationu Ln podstawionym w $BaLnMn_2O_{5+\delta}$, a charakterystyczną temperaturą procesu utleniania. Należy podkreślić, że dla większości rozpatrywanych tlenków $BaLnMn_2O_{5+\delta}$ zmierzone właściwości związane z magazynowaniem tlenu okazały się być lepsze w porównaniu do danych dla materiałów komercyjnych.

W rozdziale 7 niniejszej pracy przedstawiono szczegółową charakterystykę właściwości fizykochemicznych nowego układu $BaErMn_2O_{5+\delta}$ ($BaErMn_2O_5$ i $BaErMn_2O_6$). Opublikowana przez autorkę praca dotycząca obu tych tlenków jest pierwszy doniesieniem w literaturze na temat $BaLnMn_2O_{5+\delta}$, w którym występuje uporządkowanie kationów w podsieci A, z najmniejszym do tej pory wprowadzonym lantanowcem Er^{3+}. W rozdziale tym przedstawiono charakterystykę właściwości strukturalnych, właściwości związane z magazynowaniem tlenu, jak również dane dotyczące zależności przewodnictwa elektrycznego oraz współczynnika Seebecka od

temperatury, które pozwoliły na znaczne poszerzenie wiedzy odnośnie $BaLnMn_2O_{5+\delta}$. Dla rozważanego związku zawierającego Er udokumentowano najmniejszą zmianę objętości komórki elementarnej pomiędzy składem zredukowanym i utlenionym. Ponadto stwierdzono, że $BaErMn_2O_6$ wykazuje znacznie wyższe przewodnictwo elektryczne niż $BaErMn_2O_5$, co można powiązać z, odpowiednio, zdelokalizowaniem stanów Mn^{3+}/Mn^{4+} oraz zlokalizowaniem stanów Mn^{2+}/Mn^{3+}.

Próba optymalizacji właściwości związanych z magazynowaniem tlenu została przeprowadzona poprzez częściowe zastąpienie itru innym kationem Ln w serii związków $BaY_{1-x}Ln_xMn_2O_{5+\delta}$ (Ln: Pr, Sm, Gd; x = 0,25; 0,5 i 0,75), tak jak przedstawiono w rozdziale 8. Oprócz charakterystyki strukturalnej, która potwierdziła oczekiwane zmiany symetrii, parametrów oraz objętości komórki elementarnej materiałów wraz ze wzrostem podstawienia, badania właściwości związanych z magazynowaniem tlenu wykazały złożoność zachowań i tylko częściową korelację ze składem chemicznym. Wśród badanych tlenków najlepsze właściwości zostały zarejestrowane dla składu $BaY_{0,75}Pr_{0,25}Mn_2O_{5+\delta}$, dla którego czas redukcji w 500 °C podczas drugiego cyklu wynosił jedynie 3,4 min i uległ skróceniu do 2,6 min dla pięćdziesiątego cyklu. Ponadto, nie zaobserwowano zmian mikrostruktury po cyklowaniu, co wskazuje na bardzo dobrą stabilność tego materiału. Wykonano również systematyczne badania podwójnie podstawianych materiałów $Ba_{1-y}Sr_yY_{1-x}Ln_xMn_2O_{5+\delta}$ (Ln: Pr, Sm i Gd), a uzyskane wyniki tych pomiarów zebrane są w rozdziale 9. Wykazany został stosunkowo wąski zakres tworzenia roztworów stałych poprzez podstawienie Ba^{2+} przez kationy Sr^{2+}, co znacząco ogranicza ewentualną, spodziewaną poprawę odwracalnej pojemności OSC. Niemniej jednak, zadowalające wyniki w aspekcie magazynowania tlenu uzyskano dla składu $Ba_{0,9}Sr_{0,1}Y_{0,75}Sm_{0,25}Mn_2O_{5+\delta}$ oraz zwiększoną OSC dla materiału $Ba_{0,9}Sr_{0,1}YMn_2O_{5+\delta}$.

Możliwości znaczącej poprawy pojemności OSC zostały zbadane w testach właściwości materiałów zawierających żelazo i kobalt, jak przedstawiono w rozdziale 10. Wybrane tlenki $La_{0,6}Sr_{0,4}Co_{0,8}Fe_{0,2}O_{3-\delta}$, $La_{0,5}Sr_{0,5}Co_{0,5}Fe_{0,5}O_{3-\delta}$, $Sm_{0,5}Sr_{0,5}Co_{0,5}Fe_{0,5}O_{3-\delta}$, $La_{0,5}Ba_{0,5}Co_{0,5}Fe_{0,5}O_{3-\delta}$, a także $Sm_{0,5}Ba_{0,5}Co_{0,5}Fe_{0,5}O_{3-\delta}$ zostały scharakteryzowane pod kątem ich struktury krystalicznej, zarówno w formie zredukowanej, jak i utlenionej. W przypadku związku $Sm_{0,5}Ba_{0,5}Co_{0,5}Fe_{0,5}O_{3-\delta}$ wykazano warstwowy rodzaj uporządkowania kationów Sm^{3+} i Ba^{2+}, analogiczny do tego obecnego w badanych tlenkach zawierających Mn. Eksperymenty *in situ* XRD pozwoliły zaobserwować zmianę struktury krystalicznej od struktury typu brownmillerytu do struktury perowskitu podczas utleniania początkowo zredukowanych $La_{0,6}Sr_{0,4}Co_{0,8}Fe_{0,2}O_{3-\delta}$, $La_{0,5}Sr_{0,5}Co_{0,5}Fe_{0,5}O_{3-\delta}$ oraz

$Sm_{0,5}Sr_{0,5}Co_{0,5}Fe_{0,5}O_{3-\delta}$. Najwyższą pojemność OSC (powyżej 4 %wag.) zmierzono dla składu $La_{0,6}Sr_{0,4}Co_{0,8}Fe_{0,2}O_{3-\delta}$, natomiast największą szybkość redukcji w temperaturze 500 °C (~ 2,3 min) stwierdzono dla materiału o składzie $La_{0,5}Sr_{0,5}Co_{0,5}Fe_{0,5}O_{3-\delta}$. Materiały z tej grupy wykazują również niższą energię aktywacji transportu jonowego. Wykazano równocześnie, że związki te posiadają niewystarczającą stabilność w warunkach redukujących, w szczególności w wyższych temperaturach (≥ 500 °C), co ogranicza możliwość ich zastosowania.

Wnioski wynikające z przeprowadzonych badań oraz zaprezentowanej dyskusji wypunktowane zostały w rozdziale 11, razem z zaleceniami dotyczącymi ewentualnych dalszych badań nad właściwościami materiałów OSM.

Niniejsza praca zawiera ponadto cztery załączniki. Pierwszy z nich (A) poświęcony jest wysoce precyzyjnej identyfikacji strukturalnej wybranych $BaLnMn_2O_{5+\delta}$, którą wykonano na podstawie analizy danych synchrotronowych zebranych przy użyciu Advanced Photon Source znajdującego się w Argonne Laboratory (USA). Drugi załącznik B zawiera dodatkowe informacje odnośnie aparatury pomiarowej dyfrakcji neutronów oraz parametry dopasowań strukturalnych zebranych danych. Załącznik C przedstawia informacje na temat złożonego wniosku patentowego dotyczącego poprawy właściwości materiałów OSM w procesie mielenia wysokoenergetycznego. Dodatkowo, wybrane wyniki dotyczące bezpłomieniowego utleniania metanu przy wykorzystaniu $BaYMn_2O_6$ jako katalizatora i nośnika tlenu znajdują się w załączniku D.

日本語における博士論文のタイトル

ペロブスカイト型酸素貯蔵材料

概要

本論文は，ペロブスカイト型結晶構造を持つ酸素吸蔵材料(OSM)の酸素吸蔵に関連する特性および基本的な物理化学特性を決定するものである．$BaLnMn_2O_{5+\delta}$(Ln: Pr, Nd, Sm, Gd, Dy, Er, Y)の一般式を持つ陽イオンで秩序化したマンガン基の酸化物系，Ln サイトを置換した $BaY_{1-x}Ln_xMn_2O_{5+\delta}$ (Ln: Pr, Sm, Gd)，そして 2 種類元素を添加した $Ba_{0.9}Sr_{0.1}Y_{1-x}Ln_xMn_2O_{5+\delta}$ 系，さらに， Co と Fe を含む酸化物系材料について酸化と還元状態においての結晶構造，温度や酸素含有量に関連した結晶構造変化を調べた．これらの材料は，空気中における酸化および5vol.%水素を含むアルゴンガス雰囲気において，酸素吸蔵特性と温度の関係を調べる共に，等温測定における酸化還元速度や酸素吸蔵量(OSC)の可逆性の調査が本研究の主な部分である．選択したサンプルで微細構造および形態，マンガン陽イオンの酸化状態，電気伝導性と温度依存のゼーベック効果についても補足的に調べた．酸化物の化学組成と酸素吸蔵能力に影響を与えるような物理化学特性との相互関係の考察も試みた．本論文の結果は，現在商品化されている化合物の特性を越える，高い酸素吸蔵能および酸化還元の可逆性を持つ最適な材料を選択することを可能にする

この論文の主要パートは 11 章に分かれており，始めの第 1 章は緒言で，現在，商業的に用いられている酸素製造とその貯蔵方法（低温液化，圧力と温度による吸着，薄膜利用，酸素タンク)について述べている．第 2 章は，酸素貯蔵材料の概要および酸素吸放出のメカニズム，さらに 4 つの典型的な酸素吸蔵材料の基本特性を示した．第 3 章では，酸素吸蔵材料のいくつかの応用(三元触媒，化学循環工程，炭化水素の無炎燃焼)について議論している．

この論文では陽イオン秩序性のあるなしに関らわず，ペロブスカイト型結晶構造の化合物についての研究であるので，次の第 4 章では，基本形のABO_3タイプや陽イオン秩序性のある($AA'B_2O$, $A_2BB'O_6$) ペロブスカイト，そして $A_2B_2O_5$ 型ブラウンミラライトの構造特性について詳細な情報を示している． それらの酸化物の

酸素の非化学量論性，イオン移動そして磁気特性に関する追加データも併せて示した．

材料の準備方法と合成した化合物の特性評価に用いた実験手法は，第 5 章に示した．実験技法は次の手法を利用した：リートベルト解析を伴う室温および高温での X 線および中性子回折法，雰囲気を変化（空気から 5vol.%の水素を含むアルゴンガス）させ，さらに，温度を変化させた場合および等温下においての熱重量分析(TG)，走査型電子顕微鏡(SEM)による観察，BET 法による比表面積測定，X 線光電子分光(XPS)測定および電気電電導度およびゼーベック係数測定．　酸素吸蔵特性に評価に必要なパラメーターも第 5 章に示している．

本論文の著者によって得られた実験結果は第 6 から第 10 章にまとめている．第 6 章では，$BaLnMn_2O_{5+\delta}$ の Ln サイトに異なるランタノイド元素(Ln: Pr, Nd, Sm, Gd, Dy and Y)を用導入した場合のこれら材料の物理化学的特性における効果を評価している．酸化した $BaLnMn_2O_6$ ($\delta \approx 1$)と還元された $BaLnMn_2O_5$ ($\delta \approx 0$)の結晶構造の詳細な情報を示し，単位格子体積とランタノイド元素のイオン半径との間に比例関係があることを $BaLnMn_2O_6$ と $BaLnMn_2O_5$ の双方について明らかにした．温度を変化させた場合の結晶構造測定では，最初還元されている材料の酸化プロセスのその場観察が可能となる．ベルリンの Helmholtz Zentrum で行われた 5vol.%水素を含んだアルゴンガス雰囲気での精密な中性子回折測定は還元プロセスおよび酸素放出のメカニズム決定を可能にした．さらに，酸化サンプルの高温，低真空(～100Pa)下の還元の可能性についても調べた． XPS 研究では，酸化還元サンプルで異なった酸化段階のマンガンの存在があること，さらに，化学成分の化学的環境の変化が生じることが明らかとなった．さらに，熱重量分析測定と組織の関係を調べるために $BaLnMn_2O_{5+\delta}$ 粉末の微細組織（構造）の分析も行った．

全ての化合物の包括的なキャラクタリゼーションは，TG 法によりその酸素吸蔵関連特性に関して行った．全ての場合において，500 °C の等温実験，合成空気と 5 vol.%/H_2 を含むアルゴン雰囲気を切り替えながらの酸素吸蔵量(OSC)の測定では，理論値に近い値を記録し，雰囲気の変化に伴ってほぼ完全に酸化または還元し，完全に酸化した $BaLnMn_2O_6$ と完全に還元した $BaLnMn_2O_5$ に変化した．記録された可逆的な酸素吸蔵容量と化合物のモル質量とは強い相関関係があり，最も吸蔵量が高いのは $BaYMn_2O_{5+\delta}$ (3.71 wt.%)であり，最も低いものは $BaDyMn_2O_{5+\delta}$ (3.16

wt.%)である．すべての材料の還元プロセスは酸化プロセス(秒単位)と比較してかなり(数分単位)遅いこと，そしてそれ故に酸素吸蔵能のパフォーマンスに限界があることが分かった．これらの現象は酸化プロセスの発熱性に依存する．記録された還元時間の温度依存は，バルク中の酸素拡散に基づいて解釈でき，そのため，イオン輸送の活性化エネルギーを算出した．より大きな粒径を持つ材料はバルク中の結晶中の拡散長さが長くなるため，還元プロセスにおいて反応速度が低下する．さらに，$BaLnMn_2O_{5+\delta}$ 中に存在する Ln 陽イオンと酸化プロセスの特性温度の関係を示した．$BaLnMn_2O_{5+\delta}$ における酸素吸蔵量は商業的に実用化されている材料の特性を上回っていることを強調しておく．

第 7 章は新たな $BaErMn_2O_{5+\delta}$ システム($BaErMn_2O_5$ と $BaErMn_2O_6$)の物理化学特性の包括的な特性を示している．これらの両酸化物は，最も小さい Er^{3+}ランタノイド陽イオンを含む A サイト陽イオン秩序性をもつ $BaLnMn_2O_{5+\delta}$ に関するもので，本論文の結果は世界で初めて報告されたものとなる．構造特性のキャラクタリゼーション，酸素吸蔵能力，電気伝導率やゼーベック係数の温度依存性に関するデータは，$BaLnMn_2O_{5+\delta}$ システムについての知見を大いに広げることを可能とした．Er を含む材料の還元と酸化の間の単位体積の変化は最も小さいことが分かった．また，$BaErMn_2O_6$ は $BaErMn_2O_5$ よりも高い電気伝導性を示し，これは Mn^{3+}/Mn^{4+} の非局在化と Mn^{2+}/Mn^{3+} の局在化状態に関係していると考えられる．

第 8 章では，化合物中の酸素吸蔵能を最適化するために $BaY_{1-x}Ln_xMn_2O_{5+\delta}$ (Ln: Pr, Sm, Gd; x = 0.25, 0.5 and 0.75)のランタノイド元素をイットリウムによる部分置換を行った．結晶対称性の予測される変化を調べることのできる構造特性はさておき，置換量の増加に伴う単位格子パラメーター，格子体積および酸素吸蔵特性は複雑なふるまいを示し，ほとんど化学成分との関係を示さないことが分かった．今回調査した化合物の中で，最もよいパフォーマンスを示したのは $BaY_{0.75}Pr_{0.25}Mn_2O_{5+\delta}$ であった．このサンプルは 500 °C での 2 サイクル目の還元時間は 3.4 分であり，50 サイクル目では 2.6 分まで向上した．さらに，この測定した酸化物はサイクルを経ても構造の変化はなく，優れた安定性を示した．第 9 章には，$Ba_{1-y}Sr_yY_{1-x}Ln_xMn_2O_{5+\delta}$ (Ln: Pr, Sm and Gd)の二重部分置換の系統的な研究結果まとめた．相対的にBa^{2+}陽イオンをSr^{2+}陽イオンで置換できる量は狭い範囲であり，予測できる可逆的な酸素吸蔵能の向上を大いに制限することが分かった．そ

れにも関わらず，十分な酸素吸蔵特性は $Ba_{0.9}Sr_{0.1}Y_{0.75}Sm_{0.25}Mn_2O_{5+\delta}$ で，また，OSC の増加は $Ba_{0.9}Sr_{0.1}YMn_2O_{5+\delta}$ で得られた．

第 10 章では，OSC の大幅な向上の可能性について Fe や Co を含んだ酸化物の研究によって調査した．選択した材料の一般的な化学式は：$La_{0.6}Sr_{0.4}Co_{0.8}Fe_{0.2}O_{3-\delta}$, $La_{0.5}Sr_{0.5}Co_{0.5}Fe_{0.5}O_{3-\delta}$, $Sm_{0.5}Sr_{0.5}Co_{0.5}Fe_{0.5}O_{3-\delta}$, $La_{0.5}Ba_{0.5}Co_{0.5}Fe_{0.5}O_{3-\delta}$ および，$Sm_{0.5}Ba_{0.5}Co_{0.5}Fe_{0.5}O_{3-\delta}$ であり，それぞれ還元および酸化された形での結晶構造を調べた．$Sm_{0.5}Ba_{0.5}Co_{0.5}Fe_{0.5}O_{3-\delta}$ のケースでは，Sm^{3+}と Ba^{2+}の陽イオンが層状に秩序化した結晶構造が検出され，既に調べた Mn を含む酸化物のものと同様であった．最初に置換された $La_{0.6}Sr_{0.4}Co_{0.8}Fe_{0.2}O_{3-\delta}$, $La_{0.5}Sr_{0.5}Co_{0.5}Fe_{0.5}O_{3-\delta}$ と $Sm_{0.5}Sr_{0.5}Co_{0.5}Fe_{0.5}O_{3-\delta}$ は，酸化状態へ変化するとき，ブラウンミラライト型からペロブスカイト型に構造が変化することが XRD その場測定によって明らかになった．最も高い OSC(4 wt.%を超える)は $La_{0.6}Sr_{0.4}Co_{0.8}Fe_{0.2}O_{3-\delta}$ で，一方，500 °C において最も還元速度が速い(2.3 分)のは $La_{0.5}Sr_{0.5}Co_{0.5}Fe_{0.5}O_{3-\delta}$ であることが分かった．それらの材料は，また，イオン輸送の活性化エネルギーも小さいことが判明した．しかし，それらは，還元条件下で安定性が不足（特に高温度(500 °C 以上)するため，それらの応用の可能性を制限している．

第 11 章には，本研究の結果に基づいた結論および考察，さらに，OSM 材料の今後の研究に関する提案まとめた．また，本論文には 4 つの付録が含まれている．付録 A は，$BaLnMn_2O_{5+\delta}$ の高精度な構造解析に充てられたもので，これは米国の Argonne’s Laboratory Advanced Photon Source のシンクロトロン放射光測定のデータの解析によるものである．付録 B は，中性子回折測定のセットアップ関連の追加情報および取得したデータの構造精密化パラメータまとめた．

付録 C は，高エネルギーミリングプロセスによる OSM の特性改善に関して提出した特許出願の計画書の情報を示した．さらに，付録 D には，触媒および酸素キャリアとして用いた $BaYMn_2O_6$ とメタンの無炎酸化のいくつかの結果まとめた．

Abbreviations and symbols

AFI(CE)	Antiferromagnetic CE-type charge/orbital-ordered Insulator
AFM(A)	A-type Antiferromagnetic Metal
ASU	Air Separation Unit
BET	Brunauer-Emmett-Teller adsorption
BSCF	$Ba_{1-x}Sr_xCo_{1-y}Fe_yO_{3-\delta}$
CAGR	Compounded Annual Growth Rate
CL	Ceria-Lanthana solid solution
CLC	Chemical Looping Combustion
COI(CE)	CE-type charge/orbital-ordered Insulator
CZ	Ceria-Zirconia solid solution
DFT	Density Functional Theory
fcc	face-centered cubic phase
FM	Ferromagnetic Metal
FWHM	Full Width at Half Maximum
IGFC	Integrated Gasification Fuel Cell
ITM	Ionic Transport Membrane
J-T	Joule-Thomson cryogenic method
JTE	Jahn-Teller Effect
H-L	Hampson-Linde cycle
LSCF	$La_{1-x}Sr_xCo_{1-y}Fe_yO_{3-\delta}$
MIEC	Mixed Ionic-Electronic Conductor
MM	Mechanical milling
OSC	Oxygen Storage Capacity
OSM	Oxygen Storage Materials
PM	Paramagnetic Metal
PSA	Pressure Swing Adsorption
RT	Room Temperature
SEM	Scanning Electron Microscope
SOFC	Solid Oxide Fuel Cell
TG	Thermogravimetry
TMR	Transparency Market Research
tpd	ton per day
TSA	Temperature Swing Adsorption
TWC	Three Way Catalyst
VSA	Vacuum Swing Adsorption
XANES	X-ray Absorption Near Edge Structure
XPS	X-ray Photoelectron Spectroscopy
XRD	X-ray Diffraction

δ	Oxygen nonstoichiometry
a	Unit cell parameter *a* [Å]
a_p	Unit cell parameter of the simple cubic perovskite [Å]
b	Unit cell parameter *b* [Å]
c	Unit cell parameter *c* [Å]
C	Concentration of charge carriers [$mol \cdot m^{-3}$]
D	Diffusion coefficient [$cm^2 \cdot s^{-1}$]
D^{δ}	Bulk diffusion coefficient [$cm^2 \cdot s^{-1}$]
E_a	Activation energy [eV]
E_f	Fermi level energy [eV]
k	Boltzmann's constant [$J \cdot mol^{-1} \cdot K^{-1}$]
k^{gb}	Surface exchange coefficient on grain boundary [$cm \cdot s^{-1}$]
k^{δ}	Surface exchange coefficient [$cm^2 \cdot s^{-1}$]
m_{oxy}	Molar mass of the oxidized compound [$g \cdot mol^{-1}$]
m_{red}	Molar mass of the reduced compound [$g \cdot mol^{-1}$]
p	Total pressure [Pa, bar]
pO_2	Partial pressure of oxygen [Pa, bar]
Q	Charge [C]
r_A	Average radii of A-site cations [nm, Å]
r_B	Average radii of B-site cations [nm, Å]
r_O	Average radii of oxygen ion [nm, Å]
R_{wp}	Weighted profile residual from Rietveld refinement [%]
S	Sleight's degree of order parameter
t	Time [s]
T	Temperature [K, °C]
T_C	Curie temperature [K, °C]
T_{CO}	Temperature of charge order transition [K, °C]
T_N	Néel temperature [K, °C]
T_t	Phase transition temperature [K, °C]
t_S	Goldschmidt's tolerance factor
t_e	Goldschmidt's tolerance factor calculated from experimental data
U_{iso}	Isotropic atomic displacement parameter [$Å^2$]
V	Unit cell volume [$Å^3$]
V_f	Free volume [$Å^3$]
x_B	Fraction of (e.g) B cations in B-sublattice
α	Seebeck coefficient [$\mu V \cdot K^{-1}$]
λ	Air to fuel ratio
μ	Charge mobility [$m^2 \cdot V^{-1} \cdot s^{-1}$]
ρ_{RT}	Resistivity at RT [$\Omega \cdot cm$]
σ	Electrical conductivity [$S \cdot cm^{-1}$]
χ^2	Goodness of the fit parameter from Rietveld refinement

Publication list of the author

Directly contributing to the topic of the thesis

1. **A. Klimkowicz**, K. Świerczek, T. Rząsa, A. Takasaki, B. Dabrowski
„*Oxygen storage properties and catalytic activity of layer-ordered perovskites* $BaY_{1-x}Gd_xMn_2O_{5+\delta}$"
Solid States Ionics (2016), doi:10.1016/j.ssi.2016.01.038

2. **A. Klimkowicz**, K. Świerczek, A. Takasaki, J. Molenda, B. Dabrowski
"*Crystal structure and oxygen storage properties of* $BaLnMn_2O_{5+\delta}$ *(Ln: Pr, Nd, Sm, Gd, Dy, Er and Y) oxides*"
Materials Research Bulletin 65 (2015) 116-122, IF (2014) 2.288

3. K. Świerczek, **A. Klimkowicz**, A. Niemczyk, A. Olszewska, T. Rząsa, J. Molenda, A. Takasaki
"*Oxygen storage-related properties of substituted* $BaLnMn_2O_{5+\delta}$ *A-site ordered manganites*"
Functional Materials Letters 7(6) (2014) 1440004 1-4, IF 1.606

4. **A. Klimkowicz**, K. Świerczek, K. Zheng, M. Baranowska, A. Takasaki, B. Dabrowski
"*Evaluation of* $BaY_{1-x}Pr_xMn_2O_{5+\delta}$ *oxides for oxygen storage technology*"
Solid State Ionics 262 (2014) 659-663, IF 2.561

5. **A. Klimkowicz**, K. Świerczek, A. Takasaki, B. Dabrowski
"*Oxygen storage capability in Co- and Fe-containing perovskite-type oxides*"
Solid State Ionics 257 (2014) 23-28, IF 2.561

6. K. Świerczek, **A. Klimkowicz**, K. Zheng, B. Dabrowski
"*Synthesis, crystal structure and electrical properties of A-site cation ordered* $BaErMn_2O_5$ *and* $BaErMn_2O_6$"
Journal of Solid State Chemistry 203 (2013) 68-73, IF 2.200

7. K. Świerczek, **A. Klimkowicz**, L. Del Valle
chapter "*Technologia magazynowania tlenu w tlenkach perowskitowych*" (in Polish)
in "Paliwa i energia XXI wieku", G.S. Jodłowski (ed.)
Wydawnictwo Naukowe Akapit, 2014, ISBN 978-83-911589-6-8

8. **A. Klimkowicz**, K. Zheng, G. Fiołka, K. Świerczek
"*Modification of* $BaYMn_2O_{5+\delta}$ *perovskite in an aspect of development of oxygen storage technology in perovskite oxides*"
Chemik 67(12) (2013) 1202-1205

9. **A. Klimkowicz**, K. Zheng, G. Fiołka, K. Świerczek
"*Materiały ceramiczne z grupy perowskitów podwójnych na bazie* $BaYMn_2O_{5+\delta}$ *dla technologii magazynowania tlenu*" (in Polish)
Materiały ceramiczne / Ceramic Materials 65(1) (2013) 92-96

Other published work of the author

10. K. Świerczek, W. Zając, **A. Klimkowicz**, K. Zheng, N. Malikowa, B. Dabrowski
"*Crystal structure and proton conductivity in highly oxygen deficient* $Ba_{1-x}La_x(Zr,In,Sn)O_{3-\delta}$ *perovskites*"
Solid States Ionics 275 (2015) 58-61, IF (2014) 2.561

11. **A. Klimkowicz**, A. Takasaki, Ł. Gondek, H. Figiel, K. Świerczek
"*Hydrogen desorption properties of magnesium hydride catalyzed multiply with carbon and silicon*"
Journal of Alloys and Compounds, 645(S1) (2015) S80-S83, IF (2014) 2.999

12. K. Zheng, **A. Klimkowicz**, K. Świerczek, A. Malik, Y. Ariga, T. Tominaga, A. Takasaki
"*Chemical diffusion and surface exchange in selected Ln-Ba-Sr-Co-Fe perovskite-type oxides*"
Journal of Alloys and Compounds, 645(S1) (2015) S357-S360, IF (2014) 2.999

13. K. Zheng, K. Świerczek, J. Bratek, **A. Klimkowicz**
"*Cation-ordered perovskite-type anode and cathode materials for Solid Oxide Fuel Cells*"
Solid State Ionics 262 (2014) 354-358, IF 2.561

14. K. Świerczek, N. Yoshikura, K. Zheng, **A. Klimkowicz**
"*Correlation between crystal and transport properties in* $LnBa_{0.5}Sr_{0.5}Co_{1.5}Fe_{0.5}O_{5+\delta}$ *(Ln - selected lanthanides, Y)*"
Solid State Ionics 262 (2014) 645-649, IF 2.561

15. K. Zheng, K. Świerczek, W. Zając, **A. Klimkowicz**
"*Rock salt ordered-type double perovskite anode materials for Solid Oxide Fuel Cells*"
Solid State Ionics 257 (2014) 9-16, IF 2.561

16. K. Świerczek, K. Zheng, **A. Klimkowicz**
"*Optimization of transport properties of A-site ordered* $LnBa_{1-x}Sr_xCo_{2-y}Fe_yO_{5+\delta}$ *perovskite-type cathode materials*"
ECS Transactions 57(1) (2013) 1993-2001

Aim of the work

Oxygen is nowadays one of the most widely used industrial gas. The global market of gases, including O_2, is continuously growing, due to population and industrialization increase. Oxygen is essential for many technologies, such as: production of steel and non-ferrous metals, chemicals, petrochemicals, glass, ceramics, paper, but also it is used in healthcare and medicine. As such, relatively high costs of transportation and storage of the oxygen became a significant challenge. Regarding this, one of the possible solutions can be related to a small-scale oxygen generation in the place of use. Nevertheless, novel, cheaper and more effective ways of the oxygen production, storage and transportation has to be developed [1]. Demand for the oxygen on a large, industrial scale is fulfilled by plants using cryogenic methods. This is regarded nowadays as a mature technology [2]. On smaller scales, where purity of the obtained gas is not a main issue, so called Pressure Swing Adsorption (PSA) and related methods are considered to be suitable production routes [3, 4].

Interestingly, it seems possible to fundamentally modify PSA-type methods through usage of so called Oxygen Storage Materials (OSM) at elevated temperatures. This is due to the unique property of OSMs related to reduction and oxidation of the material, i.e. removal or incorporation of the oxygen from/into its crystal structure [5-7]. It is expected that a high-purity oxygen gas can be produced using OSMs, however, it seems also achievable to remove virtually all of the oxygen from a particular gas mixture, producing O_2-free gas.

Currently, the mentioned Oxygen Storage Materials are used commercially in Three-Way Catalysts (TWC) installed in exhaust system of nearly all vehicles powered with a petrol engine. In this application they act as additional, support catalyst, which is responsible for maintaining the suitable partial pressure of the oxygen (pO_2). This stems from the nature of three main chemical reactions occurring in the considered catalytic converters, i.e. [8]:

- oxidation of carbon monoxide,
- oxidation of unburned hydrocarbons,
- reduction of nitrogen oxides.

The reactions are catalyzed (on the main catalyst made of precious metals) in an efficient manner only if pO_2 in the flue gases remain on a certain level, close to the stoichiometric one.

In 2010 Motohashi et al. [5] published impressive data concerning oxygen storage related-properties of $BaYMn_2O_5$-$BaYMn_2O_6$ system, which seems to be the first candidate for the novel OSMs. The reported results indicate fast kinetics of reduction and oxidation reactions, as well as practical oxygen storage capacity (OSC) exceeding 3.7 wt.% at 500 °C, during gas change between air and 5 vol.% H_2 in Ar mixture, greatly exceeding that of the currently used OSMs. The published work attracted great interest of scientists, as the improved materials may be also used in many developing technologies and industrial processes, which require precise control of the oxygen partial pressure, including [5, 9-12]:

- separation of the components of air in respect to the oxygen,
- flameless combustion of hydrocarbons and other anaerobic oxidation processes,
- so called Clean Coal technologies relying on oxy-fuel, chemical looping, etc.,
- production of synthesis gas,
- high-temperature technologies that require high purity oxygen,
- photolysis of water,
- Solid Oxide Fuel Cell (SOFC) technology.

The proposed by Motohashi et al. system with reduced $BaYMn_2O_5$ and oxidized $BaYMn_2O_6$ materials belong to a wider group of cation-ordered perovskite-type oxides, which chemical composition can be written as $BaLnMn_2O_{5+\delta}$ (Ln: selected lanthanides) [5, 13, 14]. These compounds exhibit a specific layered-type ordering of Ba^{2+} and Ln^{3+} cations, and show unique transport and magnetic properties, which can be mainly associated with electronic states of manganese cations [15, 16]. However, until now, apart from the mentioned Y-containing oxides, other materials were not studied in terms of their oxygen storage-related properties. Also, no systematic data are available concerning possibility of formation of solid solutions by chemical substitution in barium or lanthanide sublattices.

Scientific aim of this work is to develop an effective synthesis route, obtain and study physicochemical properties, as well as optimize novel perovskite-based oxygen storage materials, which exhibit high oxygen storage capacity, fast reduction and oxidation

reactions kinetics, as well as show high reversibility of the processes. The precise objectives of this thesis can be described as follows:

1. Development of preparation method of single phase $BaLnMn_2O_{5+\delta}$ (Ln: Pr, Nd, Sm, Gd, Dy and Y) oxides with layered Ba-Ln cation ordering. Exploration of possibility of formation of solid solutions in Ln-site and Ba-site substituted materials with a general formula of $Ba_{1-y}Sr_yY_{1-x}Ln_xMn_2O_{5+\delta}$. Trials regarding introduction of smaller than Y^{3+} cations (e.g. Er^{3+}) into the Ln-site. Elaboration of role of ionic radii of the cations in formation of the Ba-Ln ordered structure (see Fig. 1 below).
2. Systematic characterization of the synthesized materials in terms of their crystal structure at room at high temperatures, powder morphology, oxygen stoichiometry and its influence on the structural properties, as well as oxidation state of the elements.
3. Elaboration of a model of the reduction process of $BaLnMn_2O_{5+\delta}$ materials.
4. Throughout characterization of the oxygen storage-related properties of the compounds, such as reversible oxygen storage capacity at elevated temperatures, kinetics of the reduction (oxygen removal) and oxidation (oxygen incorporation) processes, determination of the characteristic temperatures of these processes. Elucidation of the relationship between chemical composition, crystal structure and oxygen storage behavior in the considered group of oxides.
5. Optimization of the materials in terms of the chemical composition, as well as modification of the preparation method, in order to obtain compounds with the improved properties, suitable for commercial application.
6. Studies regarding next generation OSMs exhibiting OSC exceeding 4 wt.% (focused on selected group of Co- and Fe-containing perovskite-type oxides).
7. Preliminary research concerning possibility of application and catalytic activity of the OSMs in a process of flameless oxidation of methane.

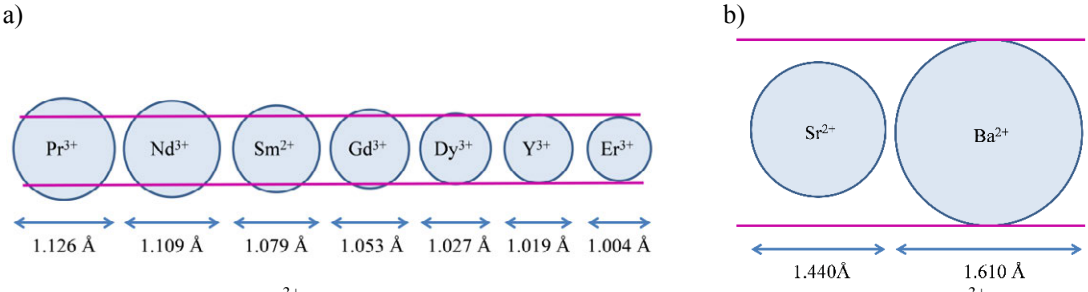

Fig. 1. a) Ionic radii of La^{3+} cations in 8-fold coordination (lines given in comparison to Y^{3+}), b) ionic radii of Ba^{2+} and Sr^{2+} cations in 12-fold coordination [17].

Introduction and literature review

1. Oxygen production and storage methods

Worldwide industrial gases market, according to Transparency Market Research (TMR) [1], was approximated at USD 38.0 billion in the year 2011, and is predicted to show a compounded annual growth rate (CAGR) of 6.3% by 2018, to the value of USD 58.4 billion. In 2011 hydrogen gas had the biggest market share, and was foreseen to be the fastest growing segment, at an estimated CAGR of 6% from 2012 to 2018. For comparison, for nitrogen the demand is estimated to reach USD 6.2 billion worldwide in the same year. Steady increase in the oxygen production and consumption is also observed, and the market is expected to expand up to USD 6.1 billion by 2018, mainly due to an increase of demand from developing countries. For industrial production processes of steel and non-ferrous metals, chemicals, petrochemicals, glass, ceramics, paper, as well as in healthcare and medicine sector, oxygen is essential.

The largest consumer of the oxygen is steel industry. It requires large amounts of this gas, on the order of 580 000 tones daily (tpd), using about 50% of the globally produced amount of O_2. Such big demand is satisfied by commercial companies (e.g. Air Liquide, Linde Group, Praxair Inc. and Air Products and Chemicals Inc.) under long-term contracts [18]. Production of steel can be proceeded in a more efficient way by implementation of enhanced technologies (such as direct coal injection or direct reduction furnaces), where oxygen is used to enrich the air, which in consequence leads to an increase of combustion temperature. Over the years, the demand for oxygen in steel production increased, from about 15 m^3 O_2 per ton of steel in 1970s up to approximately 100 m^3 O_2 per ton of steel, for some of the production processes nowadays.

Large, but diffused market for the oxygen is healthcare and medical sector. The O_2 gas is used for treatment of such respiratory diseases as chronic asthma, cystic fibrosis, chronic obstructive pulmonary disease. Also, it is used for helping patients with heart failure-related conditions, but also during a medical emergency. Oxygen therapy is often used not only in the hospitals, but also during the first aid action and in the course of transportation of the patients. Some veterinary clinics are equipped with the oxygen generation stations too. Rise of demand for the oxygen gas is also predicted in this branch of industry, which is caused by development of the health care, aging of population, unhealthy lifestyle, as well as by the increasing air pollution [1, 19, 20].

Important consumer of the oxygen is chemical industry, which is related mainly to manufacturing of refined products like petrochemicals, agrochemicals, pharmaceuticals and polymers. For instance, Gasworld [18] reports on a significant increase in the oxygen demand, which occurred over the past decade in Saudi Arabia, where the petrochemical sector is consuming now about 8,000 tpd of the oxygen.

At the moment the need for the oxygen at the large scale is mainly carried out by usage of cryogenic methods, as described in chapter 1.1 below. These methods require a complex system of production and maintenance, specific conditions of pressure and temperature, which make them energy-consuming and costly. Another applicable on the industrial scale method, based on separation of O_2 from air, is Pressure Swing Adsorption (PSA). It is based on a difference in chemical affinity of the air components in relation to the adsorbents. PSA systems are characterized by near-ambient operating temperature, and therefore are cheaper in operation. Also, their design is less complicated, comparing to the cryogenic systems. Further description of this and similar methods is given in chapter 1.2. The two mentioned technologies are nowadays considered as mature. Another proposed oxygen production method relies on application of polymeric membranes (mature technology) or ceramic ones (still in material development and testing stage), as described in more details in chapter 1.3. Comparison of the presented technologies of the oxygen production can be found in chapter 1.4, while information about systems used for the oxygen storage is included in chapter 1.5.

1.1. Cryogenic liquefaction processes

Polish scientists from Jagiellonian University in Krakow, Z. Wróblewski and K. Olszewski were the first who successfully liquefied the main constituents of air in 1883. Considering industrial application, the cryogenic liquefaction process utilizing Joule-Thompson (J-T) effect, i.e. temperature change of a gas (or a liquid) during its forced flow through a valve (or porous plug) under isenthalpic conditions [21], was firstly carried out in 1895, and then further developed by dr. Carl von Linde [22]. The basis of the method relies on a difference in condensing temperature of the gases being components of the air (Tab. 1.1). In order to carry out a gas (or gas mixture) liquefaction process, it is necessary to obtain temperature below the respective condensation temperature at the corresponding

pressure. For air, according to Linde group, the operating conditions are T_{crit} = -140.7 °C (132.5 K) and p_{crit} = 37.7 bar. It is worth noting that on a temperature versus pressure diagram, a condensation line and a boiling point line delineate differ and create a boiling point range in between [22].

Tab. 1.1. Composition of dry air and the respective boiling points under normal pressure. Based on [22].

composition of dry air		vol.%	boiling point [°C]
N_2	nitrogen	78.08	-195.8
O_2	oxygen	20.95	-183.0
Ar	argon	0.93	-185.9
CO_2	carbon dioxide	$3.8 \cdot 10^{-2}$	
He	helium	$5.0 \cdot 10^{-3}$	-268.9
Ne	neon	$1.8 \cdot 10^{-3}$	-246.1
Kr	krypton	$1.1 \cdot 10^{-4}$	-153.2
Xe	xenon	$0.9 \cdot 10^{-5}$	-108.0

The simple Linde-Hampson (L-H) cycle for gas liquefaction, with schematics of the main components of the plant, as well as thermodynamic cycle data, is depicted in Fig. 1.1. More advanced cycles can be also considered, like pre-cooled or dual-pressure L-H. Alternatively, Claude cycle can be also used for gas liquefaction, with more complicated variations like low-pressure Kapitza or high-pressure Heylandt cycles for air liquefaction. In another variant, Collins liquefier was developed to liquefy helium [23, 24].

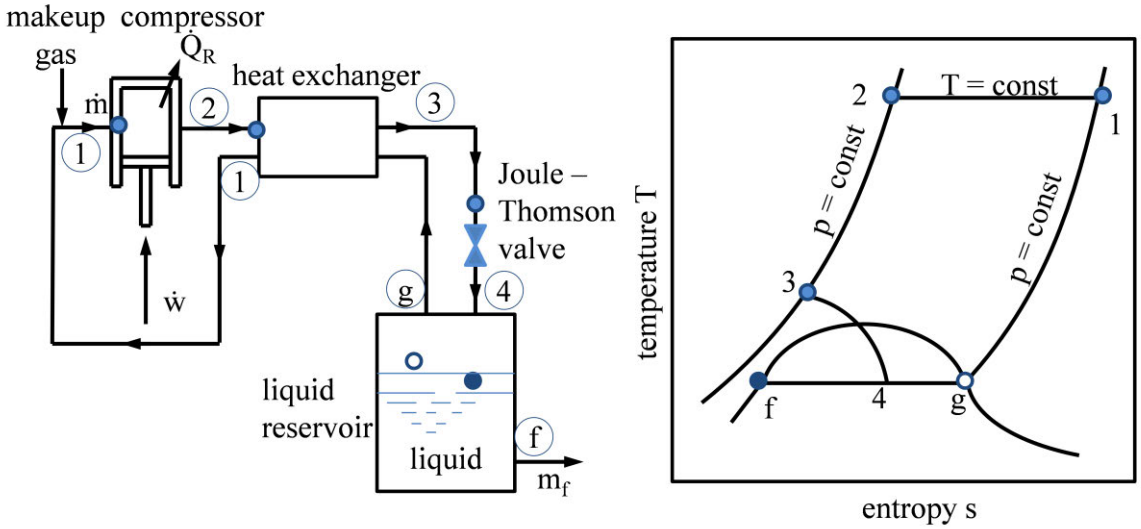

Fig. 1.1. Schematics of Linde-Hampson cycle. The numbers and symbols correspond on the left and right diagrams, respectively. ẇ - work requirement, $\dot{Q}_R$ - heat flow, $\dot{m}$ - mass flow rate. Based on [23].

In 1902 C. von Linde designed a separation plant for the oxygen production using a single column cryogenic rectification system. Further enhancements resulted in production of the oxygen and pure nitrogen simultaneously, which was achieved in a double-column rectification system.

Operation of typical, currently used system for cryogenic air separation, which allows for a production of liquid oxygen, liquid nitrogen and liquid argon, can be described in the six following steps [25-27]:

- *Compression of air*

  Ambient air is compressed at a pressure of about 6 bar. At this preliminary step dust particles are removed by a mechanical air filter.
- *Cooling and purification of air*

  At this stage processed air is water-cooled in a direct contact cooler. Dissolvable impurities are removed from the air together with CO_2, water vapor and hydrocarbons, using periodically loaded/regenerated molecular sieve-type adsorbers. For cooling, dry waste nitrogen gas, obtained in further steps of the process, is used.
- *Low-temperature heat exchange*

  The treated air is cooled down, to nearly liquefaction temperature, by countercurrent dry waste nitrogen flow.
- *Cold production and internal product compression*

  Side stream of the process air is further compressed by an air booster compressor. At the same time boosted air stream expands in a turbine, and the side stream of the boosted air expands and liquefies in a liquid separator. Oxygen and nitrogen products, in high-pressure heat exchangers, are evaporated and warmed up to the ambient temperature.
- *Cryogenic rectification of air*

  At this step pre-separation takes place in the pressure column. Oxygen-rich liquid gathers in the column sump, and pure N_2 at top of the column. Pure nitrogen is liquefied in the condenser/re-boiler using boiling oxygen. In the low-pressure column, the oxygen-enriched liquid if further executed, leading to the production of clean oxygen in the sump of the column, and nitrogen waste gas at the top.

- *Cryogenic rectification of argon*

  Argon-enriched gas is transformed to crude argon for further separation, and finally gets to pure argon column, for the last step of purification. Liquid oxygen from the crude argon column is pumped back to the low-pressure column.

1.2. Pressure-driven adsorption processes

Alternative methods used at the present time for the oxygen production on an industrial scale rely on separation of air components via pressure- and/or temperature-driven adsorption processes. Among them, Pressure Swing Adsorption (PSA) and Vacuum Swing Adsorption (VSA) methods should be mentioned. The pioneers of PSA invention were Finlayson and Sharp, who in 1932 obtained the first patent [28]. The technology, however, was developed further and introduced commercially in the 1960s. There are numerous variations of the technology available, but in general principle, the methods are based on a separation of a mixture of gases, using different chemical affinity of the adsorbing molecular sieves, in relation to the constituents of the gas mixture, depending also on the thermodynamic conditions (total pressure, partial pressure, temperature) [29-33]. The main advantage of the adsorption-type methods is a possibility to carry out the process at the temperature close to the ambient one, and therefore, there is no thermal energy exchange, as well as time and energy consuming cooling is not required. Pressure-driven adsorption and desorption processes are cyclical in nature, and consequently, a sequence of steps (adsorption, purge, equalization, evacuation, and re-pressurization) is mainly used, in which gas purification occurs successively in a number of connected vessels containing adsorbent material. Eventually (after time on the order of hours), a steady state is reached, and the composition profiles remain relatively constant at a given step, providing for example 88-94% pure oxygen as a product. PSA is often combined with the Temperature Swing Adsorption (TSA) method, for the best efficiency [26].

In general, PSA technology is mainly used for production of nitrogen or hydrogen, but also can be used to obtain oxygen-enriched gas. The conventional PSA schematics is depicted in Fig. 1.2. The purification steps of the commercial technique with two vessels containing the adsorbent can be described as follows:

- The feedstock of mixed gases is (cyclically) pumped at an elevated pressure through the system with two cylinders that contain beads of adsorbent material.
- The impurities in the feedstock gas are adsorbed onto surface of the adsorbent beads, leaving demanded, purified gas in the vessel. This step is the fastest one, and takes approximately 10 s. The purified gas is redirected through the system back to the other cylinder, for another cycle of purification.
- Release of the impurities from the adsorbent material can be done by reduction of a pressure in the cylinder. A small amount of product, purified gas, is used to rinse the waste gas out of the vessel and prepare it for another purification cycle.

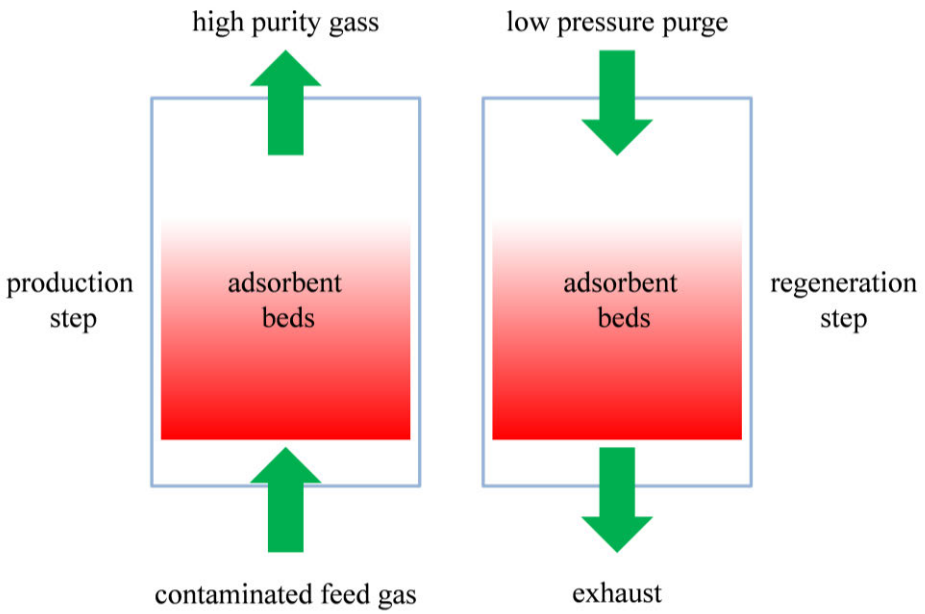

Fig. 1.2. Working principle of a conventional PSA, based on [34].

Nowadays, Pressure Swing Adsorption technique is often modified into VSA process that also commonly operates at near-ambient temperatures. The dissimilarity of this method, comparing to PSA, is in the adsorbents that adsorb the target gas at near ambient pressure, but for the regeneration of the material, the vacuum conditions are used [35].

Due to the nature of the adsorption processes, the adsorbents are required to possess specific properties, such as: developed porous surface and high capacity (amount of adsorbate taken by the material per unit of mass or volume) preferably at low pressures, selectivity and fast kinetics of the respective gas adsorption, stability in working conditions, and last, but not least, should be easily regenerated, and their production costs should be low. Rarely single adsorbent can fulfill all of these requirements. Generally, the

adsorbents can be divided in two groups: inorganic materials, such as aluminas, silicas, zeolites and organic materials, such as carbons, polymers and biomass-related [36, 37].

Currently, the most commonly used adsorbents in pressure-driven adsorption processes are zeolites with a general formula of $AB_xO_{2x}\cdot H_2O$, where A: Na, K, Li, Ca, Ba or Sr, and B: Si and Al in proportion in a range of 5:1 to 1:1. Naturally occurring zeolites do not exhibit sufficient selectivity for the separation of the oxygen from air, however, with synthetic zeolites it became possible to produce purified oxygen. Material having $Na_{12}[(AlO_2)_{12}(SiO_2)_{12}]\cdot 27H_2O$ composition shows the best performance concerning nitrogen uptake, and is used for the oxygen purification. Number of zeolites have been already used for air separation, natural gas upgrading, refined gas separation, but also for air pre-purification, gas drying and Ar/O_2 enrichment. More details, with additional examples concerning adsorbents and special zeolites can be found in the literature [38, 39 and references therein].

Nowadays many companies offer easy-to-operate and safe PSA-based systems. Such smaller-scale oxygen production units (e.g. PSA Oxygen Gas Plant [40]) are demanded in various industries, including production of the oxygen for the medical usage.

1.3. Usage of membranes for the oxygen production

Commonly available solution for production of the oxygen-enriched air relies on usage of polymer membranes, which purify demanded gas from nitrogen. For this process the driving force is a partial pressure difference between two sides of the membrane [41]. It is also worth mentioning that in the water electrolysis process, usually used for hydrogen production and based on polymer electrolyte membrane (PEM) such as Nafion®, oxygen is also produced [42]. The interested reader can find more information about application of polymer membranes for example in works [43, 44].

Recently there is a growing interest in usage of alternative, ceramic-type membranes. So called technology of ionic transport membranes (ITM), also known as dense ceramic membranes is considered a very promising alternative for the oxygen production, even though a research effort is still focused on development of new materials. Considered materials (usually a dense ceramic sinters) that effectively conduct oxygen anions belong

to groups of: perovskite-type oxides (ABO_3), fluorites (AO_2), brownmillerite-type oxides ($A_2B_2O_5$), Ruddlesden-Popper series ($A_{n+1}B_nO_{3n+1}$) or similar compounds [3, 45-47].

High oxygen ion conductivity is always necessary for the membrane to work, and with a lack of the electronic component of the conductivity, diffusion of the oxygen is driven by an applied voltage (Fig. 1.3a). An additional electronic conductivity of the membrane material results in simplification of the engineering design that reduces the operating and input costs. In this case, the driving force for the diffusion process is related to a difference of the oxygen partial pressure between both sides of the membrane (Fig. 1.3b). Considering needed high, mixed ionic-electronic conductivity, perovskite-type oxides are among the most attractive compounds for the application [3].

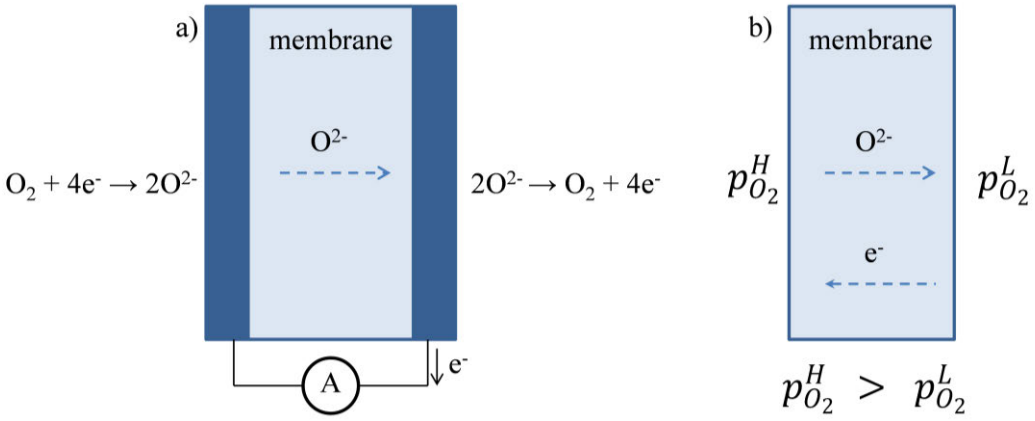

Fig. 1.3. Ceramic oxygen-conducting membranes: a) pure O^{2-} conductor, b) mixed ionic-electronic conductor (MIEC-type membrane). Based on [3].

According to da Costa et al. [3] in terms of membrane operation, five steps can be distinguished:

- *Feed side gas transport*

  The molecules of oxygen are transported from the gas phase to the membrane surface by gas diffusion.
- *Dissociation (surface reaction) on interface I (feed side)*

  The oxygen molecules are adsorbed on the membrane surface, and then disassociate, due to a catalytic activity of the ceramic material. This step is controlled by the kinetics of the surface dissociation.

- *Ionic transport (bulk diffusion)*

  The oxygen ions diffuse through the crystal lattice of the material, which is driven by a partial pressure gradient of oxygen across the membrane. Electrons are transported in the opposite direction (either in the outer electric circuit or through the membrane, see Fig. 1.3) to maintain electrical neutrality of the membrane. Effectiveness of this step depends on the thickness of the membrane and is associated with bulk diffusion.
- *Association (surface reaction) on interface II (permeate side)*

  The oxygen ions recombine into oxygen molecules and desorb from the membrane surface. The process is controlled by the kinetics of the surface association reaction.
- *Permeate side gas transport*

  The oxygen molecules are transported to the permeate stream by gas diffusion.

Among major issues still being resolved in this technology, except for a choice of the membrane material itself, problems with fabrication of desired geometry of the ceramic sinters are essential. Also, while thickness of the membrane is of great importance, and can be reduced to enhance bulk diffusion, below so called critical length, speed of the surface exchange reaction becomes a limiting factor for the operation [47] and the mechanical stability might be insufficient.

1.4. Comparison of the oxygen production methods

Comparison of selected, main types of the oxygen production methods is collected in Tab. 1.2. Choice of the applied technology depends on the required purity of the oxygen, demand on the gas, costs of the initial capital required and energy consumption during the production process, and also on suitability for joint installations. For the commercial, high-scale systems, the purest O_2 gas can be obtained via cryogenic method, and due to this, the waste nitrogen stream is of a usable quality as well [48]. Pressure-driven adsorption methods are suitable when lower volume and lower purity of the produced oxygen is sufficient. Currently commercial systems operating on the polymeric membranes are used mainly to enrich the gas up to 40 vol.% of O_2. However, it is possible to obtain high-purity gas, especially with membranes used for electrolysis of water [44]. At the present time

technology of ceramic ITMs is still being developed, but new installations will be soon operating, with much higher oxygen production capability, on the order of 100 O_2 tpd [3].

Tab.1.2. Comparison of available oxygen production methods. Based on [3].

technology	**cryogenic air separation**	**pressure swing adsorption**	**polymeric membranes**[a]	**ceramic ITMs**
current status	mature	mature	mature	demonstration
O_2 purity (vol.%) [48] (remaining impurities)	99+ (Ar)	95 (Ar)	40-100[b] (N_2, CO_2, H_2O)	100
O_2 flow rate in largest installations (O_2 tpd)	> 3000 [49]	< 350 [50]	< 20 for oxygen enriched combustion applications	5
installed capital cost in oxy-fuel or IGCC plant (USD per kWe)[c]	310-500[c] [50, 51]	150-200 for standalone PSA system producing < 150 O_2 tpd [52]	95-160 for a 30 vol.% O_2 stream [53]	260-295 [51, 53]
energy consumption in oxy-fuel or IGCC plant (kWh per 1 ton of O_2)	245-670[d] [51, 53]	~ 450-700 [54]	260 for 40 vol.% O_2 stream [55] 190-240 for hybrid membrane/cryogenic system [52]	100-655[e] [51, 53]

[a]Typical usage. [b]For the electrolyser. [c]Value in US dollars (2008) per electrical power installed in kW. [d]Wide range in these values reflects the differing O_2 flow rates required and energy integration opportunities available for oxy-fuel and IGCC applications. [e]The largest value includes heating value of natural gas for generating required operating temperatures for ITM system, whereas the smallest value represents only the electrical energy input.

1.5. Oxygen storage systems

Storage of oxygen is implemented mainly in a form of oxygen tanks, where oxygen is either cooled down and kept in a liquid form in special cryogenic tanks or stored in a gaseous form in high-pressure tanks. High pressure tanks are used for smaller volume of the oxygen needed, and are produced by many companies. Materials used for the cylinder construction vary, starting from aluminum through steel to carbon composite materials. In a typical, steel gas cylinder with a water volume of 20-50 dm^3, the oxygen pressure is equal to 150-200 atm. Tanks to store on the small scale liquefied gases, including oxygen, are vacuum-jacketed Dewar flasks. This type of container is not pressurized. The liquefied

gas is prevented from escaping and isolated from the atmospheric moisture by a loose-fitting dust cap located at a neck of a tubes. Commonly, 5- to 200-liter Dewar flasks are available [56]. On the larger scale oxygen is usually stored in special cryogenic liquid cylinders (Fig. 1.4). When the gas is required, vaporizer is used to deliver oxygen in gaseous state, however, for some technical processes, e.g. food freezing, liquefied oxygen is used. According to Air Products [56, 57], typical installation for the oxygen storage contains a tank, a vaporizer, and controls, as depicted in a schematic figure below (Fig. 1.5). Usually systems are personalized, depending on user's requirements and needs to supply gas with desired parameters, such as pressure, purity level, flow rate.

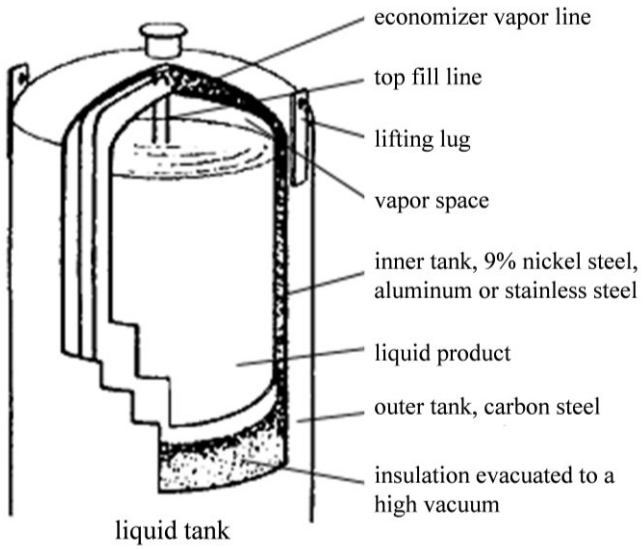

Fig. 1.4. Cutaway of a typical tank for storage of liquefied gas [57].

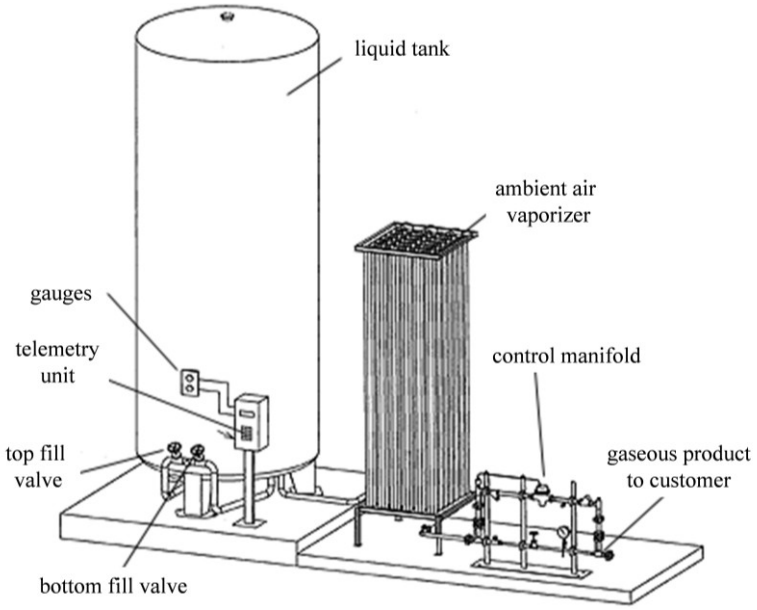

Fig. 1.5. A typical liquid storage system used for argon, nitrogen and oxygen [56].

As described above, storage of gases is commonly done in gaseous form in high-pressure cylinders or liquefied form in special tanks or Dewar-type containers. However, gas storage in solids, especially the hydrogen storage realized in a form of absorption or adsorption in various hydrides, carbon-based materials and zeolites, is worth mentioning [58].

Interestingly, with a development of OSMs, storage of the oxygen in oxides can be also conducted. Comparison of typical gas cylinder with solid oxide storage systems is presented in Tab. 1.3.

Tab. 1.3. Comparison of oxygen storage systems.

storage system	**stored oxygen [kg]**	**volume (water capacity) [dm^3]**	**mass of the system with oxygen**	**OSC [wt.%]**	**special requirements**
typical gas cylinder	7	40	70	~ 10	storage pressure: 150 atm, spatial tank,
$BaYMn_2O_5$-$BaYMn_2O_6$ system	7	35	~ 215	~ 3.7	special system to release the oxygen,

Typical gas cylinder with a water capacity of 40 dm^3 allows for a storage of approximately 7 kg of the oxygen at a pressure of about 150 atm, and weighs 70 kg (mass of the cylinder plus the mass of the stored oxygen) [59]. This corresponds to the OSC equal to about 10 wt.%. For comparison, $BaYMn_2O_5$-$BaYMn_2O_6$ system possesses reversible OSC exceeding 3.7 wt.% at 500 °C [5]. Nevertheless, considering the density of the oxidized $BaYMn_2O_6$ (~ 6.2 g·cm^{-3}), the total volume, in which the same amount of the oxygen can be stored a volume of less than 35 dm^3 of the OSM. While the total weight would be much higher than the corresponding gas cylinder (exceeding ~ 215 kg), the storage would not need any special container or expensive maintenance of a low temperature conditions. However, a special system would be necessary to release the stored oxygen (allowing for an increase of the temperature up to about 500 °C with a precisely controlled pO_2 at the same time). It seems that future development of OSMs (with much higher OSC) may bring practical possibility of storing oxygen in this way.

2. Oxygen storage in solids

Investigations of the oxygen incorporation reaction mechanism into oxides gained recently a lot of interest, mainly because of two reasons. First, from a scientific point of view, it is a fundamental case of chemical reaction between gaseous and solid state, and therefore of interest for both, theoreticians and practical scientists. By controlling of the oxygen content either via chemical or electrochemical oxidation it was possible to obtain materials with unique physicochemical properties. For instance, by electrochemical oxidation of $SrCoO_{3-\delta}$ at room temperature in KOH solution, which proceeds via topotactic-type route (so called oxygen intercalation), stoichiometric and cubic $SrCoO_3$ oxide was produced [60-62]. Second, with a rapid development and application of electrochemical devices such as gas sensors and solid oxide fuel cells, which operation relies on the reaction of the electrode material with oxygen, understanding of the electrode process allows to design novel compounds, exhibiting enhanced properties. This results in an improved performance of the device, but also may help to solve crucial issues of degradation of materials, and therefore is of a high technological relevance [63, 64]. Currently, there are many elaborated models describing the mechanism of oxygen introduction into the structure of perovskite oxide, although in the literature there is no homogenous theory developed, but rather, the case studies of selected oxides are given.

Considering the main topic of this thesis, in the following chapters oxygen storage materials are discussed in details. Chapter 2.1 shows general introduction to the topic. As discussion of the mechanism of the oxygen incorporation into oxides requires knowledge also about surface reactions and catalytic activity, the following chapter 2.2 is focused on a description of basic catalytic properties of the materials. Reported in the literature description of reaction of the oxygen with perovskite-type oxides is given in chapter 2.3. In the last part of this section, four different systems of the oxygen storage materials are presented.

2.1. Oxygen storage materials - introduction

Many oxides exhibit intrinsic oxygen nonstoichiometry, which may change significantly, depending on the temperature and the oxygen partial pressure in a surrounding atmosphere. This is, however, not enough for a particular material to be considered as the oxygen storage material. The crucial issue in this case is related to a possibility of reversible changes of the oxygen content. The ideal oxygen storage material should exhibit the following properties [65]:

- large, highly-reversible oxygen storage capacity (OSC),
- fast speed of incorporation and release of the oxygen,
- chemical and thermal stability in the working conditions,
- low operating temperature (depending on the application),
- low cost of manufacturing and operation,
- environmental friendly.

In general, two major types of the OSM can be distinguished, depending on the nature of the reduction/oxidation process. In the simplest case, systems of various metals and their simple oxides (e.g. Cu-Cu_2O-CuO, see chapter 3.4) can be used to store the oxygen. While the OSC is very high in such materials, the reaction with O_2 is accompanied by complete change of the crystal structure between the phases, and therefore, problems related to reversibility and long-term usage appear. Alternatively, in complex oxides, only part of the oxygen can be reversibly removed/introduced, and while the OSC in this case in much smaller, the reversibility can be very high. The changing oxygen content can be directly related to the oxygen nonstoichiometry level, however, the changes are beyond the simple, point defect-type range and interpretation.

So far numerous oxides have been investigated in terms of the OSM criteria listed above. Exemplary materials and their basic properties are given in Tab. 2.1. More details regarding selected oxygen storage systems are gathered in chapter 2.4.

Unit commonly used for comparison of oxygen capacity between materials is given as μmol of O stored in 1 g of the reduced material (Tab. 2.1). Another, more comfortable in usage unit, is a weight percent of stored oxygen in the oxidize material in relation to the reduced one. For example, $BaYMn_2O_5$-$BaYMn_2O_6$ system can store ~ 2400 μmol $O \cdot g^{-1}$,

which is equivalent to 3.85 wt.% of the stored oxygen. Concerning author's results, in the thesis the second unit (wt.%) will be used.

Tab. 2.1. Comparison of oxygen storage materials, based on [65].

compound	type of structure	OSC [wt.%]	OSC [µmol O·g^{-1}]	temperature and atmosphere for oxygen uptake/release processes
$Ce_{1-x}Zr_xO_{2-\delta}$ [66]	fluorite	2.78	~ 1700	oxidation in oxygen atmosphere and reversible reduction in 20 vol.% H_2 at 500 °C
$YBaCo_4O_{7+\delta}$ [67]	hexagonal	4.32	~ 2700	oxidation at 200-400 °C and reduction at 400-425 °C both in O_2
$Dy_{1-x}Y_xMnO_{3+\delta}$ [68]	hexagonal	1.97	~ 1200	oxidation under high pressure oxygen at 500 °C and reduction in H_2 at 400 °C
$Ca_2AlMnO_{5+\delta}$ [69]	brownmillerite	3.04	~ 1900	reversible oxygen intake/release at 500-700 °C in O_2
$LuFe_2O_{4+\delta}$ [70]	layered structure of alternating [LuO_2] and [Fe_2O_4] layers	2.28	~ 1400	oxidation at 200-500 °C under an oxygen pressure of ~ $0.2 \cdot 10^{-3}$ atm and reduction in H_2 from 500 °C
$BaYMn_2O_{5+\delta}$ [5, 71]	double perovskite	3.84	~ 2400	oxidation at 200-390 °C in O_2 and reduction at 200-490 °C under 5 vol.% H_2 in Ar

2.2. Surface reactions and catalytic processes

In heterogeneous system of gaseous and solid phases, surface reactions are of great importance, with adsorption of the gas species on the material being a key factor for the reactivity, including also catalytic processes. This is also of a great importance for the oxygen storage materials.

Depending on the forces acting between adsorbent and adsorbate, physical (van der Waals forces) and chemical (chemical bonds) adsorption can be distinguished. The whole process is complex and there are many physical models describing it. One of the simplest theory of adsorption at a constant temperature has been proposed by Langmuir, and is based on the following conditions [72]:

- surface of the adsorbent contains a fixed number of places (seats) for the adsorbed molecules, called active centers,
- one place can be occupied only by one molecule (it is possible to produce only a mono-molecular layer),
- heat of adsorption is constant, regardless of a degree of surface coverage,
- dynamic equilibrium is established between adsorption and desorption processes.

The Langmuir theory refers to the ideal case where the adsorption takes place on the energetically homogeneous surface, and there are no interactions between the adsorbate molecules. In this theory, with an increase of pressure, isotherm of the adsorption reaches a certain value. This theoretical model is a foundation for other, more complex models. For example in 1931, Brauner, Emmet and Teller developed a multi-molecular adsorption theory, named after the authors as BET. In their model, with an increase of pressure, the isotherm increases to infinity, which results from assumed formation of infinite-layer structure [72]. Practical accuracy of this theory is limited to certain values of pressure, when dependence of rate coverage on pressure is linear. BET theory is widely used for determination of the specific surface area of the materials (e.g. powders).

Models of reactions on catalytically-active surfaces

Adsorption processes are closely related to the catalytic activity of the materials. In heterogeneous catalysis, investigations in the matter of adsorption and desorption of gas molecules at the catalytically-active surfaces and their interaction with surface molecules of the solid, has led to a number of proposed mechanisms of reactions occurring on the surface. The most frequently used models are presented schematically in Fig. 2.1 [73].

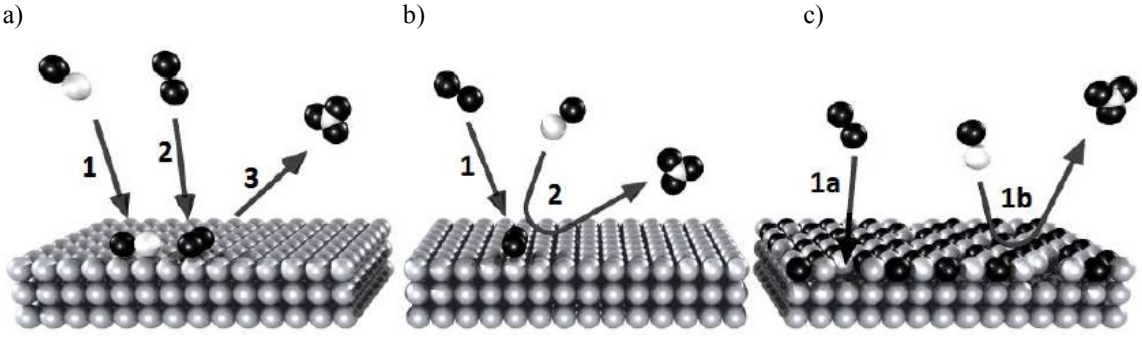

Fig. 2.1. a) Langmuir-Hinshelwood mechanism, b) Eley-Rideal mechanism, c) Mars-van Krevelen mechanism [73].

Part (a) in Fig. 2.1 shows the Langmuir-Hinshelwood mechanism, according to which both reactants are adsorbed on the surface "1" and "2", prior to the occurrence of the reaction. Catalysis itself proceeds via the collision of atoms of adsorbed molecules on the catalytic material, and the reaction product is desorbed from the surface "3". The reactivity in this type of mechanism is the highest when stoichiometric amounts of reagents are adsorbed on the surface of the catalyst. Even distribution of the reactants throughout the surface is also of importance. Majority of the catalytic reactions take place according to this mechanism, for example, oxidation of CO to CO_2 on platinum catalyst (occurring for example in the main catalyst in three-way catalytic converters used in exhaust system of petrol engine cars) [72].

When the catalytic reaction takes place according to Eley-Rideal mechanism, part (b) in Fig. 2.1, only one of the substrates is adsorbed on the surface "1", and the second one reacts directly from the gas phase, resulting in a desorption of the reaction product "2". The reaction rate in this case is proportional to the pressure of reactant in the gas phase and the surface coverage by the adsorbing substrate. Exemplary reaction taking place according to the Eley-Rideal mechanism is hydrogenation of CO_2 during synthesis of formate on the copper catalyst. In such reaction hydrogen is adsorbed on the Cu substrate [72, 73].

In Mars-van Krevelen mechanism, part (c) in Fig. 2.1, surface of the catalyst takes an active part in the reaction, involving formation of chemical bonds between it and one of the substrates with creation of a thin layer "1a". The second reactant interacts with atoms chemically bonded on the surface directly from the gas phase "1b". After desorption of the reaction product, formation of vacancies takes place. Then, the vacancies interact with another particles of the reagent to start another cycle of the catalysis process. For example, according to this model some of the oxidation reactions are catalyzed, such as the oxidation of propene to propenal on bismuth molybdate [72].

In general, efficiency of heterogeneous catalytic process is mainly related to the amount of active centers on the catalyst, on which the adsorption process occurs preferentially. In many processes, precious metals (e.g. platinum) are used as catalytic materials, and therefore, usually the catalyst is constructed as a thin layer covering the porous surface of a substrate made from much cheaper carrier material (e.g. Al_2O_3). This is to obtain the best possible surface-to-volume ratio, while minimizing catalyst manufacturing costs [72].

Taking into account the oxygen storage-related properties of the studied perovskite-type $BaLnMn_2O_{5+\delta}$ oxides, their catalytic activity might be expected in reactions involving

oxygen. For instance, as reported by Motohashi et al. [5], towards flameless methane combustion. This issue is discussed in more details below in chapter 3.2.

2.3. Mechanism of oxygen incorporation into perovskite-type oxides

As mentioned above, there is no single theory developed, which can explain all issues related to incorporation of the oxygen into oxides, but rather particular cases are studied in more details.

The authors of work [60] analyzed results of depth-resolved O-*K* and Co-*L* near edge XANES spectroscopy for series of $SrCoO_{3-\delta}$ oxides with high and different oxygen nonstoichiometry ($0.18 \leq \delta \leq 0.5$). The obtained results and their analysis indicated that surface of the particles of materials is highly-defected, which allows for a rapid diffusion of the oxygen. However, there is a big difference in the Co-O coordination type between the surface region and bulk of the grains. The chemical reaction of incorporation of the oxygen into $SrCoO_{3-\delta}$ can be described with the following steps [60]:

- Oxygen incorporation starts from surface absorption of O_2 molecule, which is filling an oxygen vacancy position next to the tetrahedrally coordinated cobalt. The molecule is also reduced to O_2^- superoxide species.
- The incorporated O_2^- is gradually reduced and split into O^{x-} intermediate species. At the same time the neighboring Co-O coordination polyhedron is changing from tetrahedron to a square-pyramid.
- In the bulk, the O^{x-} is re-oxidized to O^{z-} ($0 < z < x$), with a notable $O2_p$ ligand hole character.

The authors noticed very small chemical shifts of Co-$L_{2,3}$ edge upon oxygenation, and concluded that the described processes mostly involve electron transfers between the oxygen atoms, which do not have the formal oxidation state of -2. Generally, the whole described process of incorporation of the oxygen into $SrCoO_{3-\delta}$ oxide can be compared with intercalation of lithium into electrode materials used in lithium ion batteries. It proceeds as a topotactic (meaning that the basic framework crystal structure is maintained throughout whole process) redox-type reaction (with changes of the oxidation state of the

oxygen and cobalt), and therefore it can be named as oxygen intercalation [60]. One additional result from work [60] should be cited. The authors noticed lower diffusion coefficient of the oxygen in the bulk, comparing to the surface-related steps of the oxygen intercalation. This has profound influence on the oxygen-storage-related properties, due to a possible, limiting condition for the kinetics of the oxygen insertion and removal into/from material's structure. Generally, while the described above mechanism was discussed for $SrCoO_{3-\delta}$, it seems that it might be also used to analyze behavior of perovskite-type oxygen storage materials.

In literature there are comprehensive data available regarding oxygen nonstoichiometry δ [74-76], as well kinetics of the oxygen transport [77-80] in various Mn-, Fe- and Co-containing perovskite-type oxides. However, due to their possible application as cathode materials in Solid Oxide Fuel Cells, usually data are presented concerning operating conditions of SOFCs (e.g. T = 800 °C, air). Apart from experimental results, also density functional theory (DFT) studies are shown, and for example, Mastrikov et al. [81] demonstrated that $(Co_{1-y}Fe_y)$-O chemical bonding is strongly influenced by covalence effects in $Ba_{1-x}Sr_xCo_{1-y}Fe_yO_{3-\delta}$, with effective charges of cobalt and iron cations being smaller than their formal oxidation state +4. This result is in agreement with work [60], indicating higher than -2 state of the oxygen in $SrCoO_{3-\delta}$. The authors concluded that formation of the oxygen vacancies causes transfer of the electronic density to the nearest Fe and Co cations and reduction of their oxidation state, as expected. Also, it was found that the nearest Co cations receive larger electron density fraction, comparing to the nearest Fe cations, but unexpectedly, the increase of the averaged atomic charge is greater for Fe than for Co cations [81]. The authors also noticed that the oxygen vacancy formation energy in $Ba_{1-x}Sr_xCo_{1-y}Fe_yO_{3-\delta}$ materials is much smaller than for isostructural $LaMnO_3$ and $SrTiO_3$ oxides, and from practical point of view, it means orders of magnitude increase in vacancy concentration at elevated temperatures, which is desirable for fast oxygen transport in various energy-related applications [81].

In other theoretical works, pathways for oxygen incorporation into $La_{1-x}Sr_xMnO_{3-\delta}$ perovskites were studied by DFT-based technique (Fig. 2.2 and 2.3) [82, 83]. The authors concluded that the most favorable oxygen incorporation pathway is on the MnO_2 [001] termination of the material. This is partially due to a much lower concentration of the oxygen vacancies on the LaO termination of $La_{1-x}Sr_xMnO_{3-\delta}$. The rate-determining step can be related to a meeting between adsorbed O^- and the oxygen vacancy on the surface, which corresponds to a thermally activated diffusion of the vacancy along the surface. It

can be therefore stated that a high surface vacancy concentration and a high mobility are beneficial for a high reaction rate. At lower pO_2 a change in the rate-determining step can be ascribed to the actual dissociation of molecular oxygen.

The authors of cited works [82, 83] noticed complex nature of the oxygen incorporation into $La_{1-x}Sr_xMnO_{3-\delta}$, during which surface transport steps, as well as actual dissociation reactions can become limiting.

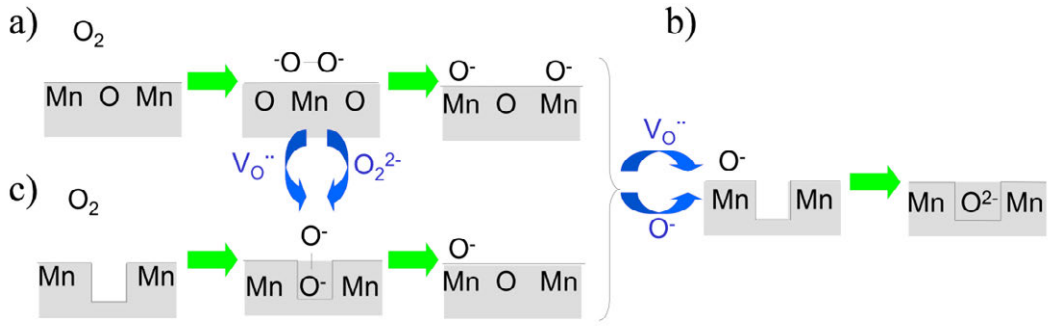

Fig. 2.2. Three possible scenarios of oxygen incorporation into $La_{1-x}Sr_xMnO_{3-\delta}$. a) O_2 adsorption and dissociation without vacancy, b) O_2 adsorption without vacancy but dissociation with the oxygen vacancy $V_O^{\cdot\cdot}$ assistance, and c) O_2 adsorption directly into vacancy [83].

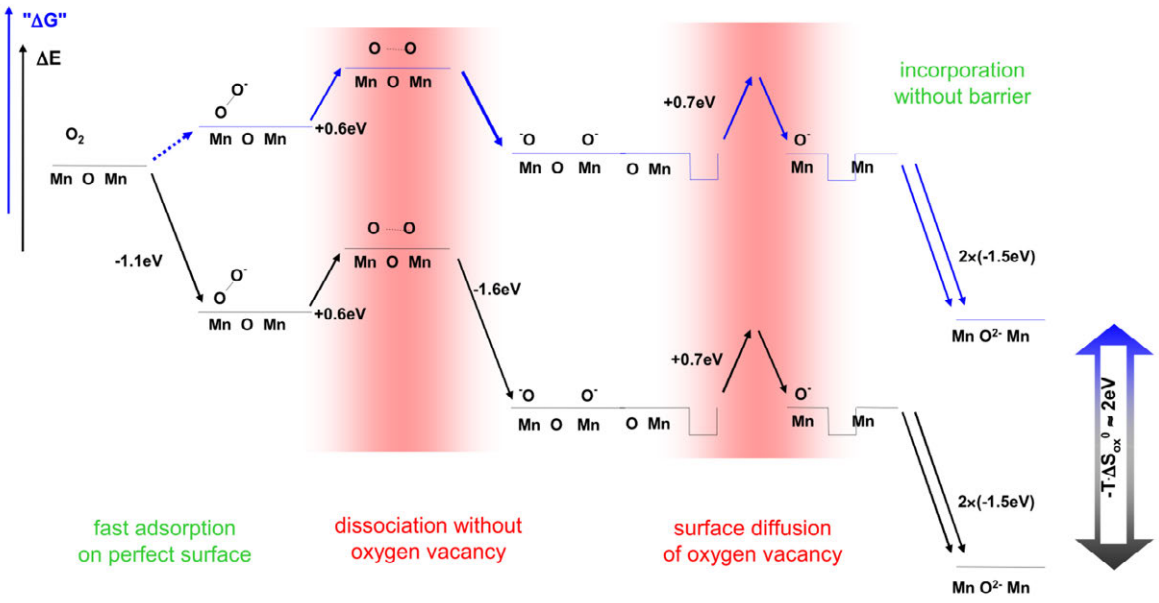

Fig. 2.3. Total energy (black) and Gibbs free energy (blue) profiles of the most probable oxygen incorporation mechanism into $La_{1-x}Sr_xMnO_{3-\delta}$. Possible rate determining steps are marked in red [82, 83].

According to Merkle and Maier [84], reaction of oxygen intake into Fe-doped $SrTiO_{3-\delta}$ sinters exhibiting mixed ionic-electronic conduction can be divided into three following steps: 1) surface reaction including chemical kinetics at the surface and transport through the subsurface layer, 2) bulk transport, 3) transport across (or along) internal boundaries. General model showing such transport processes is displayed in Fig. 2.4. Depending on the slowest (determining) processes, four sub-models can be also presented, taking into account bulk diffusion coefficient D^{δ}, the surface reaction $\bar{k}^{\delta}$ and the grain boundary $\bar{k}^{\delta}_{gb}$ constants (for simplicity assumed to be isotropic along and across the boundaries) [84, 85].

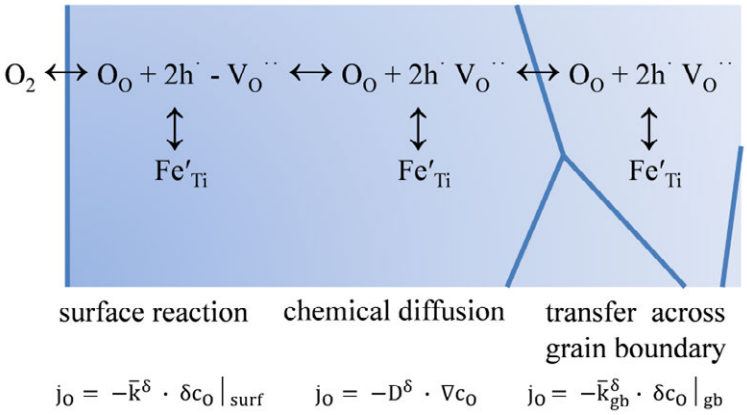

Fig. 2.4. General model of the transport process in Fe-doped $SrTiO_3$ that includes basic equations describing surface reaction, chemical diffusion and transfer across grain boundary. Based on [84, 85].

As presented in Fig. 2.5, in the first case (a) the surface reaction is fast, and there is no fast diffusion path nor blocking observed on the grain boundary. In the second situation (b) the surface reaction is slow, but the diffusion inside the grain is fast. In the next considered case (c) the surface reaction occurs fast, and the grain boundary provides fast diffusion path. In the last possibility (d) the reaction on the surface is fast but grain boundary is a limiting factor [84, 85].

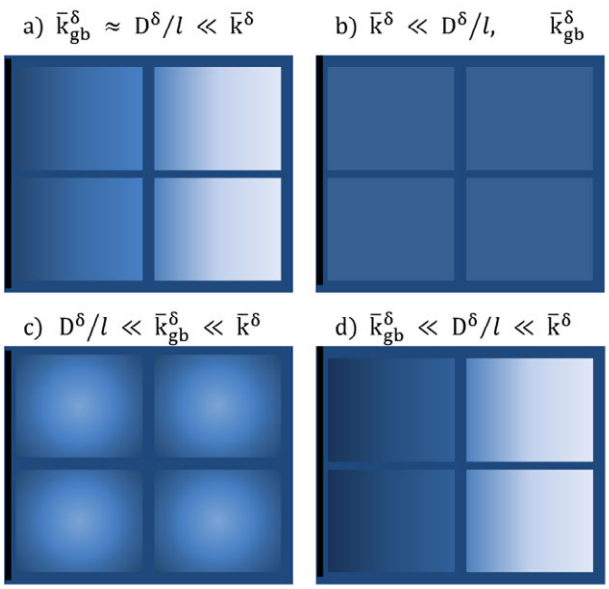

Fig. 2.5. Schematics of oxygen incorporation into a four grain crystal sample of the thickness l (shade of blue refers to the increasing oxygen concentration, dark line refers to the surface of the material). Figure based on [84, 85].

Oxygen release at high temperatures (and/or low pO_2) causes significant changes in thermal expansion and is also influencing mixed ionic-conductivity of the material. These two parameter are of crucial importance from the viewpoint of application of particular oxide in SOFC or ceramic membrane technologies [85, 86]. It should be also emphasized that many oxidation catalysts possess good mixed conducting properties, and the contribution of lattice oxygen is of great important on the catalytic activity, as well as selectivity of the material [84]. Therefore, high catalytic activity of various OSMs is both, expected and confirmed.

Changes of the oxygen content influence also electrical properties of the materials, and for example, the mentioned $SrTiO_{3-\delta}$ can transform from *n*-type to *p*-type electronic conductor with pO_2 change from 10^{-25} to 10^{-5} bar at 800 °C, corresponding to changes of the oxygen content of about 10 ppm [84]. Magnetoresistance of this compound was also shown to be dependent on the oxygen content [87]. Obviously, changes of δ may also influence crystal structure of the compound. More discussion about this issue is presented in chapter 4, where brownmillerite-type crystal structure was presented and compared with the perovskite-type one.

2.4. Oxygen storage materials systems

As presented in Tab. 2.1, various oxygen storage materials are investigated nowadays. Selected system are described below: commonly used ceria-zirconia or ceria-lanthana oxides, sulfur-based system of a particularly high OSC, $Y_{1-x}Ln_xMnO_{3+\delta}$ operating with a constant oxygen partial pressure but due a temperature swing, as well as the mentioned $BaYMn_2O_5$-$BaYMn_2O_6$ system, which is a reference for most of studied in this work OSMs.

2.4.1. Ceria-based oxygen storage materials

At the present moment $Ce_{1-x}Zr_xO_{2-\delta}$ and $Ce_{1-x}La_xO_{2-\delta}$ oxides are commercialized as oxygen storage materials. The systems are commonly referred in the literature as CZ and CL, respectively [66, 88]. In both cases, an ability of cerium for a reversible change of the oxidation state between Ce^{4+} and Ce^{3+} in the fluorite structure, which may take place depending on the temperature and the oxygen partial pressure, is utilized. For example, $Ce_{0.5}Zr_{0.5}O_{2-\delta}$ material possesses theoretical oxygen storage capacity of 0.5 mol of O_2 per mol of the compound, which corresponds to 2.78 wt.% change in relation to the reduced material. In a general case of $Ce_{1-x}Zr_xO_{2-\delta}$ redox-type reaction related to the oxygen storage can be written as (1):

$$Ce^{4+}_{1-x}Zr_xO_2 \leftrightarrow Ce^{4+}_{1-x-y}Ce^{3+}_{y}Zr_xO_{2-y/2} + y/4\,O_2 \qquad (1)$$

For commercialization on a large scale in three-way catalytic converters (see chapter 3.1) an improvement of the properties of CZ and CL was needed, and so called second and third generation OSMs (especially prepared solid solutions, as well as materials doped with Al_2O_3) were introduced. However, technology of these materials seems to reach its limits. Undoubtedly, the advantage of ceria-based systems stems for their high catalytic activity for conversion of CO, NO_x and CH_x, which is directly related to the high oxygen storage capacity [66, 88].

2.4.2. Ln_2O_2S-$Ln_2O_2SO_4$ systems

Recently, Machida et al. [89, 90] introduced novel oxygen storage materials, lanthanide oxysulfates, with a general formula of $Ln_2O_2SO_4$ (Ln: La, Pr, Nd and Sm), which work using ability of sulfur to change its oxidation state. Systems operate according to the reaction (2):

$$Ln_2O_2S^{6+}O_4 \leftrightarrow Ln_2O_2S^{2-} + 2O_2 \quad (2)$$

Theoretical oxygen storage capacity in this case is particularly high, 2 mol O_2 per mol of the compound (18.50 wt.%). However, disadvantages of this system can be related to a higher operating temperature (≥ 600 °C) and problems with sulfur evaporation [91]. Among the series of proposed materials, sample containing praseodymium possesses the lowest operating temperature, which can be related to an ability of praseodymium to change its oxidation state (i.e. Pr^{3+}/Pr^{4+}). Also, praseodymium present the surface plays a role of mediator for the sulfur redox reaction. Some additional work regarding microstructural and chemical modifications were also conducted, but reversibility of this system still remains insufficient. Despite this fact, patent application was granted on $Ln_2O_2SO_4$ materials, supported by noble metals as oxygen storage and release materials and exhaust gas purifying catalysts [92].

2.4.3. $Ln_{1-x}Y_xMnO_{3+\delta}$ systems

Some oxygen storage materials, as for example among others $Dy_{1-x}Y_xMnO_{3+\delta}$ manganites of a hexagonal structure, do not require change of oxygen partial pressure for operation (change of oxygen content), but rather change of the temperature [93, 94]. Relatively narrow range of a temperature swing between 200-400 °C depending on the composition allows to reversibly store up to even 1233 μmol $O \cdot g^{-1}$ (~ 2 wt.%) as in the case of $Dy_{0.7}Y_{0.3}MnO_{3+\delta}$ compound. This property makes the materials handy for application in production of purified gases using temperature swing absorption techniques. Introduction of other Ln cations in $Dy_{1-x}Y_x$ sublattice allows for modification of the operation temperature and also results in changes of the oxygen storage capacity as presented in Fig. 2.6.

It is worth mentioning that described materials incorporate oxygen into interstitial positions (in contrary to single perovskites $LnMO_{3-\delta}$ (M: Fe, Mn, Co, and Cu or double perovskites $BaLnMn_2O_{5+\delta}$), which is possible due to low formation energy of such defects at relatively low temperature. The stability of the oxidized phase increases with an increase of the ionic radii of Ln cation in $LnMnO_{3+\delta}$ group of oxides [92].

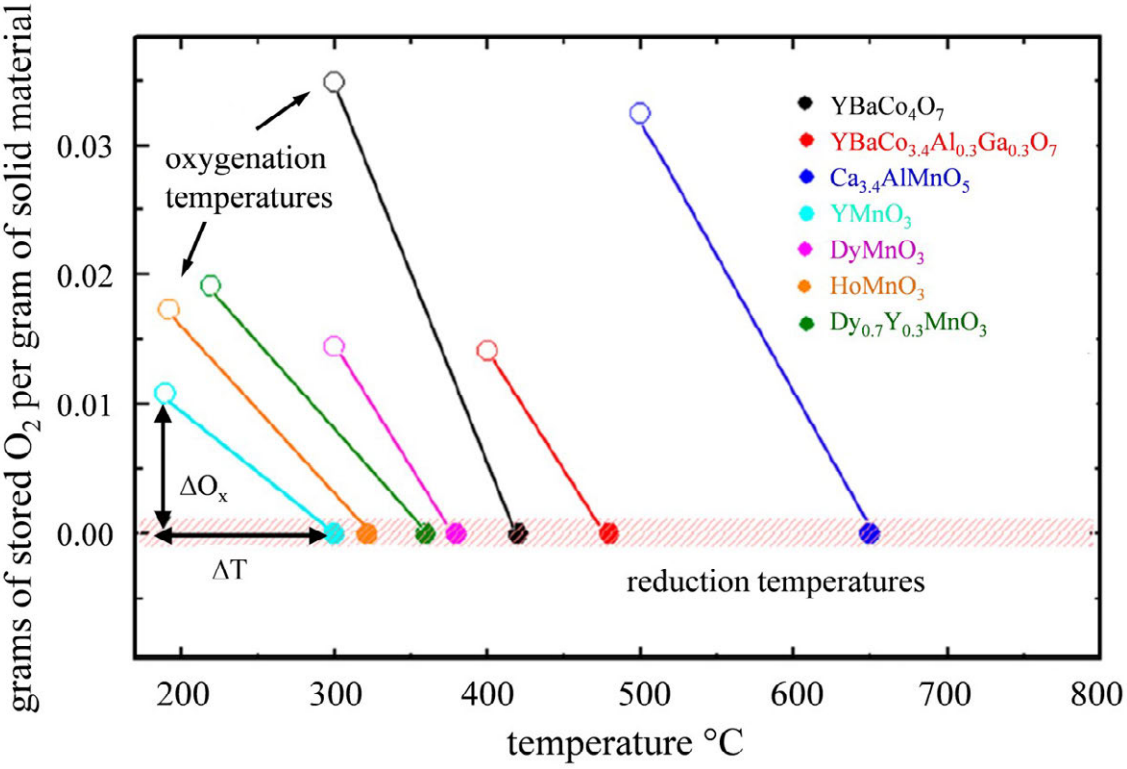

Fig. 2.6. Comparison of the temperatures of reduction (solid circles) and oxidation (open circles), the temperature sweep interval $\Delta T = T_{red} - T_{oxi}$, and the amount of stored oxygen per gram of material, ΔO_x, for several oxygen storage systems [93].

2.4.4. $BaYMn_2O_5$-$BaYMn_2O_6$ system

In 2010 Motohashi et al. reported high reversible oxygen storage capacity in the $BaYMn_2O_5$-$BaYMn_2O_6$ system, suggesting its possible practical usage [5]. Ability for reversible storage of the oxygen in $BaYMn_2O_{5+\delta}$ originates from possible changes of the oxidation state of manganese cations present in the perovskite-type structure. Oxygen storage-related reaction can be written in this case as (3):

$$BaYMn^{3+}Mn^{4+}O_6 \leftrightarrow BaYMn^{2+}Mn^{3+}O_5 + 1/2\,O_2 \qquad (3)$$

As can be seen, in the oxidized compound formally, Mn^{3+} and Mn^{4+} cations are present, which are reduced to Mn^{2+} and Mn^{3+} in $BaYMn_2O_5$. The change between the fully oxidized and the completely reduced material is accompanied by a release of 0.5 mol of O_2, which corresponds to the theoretical weight change of 3.85 wt.% of the oxidized material in relation to the reduced one. Complete oxidation of $BaYMn_2O_5$ occurs below 400 °C during annealing in air or oxygen, whereas reduction of $BaYMn_2O_6$ takes place below 500 °C in the atmosphere of 5 vol.% H_2 in Ar or at 550-600 °C in pure nitrogen [7]. These conditions correspond perfectly with the ones present in the mentioned three-way catalytic converters, and therefore the system seems attractive for application. What is more, sharpness of the oxidation and reduction processes is greater for this materials than for the other systems described above [71].

For a crystallographic point of view, during reduction of $BaYMn_2O_6$ the oxygen is preferably removed from the positions in the Y-related layer, changing coordination of the manganese cations. However, for large changes in the oxygen stoichiometry, the classical, point defect-related notation of the processes is not adequate, as such big changes of the oxygen content cause shifts of atoms and structural distortions, despite that the structural framework is preserved. More detailed description of these issues is given in chapter 4.5.

3. Application of oxygen storage materials

Oxygen storage materials, due to their ability to reversibly store oxygen in the structure and catalytic activity already found implementation in several commercial technologies. Most widespread application of OSMs is in the three-way catalytic converters, which constitute a part of the exhaust system of vehicles equipped with the petrol engine. This usage of OSMs is described in chapter 3.1. Another use is related to chemical looping combustion processes (chapter 3.2), with new results published about flameless methane combustion utilizing $BaYMn_2O_6$ as a catalyst, as presented in chapter 3.3. While many more possible applications might be considered (see Aim of the work section and references [5, 9-12]), one particular, also concerning Clean Coal technology and focused on improved Integrated Gasification Fuel Cell system, is described in more details in chapter 3.4.

3.1. Three-way catalytic converters for automotive industry

Importance of application of an effectively working three-way catalytic converter (TWC) can be emphasized by giving the estimated number of vehicles on operation that in recent past exceed 1 billion [95]. Even though some of the vehicles operate on diesel engines or are equipped with alternative power systems (hybrid or electric cars), conversion of dangerous and toxic gases (CO, CH_x and NO_x) is of importance, and the current solutions need to be improved in terms of efficiency and price. Initially, the converters were developed as two-way catalysts, allowing only for conversion of CO and CH_x. Later, a more advanced ones were constructed, which enabled to convert NO_x gases as well. These converters, dubbed as three-way catalysts, allow for the following reactions to take place:

- oxidation of carbon monoxide (4):

$$2CO + O_2 \rightarrow 2CO_2 \quad (4)$$

- combustion of unburned carbohydrates (5):

$$C_xH_{2x+2} + \left[\frac{3x+1}{2}\right]O_2 \rightarrow xCO_2 + (x+1)H_2O \tag{5}$$

- reduction of nitrogen oxides (6):

$$2NO_x \rightarrow xO_2 + N_2 \tag{6}$$

A typical construction of TWC is presented in Fig. 3.1. The main part of the device is a honeycomb-structured monolith made of ceramic or metal (aluminum oxide is most commonly used). The honeycomb structure results in a significant increase of the reaction area to volume ratio, and therefore provides maximally possible contact with the flowing exhaust gas. The monolith is a support for the embedded noble metals (the main catalyst), as well as oxygen storage material (which acts as an auxiliary catalyst) [96-98]. The most commonly used precious metal is platinum, because of its very good catalytic properties towards both, oxidation and reduction reactions. Other precious metals like palladium (as the reduction catalyst) and rhodium (as the oxidation catalyst) are also used, depending on a specific technical solution.

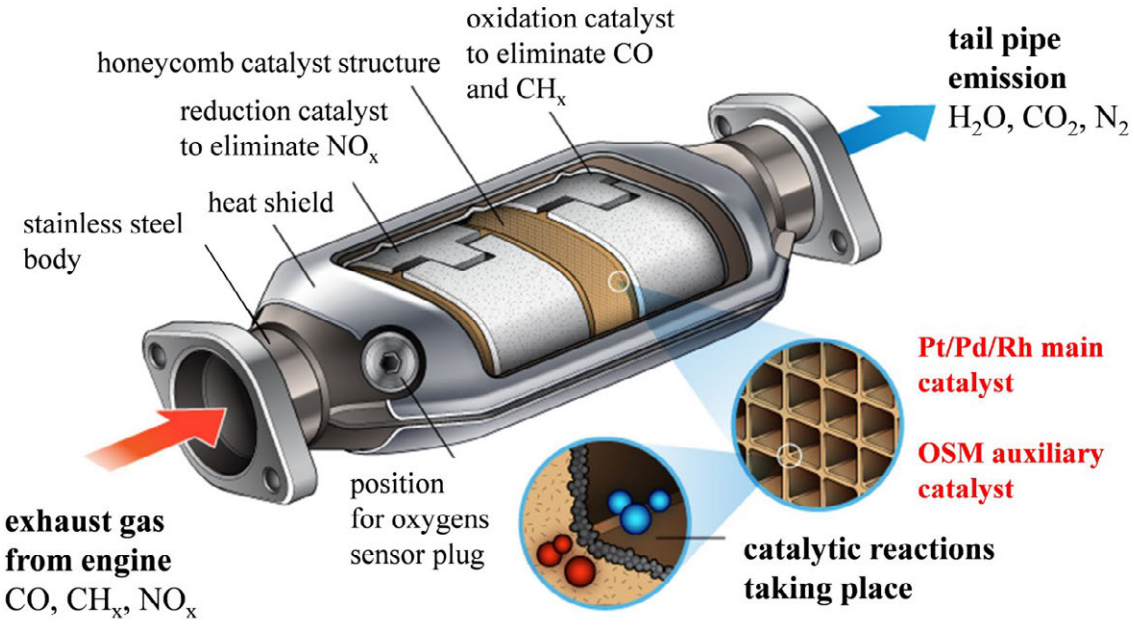

Fig. 3.1. Three-way catalytic converter, based on [99].

Nowadays, computerized closed-loop feedback injection system, equipped with at least one oxygen sensor (lambda probe) is used in commercial vehicles, with additional sensor commonly mounted for supplementary control. This system is responsible for controlling of the appropriate amount of injected fuel and supplied air. However, under rich conditions (excess of fuel), occurring in the case of rapid acceleration of the vehicle, not enough oxygen is available in the exhaust gases for the oxidation reactions (conversion of CO and CH_x) on the main catalyst. At this point the needed oxygen is released from the oxygen storage material, which therefore can be described as the auxiliary catalyst, helping to maintain the appropriate oxygen partial pressure. Oxygen storage capacity of OSM is thus one of the main indicators of quality of such catalyst, as larger capacity would allow for a longer operation time. Under lean conditions (excess of air), depleted OSM will absorb oxygen back, decreasing pO_2, and so will help to catalyze decomposition of NO_x. Consequently, it can be stated that the main role of the OSM in three-way catalytic converter is to help maintaining the appropriate oxygen partial pressure in the exhaust gas, which is crucial in terms of efficiency of the conversion rates on the main catalyst.

As presented in Fig. 3.2, in order to obtain simultaneously high conversion efficiency of carbon monoxide, unburned hydrocarbons and nitrogen oxides in the TWC, the ratio of air to fuel supplied to the engine must be kept within a narrow range. Typical gasoline engines operate at the air to fuel ratio λ oscillating between 0.997 and 1.003 [100].

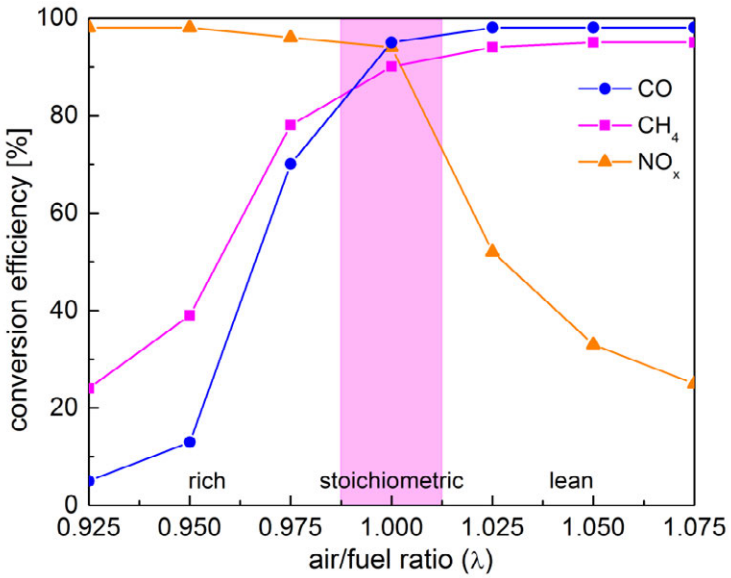

Fig. 3.2. Effect of the air to fuel ratio λ on the operation of a catalyst converter, based on [101].

Air to fuel ratio depends also on other factors, such as speed and way of driving or outside temperature, which depends on location, season and weather. Moreover, vulnerable point is a start of the vehicle, as well as the first few minutes of its operation, which generate higher emissions (so called cold start emissions) [102].

Detailed oxygen storage modeling in three-way catalytic converters can be found in works [103-105]. Nevertheless, faster kinetics, moderated reaction temperatures and higher gravimetric oxygen storage capacity seem to be important factors for the effectively working OSM. New materials, apart from the commercialized CZ and CL, such as perovskite-type oxides with a general formula of ABO_3 (A: La, Sm, Gd, etc.; B: Cr, Mn, Fe, Co, Ni, etc.) are of interest for this application [106]. This is also due to the fact that such perovskites exhibit good oxidation catalytic activity for flameless combustions of hydrocarbons, as well as can be improved by addition of a noble metals like Pt, Pd, or Rh at the B-site. It was proven, however, that noble metal tend to exsolute from the perovskite structure, and this process is not fully reversible. Nevertheless, tests of these materials applied in real-scale TWCs are now planned [106].

3.2. Chemical looping combustion

Novel combustion technology called chemical looping combustion (CLC) was developed, which relies on a principle of burning a fuel without mixing it with the molecular air, but rather with using so called oxygen carrier. This oxygen carrier is in fact also the oxygen storage material. The CLC method involves cyclic reduction and oxidation of OSM (e.g. simple Mn, Fe or Ni oxides) to provide oxygen needed for the combustion. Initially, the oxygen carrier is reduced in the reactor, and the oxidation of a fuel takes place, according to the summary reaction (7) [107]:

$$(2n + m)Me_xO_y + C_nH_{2m} \rightarrow (2n + m)Me_xO_{y-1} + nCO_2 + mH_2O \quad (7)$$

Then, the reduced OSM needs to be re-oxidized, however, this process takes place outside of the main fuel reactor, in so called air reactor. The oxidation reaction can be written as (8):

$$2Me_xO_{y-1} + O_2 \rightarrow 2Me_xO_y \quad (8)$$

In this technical solution produced stream of CO_2-containing exhaust is already suitable for sequestration or other utilization. The advantage of the CLC combustion, in comparison with the traditional one, is related to the lower emission of harmful CO and NO_x. In order to maintain high effectiveness of the process, noble metals such as platinum, palladium, rhodium or iridium (embedded and immobilized on Al_2O_3) are used [106]. The needed OSM materials, suitable for CLC, are required to have high reversible oxygen storage capacity, but also must be very stable in working conditions (i.e. high temperature, reducing atmosphere). Among materials proposed for this application are also perovskites-type ABO_3 (A: La, Sr; B: Mn, Fe, Co) oxides. These compounds exhibit interesting redox properties connected with the oxygen nonstoichiometry and can release oxygen according to the following reaction (9):

$$ABO_{(3-\delta)AR} \leftrightarrow ABO_{(3-\delta)FR} + \frac{1}{2}(\delta_{FR} - \delta_{AR})O_2 \tag{9}$$

Where AR and FR refer to air and fuel reactors, respectively [107-109].

Recently Q. Song et al. [109] demonstrated applicability of Cu-based OSM in such application. The authors proposed sintering method based on calcination of Cu-Al layered double hydroxides as precursors to obtain these novel OSMs. The synthesized composites, which operation mechanism is based on reversible phase changes between CuO, Cu_2O and Cu work effectively at temperatures in 800-1000 °C range, delivering very high OSC on the order of 12 wt.%. Usage of such the OSM is also attractive due to possible elimination of otherwise needed noble metals, which could results in decreased costs of the CLC system. A schematic representation of the proposed OSM for the chemical looping combustion is given in Fig. 3.3.

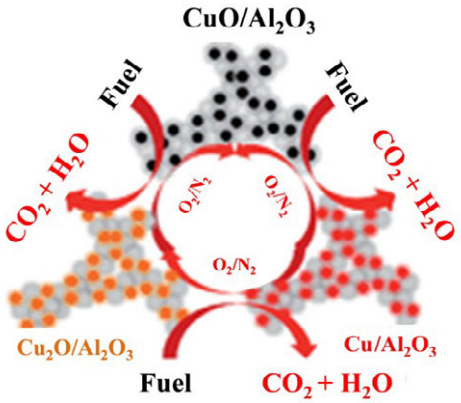

Fig. 3.3. A schematic representation of CuO/Al_2O_3 composite OSM and the corresponding chemical looping redox cycle, based on [109].

3.3. Flameless methane combustion with $BaYMn_2O_{5+\delta}$ catalyst

Interestingly, the mentioned $BaYMn_2O_5$-$BaYMn_2O_6$ OSM system was also shown to possess good catalytic properties in CLC-related flameless methane combustion process. The obtained conversion diagram of CH_4 (Fig. 3.4), published by Motohashi et al. [5], indicates that the conversion process with a help of $BaYMn_2O_{5+\delta}$ occurs already at 450 °C.

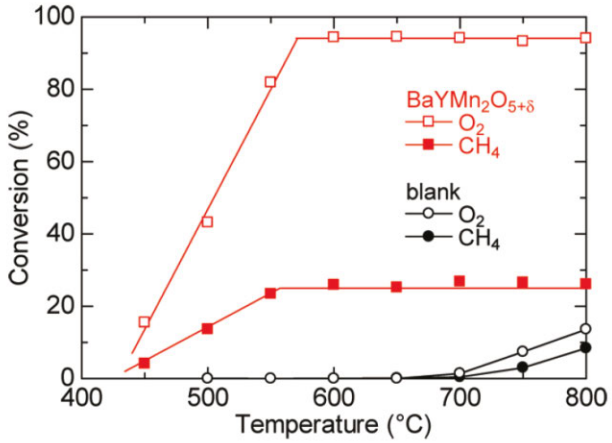

Fig. 3.4. Conversion of methane with a help of $BaYMn_2O_{5+\delta}$ as a function of temperature [5].

Numerous other perovskite-type compounds, such as $La_{1-x}Sr_xCoO_3$ (x = 0, 0.2 and 0.4) or other oxides with Fe and Ni cations present at the B-site in ABO_3, were shown to exhibit catalytic activity, and therefore can be applied in methane combustion processes [110]. Also, it was documented that formation of structural defects and level of the oxygen nonstoichiometry are both connected with catalytic activity of the perovskite-type oxides. Properties of the materials can be tailored by an appropriate substitution of the trivalent cation in the A-sublattice with a bivalent one, which causes change of the oxidation state of B-site cations. Such modification in the Co-containing perovskites leads also to a formation of the oxygen vacancies.

It should be also stated that methane conversion rate depends on the partial pressure of the CH_4, but only at low temperatures. At high temperature range, where the conversion is close to 100%, the combustion depends only on the amount of the supplied oxygen [111].

3.4. Integrated Gasification Fuel Cell system with OSM-based unit

Production of electrical power using integrated Coal Gasification Fuel Cell (IGFC) power plants that use Solid Oxide Fuel Cell (SOFC) technology gain on popularity because of high efficiency, even up to 60% [112]. Regardless actual applied solution (e.g. conventional or catalytic coal gasification) Air Separation Unit (ASU) is an inherent element. The via cryogenic method obtained oxidant [113] is mainly utilized in the coal gasifier (Fig. 3.5), however it can be also used in the sulfur recovery process and in the anode gas oxy-combustor [112].

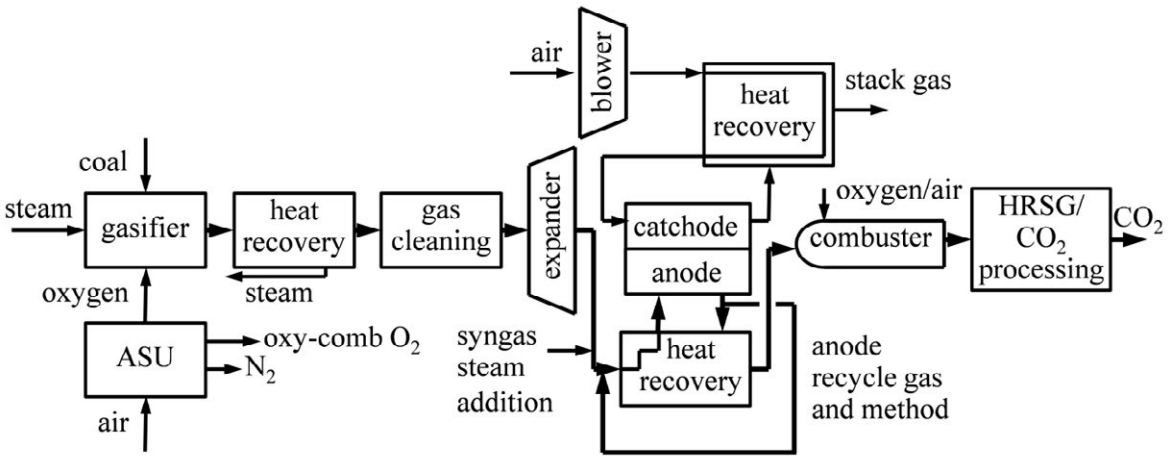

Fig. 3.5. Schema of a design of integrated gasification fuel cell system, with air separation unit, based on [114].

It seems that OSMs can be applied for integrated technologies that demand oxygen production and storage units as for example, in the mentioned Integrated Gasification Fuel Cell solution that can be equipped with the OSM-based oxygen storage unit that should help to increase the overall efficiency. This is of a crucial importance, as about a quarter of the total energy produced in the IGFC system is consumed in the syngas production section (gasifier).

A novel concept of the IGFC system equipped with the mentioned oxygen storage and also hydrogen storage units was proposed within the joined JSPS-PAN project between Poland and Japan, entitled "Development of IGFC System with Oxygen and Hydrogen Storage Units". The author of the thesis participated in the project [115].

4. Physicochemical properties of perovskite-type oxides

$BaLnMn_2O_{5+\delta}$ as well as considered in this thesis Co- and Fe-containing oxygen storage materials crystallize in a structure that can be derivative from the one of cubic ABO_3 perovskite. Understanding of the crystal structure-related properties allows for further discussion regarding oxygen nonstoichiometry and transport properties of the compounds. Consequently, chapter 4.1 presents a detailed description of the cubic and distorted perovskite-type structures, with the following chapter 4.2 focused on possible cation or anion nonstoichiometry in ABO_3-type oxides. Transport properties of such materials are discussed in chapter 4.3. In the next three chapters 4.4-4.6, physicochemical properties of A- and B-sublattice cation-ordered, perovskite-type oxides are discussed, with additional information given about perovskite-related brownmillerite structure. The last chapter 4.7 presents current knowledge about properties of $BaLnMn_2O_{5+\delta}$ oxides.

4.1. Crystal structure of perovskite-type oxides

Ideal perovskite-type structure

Formally, the "perovskite" designation is reserved for $CaTiO_3$ mineral, discovered by Gustav Rose and named after another mineralogist Lev Perovski. Soon it has been found that other compounds possess the same cubic structure and ABX_3 stoichiometry. These materials are referred as having perovskite-type structure (or simply as perovskites), although $CaTiO_3$ was later determined to exhibit orthorhombic symmetry [116]. From the crystallographic point of view, ideal perovskite structure is cubic with *Pm*-3*m* space group (group no. 221 in Hermann-Mauguin notation). In ABX_3 formula, A typically represents a large metal cation, usually belonging to lanthanide or alkaline earth metal groups. B-site cations are significantly smaller, and typically 3*d* metal cations are located in this position, however, commonly other cations can be also present, like cerium or niobium. Most typical X-site ion is the oxygen anion, but sulfide or halide anions can also occupy this site. Combination of the oxidation state of ions in ABO_3 is often A^{3+}, B^{3+} and O^{2-}, however, various different options are also possible (e.g. $\square Mo^{6+}O_3$, $Li^{+}Nb^{5+}O_3$ or $Ba^{2+}Ti^{4+}O_3$; □: unfilled position) [117]. Multiple substitution in both cationic sublattices and in

different proportion is possible and of scientific interest, since it allows to stabilize metal cations in B sublattice in unusual oxidation state such as Cu^{3+}, Bi^{4+} or Ir^{5+}.

Fig. 4.1 shows visualization of the crystal structure of the ideal perovskite unit cell. In this structure X-site anions together with A cations form a face centered cubic (*fcc*) arrangement, in which ¼ of the formed octahedral voids is occupied by B-site cations. The A-site cations are surrounded by twelve anions in 12-fold (cubo-octahedral) coordination, while B cations are surrounded by six anions in octahedral coordination (BX_6 octahedra). Regarding X anions, their coordination sphere is created by four A cations and two B cations [118]. Alternatively, the structure can be described as created by corner-sharing BX_6 octahedra, in which A cations are placed in all voids having 12-fold coordination.

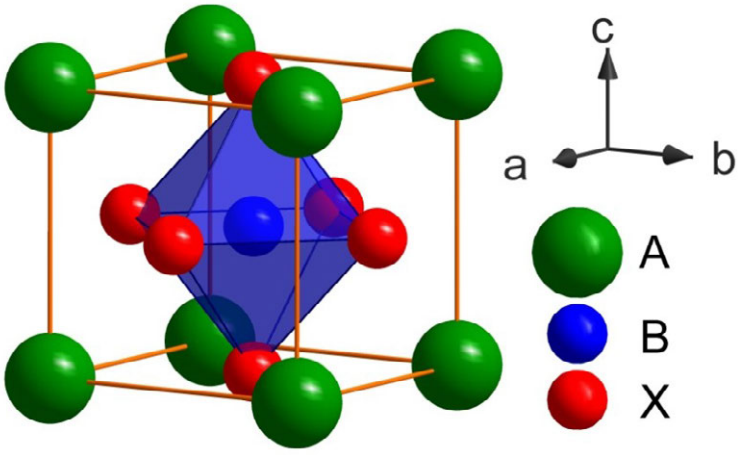

Fig. 4.1. Visualization of structure of ideal, cubic perovskite. A-site can be described with Wyckoff notation as 1a (0,0,0), B-site as 1b (½,½,½) and X-site as 3c (0,½,½). Radii of ions not to scale.

Since only a few oxides from the ABX_3 group crystallize in perfectly regular structure, in 1927 Goldschmidt introduced a structural tolerance parameter t (tolerance factor) that allows for a geometric determination of a degree of deformation of the structure from the ideal, cubic one. With approximation of the ionic radii, the following equation (10) can be derived for the tolerance parameter t_S:

$$t_S = \frac{r_A + r_X}{\sqrt{2}(r_B + r_X)} \tag{10}$$

where: r_A, r_B and r_X are respectively the Shannon's ionic radii [17] of the A and B cations, as well as the X anion. In the case of two or more different ions present in one sublattice, the respective average ionic radius should be used.

It was noticed that there is a certain correlation between the parameter t_S and the crystal symmetry, as presented in Tab. 4.1, i.e. in most cases, the closer the t_S value to unity, the higher the crystal symmetry. However, calculation of the tolerance factor for a selected chemical composition of ABX_3-type oxide does not allow to predict the actual space group, in which the material would crystallize [118].

Tab. 4.1. Dependence of the crystal structure type and the Goldschmidt's tolerance factor t_S [117, 119].

tolerance factor	**symmetry**
$t_S < 0.85$	ilmenite-type structure (not perovskite)
$0.85 < t_S < 0.90$	orthorhombic
$0.90 < t_S < 1$	rhombohedral
$t_S \approx 1$	cubic
$1 < t_S < 1.06$	hexagonal (not perovskite)

The presented above relationship should be only treated as an approximation, since various other factors, such as nonstoichiometry in A or X lattice, degree of covalent bonding, metal-metal interactions, as well as Jahn-Teller effect (JTE) affect the actual structure. From this point of view it seems more adequate to use real distances between the atoms for calculation of the tolerance factor, which can be obtained from precise structural measurements [120, 121].

Distorted perovskite-type structures

Considering the above, it is not surprising that the actual ABX_3 materials rarely adopt the ideal perovskite structure. More often they crystallize in a distorted structure, which arises from breaking of at least one of the possible symmetry elements present in the *Pm*-3*m* space group. This effect is mainly due to rotation or tilt of BX_6 octahedra, displacement of B-site cation from the center of the octahedron, distortion of the octahedra e.g. due to the JTE or increase of the covalence bonding of A-X and/or B-X [118].

Rotation or tilt of BX_6 octahedron is caused by mismatch, i.e. too large or too small size of the A cation with respect to the requirements for 12-fold coordination. To adapt, octahedron tilts, and therefore lowers the energy mode for the crystal. The rotation is manifested by a change in A-X bond lengths, which cease to be equal. Consequently, lowering of the symmetry occurs, and decrease of the coordination number of the A cation may also happen. In 1972, Glazer [122] proposed a notation, by which the octahedron tilt

is given as a rotation about each of the orthogonal Cartesian axes, and the rotation is specified as “a”, “b” and “c” symbols. Moreover, superscript are used to describe direction of the rotation, whether it is in the same direction (so called *in-phase* tilt) or contrary (*anti-phase* tilt) in relation to the previous layer. Two basic types of octahedra tilts are visualized in Fig. 4.2.

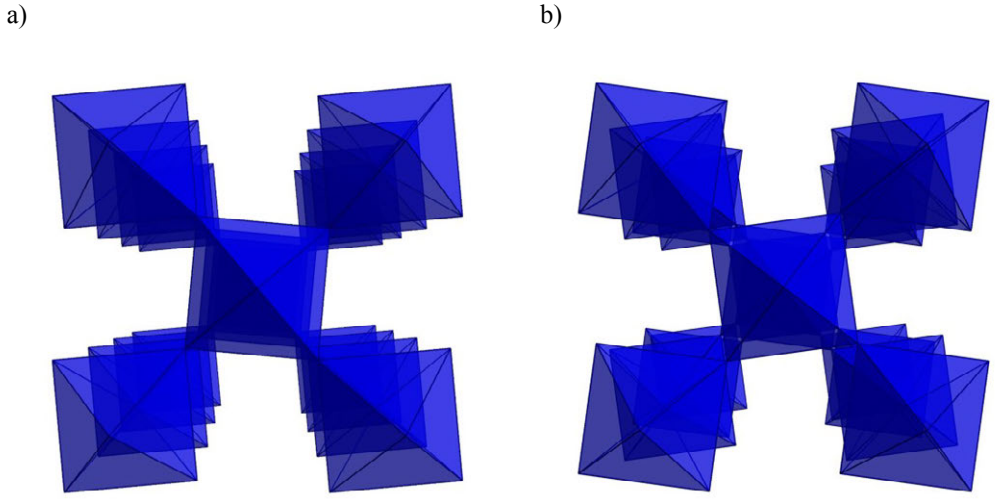

Fig. 4.2. Two main types of octahedral tilt: a) $a^0a^0c^+$ and b) $a^0a^0c^-$, seen along *z*-axis. Based on [123].

In the case of the tilt system $a^0a^0c^+$ (Fig. 4.2a), generating *P4/mbm* space group (no. 127), octahedra are tilted only along the *z*-axis, and the tilt is *in-phase*. Lack of inclination along the *x* and *y* directions is given in double a^0 notation. The *anti-phase* arrangement (Fig. 4.2b) is described as $a^0a^0c^-$, generating *I4/mcm* space group (no. 221). The octahedra tilt in this case is also along the *z*-axis only, but the following layer (in relation to one selected) is titled in the opposite direction. This is noted by c^- symbol. In the notation repeating of the symbol indicates the same angle of rotation relative to the *x*-, *y*- or *z*-axis, while the superscript 0 indicates a lack of rotation. Consequently, the regular structure of the ideal perovskite with no distortions present can be assigned with $a^0a^0a^0$ notation.

Initially, Glazer described 23 possible different combinations of the tilts. This number was eventually reduced by Howard and Stokes down to 15 [124]. Fig. 4.3a. presents the theoretical relationship between the space groups in ABX_3 perovskites, with possible phase transitions associated to a particular tilt system change. These transitions may occur due to change of the pressure, partial pressure of the oxidizer, temperature, as well as chemical composition. However, in literature there is no consensus, and somewhat different diagram for selected space groups was proposed by Thomas [125] (Fig. 4.3b).

a)

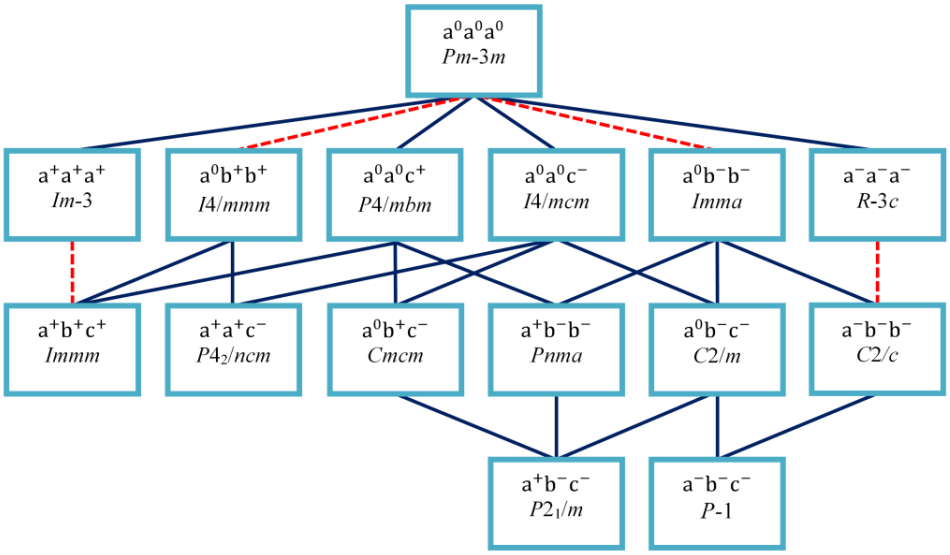

b)

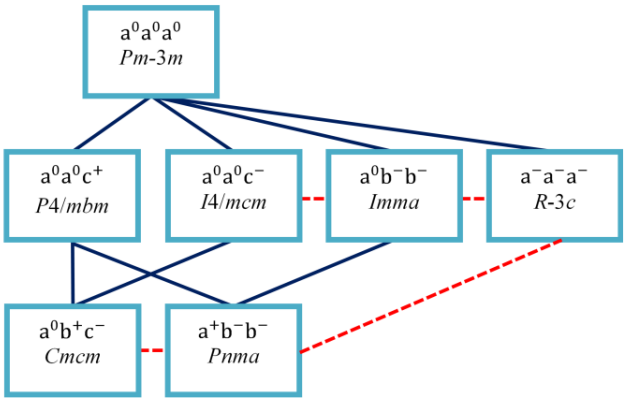

Fig. 4.3. a) Classification of space groups and possible phase transitions between perovskite-type structures, as discussed in work [124]. b) Different diagram presented in work [125]. Solid lines indicate second order phase transition, while dashed lines specify first order phase transformations. Based on [124, 125].

4.2. Nonstoichiometric perovskites

Characteristic feature of perovskite family of compounds is a nonstoichiometry accompanied by presence of cation and anion vacancies. Materials that exhibit such nonstoichiometry form a significant part of the perovskite-type oxides in general. As mentioned before, various perovskites with different chemical composition and charge state of the ions can be formed, and for example, presence of the cation vacancies in the A-sublattice is realized in a group of $A_{1-x}\square_xBX_3$, where $0 \leq x < 1$. In the case of Na_xWO_3 ($x < 0.75$) and similar materials the compounds are called bronzes, while for instance for $Th_{0.25}NbO_3$ ($x \geq 0.75$) usually A-site-deficient perovskite term is used [117, 118, 126].

A novel class of Li-conducting $La_{2/3-x}Li_{3x}TiO_3$ ($0 < x < 1/6$) electrolytes was recently studied, in which Li^+ transport is realized via A-site vacancies [127].

Nonstoichiometry in the anion sublattice is very common for $ABO_{3-\delta}$ perovskite-type oxides. It can occur either when B-site cation is a transition metal able to exist in two valence states (with similar ionic radii) or when A or/and B is partially replaced by another cation, in order to change total oxidation state of A + B. Values of δ can be quite high, and for example for $SrCoO_{3-\delta}$ it can exceed 0.7 [128]. Additionally, depending on the chemical composition, oxygen partial pressure and temperature, value of the equilibrium constant for the oxygen vacancies creation, and ability for reduction/oxidation of the transition metal cations, the deviation from the stoichiometric composition will vary. Important fact should be mentioned that due to the close packing-type arrangement of ions, in the case of ABO_3 oxides with perovskite-type structure, the existence of excessive, interstitial oxygen is hardly possible [129]. As it is common in various other oxides, oxygen nonstoichiometry in the materials can change their structure and also modify their transport and catalytic activity, therefore, precise determination of oxygen content is of high importance for proper characterization of the studied compounds.

4.3. Transport properties of perovskite-type oxides

Understanding of transport properties of perovskite-type oxides is directly related to their crystal structure and chemical composition. Typically, A-site cations do not participate in formation of the band structure near the Fermi level (E_F), and considering electrical conductivity, double exchange mechanism via oxygen anions (B-O-B) is responsible for the electron transfer [130, 131]. Electronic structure of these materials in the vicinity of E_F can be approximated by ligand field theory, based on which an electronic diagram for BO_6 cluster can be derived (Fig. 4.4) [132].

Electrical conductivity of perovskites is strongly related to the chemical composition, which affects structural distortions, average oxidation state of B-site cations, and therefore may or may not lead to presence of mixed valence of 3*d* metals and/or oxygen nonstoichiometry. In two main approaches, properties of the material can be modified by so called bandwidth control, which is based on selection of the appropriate size of A-site cation (or mixture of cations), in order to obtain materials with $t_S \approx 1$. Because one-

electron bandwidth in an approximation of strong ligand field theory is proportional to the cosine of angle between two octahedra (Fig. 4.5), a metallic properties can be expected, as for instance in $LnNiO_3$ series with larger Ln^{3+} cations [133].

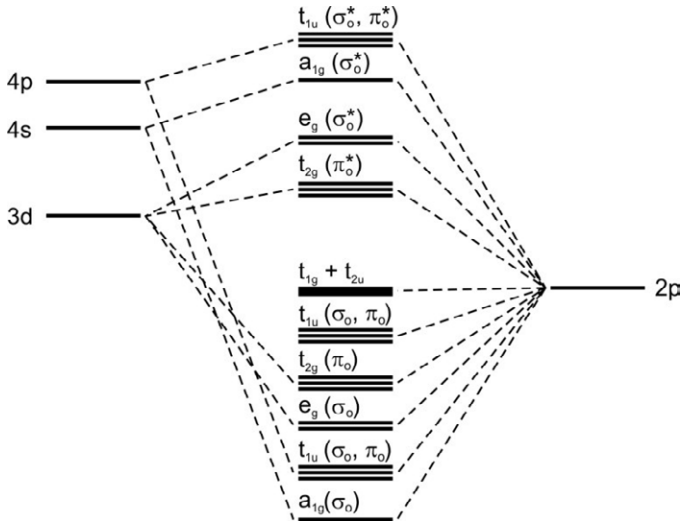

Fig. 4.4. Electronic diagram of BO_6 cluster. Based on [132].

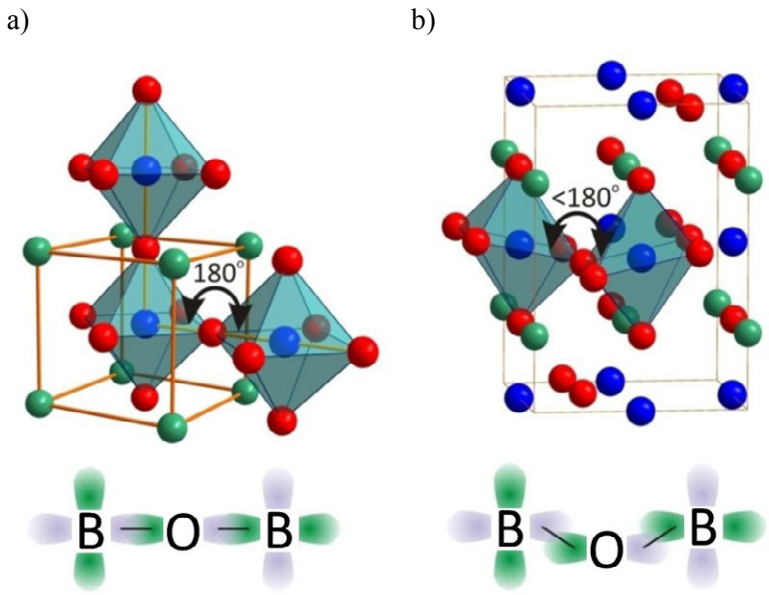

Fig. 4.5. Visualization of angle between octahedra, corresponding to B-O-B angle in: a) cubic *Pm*-3*m*, and b) distorted, orthorhombic *Pnma* ABO_3 perovskite, radii of ions not to scale.

In another approach, called filling control, A-site cation is usually partially replaced by another one having +2 oxidation state (e.g. Sr^{2+} or Ba^{2+}), which causes an appearance of mixed valence states of B cations. The typical example is $La_{1-x}Sr_xMnO_3$ with different amount of Mn^{3+} and Mn^{4+} cations present, depending on the substitution level [123]. Such

substitution, however, may also cause presence of the oxygen vacancies, which at elevated temperatures become mobile, giving rise to the ionic component of the electrical conductivity. If fact, most of $La_{1-x}Sr_xCo_{1-y}Fe_yO_{3-\delta}$ oxides exhibit mixed ionic-electronic conductivity [134, 135].

According to authors of works [136, 137], efficient ionic transport via vacancy-type mechanism in nonstoichiometric perovskite-type oxides depends on several factors, among which the most important are: high concentration of vacancies, comparable energy level for all positions in the oxygen sublattice, low melting point associated with a relatively low bond strength, and free paths for diffusion of the oxygen anions. More detailed structural criteria for good ionic conductivity of such materials can be given [138, 139]:

- stress-free lattice,
- Goldschmidt's tolerance factor t_S close to unity,
- low mean value of metal-oxygen bonding energy,
- large critical radius r_c,
- large free volume V_f.

Transfer of oxygen anion from its position to another, empty one requires certain amount of energy. A critical stage in a single jump is a mid-point between the two A cations and one B cation, as illustrated in Fig. 4.6.

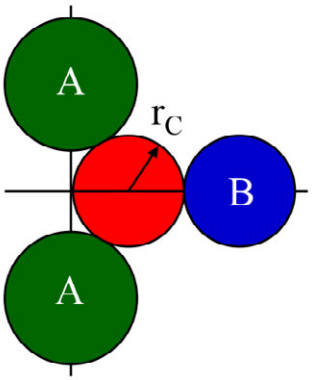

Fig. 4.6. Geometry of the midpoint position of O^{2-} ion in the $ABO_{3-\delta}$ structure, radii of ions not to scale. Based on [140].

The illustrated critical radius r_c depends on the unit cell parameter a_0 of a pseudo-regular perovskite structure and on the ionic radii of A and B cations r_A and r_B, and the dependence is given by the equation (11) [140]:

$$r_c = \frac{a_0\left(0.75a_0 - \sqrt{2}r_B\right) + r_B^2 - r_A^2}{2(r_A - r_B) + \sqrt{2}a_0} \quad (11)$$

As stated in work [129], since r_c usually do not exceed 0.105 nm [141], it is smaller than oxygen ionic radii (0.136 nm in 3-fold coordination), and therefore, in the ionic transport thermal vibrations play a significant role. The amplitude of these vibrations for A and B cations will be inversely proportional to their weight, and consequently it can be expected that presence of lighter elements in these positions should favor ionic conductivity. In addition, increase of r_c can be achieved by increasing r_B radius and/or reducing r_A [142]. Another important structural parameter associated with ionic conductivity is free volume V_f [139], which is calculated by subtracting volume occupied by all ions from the unit cell volume. It can be expected that an increase of V_f should cause an increase of the ionic conductivity. Unfortunately, since the above parameters are related, optimization of one results in deterioration of the other.

Brouwer diagram of $Ln_{1-x}A_xBO_{3\pm\delta}$

Electrical conductivity of perovskite-type oxides is linked to their oxygen nonstoichiometry and both these parameters depend on oxygen partial pressure. Their mutual relationship can be presented in one graph, so called Brouwer diagram. Such exemplary graph for $Ln_{1-x}A_xBO_{3\pm\delta}$ (Ln: lanthanide, A: alkaline earth metal) oxides is presented in Fig. 4.7. According to commonly used in literature convention "+δ" symbol does not indicate real excessive oxygen, but represents existence of vacancies in the A and B sublattices. The general condition of electroneutrality, which includes formation of the oxygen vacancies ($V_O^{\bullet\bullet}$) and vacancies in both cationic sublattices ($V_{Ln}^{'''}$, $V_B^{'''}$) can be presented as (12) [123]:

$$3\left[V_{Ln}^{'''}\right] + 3\left[V_B^{'''}\right] + \left[A_{Ln}^{'}\right] + \left[B_B^{'}\right] = 2\left[V_O^{\bullet\bullet}\right] + \left[B_B^{\bullet}\right] \quad (12)$$

In general, this condition can be simplified to five different cases, corresponding to five regions in Fig. 4.7. The simplified electronegativity conditions are given below (13-17):

I $$3\left[V_{Ln}^{'''}\right]+3\left[V_{B}^{'''}\right]=\left[B_{B}^{\bullet}\right] \quad (13)$$

II $$\left[A_{Ln}^{'}\right]=\left[B_{B}^{\bullet}\right] \quad (14)$$

III $$\left[A_{Ln}^{'}\right]=2\left[V_{O}^{\bullet\bullet}\right]+\left[B_{B}^{\bullet}\right] \quad (15)$$

IV $$\left[A_{Ln}^{'}\right]=2\left[V_{O}^{\bullet\bullet}\right] \quad (16)$$

V $$\left[B_{B}^{'}\right]=2\left[V_{O}^{\bullet\bullet}\right] \quad (17)$$

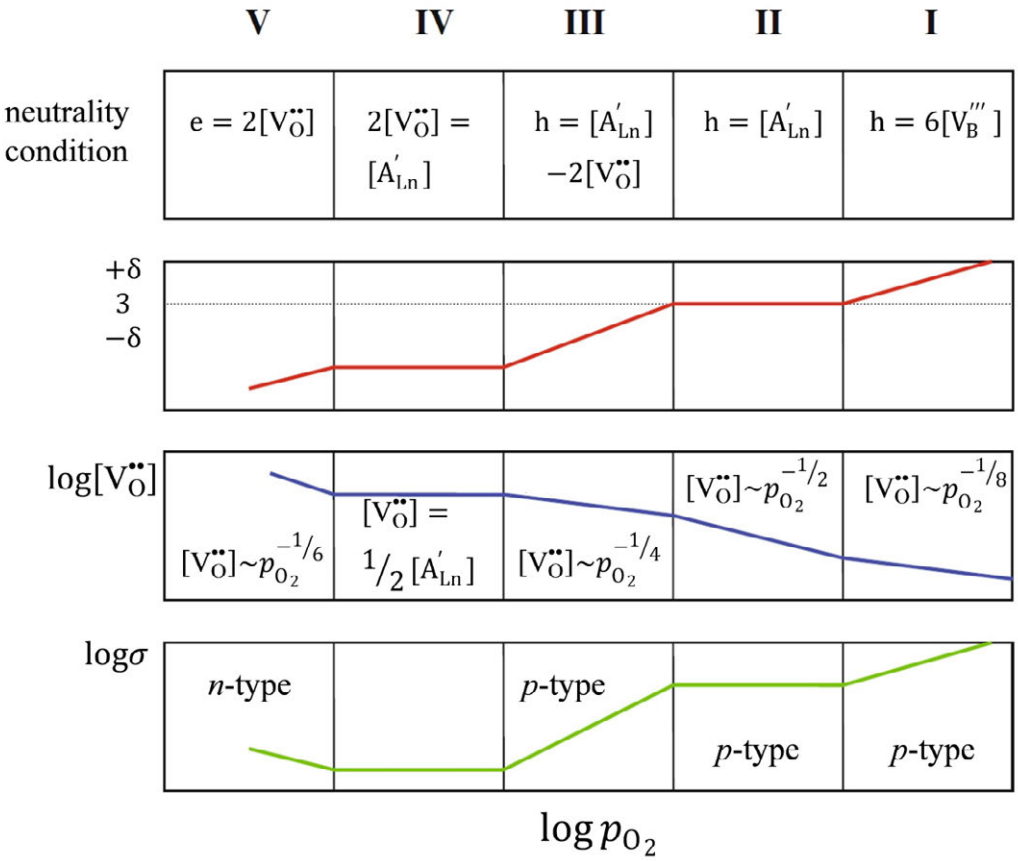

Fig. 4.7. Brouwer diagram for $Ln_{1-x}A_xBO_{3\pm\delta}$. Based on [143].

For the highest oxygen partial pressure (range I in Fig. 4.7) general condition simplifys, and amount of created electronic holes is proportional to the total concentration of the cationic vacancies. In the second range no oxygen nonstoichiometry is present ($\delta = 0$), and behavior of the material depends on the B cation oxidation state, which is determined by level of doping (x in $Ln_{1-x}A_x$). For lower pO_2 compensation of charge is maintained partially by change of the oxidation state of B cation and partially by formation of the oxygen vacancies. For even lower oxygen partial pressure (region IV), additional charge caused by doping is compensated only by the oxygen vacancies. Further lowering of the oxygen pressure leads to a progressive reduction of material, while formation of the

oxygen vacancies is accompanied by trapping of electrons on the B cations. Analyzing Fig. 4.7, a change of the dominant charge carriers from holes to electrons while lowering the pO_2 is evident (from region III through IV to V).

Jahn-Teller effect in perovskite-type oxides

Jahn-Teller effect originates from a fact that electron configurations with uneven occupancy of degenerated orbitals are not stable, and therefore in some (e.g. octahedral BO_6) complexes lowering of the energy and stabilization is obtained by a crystal distortion. As written by Mitchell [118] the first order JTE can be observed for compounds containing transition metals with uneven number of *d*-electrons in the e_g orbitals. The first order Jahn-Teller effect operates to lift degeneracy of the e_g orbitals, which causes distortion of the regular octahedron. Usually, two modes (Q_2 and Q_3) of the octahedral complex are considered, with the dominant Q_3 one causing formation of two longer bonds (elongation) along *z*-axis (tetrahedral distortion), while in the other one (Q_2) two shorter and two longer bonds appear on the opposite sites of the middle plane of the octahedron (orthorhombic distortion) [144]. High spin $Mn^{3+}O_6$ octahedra, as well as various complexes of Cu^{2+} exhibit JTE. More complicated second order JTE is also known. It is worth mentioning that Jahn-Teller effect may appear independently from octahedron tilting or together with it, causing further lowering of the symmetry in perovskites [118].

Physical properties and application of selected perovskite-type oxides

Perovskite-type oxides exhibit different electrical properties, from insulating through semiconducting to metallic. For example, if B-site cations possess no *d*-electrons, like in $ATiO_3$ (A: Ca, Sr or Ba) and also in $LaBO_3$ (B: Al, Ga), the materials exhibit insulating properties, having resistivity ρ at RT on the order of 10^{12} Ω·cm. On the other hand, $LaCrO_3$, $LaMnO_3$, $LaRhO_3$ or $CaRuO_3$ perovskites exhibit semiconducting properties with ρ_{RT} values in 10^1-10^5 Ω·cm range. Furthermore, $CaVO_3$, $SrMoO_3$, $SrRuO_3$ and $LaBO_3$ (B: Ni, Cu or Ru) show electrical conductivity typical for metals, with ρ_{RT} in 10^{-3}-10^{-6} Ω·cm range. For some of the oxides the main electric carriers are electrons ($SrMoO_3$), while for others electronic holes ($LaCuO_3$) [117]. Currently various perovskites find their application as ceramic, refractory or electronic materials. Selected compounds with their properties and applications are gathered in Tab. 4.2.

Tab. 4.2. Lists of properties and applications of selected perovskite-type oxides. Based on [116, 117].

property	application	exemplary compounds
conducting properties		
insulator	ceramic insulators	$LaTaO_3$, $CaTiO_3$, $LaAlO_3$
semiconductor		$LaVO_3$, $LaMnO_3$, $LaNi_{3/4}Mo_{1/4}O_3$
metal		RrO_3, Na_xWO_3, $CaMoO_3$, $LaNiO_3$, $Na_{1/4}Cu_{3/4}RuO_3$
MIEC	SOFC cathodes	$La_{1-x}Sr_xCo_{1-y}Fe_yO_{3-\delta}$, $Ba_{1-x}Sr_xCo_{1-y}Fe_yO_{3-\delta}$
superconductor	superconductors	$BaPb_{1-y}Bi_yO_3$, $Ba_{1-x}K_xBiO_3$
dielectric material	multilayer capacitor, dielectric resonator, thin film resistor	$BaTiO_3$, $BaZrO_3$
ionic conductor	solid electrolyte	$La_{1-x}Sr_xGa_{1-y}Mg_yO_{3-\delta}$
proton conductor	SOFC electrolyte, hydrogen sensor	$BaCeO_3$, $SrCeO_3$, $SrZrO_3$, $La_{1-x}Sr_xMnO_{3-\delta}$
magnetic properties		
magnetic/ferromagnetic	magnetic bubble memory, ferromagnets	$GdFeO_3$, $LaMnO_3$, $LnFeO_3$, $SrRuO_3$, $BiMnO_3$
ferroelectric/piezoelectric	piezoelectric transducer, PTC thermistor, electrostrictive actuator	$BaTiO_3$, $PbZr_{1-y}Ti_yO_3$, $PbMg_{1-y}Nb_yO_3$
antiferromagnetic		$CaRuO_3$, $LaFeO_3$, $BiFeO_3$
paramagnetic		$UTiO_3$, $LaHoO_3$
other properties		
catalytic activity	catalyst, e.g. catalyst for CO oxidation and NO_x reduction	$LaFeO_3$, $LaCe_{1-y}Co_yO_3$, $La_{1-x}Pb_xMnO_3$
optical properties	electro-optical modulator, laser host, switch, second harmonic generator	$La_{1-x}Pb_xZr_{1-y}Ti_yO_3$, $YAlO_3$, $LiNbO_3$, $KNbO_3$, $LaInO_3$, $LaAlO_3$
sensitivity for atmosphere composition	gas sensors for NO_x/SO_2	$BaSnO_3$
optical activity	photo-anodes for solar energy conversion	$SrTiO_3$, $BaTiO_3$, $YFeO_3$, $LuRhO_3$
catalytic activity/conductivity	oxygen electrodes/membranes	$La_{1-x}Sr_xCoO_3$ $LaNiO_3$, $LaFe_{1-y}Co_yO_3$, $LaMn_{1-y}Co_yO_3$

4.4. Physicochemical properties of ordered perovskite-type oxides

In various perovskite-type materials with more complicated chemical formula, presence of a specific arrangement of cations is often observed. In so called double perovskites, which chemical formula can be generally specified as $A_2B_2X_6$, two different cations are present in A or/and B sublattice in a 1:1 ratio, corresponding to $AA'B_2X_6$, $A_2BB'X_6$ or $AA'BB'X_6$ notation. While both, A and A' cations occupy structural A-site, and B and B' cations occupy structural B-site, they may be organized in a specific manner, as shown in Fig. 4.8 [118, 145].

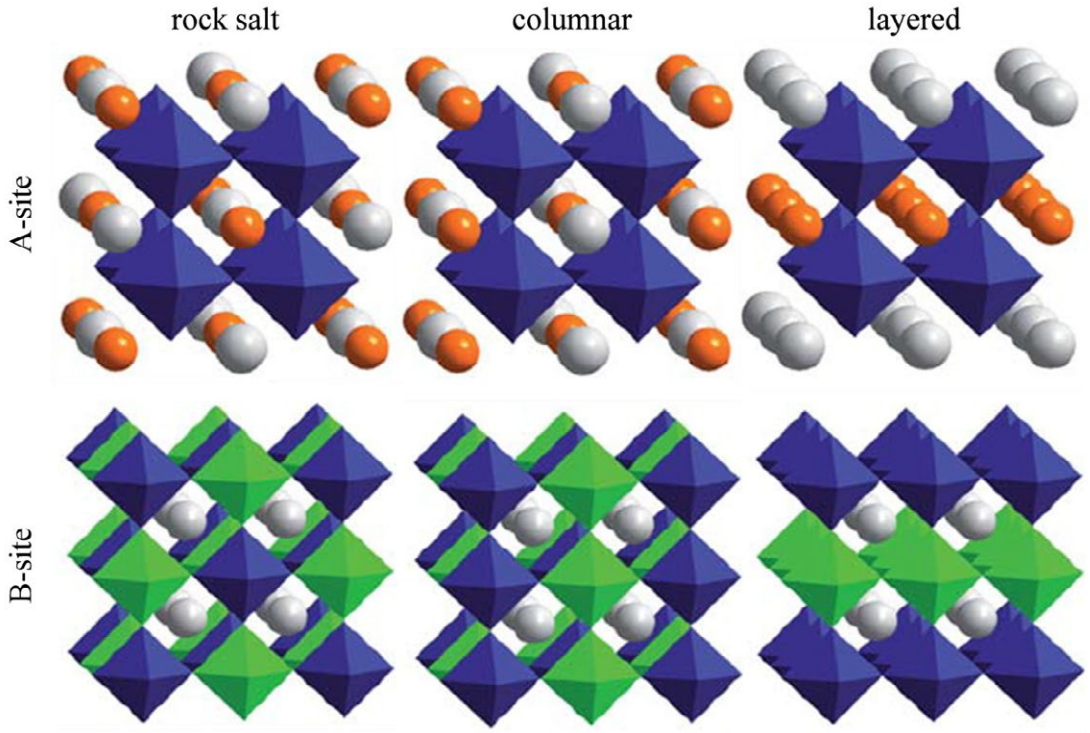

Fig. 4.8. Ordering schema in 1:1 cation-ordered perovskite-type materials. Based on [145].

As demonstrated in work [145], three basic types of arrangement of cations in the unit cell can be distinguished: the most symmetrical one is called rock salt structure, since the arrangement of A and A' or B and B' cations corresponds to the placement of anions and cations in crystal structure of NaCl. This ordering is also referred to 0D (zero-dimensional) because $B'X_6$ octahedra (or $A'X_{12}$ polyhedra) are separated from each other through BX_6 octahedra (AX_{12} polyhedra), and vice versa. This arrangement was found to be typical for majority of 1:1 B-site ordered $A_2BB'X_6$-type perovskites. Second type of arrangement is the columnar ordering, corresponding to 1D structure, because it represents

the connection of $B'X_6$ octahedra (or $A'X_{12}$ polyhedra) in one dimension. Consequently, layered-type of arrangement allows $B'X_6$ octahedra (or $A'X_{12}$ polyhedra) to connect in two dimensions, and therefore it is called 2D (layered) ordering. Another notation specifies the plane containing the same atoms and determines the arrangement of the type of rock salt, columnar and layered, as respectively: (111), (110) and (001) [145].

Assuming that one of the cations (A' or B') is of higher charge than the other one present in the same sublattice (A or B), electrostatic interactions can be considered important for determination of the type of the adopted structure. From this point of view, the most preferred ordering is the rock salt one, since it provides a maximum distance between the cations having higher oxidation state. Column ordering, in which each B' (A') cation has four B (A) and two B' (A') neighbors is the next preferred arrangement. Layered-type ordering is the least likely to be adopted, as in this arrangement B' (A') cation is surrounded by four B' (A') and two B (A) neighbors [145]. It should be noted that in general, ordering in the A-sublattice occurs less common than in the B-sublattice, and number of materials adopting this structure is rather small [118], however, the considered in this work $BaLnMn_2O_{5+\delta}$ oxides are A-site cation-ordered.

Explanation why B-site ordering is more common can be related to a fact that difference of the oxidation state of cations occupying B-sublattice can be as high as 6, as for Sr_2LiReO_6, while for A-sublattice normally it does not exceed two. However, this does not explain why A-site ordered materials typically exhibit layered ordering, while for the B-site ordered materials the preferred arrangement is of a rock salt-type. The explanation of this phenomenon can be given as follows [118]: for a single ABX_3 perovskite each anion is surrounded by two cations from B-sublattice and four from A-sublattice, and when B cations adopt rock salt-type structure, all positions of anions remain chemically and crystallographically equivalent with each anion surrounded by one B cation and one B' cation. This enables the anion to move in a direction of the smaller of B-site cations, in order to optimize length of the chemical bond. In contrast, layered-type of arrangement in B-sublattice creates three chemically different crystallographic environments. One sixth of anions is in the layers, where they are surrounded by two B' cations having higher oxidation state, the next one sixth of the anions is surrounded by cations of a lower oxidation state. The remaining two thirds of the anions are coordinated with one B' and one B cation, as in the rock salt-type system. This arrangement, however, does not comply with the fifth Pauling principle, that, if possible, the same ions should have the same chemical environment [118].

Similar reasoning can be carried out for perovskites characterized by A-sublattice arrangement: rock salt-type system provides the same environment for all anions, but the occupied positions are centrally-symmetric, and therefore, there is no possibility to change the bond lengths of A'-X or A-X, to accommodate the difference in size of A' and A cations. The columnar arrangement creates three different environments for anions, as it was in the case for the B-sublattice. The most common type of ordering for $AA'B_2X_6$ materials is the layered arrangement, as the structure is stabilized by difference in ionic radii of A and A' cations (see chapter 4.4.1), as well as by characteristic for these materials anionic (e.g. oxygen) vacancies [118].

In addition, $AA'BB'X_6$ materials exhibit a mixed arrangement: layered for the A-sublattice and rock salt in the B-sublattice. Also, there are known examples of materials in which ratio of A and A' (B and B ') cations differ from perfect 1:1, and yet they exhibit the ordered structure [118, 145].

It is worth mentioning that simple ABO_3-type perovskites having different cations present at the A- or/and B-site (e.g. $A_{0.5}A'_{0.5}BO_3$, $AB_{0.5}B'_{0.5}O_3$) can be treated as completely disordered end members of a series starting from perfectly ordered double perovskites and comprising also materials exhibiting partial order. This fact is worth emphasizing, since in some of the cases, depending on the preparation method, it is possible to obtain compound with the same chemical composition, which does or does not possess cation ordering. Quantitative analysis of the ordering effect was established by Sleight [146] in a form of degree of order parameter $S = 2x - 1$, where x is defined as a fraction of cations present at their proper site (e.g. A' cations at the A'-site). In two extreme cases, when $x = 1$ than $S = 1$ and the structure is fully ordered, while for $x = 0.5$ the order parameter $S = 0$, and the structure is fully disordered.

From crystallographic point of view presence of cation ordering in $AA'B_2X_6$ or $A_2BB'X_6$ always results in a decrease of the crystal symmetry, in relation to the aristotype *Pm*-3*m* one of ideal perovskite. Furthermore, reduction of the symmetry is also observed as resulting from presence of various structural distortions.

4.4.1. Perovskites with layered-type of A-site ordering

Apart from the mentioned in previous chapter layered $AA'B_2X_6$ materials having 1:1 ratio of A and A' cations, also compounds with 1:2 ($AA'_2B_3O_9$, with famous, oxygen nonstoichiometric $YBa_2Cu_3O_7$ superconductor) and 1:3 proportion ($AA'_3B_4O_{12}$) are

known. The 1:1 layered ordering of A-site cations creates three different environments for the anions. As can be seen in Fig. 4.9, the first position X(1) is coordinated by four A (bigger) cations and two B-site cations. On the other hand, X(3) position is surrounded by four A' (smaller) cations and two B cations, while X(2) site is coordinated by two A and two A' cations arranged in *cis* configuration, as well as by two B-site cations. Since the X anions are in different chemical surrounding, in order to relieve the bonding instability, additional effects may appear, with three possibilities mentioned in work [145]:

- presence of simultaneous, layered ordering of anion vacancies in the A'-related layer (X(3) position), as in $AA'B_2X_{6-\delta}$ perovskites,
- presence of layered ordering of A-site cation vacancies coupled with second order JTE distortions of cations on the B-site,
- presence of rock salt-type ordering of B and B' cations coupled with second order JTE distortions, as in $AA'BB'X_6$ perovskites.

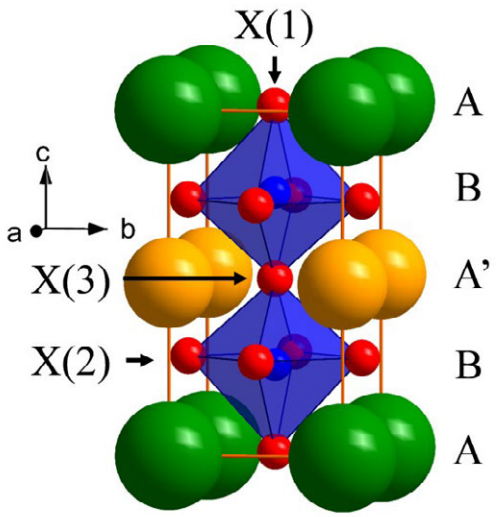

Fig. 4.9. *P*4/*mmm* aristotype unit cell for $AA'B_2X_6$ perovskites with A-site layered ordering of cations. Three different X positions can be distinguished in the structure. Radii of ions not to scale.

The structure presented in Fig. 4.9 is the aristotype one for $AA'B_2X_6$ compounds having A-site layered arrangement of cation, which corresponds to tetragonal *P*4/*mmm* (no. 123) space group. The unit cell in this case is created by a doubling of the simple perovskite lattice constant a_p along *c*-axis, which is often noted as $1a_p \times 1a_p \times 2a_p$, or simply as $1 \times 1 \times 2$ [147]. It can be also stated that since the ionic radius ratio of the oxidant (usually oxygen) and metal present in 12-fold coordination in ABX_3 perovskites is

approximately equal to one, similarly, the average ionic radius of A and A' cations in $AA'B_2X_6$ should be equal to the radius of the oxidant as well, despite that one of the cations is substantially larger than the other one.

With advanced mathematical and crystallographic considerations it was possible to derive relationship between possible lower symmetry structures, which are related to the basic *P*4/*mmm* one [147]. Graph showing this relationship is given in Fig. 4.10.

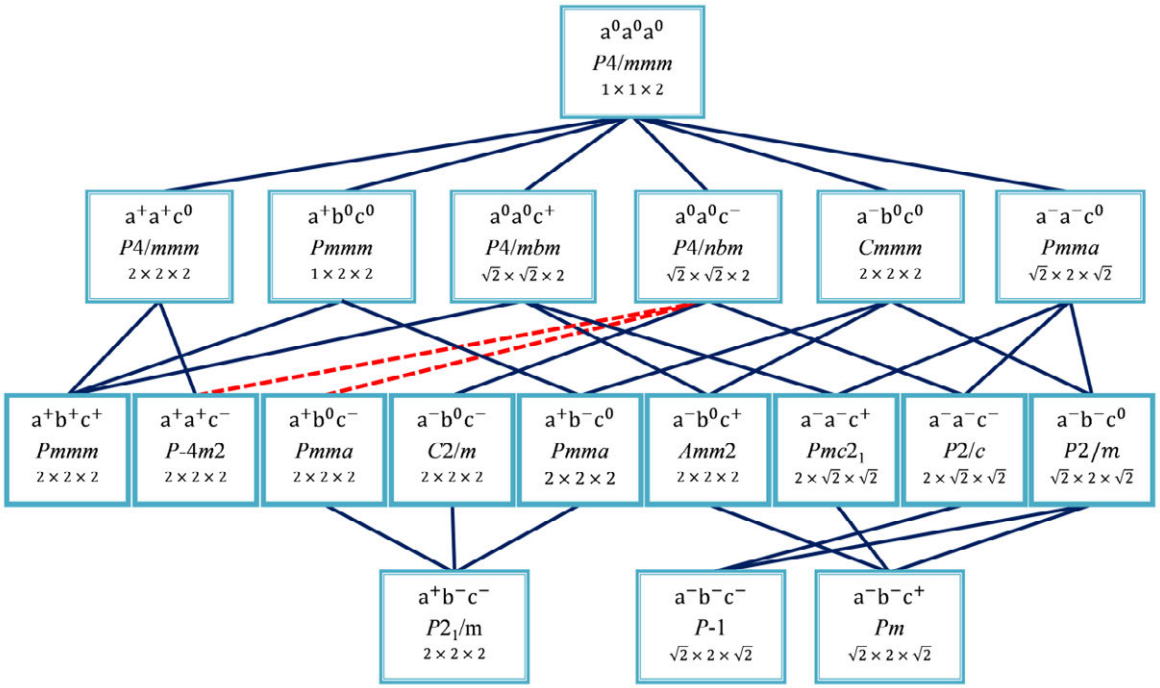

Fig. 4.10. Schematic drawing showing different possible structures generated by the layered-type of ordering of cations in the A-site, which is followed by the corner-linked tilting of BX_6 octahedra in $AA'B_2X_6$ perovskites. The approximate cell dimensions in comparison to the cell edge a_p of the *Pm*-3*m* aristotype structure are included in the diagram. Glazer notation is used for the octahedra tilts. Solid lines indicate second order phase transition, while dashed lines specify first order phase transformations. Figure based on [147].

4.4.2. Perovskites with rock salt-type of B-site ordering

Double perovskites exhibiting ordering of cations in the B-sublattice constitute a majority of the ordered perovskites group in general. While the most common ratio of the B and B' cations is 1:1 ($A_2BB'O_6$) or 1:2 ($A_3BB_2'O_9$), there are also known examples of materials having 1:3 ratio ($A_4BB_3'O_{12}$) [118].

Ordering mechanism of cations in such double perovskites is complex and depends on many factors. Degree of order S depends not only on the size, charge and polarization properties of the ions, but also on a method of synthesis of the material (sintering

temperature and time, pO_2). An example for such behavior is found for Ba_2NiMoO_6 compound with rock salt-type ordering of Ni^{2+} and Mo^{6+} cations. It is generally accepted that the higher temperature of the synthesis (but within certain limit), the higher the degree of order. Materials in which both B-site cations are transition metals exhibit usually no or a low degree of order, however this is not a general rule. When one of the B cations is a non-transition element, tendency for ordering was found to increase significantly [118]. Interestingly, charge-ordering effects of the same type of cation present in the B-sublattice can also give rise to formation of the rock salt ordering, as documented in Mn-containing $BaLnMn_2O_{5+\delta}$ (see chapter 4.7).

Double perovskites with the perfect rock salt-type arrangement in B-sublattice possess regular structure with *Fm*-3*m* (no. 225) space group, the same as for the materials characterized by the rock salt order of cations in the A-sublattice [148]. This structure can be considered as created by doubling of the simple perovskite unit cell in all directions, and can be written as $2a_p \times 2a_p \times 2a_p$ [114, 143, 144]. Similarly as for the A-site layered $AA'B_2X_6$, using mathematical and crystallographic reasoning it was possible to derive relationship between the aristotype *Fm*-3*m* structure and possible distorted structures. For the respective diagram see work [148].

4.4.3. Anion vacancy-ordered brownmillerite-type structure

Apart from ordering effects of cations in perovskite-type oxides, presence of a specific arrangement in the X-sublattice is also possible in nonstoichiometric perovskite-type materials. It can be considered that brownmillerite-type structure (Fig. 4.11) represents such type of ordering.

Originally the designation “brownmillerite” concerned a mineral with $Ca_2(Al,Fe)_2O_5$ formula. Its discovery is somewhat unclear, but the mineral was named after Lorrin Thomas Brownmiller. Soon, other oxides were determined to exhibit similar crystal structure [118]. General chemical formula of these materials can be written as $A_2B_2O_5$ ($ABO_{2.5}$), and the basic structure possesses orthorhombic unit cell. Corner-sharing BO_6 octahedra and BO_4 ($B'O_4$) tetrahedra create alternating layers along *c*-axis (Fig. 4.11). Presence of ordering of the oxygen vacancies along [101] direction is a characteristic feature of this structure. In general, vacancy ordering in such type of compounds causes lowering of the oxygen conductivity despite comparably large number of oxygen-vacant sites [149-151]. Good example of this effect was documented for $Ba_2In_2O_5$, for which in

the oxygen vacancy-ordered phase (below ~ 900 °C) ionic conductivity is much lower, comparing to the high temperature disordered phase [152]. Brownmillerite-type phase has been also observed in properly reduced $La_{1-x}Sr_xFe_{1-y}Co_yO_{3-\delta}$ and La-rich $La_{1-x}Sr_xMnO_{3-\delta}$ materials [151].

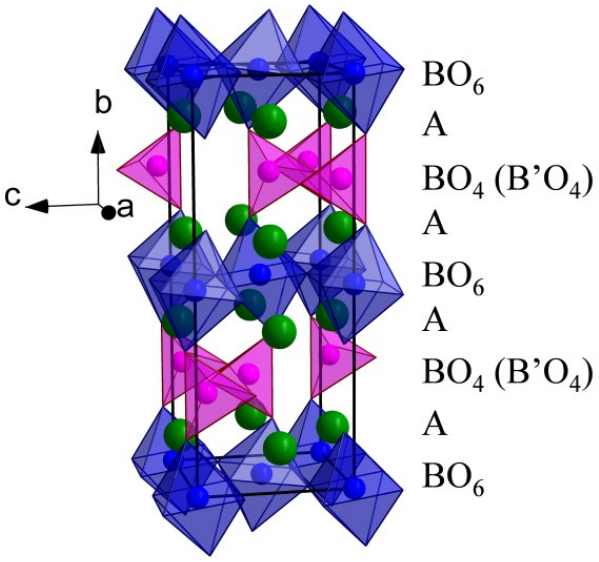

Fig. 4.11. Orthorhombic structure of brownmillerite with oxygen vacancy ordering present along [101] direction. Radii of ions not to scale.

4.5. Oxygen nonstoichiometry in A-site layered $AA'B_2O_{5+\delta}$

As described in chapter 4.4.1, in $AA'B_2X_6$ materials exhibiting A-site layered ordering, presence of anion vacancies, which appear in the A'-related layer is often observed, as it allows to minimize bonding instability caused by the layered ordering [145]. In many such oxides the oxygen nonstoichiometry δ level can be very high, on the order of 1. Likely because of that in the literature there is a convention of describing chemical composition of these materials with $AA'B_2X_5$ reduced material taken as the basis, which corresponds to $AA'B_2X_{5+\delta}$ notation, rather than $AA'B_2X_{6-\delta}$ one. In this thesis the commonly used naming scheme was also applied.

For $AA'B_2O_5$ oxides ($\delta = 0$), in A'-related layer (Fig. 4.9) there is no oxygen present, which changes coordination environment of the B-site cations from octahedral to square-pyramidal one, and at the same time A' coordination number is reduced from 12 to 8. Considering typical $BaLnB_2O_5$ (B: Mn, Fe, Co) materials, the described above behavior

results in presence of BaO_{12} and LnO_8 polyhedra. However, it seems that there is a fundamental difference in the overall behavior of these compounds with changing oxygen content. In the case of Mn-containing $BaLnMn_2O_{5+\delta}$ three distinct phases appear: $BaLnMn_2O_5$, $BaLnMn_2O_{5.5}$ and $BaLnMn_2O_6$, as depicted in Fig. 4.12 for the exemplary $BaYMn_2O_{5+\delta}$ [7]. As can be seen in Fig. 4.12, $BaYMn_2O_{5.5}$ possesses specific oxygen vacancy ordering. In this structure the coordination number of yttrium is 10, and Y^{3+} cations are surrounded by four MnO_6 octahedra (contributing 6 oxygens) and four MnO_5 square-pyramids (contributing 4 oxygens). On the other hand, for Co-containing $BaLnCo_2O_{5+\delta}$ oxides, solid solution-like compositions with various values of δ are known [153], while the oxygen vacancy ordering may take place if $\delta \approx 0.5$ [154]. Regarding $BaLnFe_2O_{5+\delta}$ materials, there are no clear data available in the literature concerning formation of similar oxygen vacancy-ordered $BaLnFe_2O_{5.5}$ phases.

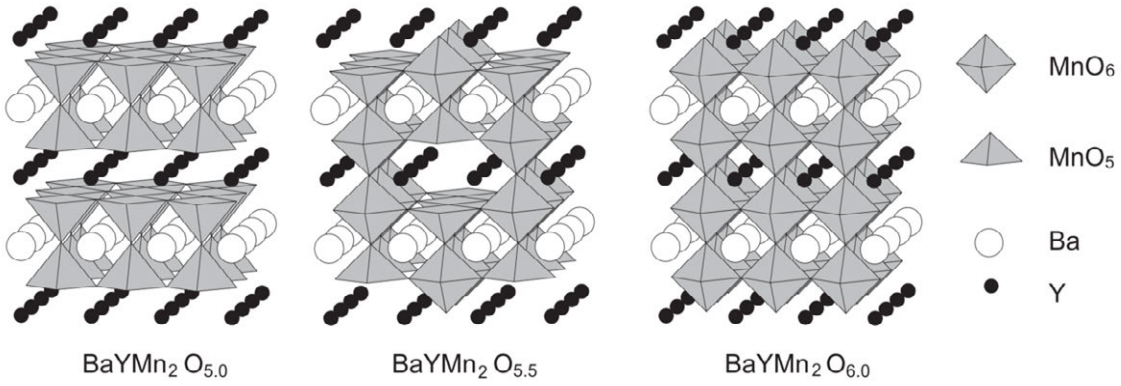

Fig. 4.12. Schematic illustration of the crystal structure of three compounds: $BaYMn_2O_5$, $BaYMn_2O_{5.5}$ and $BaYMn_2O_6$. Figure from [7].

Interestingly, it was found that the amount of incorporated oxygen δ depends on the size of the rare earth cation in $BaLnFe_2O_{5+\delta}$. Oxides containing smaller Ln^{3+} ions, such as Y^{3+}, Ho^{3+}, and Tb^{3+}, can accept only very small amounts of additional oxygen into their structure, while for larger lanthanides, such as Sm^{3+} and Nd^{3+}, the value of δ can be as high as 0.65 and 0.79, respectively. For even larger La^{3+} cation δ reaches 1, but the layered cation ordering disappears [118].

In general, due to possible partial substitution of different 3*d* cations in the B-site (e.g. [155]), there is no general description available in the literature, which would give global overview concerning nonstoichiometry in substituted $BaLnMn_2O_{5+\delta}$.

4.6. Transport properties of selected A-site layered $AA'B_2O_{5+\delta}$

Due to a very wide range of chemical compositions of $AA'B_2O_{5+\delta}$ oxides, transport properties of these materials may differ considerably. However, it is obvious that oxygen nonstoichiometry will have crucial influence, because of the corresponding changes of the average oxidation state of the B-site cations. Detailed discussion about this matter is beyond scope of this thesis. Nevertheless, transport properties of Co-containing materials should be mentioned, as these oxides may exhibit very high mixed-ionic electronic conductivity, making them attractive for application, for instance as cathode materials in Solid Oxide Fuel Cells [153, 155]. Exemplary data of electrical conductivity dependence on temperature for $BaLnCo_2O_{5+\delta}$ (Ln: La, Pr, Nd and Sm) oxides with corresponding results about temperature variation of the oxygen content in air are shown in Fig. 4.13a and b.

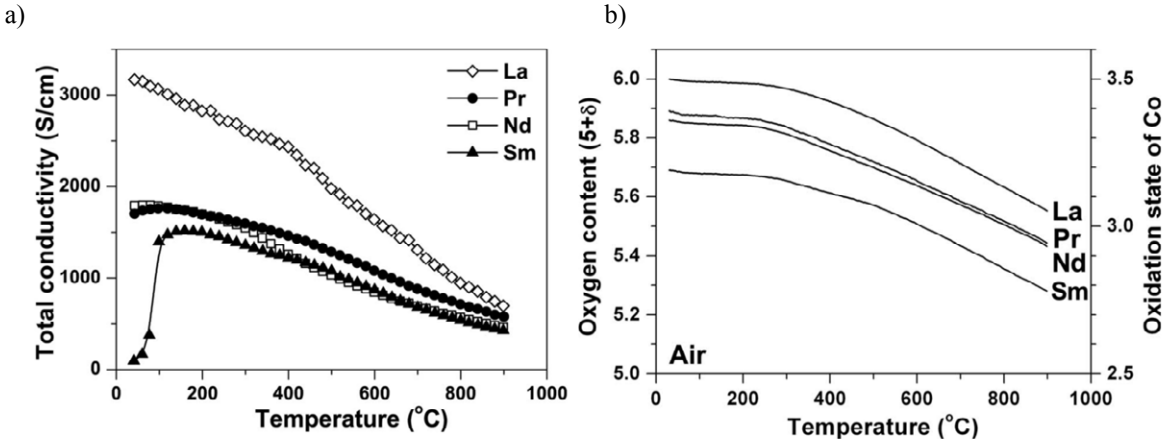

Fig. 4.13. a) Temperature dependence of the total conductivity and b) changes of the oxygen content and the oxidation state of cobalt in $BaLnCo_2O_{5+\delta}$ (Ln: La, Pr, Nd, Sm) with temperature in air. Figures from [153].

It can be noticed that at lower temperatures total conductivity of $BaLnCo_2O_{5+\delta}$ differs significantly between the compounds, however, it correlates with the initial oxygen nonstoichiometry and radius of Ln^{3+} cation. The highest conductivity was measured for almost stoichiometric $BaLaCo_2O_6$, with the biggest La^{3+} present. Interestingly, all materials exhibit metallic type of electrical conductivity (i.e. conductivity decreases with an increase of the temperature) above about 150 °C. Nevertheless, very high values of σ, considerably exceeding 100 $S \cdot cm^{-1}$ are characteristic for all discussed $BaLnCo_2O_{5+\delta}$ at high temperatures [153].

In another work Fe-containing $GdBa_{0.5}Sr_{0.5}Co_{1.5}Fe_{0.5}O_{5+\delta}$ was found to exhibit total conductivity of about 500 $S \cdot cm^{-1}$ at 800 °C with separated ionic component of 0.04 $S \cdot cm^{-1}$ at the same temperature [155].

More discussion about electrical and magnetic properties of manganese-containing $BaLnMn_2O_{5+\delta}$ oxides is given in the chapter below.

4.7. Electrical and magnetic properties of $BaLnMn_2O_{5+\delta}$ oxides

Magnetic (e.g. magnetoresistance-related) properties are characteristic for the certain manganese oxides, particularly for rare earth manganates having perovskite-type structure, which attracted attention of many scientists [15, 156-158]. Among various compounds, Mn-containing oxidized $BaLnMn_2O_6$ (Ln: La-Ho and Y) group of compounds is well-studied with electronic phase diagram available. Results of investigations of these materials, having the described in previous chapters layered type of cation ordering in the A-sublattice, was published in works [15, 158, 159]. As presented in Fig. 4.14, depending on the ionic radius of Ln^{3+} the compounds can be classified into three groups:

- For small cations (Ho^{3+}, Y^{3+}, Dy^{3+} and Tb^{3+}), $BaLnMn_2O_6$ oxides exhibit three phase transitions that occurs with lowering of the temperature: structural change from paramagnetic metal (PM) triclinic phase to different metallic-type PM' phase with monoclinic symmetry, which is followed by another transition into charge order insulator (noted as COI (CE) phase), and one more transformation into CE-type antiferromagnetic phase with charge order also present. Temperature of charge order transition increases with a decrease of the Ln^{3+} ionic radius, and for $BaYMn_2O_6$ equals to $T_{CO} \approx 200$ °C, which is one the highest among manganese oxides (however, see chapter 7).
- Materials with cations of the intermediate ionic radii (Gd^{3+}, Eu^{3+}, Sm^{3+}) exhibit no structural transition (in the paramagnetic metallic phase). The transition from PM to COI (CE) phases occurs in lower temperature range, comparing to first group of materials. However, transformation from CE-type charge/orbital-order insulator phase to antiferromagnetic (AFI) CE-type charge/orbital-order insulator occurs at slightly higher temperatures, depending on the substituted cation.

- For compounds having large cations such as Nd^{3+}, Pr^{3+} and La^{3+}, ferromagnetic transition occurs in the vicinity of room temperature. Unlike for $BaLaMn_2O_6$, in the case of $BaNdMn_2O_6$ and $BaPrMn_2O_6$ materials, an additional phase transition from FM to A-type antiferromagnetic metal is present.

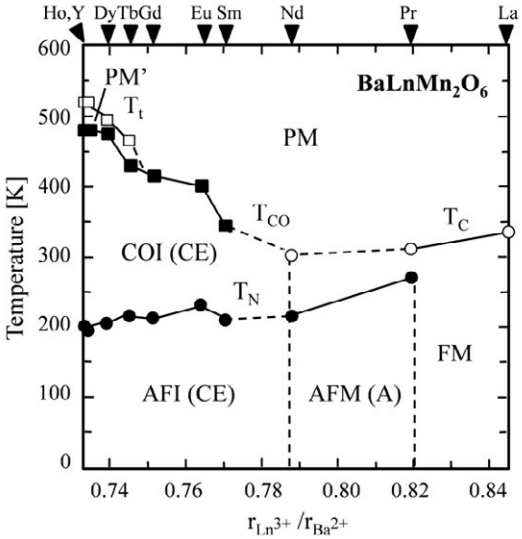

Fig. 4.14. Generalized phase diagram for $BaLnMn_2O_6$ oxides. FM: ferromagnetic metal, AFM (A): A-type antiferromagnetic metal, COI (CE): CE-type charge/orbital-ordered insulator, AFI (CE): antiferromagnetic CE-type charge/orbital-ordered insulator, PM: paramagnetic metal phase. T_{CO}: temperature of charge order transition, T_C: Curie temperature, T_t: phase transition temperature, T_N: Néel temperature. Figure adapted from [158].

Unfortunately, no similar (like shown in Fig. 4.14) electronic phase diagram is available for reduced $BaLnMn_2O_5$. However, half-integer oxidation states (i.e. Mn^{2+}/Mn^{3+}) also contribute to a formation of charge ordering, and consequently, charge and orbital ordering in a form of rock salt arrangement of cations is stabilized even above room temperature [145, 160, 161].

What is of important scientific matter, materials with similar composition to $BaLnMn_2O_6$ can be also obtained without cation ordering present, however, in these oxides larger Ba^{2+} cations are usually substituted by smaller Sr^{2+} or Ca^{2+} ions. Actually, most of the early studies concerning electrical and magnetic properties of disordered manganates focused on $A_xLn_{1-x}MnO_3$ oxides, in which Ln^{3+} and A^{2+} cations are randomly distributed. Phase diagram of the exemplary $A_{0.5}Ln_{0.5}MnO_3$ is depicted in Fig. 4.15. According to Ueda et al. [158], near $t_S = 1$ the ferromagnetic metal (FM) phase dominates, while in the lower t_S region (< 0.975), the CE-type charge/orbital-ordered insulator phase exists. In the middle region, where $t_S \sim 0.975$, the competition between the ferromagnetic (generated by

double exchange) and antiferromagnetic (generated by charge and orbital order) interactions results in various phenomena including transition from the ferromagnetic metal to antiferromagnetic charge/orbital-ordered insulator [158].

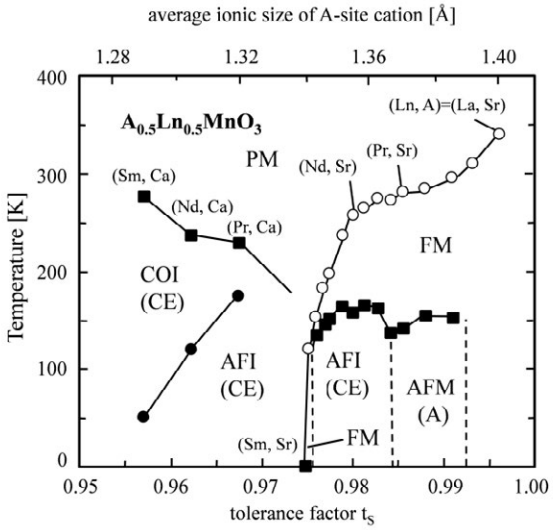

Fig. 4.15. Phase diagram for $A_{0.5}Ln_{0.5}MnO_3$. Designation have the same meaning as in Fig. 4.14. Figure adapted from [158].

Apart from the mentioned above $Sr_xLn_{1-x}MnO_3$ and $Ca_xLn_{1-x}MnO_3$, also there are available data regarding Ba-containing disordered $Ba_xLn_{1-x}MnO_3$. Such results allow for direct comparison between the ordered and disordered materials of the same composition, as shown in Fig. 4.16 [159].

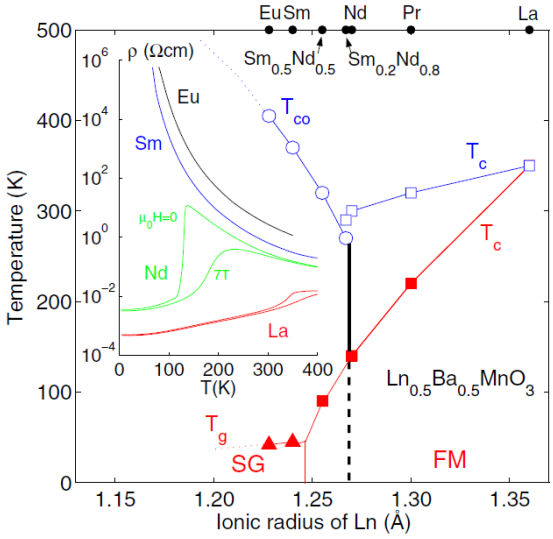

Fig. 4.16. Electronic phase diagram for selected A-site ordered $BaLnMn_2O_6$ (full symbols) and disordered $Ba_{0.5}Ln_{0.5}MnO_3$ (open symbols). Inset shows electrical resistivity measured without and with magnetic field of 7 T. T_{CO}: temperature of charge order transition, T_C: Curie temperature. T_g the spin-glass (SG) phase transition obtained from dynamical scaling. Figure from work [159].

Methodology

5. Methodology

In this chapter reasoning behind selection of the materials for studies, synthesis methods of their preparation, as well data regarding experimental techniques, used for characterization of the physicochemical properties of the considered compounds, are given.

5.1. Selection of chemical composition of the materials

As described in previous chapters, in year 2010 Motohashi et al. [5] published paper showing remarkable oxygen storage properties of the $BaYMn_2O_5$-$BaYMn_2O_6$ system. As mentioned, both, the oxidized (O_6) and the reduced (O_5) compounds belong to a larger group of $BaLnMn_2O_5$-$BaLnMn_2O_6$, which were shown in the literature to exists for Ln: La, Pr, Nd, Sm, Eu, Gd, Tb, Dy and Ho [158, 162-165]. Until now, however, their oxygen storage-related properties were not studied in details. It should be also noticed that Ho^{3+} cations are only slightly smaller than Y^{3+} [17]. Because of a large difference of ionic radii between Ba^{2+} and Ln^{3+}(Y^{3+}), it can be expected that introduction of smaller cations at Ln site may be highly hindered.

Considering the above, for the studies, apart from the reference $BaYMn_2O_{5+\delta}$, also materials with Ln: Pr, Nd, Sm, Gd and Dy were selected (results are presented in chapter 6). In addition, a possibility of formation of $BaErMn_2O_{5+\delta}$, with even smaller Er^{3+} cations was explored, and as documented below (chapter 7), the experiments yielded positive results. Because all Ln^{3+} cations are heavier than Y^{3+}, a decrease of the OSC is expected for $BaLnMn_2O_{5+\delta}$. Taking this into account, for selected lanthanides (Pr, Sm and Gd) formation of partially substituted compounds was investigated, with assumed chemical composition $BaY_{1-x}Ln_xMn_2O_{5+\delta}$ (chapter 8). Furthermore, possibility of replacement of Ba^{2+} by lighter Sr^{2+} in such compounds was also studied (chapter 9). Due to the expected, large oxygen stoichiometry changes in Co- and Fe-containing perovskite-type oxides [166, 167], which may exceed 4 wt.%, a selected group of such materials was also studied concerning their oxygen storage properties (chapter 10).

In Tab. 5.1, data regarding chemical composition of all of the successfully synthesized and investigated materials are gathered.

Tab. 5.1. Chemical composition of the synthesized and studied materials.

$BaLnMn_2O_{5+\delta}$	$BaY_{1-x}Ln_xMn_2O_{5+\delta}$	$Ba_{0.9}Sr_{0.1}Y_{1-x}Ln_xMn_2O_{5+\delta}$	Fe- and Co- containing materials
$BaPrMn_2O_{5+\delta}$	$BaY_{0.75}Pr_{0.25}Mn_2O_{5+\delta}$	$Ba_{0.9}Sr_{0.1}Y_{0.75}Pr_{0.25}Mn_2O_{5+\delta}$	$La_{0.6}Sr_{0.4}Co_{0.8}Fe_{0.2}O_{3-\delta}$
	$BaY_{0.5}Pr_{0.5}Mn_2O_{5+\delta}$		$La_{0.5}Sr_{0.5}Co_{0.5}Fe_{0.5}O_{3-\delta}$
	$BaY_{0.25}Pr_{0.75}Mn_2O_{5+\delta}$		$Sm_{0.5}Sr_{0.5}Co_{0.5}Fe_{0.5}O_{3-\delta}$
$BaNdMn_2O_{5+\delta}$			$La_{0.5}Ba_{0.5}Co_{0.5}Fe_{0.5}O_{3-\delta}$
$BaSmMn_2O_{5+\delta}$	$BaY_{0.75}Sm_{0.25}Mn_2O_{5+\delta}$	$Ba_{0.9}Sr_{0.1}Y_{0.75}Sm_{0.25}Mn_2O_{5+\delta}$	$Sm_{0.5}Ba_{0.5}Co_{0.5}Fe_{0.5}O_{3-\delta}$
	$BaY_{0.5}Sm_{0.5}Mn_2O_{5+\delta}$	$Ba_{0.9}Sr_{0.1}Y_{0.5}Sm_{0.5}Mn_2O_{5+\delta}$	
	$BaY_{0.25}Sm_{0.75}Mn_2O_{5+\delta}$	$Ba_{0.9}Sr_{0.1}Y_{0.25}Sm_{0.75}Mn_2O_{5+\delta}$	
		$Ba_{0.9}Sr_{0.1}SmMn_2O_{5+\delta}$	
$BaGdMn_2O_{5+\delta}$	$BaY_{0.75}Gd_{0.25}Mn_2O_{5+\delta}$	$Ba_{0.9}Sr_{0.1}Y_{0.75}Gd_{0.25}Mn_2O_{5+\delta}$	
	$BaY_{0.5}Gd_{0.5}Mn_2O_{5+\delta}$		
	$BaY_{0.25}Gd_{0.75}Mn_2O_{5+\delta}$		
$BaDyMn_2O_{5+\delta}$			
$BaYMn_2O_{5+\delta}$		$Ba_{0.9}Sr_{0.1}YMn_2O_{5+\delta}$	
$BaErMn_2O_{5+\delta}$			

5.2. Preparation method of the studied oxides

It is known that so called soft chemistry methods usually yield materials (oxides) having more homogenous distribution of the elements [168]. Consequently, such methods are suitable for preparation of compounds with complicated chemical formula. Also, in majority of cases, a lower final sintering temperature can be used in order to obtain single phase samples, comparing to the simple, high temperature solid-state synthesis route.

For preparation of the considered in this work Mn-containing oxides, a modified sol-gel method was utilized. Respective metal nitrates, with 99.9% purity were dissolved in stoichiometric proportions in a small amount of deionized water. To form cation complexes in the solution, certain amount of ammonia salt of ethylenediaminetetraacetic acid (EDTA) was added. The prepared mixtures were slowly heated in quartz evaporators in air, with an increase of temperature up to about 400 °C (200 °C in the case of $BaErMn_2O_{5+\delta}$). The heating process resulted in an evaporation of water, a sol-gel transition, a decomposition of excessive ammonium nitrate and combustion of the residual carbon, originating from EDTA complexes. The obtained xerogel-type precursors were ground and pressed into pellets (~ 1 mm thickness) with a pressure of 100 MPa.

Such prepared pellets were annealed at high temperatures in reducing conditions. Depending on the chemical composition of the material, the final sintering step was appropriately chosen. For most of the materials ($BaLnMn_2O_{5+\delta}$ Ln: Pr, Nd, Sm, Gd and Y, all $BaY_{1-x}Ln_xMn_2O_{5+\delta}$ and $Ba_{0.9}Sr_{0.1}Y_{1-x}Ln_xMn_2O_{5+\delta}$, see Tab. 5.1) temperature of 1100 °C with 100 $cm^3 \cdot min^{-1}$ gas flow of 1 vol.% of H_2 in Ar mixture and 8 h annealing time conditions were found to be optimal. In the case of $BaDyMn_2O_{5+\delta}$ sample, the annealing was repeated three times, with the final one conducted at 1000 °C. Details of the sintering process, which was developed for $BaErMn_2O_{5+\delta}$ oxide are given in chapter 7. For preparation of the powdered samples, which were needed for X-ray diffraction, microstructural and thermogravimetric studies, after the sintering, the pellets were thoroughly ground and the powders were sieved on 100 μm sieve.

As described above, the considered materials were synthesized in the reducing conditions. This is due to a fact that direct synthesis (e.g. in air) of the oxidized $BaLnMn_2O_6$ is either very difficult or even impossible for many Ln cations. While an explanation of this effect needs additional studies, it can be supported by two effects: strong tendency of formation of $BaMnO_3$ and $LnMnO_3$ while the synthesis is performed in the oxidizing atmospheres, as confirmed by XRD analysis of materials obtained in such experiments, and crystallographic reason related to a fact that relatively small Ln^{3+} cations seem to be too small for 12-fold coordination, in which they are present in the oxidized $BaLnMn_2O_6$. However, in the reduced $BaLnMn_2O_5$ material, the coordination of Ln^{3+} is decreased to 8, due to the preferential removal of oxygen from Ln-related layer, and therefore, the synthesis can be conducted successfully. Nevertheless, the oxidized $BaLnMn_2O_6$ can be easily obtained at relatively low temperatures by oxidation process performed in air (or oxygen) [158].

Regarding the listed Co- and Fe-containing perovskite-type oxides (Tab. 5.1) the sintering was conducted in air at 1200 °C for 24 h. Then, the pellets were slowly cooled to the room temperature.

In order to elucidate influence of the grain size on the oxygen storage-related properties, $BaYMn_2O_{5+\delta}$ and $BaNdMn_2O_{5+\delta}$ oxides were prepared also by solid-state reaction method, which yielded samples with significantly larger grains. The materials were studied in collaboration with Prof. Bogdan Dabrowski from Northern Illinois University, DeKalb, USA. For the synthesis, the respective oxides and carbonates were used. The synthesis was performed in high-purity Ar flow at 1400 °C for 12 h. Materials obtained using this method are tagged in this work as II (e.g. $BaYMn_2O_{5+\delta}$ II).

5.3. Structural characterization and Rietveld analysis

Structural identification of collected data was done using ICDD PDF4+ database. For Rietveld analysis, GSAS/EXPGUI set of software was used [169, 170].

To evaluate how accurate the refinement is, number of parameters can be calculated. The most commonly used in the literature are χ^2 called also a "goodness of fit" and is defined in the manual for GSAS [169] as (18):

$$\chi^2 = \frac{M}{N_{obs} - N_{var}} \tag{18}$$

where N_{obs} is the total number of observations in all histograms and N_{var} is the number of variables in the least squares refinement, M is a minimization function defined as (19, 20):

$$M = f_p \sum M_p \,, \tag{19}$$

$$M_p = \sum w(I_o - I_c)^2 \tag{20}$$

where f_p is a weighting factor in the case of multi histogram refinement, w stands for weights, I_o means normalized profile intensity and I_c is a calculated intensity, taking into account among others background and scale factors (see more in [169]).

Additionally, the quality of the refinement can be indicated by residuals, where the most commonly used is weight profile R-factor, defined as (21):

$$R_{wp} = \sqrt{M_p \Big/ \sum w I_o^2} \tag{21}$$

In general, the closer to unity χ^2 value is and the smaller the R_{wp} value, the better the refinement, however even $\chi^2 \approx 1$ does not guarantee that the applied model is fully correct [169]. Calculated error values of the refined structural parameters are included in the presented tables. Considering accuracy of the used equipment, the absolute error values of the calculated unit cell parameters can be established as lower than 0.001 Å.

5.3.1. X-ray diffraction

Structural studies of the synthesized oxides were carried out in 10-110 deg range with CuK_α radiation, using Panalytical Empyrean diffractometer or Rigaku Ultima IV diffractometer equipped with a monochromator. Initial data were collected on the as prepared materials for evaluation of the phase composition and selection of single phase materials for further studies. Results of the structural analyses presented in the following chapters concern fully reduced ($\delta \approx 0$) or fully oxidized ($\delta \approx 1$) samples, unless stated otherwise. For such studies, the initial materials were reduced at 500 °C in 5 vol.% H_2 in Ar or oxidized in air at the same temperature.

For high-temperature measurements, Anton Paar HTK 1200N oven-chamber was installed on Panalytical Empyrean diffractometer. Measurements were performed in air, and for selected samples in Ar and in a low vacuum (~ 100 Pa). Temperature range, heating rate, angular range and time of data collection for these measurements are given in the description of the respective figures. Data recorded during high-temperature studies enabled to evaluate thermal expansion coefficient of the samples. Linear TEC values were estimated using isotropic expansion approximation that assumes 1/3 of the volumetric thermal expansion coefficient. The refined values of the unit cell volume changes as a function of temperature were taken for such calculations. Because the studied perovskite-type oxides vary in terms of the crystal structure, having different space groups, in order to make direct comparison between the samples, both, unit cell volume and cell parameters were normalized (i.e. appropriately divided) to the simple, cubic perovskite structure. More details of the procedure are given in the respective figures and tables.

For the perovskite-type materials Goldschmidt's tolerance factor t_S can be calculated on a basis of Goldschmidt's equation (see chapter 4, equation (10)) [118]. In this work the arithmetic average of the respective ionic radii (for the appropriate coordination number) was taken, if one of the sublattices was occupied by more than one cation type.

Tolerance factor was also calculated using experimental data of crystallographic analysis according to the equation (22):

$$t_e = \frac{< A/A' - O >_n}{\sqrt{2} < B - O >_m} \tag{22}$$

where $<A/A'–O>_n$ and $<B–O>_m$ are the mean interatomic distances in the polyhedra with the corresponding coordination number n and m for the A- and B-site respectively [171].

5.3.2. Neutron diffraction

Diffraction of the neutrons is considered as non-destructive investigation technique, which allows to study an atomic and molecular structure of a material [172]. As it is shown in chapter 6.2, it is possible to study the oxidation process of selected $BaLnMn_2O_{5+\delta}$ by *in situ* structural experiments using laboratory-scale XRD diffractometer, as well as record changes of the crystal structure of the materials upon heating in vacuum conditions (~ 100 Pa). However, it is not possible to conduct *in situ* reduction experiments, analogous to the ones performed during TG studies (see chapter 5.4), i.e. in 5 vol.% H_2 in Ar atmosphere, due to technical limitations of the Anton Paar XRD oven-chamber. Also, it is know that sensitivity of XRD technique for relatively light oxygen is small. On the contrary, structural features related to oxygen can be easily observed in neutron diffraction studies [173-175] since the scattering cross-section for oxygen is on the same order as for other constituents, as presented in Tab. 5.2.

Tab. 5.2. Neutron cross section for absorption and scattering for the selected elements [176].

element	scattering cross section	absorption cross section
O	4.232	0.00028
Mn	2.15	13.30
Ba	3.38	1.10
Pr	2.66	11.50
Nd	16.6	50.5(1.2)
Sm	39(3)	5922(56)
Gd	180(2)	49700(125)
Dy	90.3	994(13)
Y	7.7	1.28
Er	8.7	159(4)

Considering the above and taking into account absorption cross section, praseodymium, neodymium and yttrium containing samples were selected and a proposal entitled "*In-situ reduction of $BaLnMn_2O_6$ (Ln: Y, Nd, Pr) perovskites*" have been submitted to Helmholtz Zentrum Berlin (HZB), in order to perform high-quality neutron diffraction experiments on fine-resolution angle-dispersive powder diffractometer E9 (FIREPOD) [177]. For detailed description of the measurement setup, please see appendix B.

For the measurements, high-quality powdered samples of about 5 g mass with precisely established oxygen content $\delta = 6.0$ were used. Neutron beam is more penetrating

than X-rays that is why grater amount of sample is required in comparison with XRD technique, which is available for samples even as small as ~ 30 mg (e.g. after TG measurements). In the considered experiment, the powder was placed near a bottom of a quartz tube. Long scans at ambient conditions before and after high-temperature measurements were conducted to establish precise structural parameters. The *in situ* studies of the reduction process were performed at the temperatures starting from 200 °C up to 500 °C (every 100°C) with 12 consecutive measurements at every temperature, unless described otherwise in the result section. Constant flow of 20 $ml \cdot min^{-1}$ of 5 vol.% H_2 in Ar gas was maintained by an embedded in the material quartz tube. The single scan, performed in the angular range of 5-140 deg, took approximately 30-35 min. Neutron wave length λ = 1.7982(1) Å from Ge(511) was used during the measurements.

The obtained data were refined using Rietveld refinement technique using GSAS/EXPGUI set of software [166, 167]. The background was fitted graphically using Shifted Chebyshev polynomials (28 terms). To facilitate comparison, obtained structural parameters presented in the graphical form were normalized to a single, cubic perovskite-type structure, while in the tables the exact values are presented, with the refined errors given.

5.4. Thermogravimetric studies

Oxygen storage-related properties including reduction/oxidation runs as a function of temperature or at constant temperature were determined using thermogravimetric (TG) method. Experiments were conducted on TA Q5000IR apparatus using platinum pans or on TGD-9600 Advance Riko Inc. using Al_2O_3 crucibles. The measurements were done on previously powdered samples, as described in chapter 5.2. Atmosphere of 5 vol.% H_2 in Ar was used for the reduction, while the oxidation process was studied in the synthetic air flow. For all studies, gas flow of 100 $cm^3 \cdot min^{-1}$ and heating rate of 5 $° \cdot min^{-1}$ were set up as the experimental conditions. In TA Q5000IR equipment, a protection gas flow (He) of 10 $cm^3 \cdot min^{-1}$ was set on the balance. For every measurement, comparable amount of the respective powder (c.a. 50 mg) was placed on the holder, and evenly spread to ensure fast gas change in the vicinity of the sample. Additionally, influence of the weight change in the experiments was studied, showing virtually the same results for 30 mg and 70 mg

amounts of the selected $BaGdMn_2O_{5+\delta}$ sample. The error of weight measurements on both thermobalances is small enough to be neglected.

Standard temperature of isothermal reduction/oxidation runs was selected at 500 °C [5], however, further studies in a temperature range of 400-600 °C were also conducted for the chosen samples. These studies allowed to estimate activation energy E_a of the oxygen transport. Details about method of calculation of E_a are given below in chapter 5.5.

Calculation of the reversible oxygen storage capacity (OSC) during non-isothermal runs was corrected for buoyancy effect, which was established on a basis of runs performed without material (empty holder) in the same conditions (i.e. gas flow, temperature range).

Determination of the oxygen content, OSC and the rate of oxygen incorporation and release is undoubtedly affected by TG measurement errors. The important buoyancy effect during change of the atmosphere, which, for example is causing a slight increase of the mass with a change from air to 5 vol.% H_2 in Ar gas flow is depicted in Fig. 5.1. As can be seen, the effect was measured to be smaller than 0.01 wt.%, and as such, not influencing significantly the OSC values. Nevertheless, the given results are corrected for the buoyancy effect.

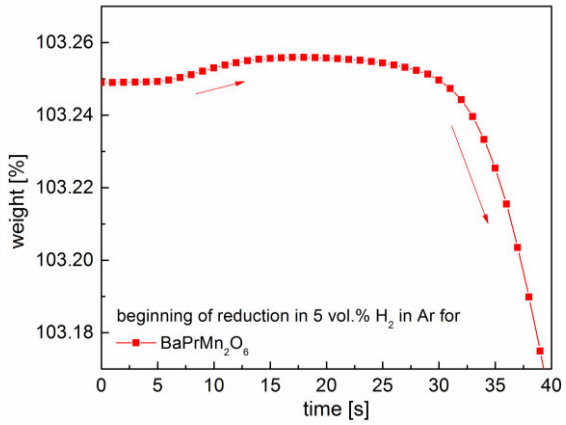

Fig. 5.1. Buoyancy effect correlated to the gas change from synthetic air to 5 vol.% H_2 in Ar, visible during the initial stage of the reduction process. Exemplary data are shown for $BaPrMn_2O_6$ sample.

Another important effect, which was measured during the isothermal oxidation and reduction process can be related to the emitted and absorbed heat associated with the respective intake and release of the oxygen form the material. In the case of $BaYMn_2O_{5+\delta}$, such effect was calculated to be about -200 $kJ \cdot mol^{-1}$ for the oxidation [178]. As can be seen in Fig. 5.2, during the longer (minutes) reduction process, the TG device is able to maintain the desired temperature precisely. However, during the much faster (seconds)

oxidation process, the temperature variation exceeds ±3 °. Since all studied materials are expected to exhibit similar enthalpy of oxidation, comparable temperature instability is likely to occur. While the overall changes appear to be not significant, such amount of heat released during oxidation may cause local overeating of the material, which actually can be associated with much faster kinetics of the oxidation, comparing to the reduction [165].

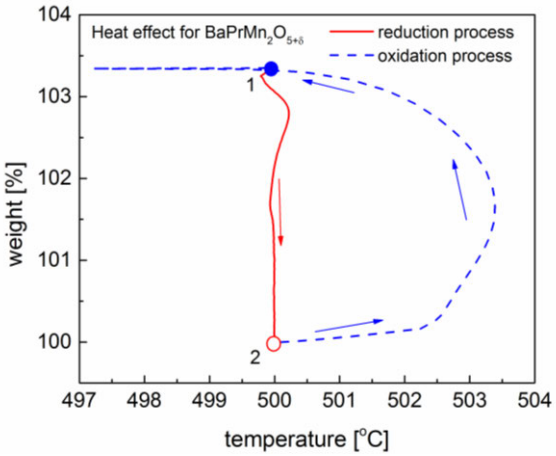

Fig. 5.2. Temperature recorded by TG sensor during oxidation and reduction at 500 °C of $BaPrMn_2O_{5+\delta}$. 1 - starting point on reduction, 2 - starting point on oxidation.

5.5. Estimation of the activation energy of the oxygen transport

In the conducted TG experiments it was possible to measure time needed for the oxidation or, which is of a greater importance from a point of view of practical application, reduction time (in 5 vol.% H_2 in Ar) of the samples at various temperatures (400-600 °C). As these processes can be associated with insertion and removal of the oxygen from the bulk of the grains (through surface), comparison of the time needed for a certain change of mass of the sample at different temperatures should allow for an evaluation of oxygen transport-related parameters (theoretical approach). Using the approximation below, it can be assumed that the activation energy of the bulk diffusion of the oxygen can be evaluated.

Process of the oxygen transport can be divided into bulk diffusion and surface exchange part, and consequently, determination of the diffusion coefficient D and surface exchange constant k would be of interest. However, as changes of the oxygen content in the presented studies are close to one mole per mole of compound, the recorded weight change characteristics cannot be used as "relaxation profiles" for fitting of D and k. Also, the mechanism of the oxygen release has two-phase nature (see chapter 6.2.2 and appendix

B for more information), and as such, there is no way to conduct experiment in a way that the data could be analyzed like it is done in standard relaxation-type studies with small changes of the oxygen content.

The recorded time needed for the reduction presented in Arrhenius coordinates for ionic conduction (i.e. in $\log(T/t)$ versus $1/T$ coordinates, t – time, T – temperature) shows activated character (linear behavior), which allows to calculate E_a for the respective material. To parameterize the process, change of 95% of total weight change and time needed to attain this value at respective temperature was chosen as characteristic, and such data will be presented further in this work (chapters 8.3.3, 9.5 and 10.6). However, for early considerations based on $BaY_{1-x}Gd_xMn_2O_{5+\delta}$ series of oxides, E_a was calculated assuming change of weight as 3 wt.% = 1875 $\mu molO \cdot g^{-1}$, 2 wt.% = 1250 $\mu molO \cdot g^{-1}$, 1 wt.% = 625 $\mu molO \cdot g^{-1}$, and also 99% , 95% and 90% of change of the total weight change, and such results are gathered in Tabs. 5.3-5.8. Please notice that there are no results presented for $BaYMn_2O_{5+\delta}$ at 400 °C, due to a very slow rate of the reduction process.

Tab. 5.3. Time needed for 3 wt.% change of weight of $BaY_{1-x}Gd_xMn_2O_{5+\delta}$, during reduction at respective temperatures together with activation energy of the process.

chemical composition	**time of reduction [min] at respective temperature 3 wt.% = 1875 $\mu molO \cdot g^{-1}$**					**E_a [eV]**
	400 °C	450 °C	500 °C	550 °C	600 °C	
$BaGdMn_2O_{5+\delta}$	49.70	13.15	5.88	3.47	2.18	0.85
$BaY_{0.25}Gd_{0.75}Mn_2O_{5+\delta}$	33.08	12.25	6.48	3.65	2.48	0.72
$BaY_{0.5}Gd_{0.5}Mn_2O_{5+\delta}$	44.67	18.92	8.40	3.87	2.28	0.83
$BaY_{0.75}Gd_{0.25}Mn_2O_{5+\delta}$	34.37	10.55	5.12	2.92	2.00	0.78
$BaYMn_2O_{5+\delta}$		21.75	7.10	3.82	2.53	0.85

Tab. 5.4. Time needed for 2 wt.% change of weight of $BaY_{1-x}Gd_xMn_2O_{5+\delta}$, during reduction at respective temperatures together with activation energy of the process.

chemical composition	**time of reduction [min] at respective temperature 2 wt.% = 1250 $\mu molO \cdot g^{-1}$**					**E_a [eV]**
	400 °C	450 °C	500 °C	550 °C	600 °C	
$BaGdMn_2O_{5+\delta}$	13.28	4.13	2.33	1.68	1.22	0.65
$BaY_{0.25}Gd_{0.75}Mn_2O_{5+\delta}$	10.25	4.87	3.27	2.13	1.57	0.53
$BaY_{0.5}Gd_{0.5}Mn_2O_{5+\delta}$	13.28	6.36	3.70	2.11	1.42	0.63
$BaY_{0.75}Gd_{0.25}Mn_2O_{5+\delta}$	10.72	4.67	2.68	1.80	1.33	0.59
$BaYMn_2O_{5+\delta}$		6.40	3.12	2.05	1.56	0.58

Tab. 5.5. Time needed for 1 wt.% change of weight of $BaY_{1-x}Gd_xMn_2O_{5+\delta}$, during reduction at respective temperatures together with activation energy of the process.

chemical composition	time of reduction [min] at respective temperature 1 wt.% = 625 µmolO·g^{-1}					E_a [eV]
	400 °C	450 °C	500 °C	550 °C	600 °C	
$BaGdMn_2O_{5+\delta}$	4.82	1.77	1.13	0.92	0.70	0.53
$BaY_{0.25}Gd_{0.75}Mn_2O_{5+\delta}$	4.33	2.42	1.78	1.20	0.92	0.45
$BaY_{0.5}Gd_{0.5}Mn_2O_{5+\delta}$	4.70	2.65	1.83	1.67	0.86	0.46
$BaY_{0.75}Gd_{0.25}Mn_2O_{5+\delta}$	3.98	2.02	1.48	1.03	0.80	0.46
$BaYMn_2O_{5+\delta}$		2.36	1.67	1.22	0.98	0.39

Tab. 5.6. Time needed for 99% change of total weight change of $BaY_{1-x}Gd_xMn_2O_{5+\delta}$, during reduction at respective temperatures together with activation energy of the process.

chemical composition	time of reduction [min] at respective temperature 99% change of total weight change					E_a [eV]
	400 °C	450 °C	500 °C	550 °C	600 °C	
$BaGdMn_2O_{5+\delta}$	60.50	22.86	9.30	5.25	3.18	0.82
$BaY_{0.25}Gd_{0.75}Mn_2O_{5+\delta}$	46.43	27.20	10.58	6.03	5.38	0.66
$BaY_{0.5}Gd_{0.5}Mn_2O_{5+\delta}$	72.25	42.42	19.45	6.15	3.30	0.88
$BaY_{0.75}Gd_{0.25}Mn_2O_{5+\delta}$	55.80	24.08	9.68	5.15	3.40	0.79
$BaYMn_2O_{5+\delta}$		51.50	16.20	10.98	8.20	0.72

Tab. 5.7. Time needed for 95% change of total weight change of $BaY_{1-x}Gd_xMn_2O_{5+\delta}$, during reduction at respective temperatures together with activation energy of the process.

chemical composition	time of reduction [min] at respective temperature 95% change of total weight change					E_a [eV]
	400 °C	450 °C	500 °C	550 °C	600 °C	
$BaGdMn_2O_{5+\delta}$	46.08	14.43	6.38	3.80	2.30	0.82
$BaY_{0.25}Gd_{0.75}Mn_2O_{5+\delta}$	35.11	15.75	7.65	4.30	2.82	0.71
$BaY_{0.5}Gd_{0.5}Mn_2O_{5+\delta}$	54.25	28.28	13.08	4.98	2.60	0.85
$BaY_{0.75}Gd_{0.25}Mn_2O_{5+\delta}$	42.8	15.70	6.78	3.70	2.38	0.80
$BaYMn_2O_{5+\delta}$		33.93	10.14	5.45	3.56	0.88

Tab. 5.8. Time needed for 90% change of total weight change of $BaY_{1-x}Gd_xMn_2O_{5+\delta}$, during reduction at respective temperatures together with activation energy of the process.

chemical composition	time of reduction [min] at respective temperature 90% change of total weight change					E_a [eV]
	400 °C	450 °C	500 °C	550 °C	600 °C	
$BaGdMn_2O_{5+\delta}$	35.42	10.80	5.23	3.16	2.03	0.78
$BaY_{0.25}Gd_{0.75}Mn_2O_{5+\delta}$	27.38	12.06	6.43	3.68	2.53	0.67
$BaY_{0.5}Gd_{0.5}Mn_2O_{5+\delta}$	41.47	20.25	9.42	4.13	2.36	0.81
$BaY_{0.75}Gd_{0.25}Mn_2O_{5+\delta}$	33.33	12.00	5.68	3.16	2.13	0.77
$BaYMn_2O_{5+\delta}$		25.01	8.12	4.45	2.90	0.85

Data presented in the above tables suggest that E_a increases (almost linearly) with the increasing value of weight change taken as the end point of the time measurement. It seems

therefore that the mechanism of the oxygen release changes as the process proceeds, which was expected taking into account two-phased nature of the process. Furthermore, the samples can be compared between each other using values of E_a because:

- Assumed different weight changes for the calculation of E_a of the samples corresponds to the release of (in each case) a very similar amount of the oxygen from all studied samples per volume (alike density) and per weight (alike molar mass).
- As microstructure of the powders is very similar with comparable grain size distribution and BET specific surface, the average diffusion distance for the oxygen to be released from grains will be comparable, and also total surface, through which the oxygen will be released will be very similar (see chapter 6.3).

However, more assumptions can be also made and justified taking into account the following information:

- For most of the perovskite-type oxides the available literature data suggest that the surface exchange coefficient k is at least 2-3 orders of magnitude higher than the diffusion coefficient D (calculated from tracer methods or relaxation studies) [123]. See also discussion in chapter 2.3, and referenced work [60].
- For powder morphology, (see chapter 6.3) the oxygen release process is highly unlikely to be limited by the surface exchange reaction only. Therefore, it is rather the bulk diffusion in the grains, which is a limiting factor.
- It is also known that k often does not show clearly defined temperature dependence, from which E_a can be calculated. On the contrary, D often shows activated character on temperature, with values below 1 eV being observed [123].
- Structural modification during oxygen release from $BaYMn_2O_6$ through $BaYMn_2O_{5.5}$ to $BaYMn_2O_5$ (or reverse, oxygen uptake [7]) occurs with preservation of the structural framework (see chapter 6.2.2).

Considering above, the calculated E_a (for times representing most of the actual weight change) can be correlated with changes of the oxygen transport in the materials as a function of temperature, and since surface exchange reaction and structural changes can

be neglected as not limiting, the E_a values can be associated to the diffusion process of the oxygen in bulk of the grains, but likely, in the final step of the oxygen release process.

Since in the powdered sample the grains of different size and shape are present, no simple model can be used to evaluate behavior of the oxygen release, however, because statistically the samples are similar, averaged values can be considered. It is well known that mean square displacement of diffusing species is proportional to the diffusion coefficient and time as (23):

$$< x >^2 \sim Dt \tag{23}$$

If conditions of the transport (as documented above) are similar, release of the oxygen from the material would directly correspond to the same mean square displacement (of the oxygen in all grains). And consequently (24):

$$< x >^2 \sim D_{T1}t_{T1} = D_{T2}t_{T2} \;\rightarrow\; \frac{D_{T2}}{D_{T1}} = \frac{t_{T1}}{t_{T2}}, \text{ where } T_1 < T_2 \tag{24}$$

Therefore, temperature dependence of diffusion coefficient in Arrhenius coordinates (activation energy of D) would be the same like activation energy of reduction time. Also, considering ionic conductivity of the oxygen, and taking into account Einstein equation, it can be written that oxygen mobility μ is proportional to the (average or effective) diffusion coefficient at the particular temperature (25):

$$\frac{D}{\mu} = \frac{kT}{q} \;\rightarrow\; D \sim \mu \rightarrow \frac{\mu_2}{\mu_1} \sim \frac{t_1}{t_2} \tag{25}$$

Electrical conductivity is known to depend on charge, concentration and mobility of the charge carriers according to the equation (26):

$$\sigma = C\mu q \tag{26}$$

With constant value of q and the same value of C, it can be stated that the activation energy of the ionic conductivity of the mobile oxygen at the final stages of the oxygen release process would be the same as the activation energy of the reduction time. Of course, since

it corresponds to almost all of the oxygen being released from the material, and it was shown that there is no single D value characterizing whole process, the above diffusion coefficient can be treated as effective one. But, anyway, the calculated activation energy on the order of 0.7-0.8 eV can be related to the activation energy of the oxygen mobility. While this is only a very rough approximation, it seems reasonable, with values being typical for the oxygen diffusion in oxides. Please notice that the actual values of D are not provided, but only the activation energy.

5.6. Microstructural studies

Studies of powder microstructure of the synthesized samples were conducted on FEI Nova NanoSEM 200 scanning electron microscope equipped with a low vacuum detector and EDX detector (EDAX), used for evaluation of the chemical composition. Typically, 1000-10000 magnification was used for observation of the powders. Average particle size was evaluated by computer-supported statistical analysis of the micrographs. EDX spectroscopy was used to confirm element content of the studied materials. It should be noticed that some amount of carbon was also detected on the surface of the samples, likely originating from the preparation method. However, it can be also related to the adsorbed on surface of the grains CO_2.

Additional studies of the specific surface area of the considered selected powders were conducted by N_2 adsorption method using Gemini V Micromeritics apparatus. Typically, about 1 g of the powdered material was used in the experiments. Data were analyzed assuming Brunauer-Emmett-Teller (BET) isotherm. Error associated with BET experiments was evaluated not to exceed 0.03 $m \cdot g^{-1}$.

5.7. XPS measurements

X-ray photoelectron spectroscopy (XPS) system, Kratos AXIS-ULTRA, was used for investigation of the selected oxides in reduced and oxidized form. The used X-ray source was AlKα (hv = 1486.6 eV) with monochromator. The results were analyzed using Igor Pro 6.37 software with background fitted cubically and peaks fitted using Gauss function.

5.8. Electrical conductivity and Seebeck coefficient measurements

Additional studies of electrical conductivity and thermoelectric power (Seebeck coefficient) were measured for selected samples using a four-probe system (with direct current applied). The system is a custom-made equipment, developed at the Department of Hydrogen Energy, Faculty of Energy and Fuels, AGH University of Science and Technology, which allows for simultaneous measurements of both of these properties. For the measurements, sinter of the considered oxide was cut in a rectangular shape. The studies were carried out in 5 vol.% H_2 in Ar or in synthetic air atmosphere. The sample holder in the equipment consists of four electrodes arranged in a short distance from each other (~ 3 mm) and being in electrical contact with the surface of the sample. The two outer electrodes (made from gold) act as current collectors. The inner electrodes (made from platinum wire wrapped several times around the sample) act as voltage electrodes. In order to calculate electrical conductivity, the measured voltage drop was divided by the value of the electrical current, and corrected concerning size of the studied sample. During Seebeck coefficient measurements, temperature gradient on the both ends of the sample, of about 2-5 °C, was enforced.

The relative error of electrical conductivity evaluation, which takes into account errors related to accuracy of used gauges, sample's porosity (Bruggeman's effective medium approximation was applied, with a suitable porosity-related correction [179]) and dimensions and distances between electrodes is estimated to be on the order of 10%, which can be translated to a possible shift of electrical conductivity of about ±0.1 (in the Arrhenius coordinates). The maximum error value of the activation energy of the electrical conductivity is estimated to be smaller than 0.01 eV. Concerning Seebeck coefficient measurements, the error is estimated to be below $\leq 5\ \mu V \cdot K^{-1}$.

5.9. Calculation of parameters for evaluation of the oxygen storage properties

As described in chapter 2.1, usefulness of the potential storage material can be evaluated taking into account the following factors: reversible oxygen storage capacity

(OSC), speed of incorporation and release of the oxygen, characteristic temperatures of this processes and cyclability.

Theoretical oxygen storage capacity of materials was calculated as a difference in molar mass between oxidized (m_{oxy}) and reduced material (m_{red}) and divided by the mass of the material in reduced state according to the equation (27):

$$OSC = \frac{m_{oxy} - m_{red}}{m_{red}} \quad (27)$$

The theoretical value of OSC was calculated assuming maximal change of oxygen content as 1 mol of oxygen per 1 mol of compound in the case of double perovskites (change between $Ba_{1-y}Sr_yY_{1-x}Ln_xMn_2O_6 \leftrightarrow Ba_{1-y}Sr_yY_{1-x}Ln_xMn_2O_5$ accompanied by change of oxidation state of the manganese) and 0.5 mol of O for brownmillerite-type materials containing 0.5 mol of Co (e.g. $Sm_{0.5}Sr_{0.5}Co_{0.5}Fe_{0.5}O_3 \leftrightarrow Sm_{0.5}Sr_{0.5}Co_{0.5}Fe_{0.5}O_{2.5}$). For $La_{0.6}Sr_{0.4}Co_{0.8}Fe_{0.2}O_{3-\delta}$, theoretical value of δ is equal to 0.6, due to a higher amount of cobalt, which can change its oxidation state during reduction/oxidation process in +4 to +2 range. Measured OSC was calculated on the same principio as the theoretical one, using weight change during isothermal TG measurements at 500 °C while change of the atmosphere between air and 5 vol.% H_2 in Ar. Another parameter calculated out of this test is a time needed particular (e.g. 99%) of a total weight change, which allows for comparison of the kinetics of oxygen incorporation and release processes.

Characteristic temperatures of oxidation and reduction processes were determined based on non-isothermal TG measurements (from RT to 500 °C in atmosphere of air or 5 vol.% H_2 in Ar respectively) by reading off an extremum on derivative curve.

Results and discussion

6. Properties of $BaLnMn_2O_{5+\delta}$ (Ln: Pr, Nd, Sm, Gd, Dy and Y) oxides

As mentioned in chapter 4, available literature data, including the works of the author suggest that Mn-based perovskite-type cation-ordered oxides (e.g. $BaYMn_2O_{5+\delta}$ or related) should be considered as one of the most promising oxygen storage materials. Although, presented data concerning crystal structure and oxygen storage-related properties of these compounds were until now highly limited. In this chapter, results of the characterization of basic properties of $BaLnMn_2O_{5+\delta}$ (Ln: Pr, Nd, Sm, Gd, Dy and Y) oxides are gathered. While Y-containing material exhibits the highest theoretical capacity in the series, due to its lowest molar mass, motivation behind the presented work was to study possibility of enhancement of other properties, important from the view point of oxygen storage technology, which seem to be related to the choice of Ln cation. Most important presented below data were published in the cited work [180] by the author.

6.1. Crystal structure of $BaLnMn_2O_5$ and $BaLnMn_2O_6$ oxides at room temperature

Initial XRD structural measurements were performed on the as prepared $BaLnMn_2O_{5+\delta}$ samples, showing formation of the desired structure and no or minimal amount of secondary phases. Following this, precise structural characterization was carried out on practically fully oxidized (in air at 500 °C, $\delta \approx 1$) and reduced (in 5 vol.% H_2 in Ar at 500 °C, $\delta \approx 0$) materials [5]. According to the literature, presence of (001) peak in the vicinity of 11.5 deg for both, reduced and oxidized compounds indicates formation of the A-site cation-ordered phase (layered-type of Ba-Ln arrangement, see chapter 4.4.1) [15]. Exemplary XRD data together with Rietveld refinement for $BaLnMn_2O_5$ and $BaLnMn_2O_6$ (Ln: Pr, Sm, Gd and Dy) oxides are shown respectively in Figs. 6.1a-d. As can be seen, intensity of the mentioned (001) peak is rather small, especially for materials with larger Ln^{3+} cations, suggesting possible partial mixing between Ln^{3+} and Ba^{2+}. However, as no significant improvement of the refinements with assumption of such mixing could be obtained, reliable estimation of a degree of the mixing was not possible, despite good quality data. This is mainly due to a comparable atomic mass of Ln and Ba cations. For more details about this issue see Appendix A, presenting precise, synchrotron data.

Because $BaNdMn_2O_{5+\delta}$ and $BaYMn_2O_{5+\delta}$ were synthesized also by the solid state, high-temperature reaction (see Experimental section), a comparison of the influence of the preparation method on the structural properties can be done. As visible in Figs. 6.2a-d, while no major differences could be observed between the materials obtained by both routes (the same space group allowed to refine the data successfully), data presented in Tab. 6.1 indicate somewhat different unit cell parameters and volume. The mentioned Tab. 6.1 shows the obtained structural parameters and also information about accuracy of the refinement of reduced and oxidized $BaLnMn_2O_{5+\delta}$ compounds. It is worth mentioning that the calculated theoretical tolerance factor is linearly dependent on the ionic radii of Ln, while the one calculated from X-ray diffraction data shows no such correlation. However, values for the oxidized materials are higher.

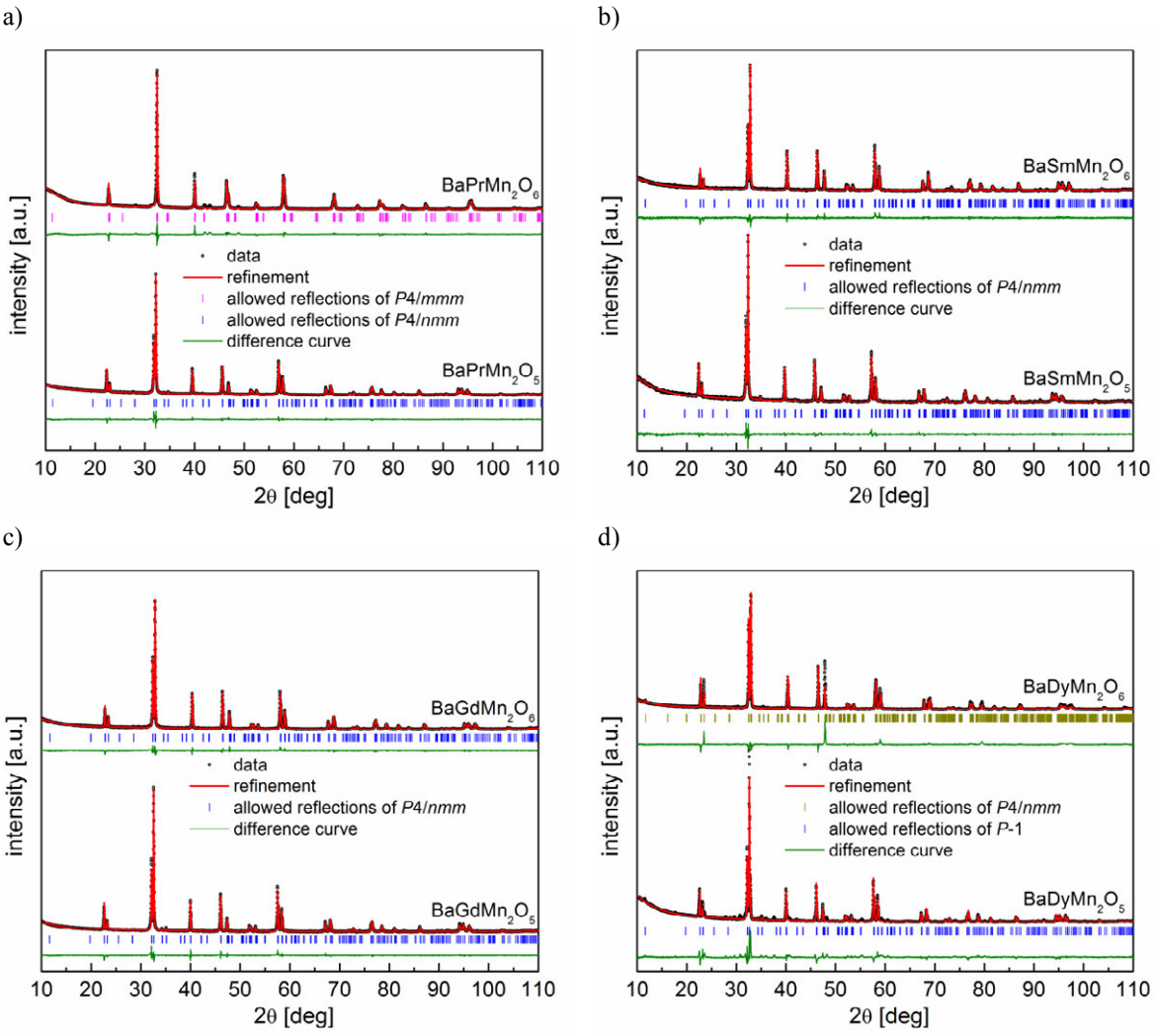

Fig. 6.1. Diffractograms with Rietveld analysis for: a) $BaPrMn_2O_{5+\delta}$, b) $BaSmMn_2O_{5+\delta}$, c) $BaGdMn_2O_{5+\delta}$ and d) $BaDyMn_2O_{5+\delta}$ samples in oxidized and reduced form recorded at room temperature. In the case of Dy-containing material, having small amount of secondary phases, intensity of some of the peaks could not be refined correctly. Notice that color of symbols of allowed reflections is related to the space group.

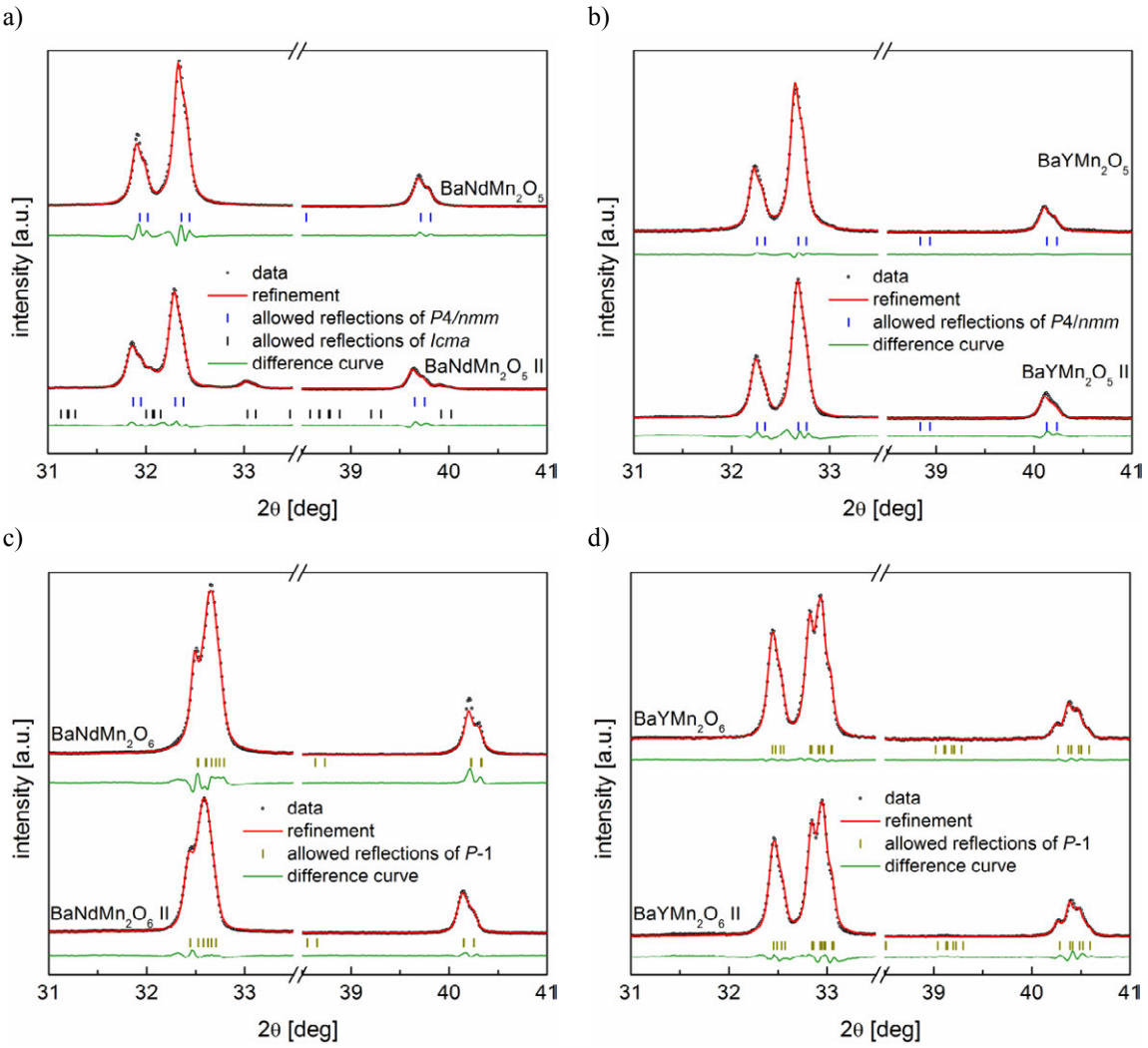

Fig. 6.2. Selected angular range of recorded diffractograms with Rietveld analysis for: a) $BaNdMn_2O_5$ and $BaNdMn_2O_5$ II, b) $BaYMn_2O_5$ and $BaNdMn_2O_5$ II, c) $BaNdMn_2O_6$ and $BaNdMn_2O_6$ II and d) $BaYMn_2O_6$ and $BaYMn_2O_6$ II samples at room temperature, refined assuming *P*-1 triclinic space group for the oxidized materials and *P*4/*nmm* structure for the reduced ones. $BaNdMn_2O_5$ II contains ~ 15 wt.% of $BaNdMn_2O_{5.5}$ with *Icma* symmetry.

Considering the oxidized materials and starting from the biggest Pr^{3+} cation, in the case of $BaPrMn_2O_6$, crystal structure of the compound can be refined at room temperature using aristotype *P*4/*mmm* symmetry. This basic structure represents simple doubling of the perovskite-type cell along *c*-axis (i.e. $1a_p \times 1a_p \times 2a_p$), with only single crystallographic position for all manganese cations. Considering that the average oxidation state of the Mn cations in the oxidized $BaLnMn_2O_6$ is +3.5, it likely indicates no charge-ordering effects taking place.

Tab. 6.1. Structural parameters of reduced and oxidized $BaLnMn_2O_{5+\delta}$ materials at room temperature. Data gathered from author's publications [6, 165, 180-182].

chemical composition	space group	a [Å] b [Å] α [deg] β [deg]	c [Å] γ [deg]	V [Å^3]	relative increase of V after reduction[a] [%]	χ^2	R_{wp} [%]	t_s	t_e
$BaPrMn_2O_5$	*P*4/*nmm*	5.6263(1)	7.7565(1)	245.53(1)	3.99	2.8	3.4	0.985	0.963
$BaPrMn_2O_6$	*P*4/*mmm*	3.9004(1)	7.7480(1)	117.87(1)		6.3	5.7	0.990	1.000
$BaNdMn_2O_5$	*P*4/*nmm*	5.6160(1)	7.7422(1)	244.18(1)	3.66	3.2	3.6	0.982	0.965
$BaNdMn_2O_6$	*P*-1	5.5177(1) 5.5167(1) 90.00(3) 90.00(2)	7.7282(1) 90.10(1)	235.24(1)		5.7	4.9	0.986	0.998
$BaNdMn_2O_5$ II[b]	*P*4/*nmm*	5.6142(1)	7.7374(1)	243.88(1)	3.70	2.4	3.3	0.982	0.963
$BaNdMn_2O_6$ II	*P*-1	5.5139(1) 5.5137(1) 90.00(1) 90.00(1)	7.7247(1) 90.16(1)	234.85(1)		2.3	3.1	0.986	0.995
$BaSmMn_2O_5$	*P*4/*nmm*	5.5963(1)	7.7105(1)	241.48(1)	3.01	1.2	4.3	0.976	0.960
$BaSmMn_2O_6$	*P*4/*nmm*	5.5430(1)	7.6227(1)	234.21(1)		1.3	5.0	0.979	0.998
$BaGdMn_2O_5$	*P*4/*nmm*	5.5808(1)	7.6876(1)	239.43(1)	2.59	3.0	3.1	0.972	0.955
$BaGdMn_2O_6$	*P*4/*nmm*	5.5352(1)	7.6121(1)	233.23(1)		2.4	2.7	0.974	0.996
$BaDyMn_2O_5$	*P*4/*nmm*	5.5663(1)	7.6658(1)	237.18(1)	1.94	15.7	6.5	0.967	0.963
$BaDyMn_2O_6$	*P*-1	5.5293(1) 5.5269(2) 90.00(1) 90.29(1)	7.6103(2) 89.95(1)	232.57(1)		11.6	5.9	0.970	0.995
$BaYMn_2O_5$	*P*4/*nmm*	5.5496(1)	7.6548(1)	235.75(1)	1.54	1.6	4.5	0.966	0.954
$BaYMn_2O_6$	*P*-1	5.5253(1) 5.5198(1) 90.01(1) 90.30(1)	7.6105(1) 89.96(1)	232.11(1)		1.4	4.5	0.969	0.991
$BaYMn_2O_5$ II	*P*4/*nmm*	5.5509(1)	7.6560(1)	235.90(1)	1.57	4.2	3.6	0.966	0.956
$BaYMn_2O_6$ II	*P*-1	5.5265(1) 5.5207(1) 90.00(1) 90.29(1)	7.6103(1) 89.94(1)	232.19(1)		2.9	3.1	0.969	0.994
$BaErMn_2O_5$[c]	*P*4/*nmm*	5.5424(1)	7.6422(1)	234.76(1)	1.31	8.4	4.9	0.963	0.956
$BaErMn_2O_6$[c]	*P*-1	5.5206(1) 5.5147(1) 90.01(1) 90.29(1)	7.6100(1) 89.92(1)	231.68(1)		6.1	4.6	0.966	0.975

[a]Calculated using unit cell volume normalized to *P*4/*nmm* structure. [b]Despite 220 min reduction at 500 °C in 5 vol.% H_2 in Ar, the sample contained ~ 15 wt.% of $BaNdMn_2O_{5.5}$ phase with *Icma* symmetry. [c]See chapter 7 for more detailed discussion.

In the case of $BaNdMn_2O_6$ obtained from both synthesis methods, an evident split of (200) peak in the vicinity of 46.5 deg was recorded at the room temperature, indicating a decrease of the symmetry. This distortion, however, completely disappears while heating up to 100 °C (see chapter 6.2, Fig. 6.5a) [183]. Because in the reported electronic phase diagrams [157-159], there is an indication of a phase transition occurring near RT, it is possible that the distortion originates from the magnetic effects (see chapter 4.7). For this compound the structural refinement was conducted assuming *P*-1 space group.

For the oxidized (O_6) samples with smaller Ln^{3+} cations (Sm^{3+}, Gd^{3+}), good quality refinements of the structural data were obtained assuming tetragonal *P*4/*nmm* space group representing $\sqrt{2}a_p \times \sqrt{2}a_p \times 2a_p$ superstructure. As suggested in the literature [158], in this arrangement manganese cations present at B-site form a rock salt-like charge order, where Mn^{3+} and Mn^{4+} states occupy different crystallographic positions [145, 184].

Furthermore, in the case of samples with even smaller Dy^{3+} and Y^{3+} cations, the actual symmetry seems to be lowered to either monoclinic *P*121 or triclinic *P*-1 space group [7, 184, 185]. Considering the published results, the measured structural data for the considered compounds were refined using triclinic symmetry. For discussion about synthesized $BaErMn_2O_6$ see the following chapter 7.

All reduced $BaLnMn_2O_5$ oxides could be refined successfully assuming *P*4/*nmm* symmetry, with charge order of Mn^{2+} and Mn^{3+} cations present, forming the mentioned rock salt-type arrangement. While no electronic phase diagram is available for all considered $BaLnMn_2O_5$, presence of two, clearly defined positions of the manganese cations in the crystal structure likely indicates that the materials should possess notably lower electrical conductivity than the oxidized ones. This effect is further discussed in chapter 7.

As can be seen in Tab. 6.1 and in Fig. 6.3, for both series, $BaLnMn_2O_5$ and $BaLnMn_2O_6$ there is a linear dependence ($R^2 > 0.99$) observed between unit cell volume and ionic radius of Ln^{3+}. In order to compare materials having different structural space groups, the data were normalized, i.e. appropriately divided, to obtain cubic-like $1a_p \times 1a_p \times 1a_p$ unit cell volume. Also, since the ionic radius of smaller Ln^{3+} is untypically small for 12-fold coordination, data are presented for 8-fold coordination. All reduced materials possess larger unit cell than respective oxidized ones, which can be related to the increase of average Mn-O bond length, which originates from a decreased average oxidation state of manganese cations, but also from generally weaker bonding, as

less oxygen anions are present in the structure of $BaLnMn_2O_5$. Interestingly, slope of these two dependences is different, and unit cell of oxides with smaller Ln^{3+} cations does not expand so much upon reduction (Fig. 6.3). This behavior seems to be associated with a fact that cubo-octahedral void is not fully filled when occupied by smaller Ln^{3+} cations.

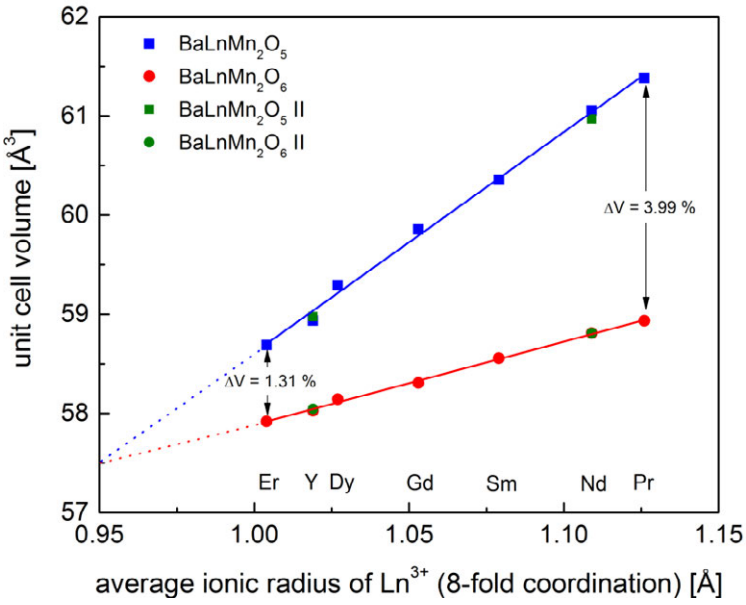

Fig. 6.3. Unit cell volume of $BaLnMn_2O_5$ and $BaLnMn_2O_6$ as a function of Ln^{3+} ionic radius.

Small change of the unit cell volume upon reduction and oxidation seems to be important factor, considering oxygen storage-related application, during which the material is subjected to numerous cycles of the oxygen release and intake. While the smallest variation was observed for $BaErMn_2O_{5+\delta}$ oxide (see chapter 7), the extrapolated lines in Fig. 6.3 suggest that if it was possible to obtain compounds with introduced even smaller lanthanides (e.g. Yb^{3+}) or In^{3+}, such change should be indeed very small. Unfortunately, all attempts to synthesis $BaYbMn_2O_{5+\delta}$ were so far unsuccessful (see also [157]).

6.2. In situ structural measurements

Structural measurements *in situ* were conducted in both oxidizing and reducing atmospheres, corresponding with the one used during TG-studies of oxygen storage properties, and also in vacuum conditions. That allowed for the description of the possible mechanism of the reduction process of $BaLnMn_2O_{5+\delta}$ (Ln: lanthanides and Y) oxides.

6.2.1. Changes of the crystal structure during oxidation process

It was reported that oxidation of $BaYMn_2O_5$ occurs rapidly in air above 250 °C, and the process is fast, taking seconds [5]. Precise XRD measurements while such oxidation process is ongoing are problematic, due to fast reaction rate. However, it was possible to conduct *in situ* structural studies during heating in air of $BaNdMn_2O_5$ II sample. This material was obtained by solid state reaction at high temperatures, which resulted in formation of significantly larger grains (compare Fig. 6.12a-d and Fig. 6.13a-d). Consequently, as the oxygen diffusion path is much longer in such grains, the oxygen incorporation process is slow enough to be observed in precise (one hour per scan, 10-100 deg range) XRD studies. Exemplary diffractograms at RT, 500 °C and 800 °C, recorded during these measurements for $BaNdMn_2O_5$ II are shown in Fig. 6.4a. For comparison, similar data are shown for the oxidized $BaNdMn_2O_6$ II material.

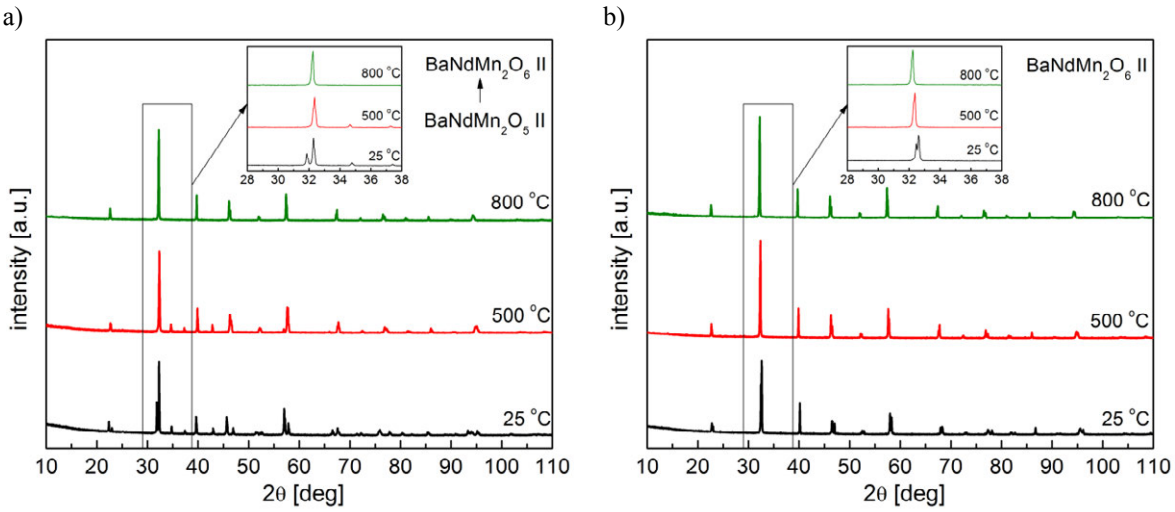

Fig. 6.4. a) Exemplary XRD diffractograms recorded at 25 °C, 500 °C and 800 °C for a) $BaNdMn_2O_5$ II and b) $BaNdMn_2O_6$ II during heating in air.

In Fig. 6.5a and b, the measured data are presented in a different manner, focused on temperature evolution of the main peaks, which are present in a vicinity of 32 deg. Calculated unit cell parameters and volume change with increasing temperature are given, which allowed also to estimate the thermal expansion coefficient (TEC) of the studied samples. It is evident that the oxidation process, which in this particular case occurs in 175-200 °C range, causes a decrease of the unit cell parameters and volume of the material, and change of the space group from *P*4/*nmm* to *P*4/*mmm*. Prior and after the oxidation only the thermal expansion-related shift of the peaks towards lower angles can be noticed.

Interestingly, TEC of the reduced material is lower, comparing to the oxidized one, which is most likely due to larger average Mn-O bond length. One additional information was deduced from the conducted experiments, as mentioned above, the structural triclinic (*P*-1) distortion present at RT (Tab. 6.1), disappears completely at 100 °C.

a)

b)

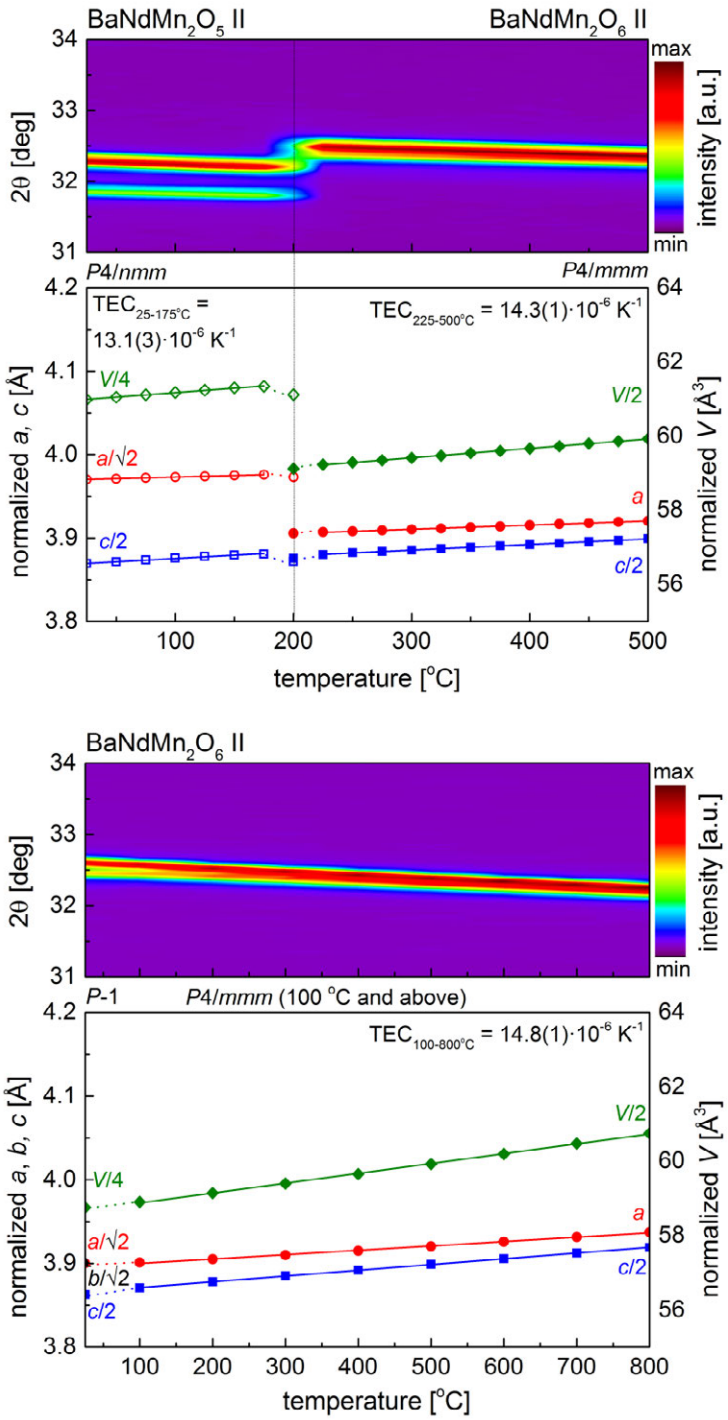

Fig. 6.5. Structural evolution of a) reduced $BaNdMn_2O_5$ II and b) $BaNdMn_2O_6$ II sample during heating in air. Intensity data shown for selected angular range (main peaks). Corresponding temperature dependence of normalized unit cell parameters and volume, as well as calculated thermal expansion coefficients data are given.

It is also worth mentioning that during the structural transformation occurring with oxidation, the registered peak intensities are much lower, comparing to the ones observed before and after oxidation. This may be explained taking into account that during the oxidation process the structural coherence length is considerably shortened, but after the process the structure is rebuilt.

Similar behavior upon oxidation process can be expected for all other $BaLnMn_2O_5$ samples, although, materials obtained by the soft chemistry method were found to oxidize too fast to be able to precisely observe the intermediate steps related to the structural changes during regular XRD scans.

6.2.2. Changes of the crystal structure during reduction process in 5 vol.% H_2 in Ar and mechanism of oxygen release from $BaLnMn_2O_6$ oxides

Evolution of the crystal structure of $BaLnMn_2O_6$ (Ln: Nd, Pr, Y) during reduction in atmosphere of 5 vol.% H_2 in Ar at elevated temperatures was a subject of investigations during neutron diffraction measurements in Helmholz Zentrum Berlin. Figs. 6.6-6.8 represent ongoing changes visible in the selected angular range of 90-110 deg, together with evolution of the structural parameters, weight ratio of present phases, as well as graphical representation of the observed different crystal structures for Pr-, Nd- and Y-containing materials at temperature of: a) 300 °C and b) 400 °C, respectively. For additional neutron diffraction results gathered at other temperatures, see Appendix B. The given parameters were normalized to simple perovskite cell (a, c/2, V/2 in the case of *P*4/*mmm* structure, and a/2, b/2, c/4 and V/16 in the case of *Icma* space group). Please notice that the reduced and oxidized materials exhibit the same *P*4/*mmm* structure, buy varying in the oxygen content.

At temperature of 300 °C oxidized $BaPrMn_2O_6$ sample, refined as having *P*4/*mmm* structure, begins to slowly release the stored oxygen and the *Icma* phase with oxygen content equal to 5.5 ($\delta = 0.5$) starts to gradually appear (time data in Figs. 6.6-6.8 represent total time since beginning of the heating process at room temperature). Consequently, the material becomes two-phased system, with a phase wt. ratio shifting towards *Icma* structure, as can be seen in the consecutive measurements. After approximately 5 h, first step of reduction is completed, and sample became *Icma* single phase with $BaPrMn_2O_{5.5}$ composition. After an increase of temperature up to 400 °C initial test showed presence of only partially reduced ($\delta = 0.5$) phase. Analogously, as during the first step of reduction,

throughout the second step, the completely reduced phase ($BaPrMn_2O_5$ refined as having *P*4/*mmm* space group) starts to gradually appear, and after approximately 4 hours the sample became fully reduced. While comparing first and second step of reduction, especially taking into account the phase wt. ratio, it can be seen, that the first one occurs only slightly slower, despite 100 °C lower temperature.

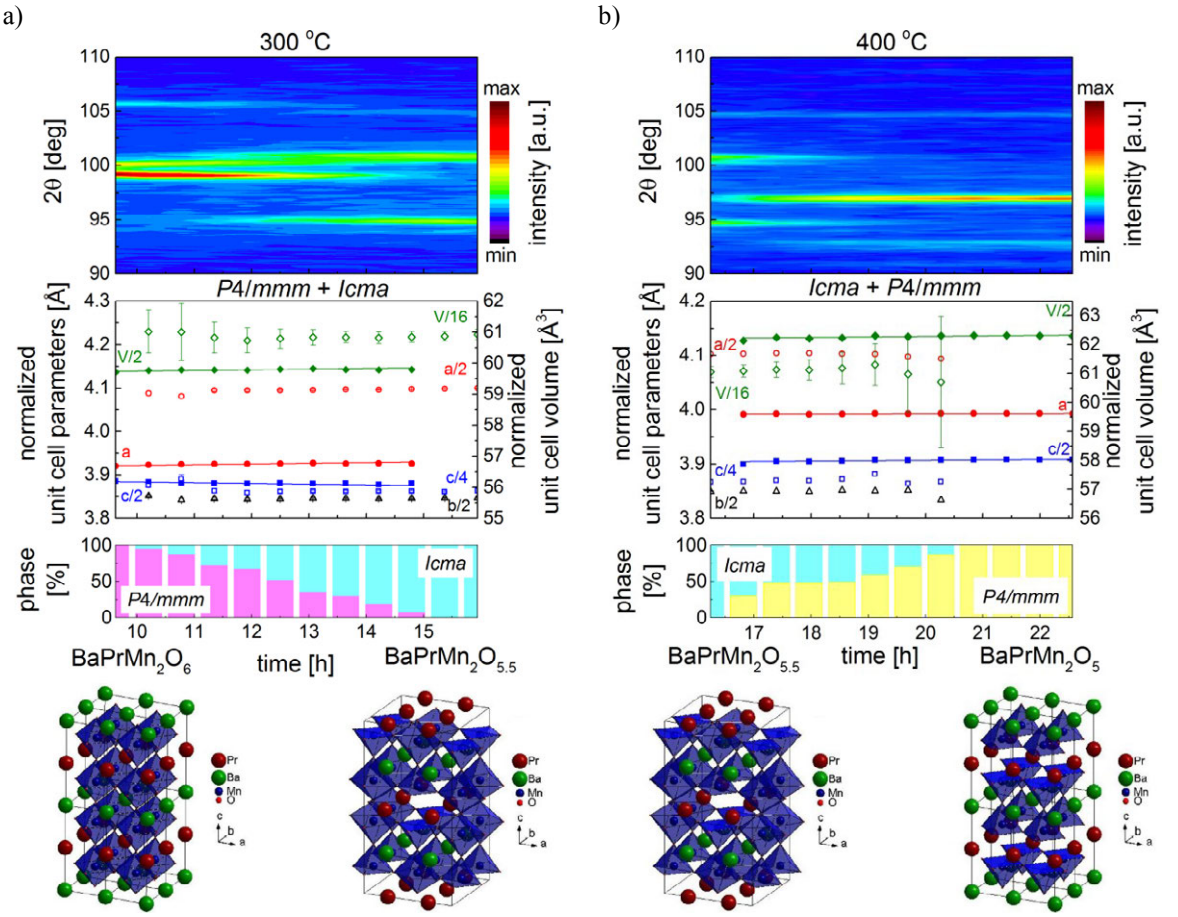

Fig. 6.6. Structural evolution of oxidized $BaPrMn_2O_6$ sample during heating in 5vol.%H_2 in Ar in a) 300° C and b) 400 °C. Intensity data shown for selected angular range. Corresponding temperature dependence of normalized unit cell parameters and volume data together with the unit cells for oxidized (*P*4/*mmm*) $BaPrMn_2O_6$ partially reduced (*Icma*) $BaPrMn_2O_{5.5}$ and fully reduced (*P*4/*mmm*) $BaPrMn_2O_5$ are given.

Please note, that for the *P*4/*mmm* structures graphs represents 2×2×2 supercell and unit cell in the case of *Icma* space group.

In the case of $BaNdMn_2O_6$, reduction process proceed very similarly to praseodymium reach sample, however, reduced *P4*/*mmm* $BaNdMn_2O_5$ phase appear already during the first scan in 400 °C. What is more, oxygen is completely removed after shorter time than for the $BaPrMn_2O_{5+\delta}$.

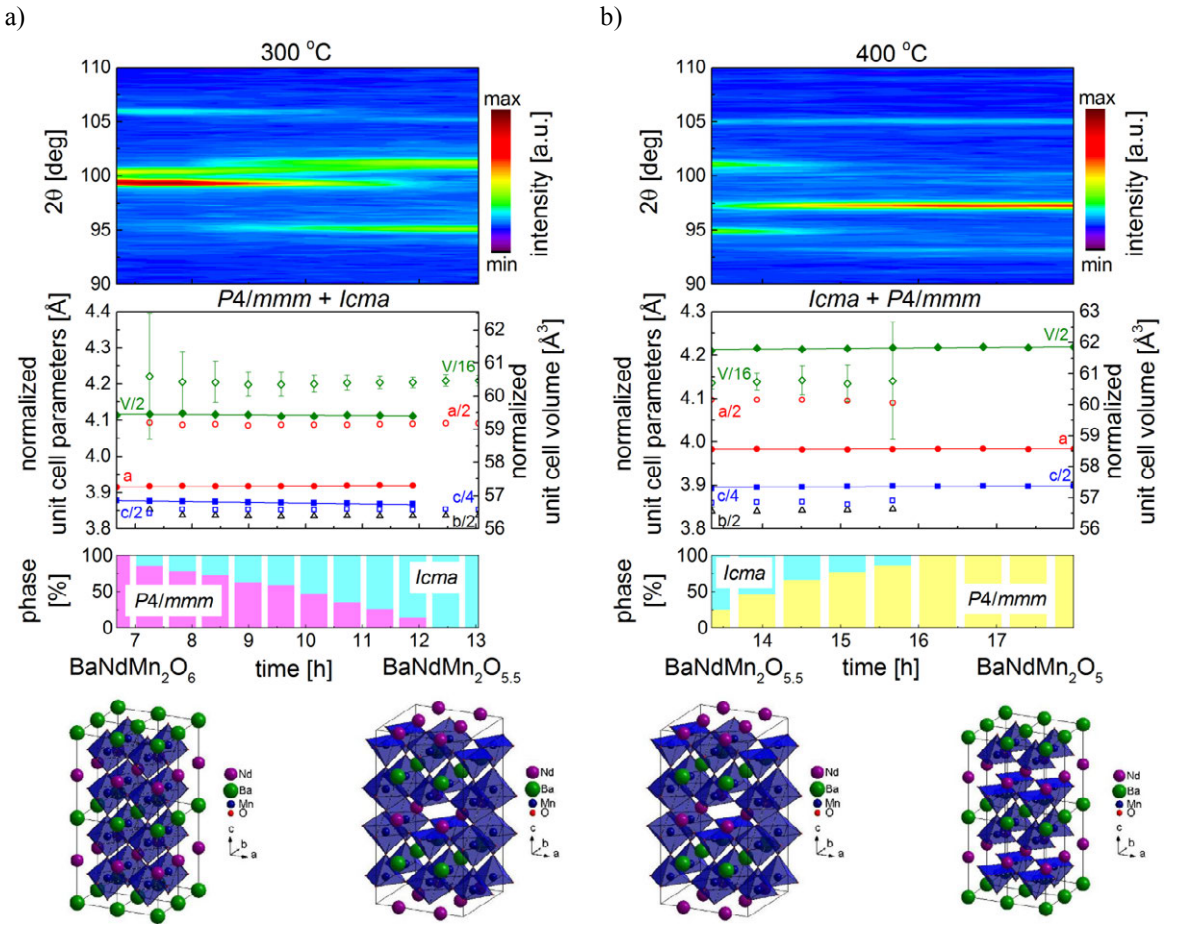

Fig. 6.7. Structural evolution of oxidized $BaNdMn_2O_6$ sample during heating in 5 vol.% H_2 in Ar in a) 300° C and b) 400 °C. Intensity data shown for selected angular range (main peaks). Corresponding temperature dependence of normalized unit cell parameters and volume data together with the unit cells for oxidized (*P*4/*mmm*) $BaNdMn_2O_6$ partially reduced (*Icma*) $BaNdMn_2O_{5.5}$ and fully reduced (*P*4/*mmm*) $BaNdMn_2O_5$ are given.

For yttrium-rich sample, first step of reduction revealed some differences to the previously presented result for Pr- and Nd-containing samples. Already the first measurement at 300 °C revealed presence of over 75 wt.% of partially reduced $BaYMn_2O_{5.5}$ phase, and in the 4th scan (Fig. 6.8a) there is already no sign of the oxidized *P*4/*mmm* phase. This behavior indicates both, lower temperature of reduction and faster kinetics of the first part of the reduction process for yttrium-containing material in the conditions of the experiment (isothermal studies, temperature step 100 °C, significantly bigger amount of the used sample than for TG tests; see also chapter 6.4). The second step of the reduction process, however, seems to occur similarly to the previously presented results, but with a small amount of *P*4/*mmm* phase appearing already during the first scan in 400 °C (Fig. 6.8b).

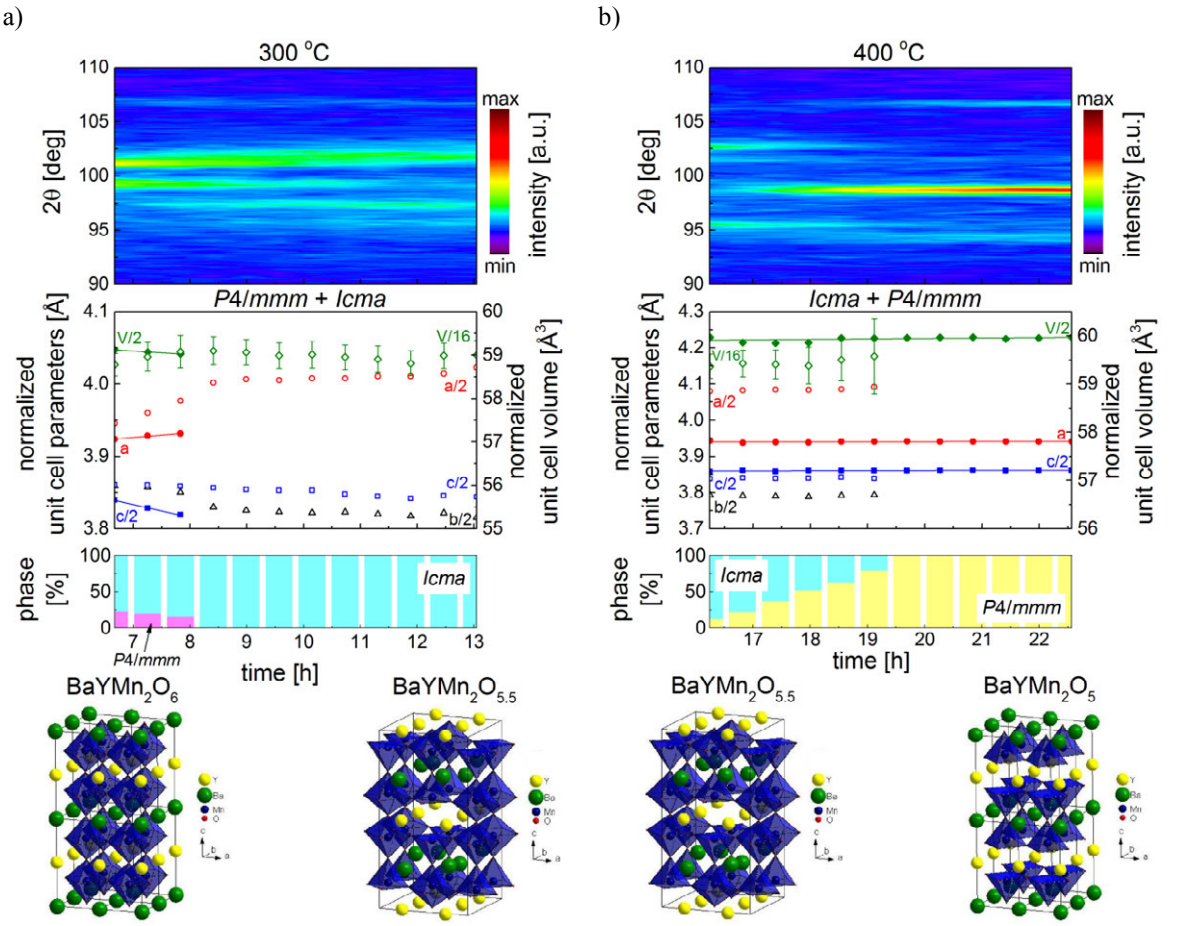

Fig. 6.8. Structural evolution of oxidized $BaYMn_2O_6$ sample during heating in 5vol.%H_2 in Ar in a) 300° C and b) 400 °C. Intensity data shown for selected angular range (main peaks). Corresponding temperature dependence of normalized unit cell parameters and volume data together with the unit cells for oxidized (*P*4/*mmm*) $BaYMn_2O_6$ partially reduced (*Icma*) $BaYMn_2O_{5.5}$ and fully reduced (*P*4/*mmm*) $BaYMn_2O_5$ are given.

It has to be mentioned that the relatively large refinement error of the unit cell volume of *Icma* space group, especially when the quantity of the phase is low, somewhat disturbs interpretation of the results. Nevertheless, significantly higher values of normalized V for the reduced $BaLnMn_2O_5$ materials, comparing to the oxidized $BaLnMn_2O_6$ samples, is clear, and the results of ΔV are comparable to the ones presented in Tab. 6.1 and Fig. 6.3, for respective compounds.

All investigated samples showed step-like character of the reduction process, with presence of the phase with intermediate oxygen content, $BaLnMn_2O_{5.5}$, refined as having *Icma* space group. It seems that the second part of the oxygen release process (from $BaLnMn_2O_{5.5}$ to $BaLnMn_2O_5$) requires higher temperature than the first step, and it occurs slower. This is in agreement with the results obtained during the TG-measurements (see chapter 6.4), for the materials that exhibit visible inflection at about half of their oxygen storage capacity. While at 500 °C the inflection may not be visible on the TG curves for all

materials, it can be stated that tendency of formation of $BaLnMn_2O_{5.5}$ oxygen vacancy-ordered phase is detrimental, considering oxygen storage properties. This statement is in accordance with results presented in Appendix C, where initially distorted materials showed faster kinetics of reduction and lower tendency for $BaLnMn_2O_{5.5}$ phase formation. Particularly, after high-energy mechanical milling, the initially present inflection on the TG characteristics ceased to be visible.

Even though the above discussion and reasoning was conducted on a basis of results gathered for praseodymium-, neodymium- and yttrium-containing materials, since the mentioned cations are of both, large (Pr and Nd) and small (Y), it seems that the general description of the mechanism of the oxygen release from $BaLnMn_2O_6$ can be extended to the other materials from this series of oxides.

6.2.3. Changes of the crystal structure during reduction process in vacuum

Due to technical limitations it is not possible to use reducing atmosphere (e.g. H_2-containing) in Anton Paar HTK 1200N oven-chamber, which was used for some of the high temperature studies in this work. However, this device allows for *in situ* studies on heating under hydrogen free atmospheres, including vacuum. It is also known that the reduction process is much slower (taking minutes), even under relatively strong reducing atmosphere of 5 vol.% H_2 in Ar and at elevated temperature of e.g. 500 °C [5], comparing to the oxidation (taking seconds). Considering this, samples for the experiment were selected from those obtained using the soft chemistry method.

Structural data obtained during reduction of $BaLnMn_2O_6$ on heating under ~ 100 Pa vacuum are shown in Fig. 6.9a. The corresponding, calculated unit cell parameters and volume changes on temperature, together with TEC data are presented in Fig. 6.9b. Interestingly, for Pr-containing material significant structural changes were observed already at 300 °C, at which presence of a mixture of two phases could be deduced from the recorded data. Apart from the initial *P*4/*mmm* phase, additional peaks, which could be indexed using *Icma* symmetry could be seen. At 400 °C the recorded diffractogram was successfully refined using single phase *Icma* structure, which was previously reported for the oxygen vacancy-ordered $BaYMn_2O_{5.5}$ [174]. This indicates a loss of 0.5 mol of oxygen from the sample. At 600 °C the material transforms to another *P*4/*mmm* structure (with no Mn^{2+}/Mn^{3+} charge ordering), which can be expected for the reduced ($\delta = 0$) compound at elevated temperatures. Furthermore, the recorded unit cell volume at this temperature

corresponds very well with the expected value for the completely reduced $BaPrMn_2O_5$. The behavior is essentially the same, like observed during neutron diffraction experiments discussed in previous chapter.

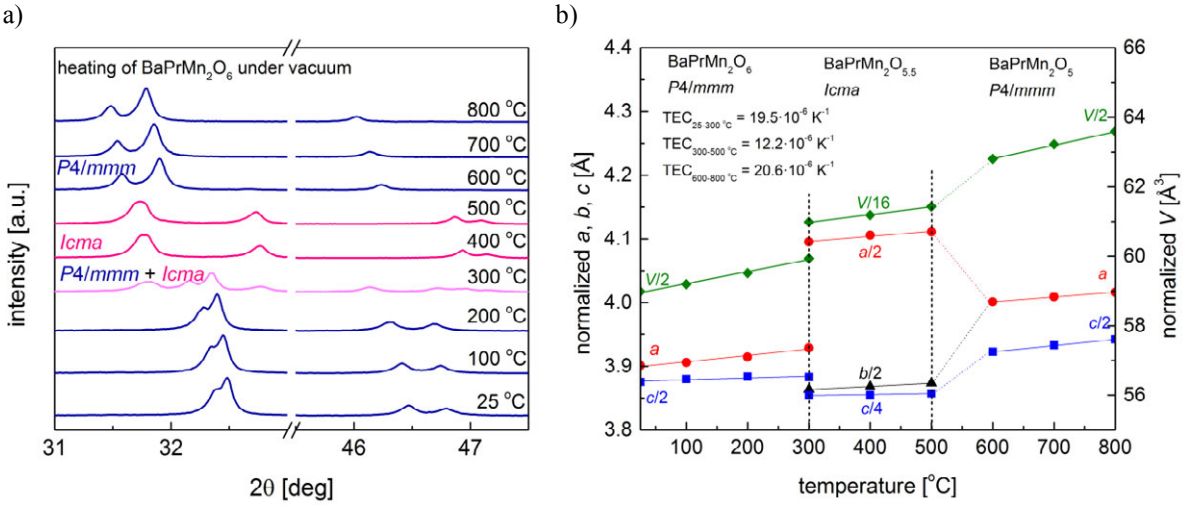

Fig. 6.9. a) Structural evolution of the oxidized $BaPrMn_2O_6$ material during heating in vacuum of ~ 100 Pa (data shown for selected angular range), and b) temperature dependence of the normalized unit cell parameters and volume, together with calculated thermal expansion coefficients.

The observed structural transformations under heating in vacuum for the other studied $BaLnMn_2O_6$ (Ln: Nd, Gd and Y) oxides are shown in Figs. 6.10 and 6.11 below. Unfortunately, the results obtained for other than $BaPrMn_2O_6$ compounds are different, with generally much smaller changes of the oxygen content on heating. For example, for Nd-containing material the oxygen loss was estimated as only ~ 0.15 at 800 °C. On the other hand, for Gd- and Y-containing perovskites a formation of the $O_{5.5}$-type phase and release of 0.5 mol of oxygen up to 800 °C was documented, comparable to published data in work [71]. It is not evident why such different behavior was observed for the considered samples.

Gathered results of the discussed experiments, containing specific temperatures, at which structural transformations and associated oxygen release occur, together with the space groups used for XRD data refinements are presented in Tab. 6.2.

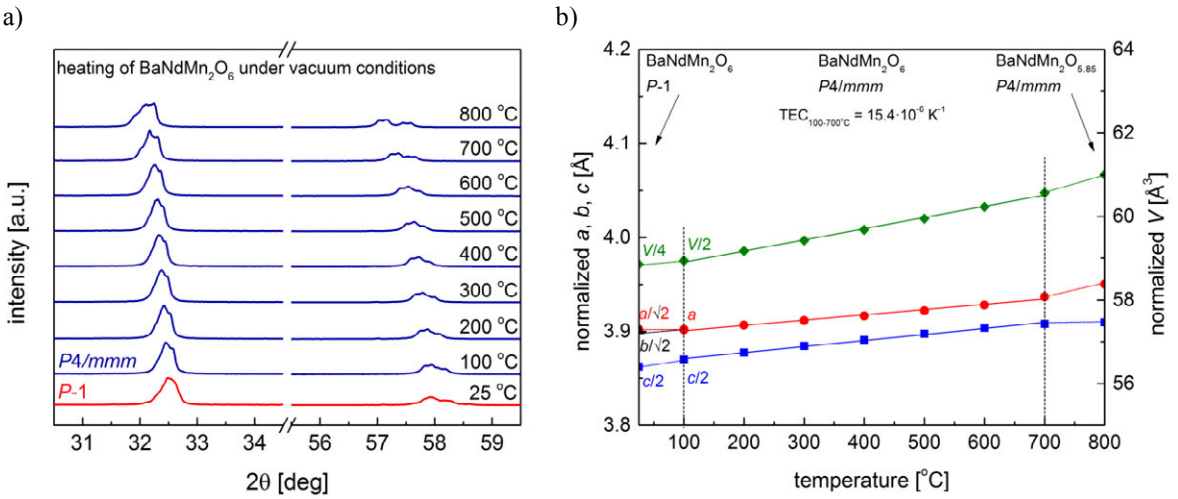

Fig. 6.10. a) Structural evolution of the oxidized $BaNdMn_2O_6$ material during heating in vacuum of ~ 100 Pa (data shown for selected angular range), and b) temperature dependence of the normalized unit cell parameters and volume, together with calculated thermal expansion coefficients.

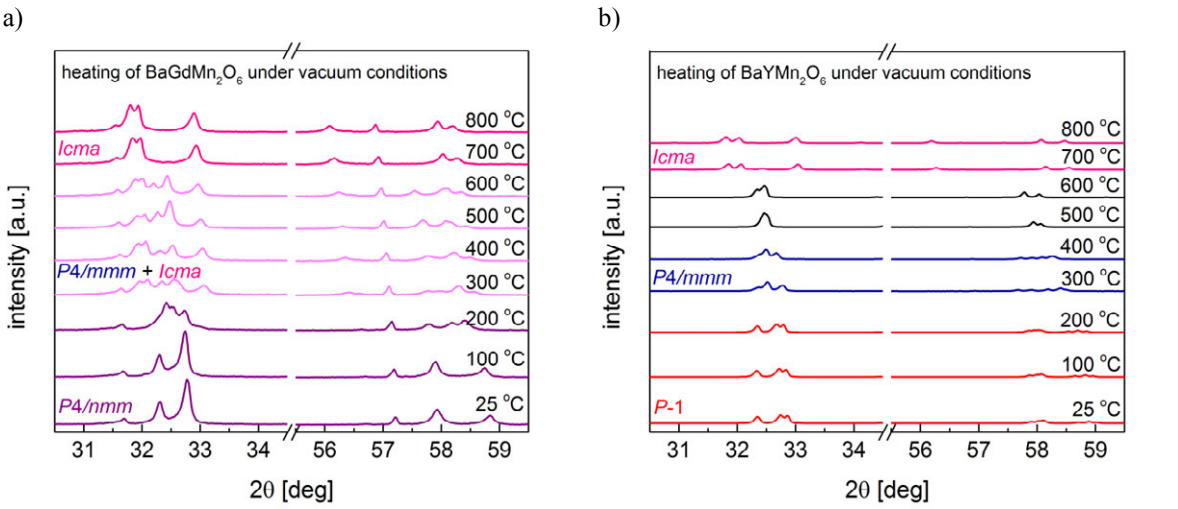

Fig. 6.11. Structural evolution of the oxidized a) $BaGdMn_2O_6$ and b) $BaYMn_2O_6$ materials during heating in vacuum of ~ 100 Pa (data shown for selected angular range).

Tab. 6.2. Structural modification of selected $BaLnMn_2O_6$ at high temperatures under vacuum (~ 100 Pa).

chemical composition	temperature [°C]	space group	unit cell volume under vacuum [Å^3]	oxygen release
$BaPrMn_2O_{5+\delta}$	300	50 wt.% *P*4/*mmm* (O_6)	119.88(1)	~ 0.25
		50 wt.% *Icma* ($O_{5.5}$)	975.75(11)	
	400	*Icma* ($O_{5.5}$)	979.00(6)	~ 0.5
	600	*P*4/*mmm* (O_5)	125.62(2)	~ 1
	800	*P*4/*mmm* (O_5)	127.18(1)	~ 1
$BaNdMn_2O_{5+\delta}$	800	*P*4/*mmm* (O_6)	122.01(1)	~ 0.15
$BaGdMn_2O_{5+\delta}$	300	35 wt.% *P*4/*mmm* (O_6)	118.28(5)	~ 0.3
		65 wt.% *Icma* ($O_{5.5}$)	959.90(26)	
	700	*Icma* ($O_{5.5}$)	972.15(26)	~ 0.5
	800	*Icma* ($O_{5.5}$)	975.92(25)	~ 0.5
$BaYMn_2O_{5+\delta}$	600	*P*4/*mmm* (O_6)	118.57(2)	~ 0
	700	*Icma* ($O_{5.5}$)	961.98(14)	~ 0.5
	800	*Icma* ($O_{5.5}$)	964.66(14)	~ 0.5

Summarizing this part one may notice irregular behavior of the reduction process in respect to the chemical composition in the studied series of oxides, which is not following Ln^{3+} radius or (for instance) its electronegativity. The mechanism of oxygen release from the material might be somehow different than when the reducing atmospheres are being used. This may rise from the fact, that for the hydrogen containing atmospheres reaction of water formation (recombination of O and H) can occurs on the surface of the material, between molecular oxygen and hydrogen in gaseous form or adsorbed on the surface, while for oxygen release in vacuum condition such reaction would not occur and the limiting factor for oxygen release would be oxygen partial pressure.

Nevertheless, possibility of "pumping out" oxygen from $BaLnMn_2O_6$ at moderate temperatures in atmospheres without hydrogen, may be of interest from a point of view of possible application, for instance, for separation of oxygen from air. This issue, however, requires further studies.

6.3. Microstructure of $BaLnMn_2O_{5+\delta}$ powders

Exemplary results of microstructural SEM studies are presented in Figs. 6.12 and 6.13 for the reduced and the oxidized $BaNdMn_2O_{5+\delta}$ and $BaYMn_2O_{5+\delta}$ obtained by two synthesis routes.

A clear difference of powder morphology between materials obtained by solid state and soft chemistry methods can be observed. However, there are no visible differences between morphology of the same materials in reduced and oxidized forms.

Complementary EXD analyses of chemical composition of the samples were also performed. These studies confirmed the assumed chemical composition, within accuracy of the method. However, presence of carbon was also detected, likely from adsorbed CO_2 or being a residue from the synthesis route.

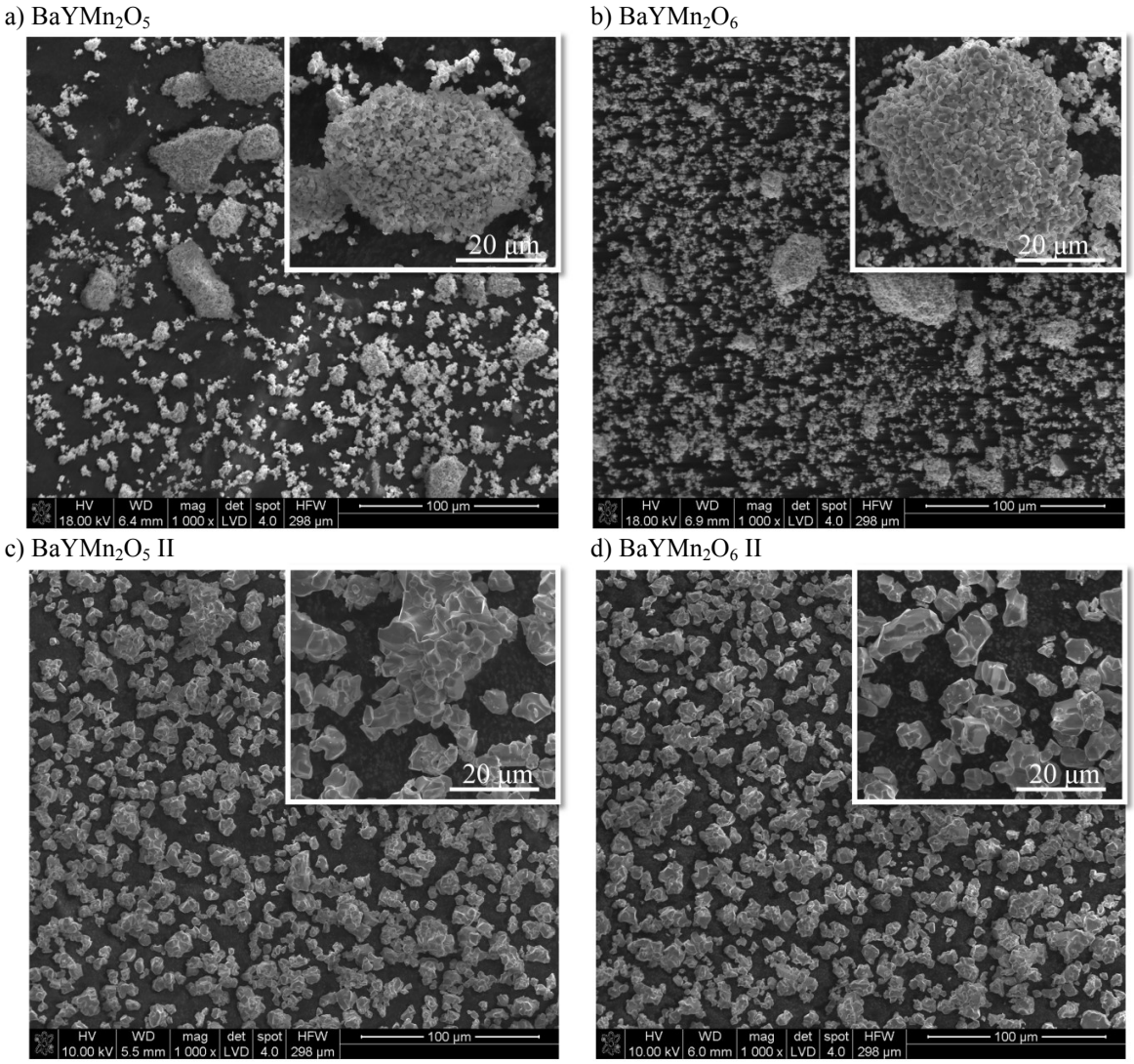

Fig. 6.12. SEM micrographs for: a) $BaYMn_2O_5$, b) $BaYMn_2O_6$, c) $BaYMn_2O_5$ II and d) $BaYMn_2O_6$ II.

It should be pointed out that for materials synthesized by the soft chemistry route the secondary particles appear as porous agglomerates. Such morphology, apart a decrease of the specific surface area of the sample, also helps with an exchange of gasses, and therefore should be beneficial in terms of kinetics of reduction and oxidation processes. For comparison, in the case of compounds obtained by the solid state method, the secondary particles are in a form of well-sintered (non-porous) aggregates. This in turn allowed to prolong the oxidation process, so it was visible during *in situ* structural experiments (chapter 6.2).

Results of statistical analysis of the recorded micrographs for $BaYMn_2O_5$ oxide obtained by the mentioned methods are shown in Figs. 6.14a and b. As expected, significantly smaller mean size of the particles (~ 4 µm) was found for the material from the soft chemistry route, while for the other material it was estimated as ~ 6.7 µm.

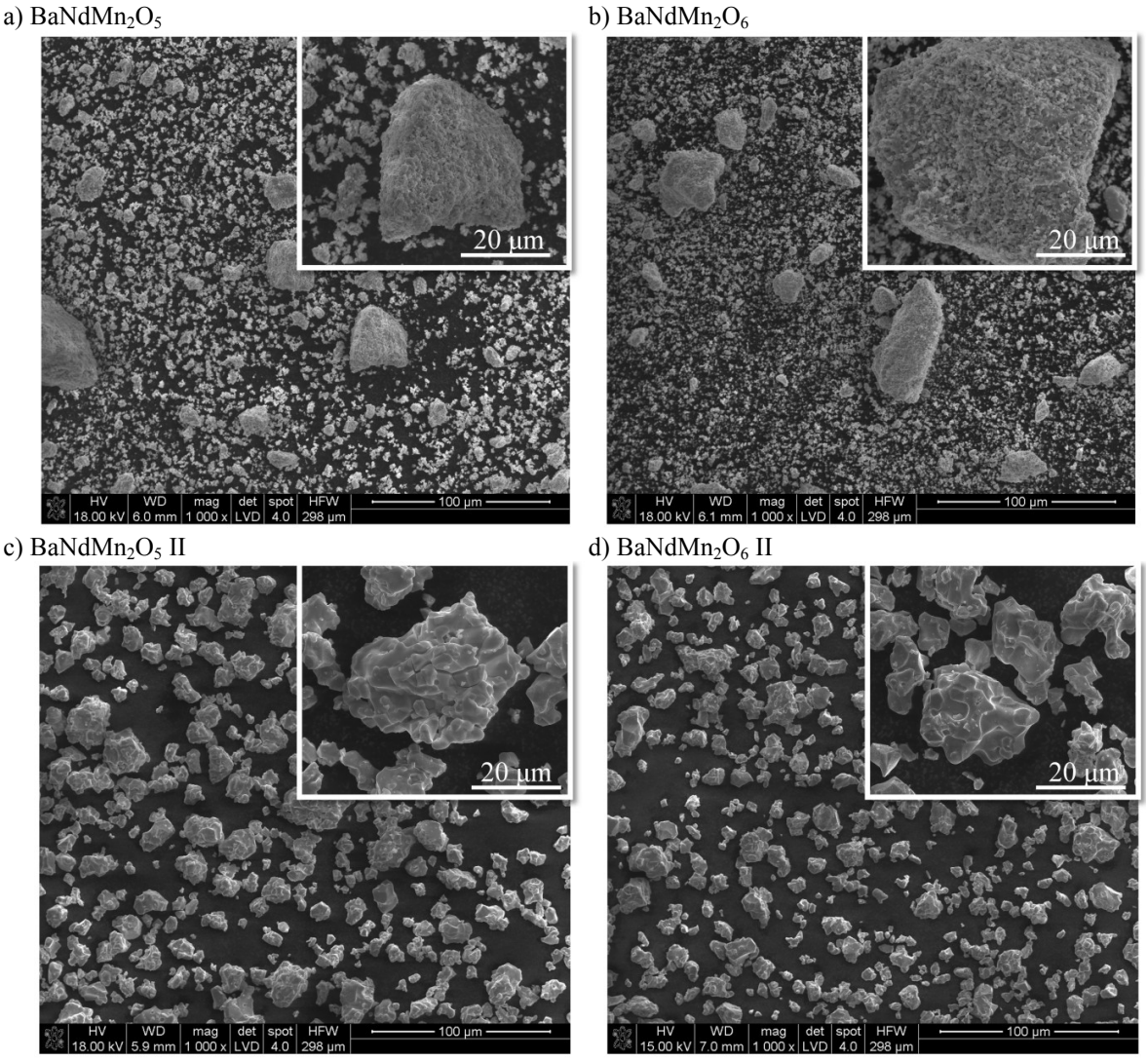

Fig. 6.13. SEM micrographs for: a) $BaNdMn_2O_5$, b) $BaNdMn_2O_6$, c) $BaNdMn_2O_5$ II and d) $BaNdMn_2O_6$ II.

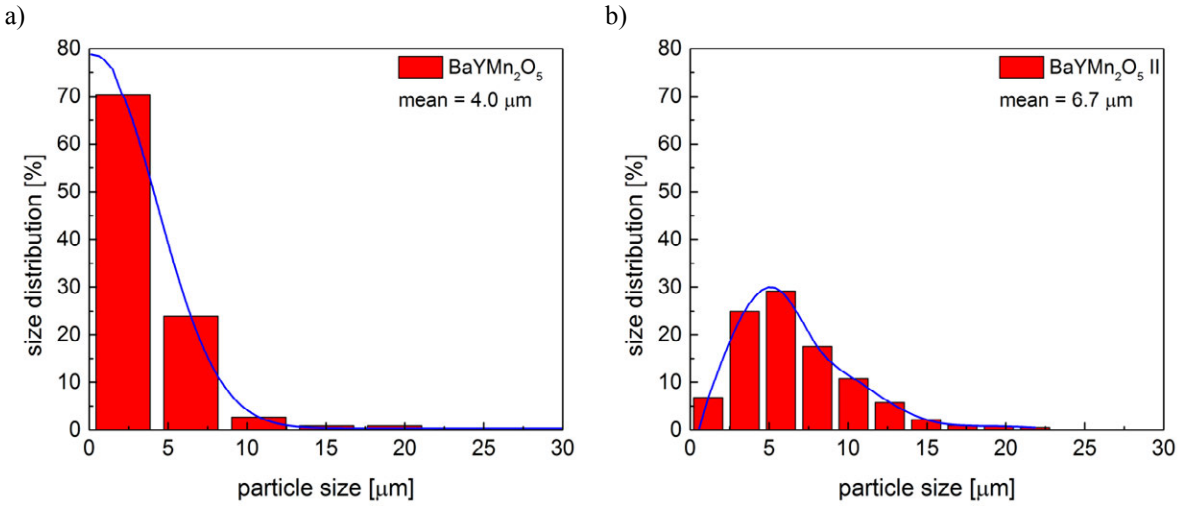

Fig. 6.14. Grain size distribution estimated for $BaYMn_2O_5$ powder obtained via a) soft chemistry and b) solid state reaction methods.

Additional measurements of the specific surface area of the materials were performed using BET-based technique. For the studied $BaLnMn_2O_{5+\delta}$ perovskites synthesized by the soft chemistry method it was found to be in 1.0-2.5 $m^2 \cdot g^{-1}$ range.

6.4. Oxygen storage properties

Results of the most important, from a point of view of this thesis, studies of the oxygen storage-related properties of $BaLnMn_2O_{5+\delta}$ oxides are reported in this chapter. The reduction process was conducted in 5 vol.% H_2 in Ar, while the oxidation was done in synthetic air. For more details concerning methodology of the studies, see chapter 5.4.

Thermogravimetric data of temperature dependence of weight of the samples recorded during heating up to 500 °C in the mentioned 5 vol.% H_2 in Ar atmosphere (reduction of O_6 phase) or in air (oxidation of O_5 phase) are depicted in Figs. 6.15a-f. Before these studies, the materials were initially cycled five times isothermally at 500 °C. As can be seen, all samples behave similarly on reduction and oxidation to the reference $BaYMn_2O_{5+\delta}$ material, for which such characteristics were given previously by Motohashi et al. in work [5].

Comparing all figures one may notice difference of the onset of oxidation and reduction processes. To qualitatively analyze this effect, a characteristic temperature of reduction (or oxidation) parameter was introduced. It was calculated as a temperature of the extremum on the derivative of the mass weight curve. Estimated temperatures are included in the figures and in Tab. 6.3.

Analyzing the presented above data, a general trend can be noticed that significantly lower temperatures are needed for the oxygen incorporation than for reduction, with the characteristic temperatures being in 210-350 °C and 370-485 °C ranges, respectively. However, there is no evident dependence of value of the characteristic temperature of reduction on the ionic radius of Ln^{3+}. Among the studied oxides, only in the case of $BaYMn_2O_6$ sample, the reduction process was not fully completed before reaching 500 °C. However, the heating rate in this experiment was five times faster than the one reported by Motohashi et al. [5].

Interestingly, for oxides having bigger cation introduced in the Ln-sublattice (i.e. Pr^{3+}, Nd^{3+} and Sm^{3+}), an inflection on the reduction curves can be noticed, which can be

related to a formation of the oxygen vacancy-ordered $BaLnMn_2O_{5.5}$-type phase. It is also worth noting that for $BaPrMn_2O_6$ oxide a slight decrease of the weight occurs in the low temperature range (30-250 °C), and only for this material it was possible to remove one mol of oxygen during heating in vacuum (Fig. 6.6a).

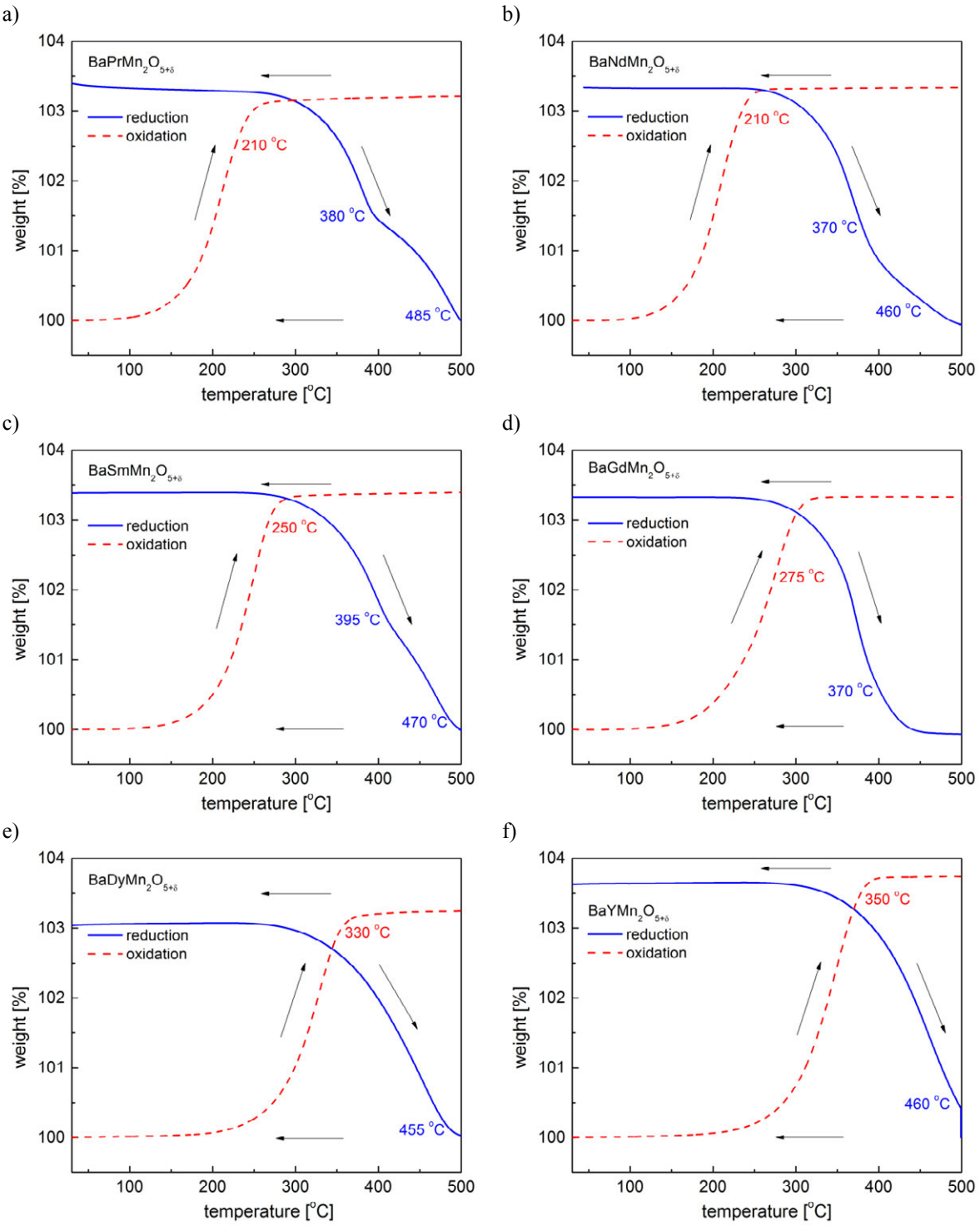

Fig. 6.15. TG data of reduction (in 5 vol.% H_2 in Ar) and oxidation (in air) processes for: a) $BaPrMn_2O_{5+\delta}$, b) $BaNdMn_2O_{5+\delta}$, c) $BaSmMn_2O_{5+\delta}$, d) $BaGdMn_2O_{5+\delta}$, e) $BaDyMn_2O_{5+\delta}$ and f) $BaYMn_2O_{5+\delta}$.

Difference in behavior of Y-containing material on non-isothermal reduction during TG and neutron diffraction experiments is unclear. Possibly it stems from a fact that about two times smaller amount of $BaYMn_2O_6$ powder was used, comparing to other used samples during neutron diffraction studies, while gas flow was the same, which allowed for the reduction to occur faster and at lower temperatures.

In the case of oxidation process, there is an obvious dependence between the characteristic temperature and radius of Ln^{3+}. Compounds having bigger Ln^{3+} oxidize at significantly lower temperatures. This result is important considering possible application.

Results concerning time needed for the reduction and oxidation of the respective materials at 500 °C are given in Figs. 6.16a-d. Data are shown for the 2nd and 5th process. As can be seen, reduction of the materials occurs much slower than the oxidation, and therefore it is the limiting process of the oxygen storage-related cycling (following reduction and oxidation processes). This phenomenon can be easily understood taking into account that the oxidation process is exothermic ($\Delta H \approx$ -220 $kJ \cdot mol^{-1}$ for oxidation of $BaYMn_2O_5$ [178]), which can cause local over-heating of the material, speeding up the diffusion of the oxygen in the bulk. It can be stated that reduction on 5th cycle is faster than the one on 2nd cycle, which can be explained due to activation of the surface of the materials, from which possible contaminations (e.g. adsorbed CO_2) are removed.

Summary data of the isothermal studies at 500 °C, concerning the measured oxygen storage-related properties of $BaLnMn_2O_{5+\delta}$ oxides with theoretical and measured OSC, characteristic temperatures, as well as reduction and oxidation times are gathered in Tab. 6.3. It can be noticed that the observed oxygen storage capacity is close to the theoretical one, indicating changes of the oxygen nonstoichiometry $\delta > 0.96$. Obviously, OSC decrease with the increasing molar mass of the Ln^{3+} element, and is the lowest for $BaDyMn_2O_{5+\delta}$, however, this is still above the OSC of commercial CZ materials (chapter 2.4.1). While the oxidation time was found to be very similar, in 18-24 s range, time of the reduction was the fastest for Gd-containing material (< 5 min) and the slowest for $BaSmMn_2O_6$ (~ 14 min).

Interestingly, the improved characteristics of the $BaGdMn_2O_5$-$BaGdMn_2O_6$ system cannot be ascribed to the microstructure-related effect, as the morphology of the powder was the same like for other studied samples, with BET specific surface area of 1.4 $m^2 \cdot g^{-1}$.

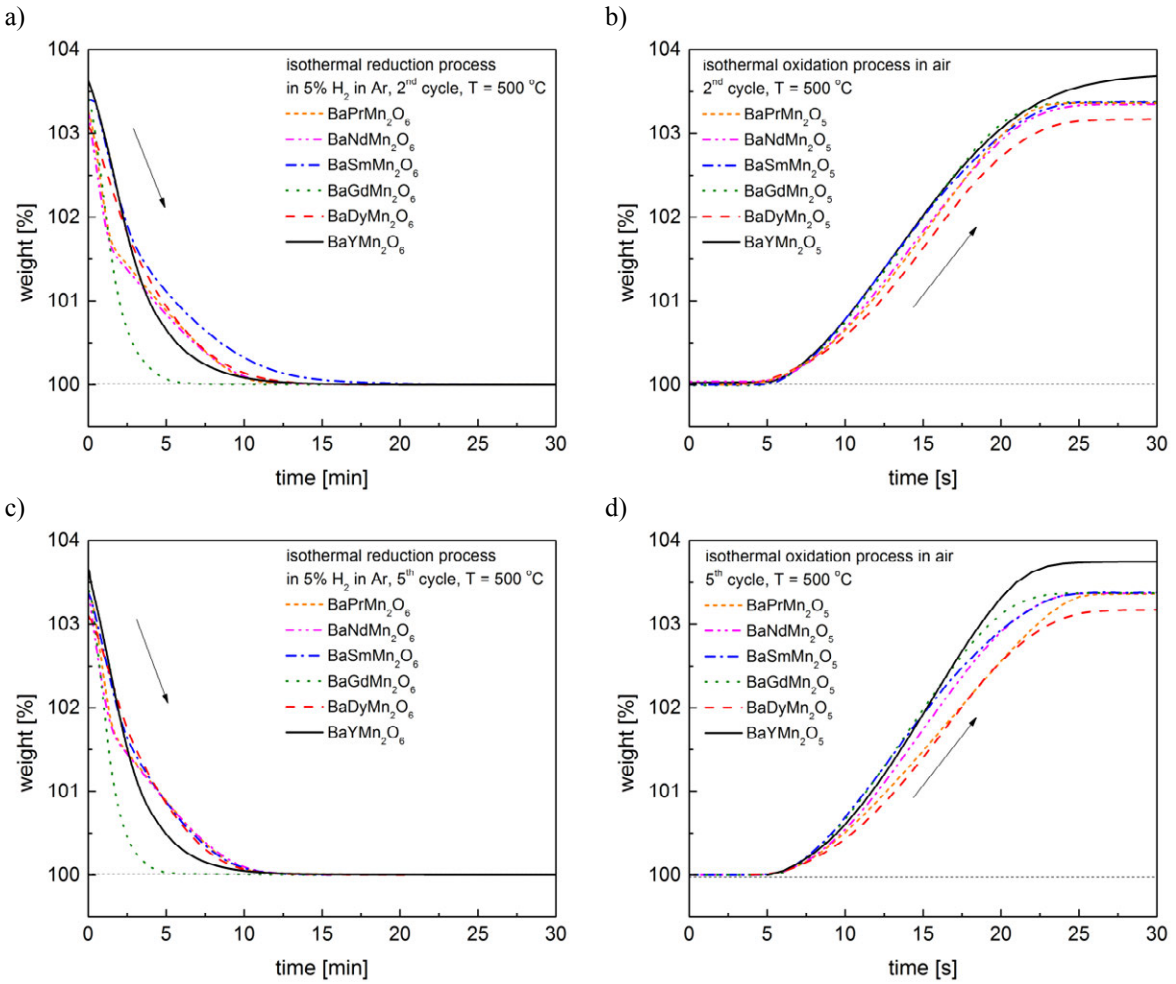

Fig. 6.16. Isothermal a) reduction in 5 vol.% H_2 in Ar, and b) oxidation in synthetic air at 500 °C of $BaLnMn_2O_6$ (Ln: Pr, Nd, Sm, Gd, Dy and Y).

Tab. 6.3. Oxygen storage properties of the considered $BaLnMn_2O_{5+\delta}$ materials. Some results presented also in works [6, 180-182].

chemical composition	theoretical capacity [wt.%]	measured capacity (5^{th} cycle at 500 °C) [wt.%]	characteristic temperature of oxidation [°C]	characteristic temperature of reduction [°C]	time of reduction (99% of total mass change, 5^{th} cycle) [min]	time of oxidation (99% of total mass change, 5^{th} cycle) [s]
$BaPrMn_2O_{5+\delta}$	3.42	3.34	210	380, 485	11.0	21
$BaNdMn_2O_{5+\delta}$	3.39	3.33	210	370, 460	10.3	18
$BaSmMn_2O_{5+\delta}$	3.35	3.32	250	395, 470	13.8	18
$BaGdMn_2O_{5+\delta}$	3.30	3.32	275	370	4.5	18
$BaDyMn_2O_{5+\delta}$	3.27	3.16	330	455	11.2	21
$BaYMn_2O_{5+\delta}$	3.85	3.71	350	460	10.9	24

Comparison of measured oxygen storage capacity, calculated as an average of the mass changes on non-isothermal processes (Figs. 6.15a-f), isothermal studies at 500 °C (Figs. 6.16a-d), and theoretical OSC data is given in Fig. 6.17.

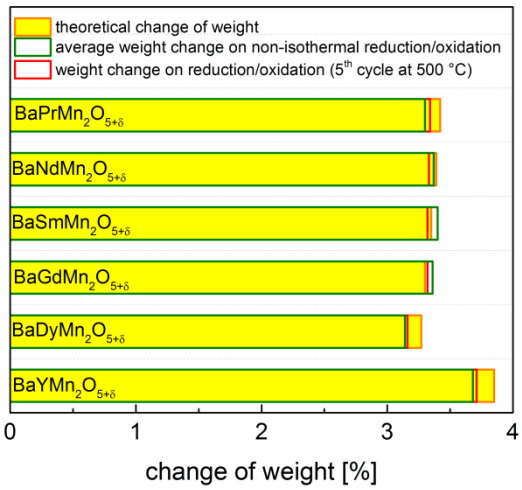

Fig. 6.17. Theoretical and measured OSC values for all studied $BaLnMn_2O_{5+\delta}$ (Ln: Pr, Nd, Sm, Gd, Dy and Y) oxides.

Analyzing data in Fig. 6.17 it can be stated that incorporation of smaller than theoretical amount of oxygen for most of the materials, measured during isothermal and non-isothermal cycles, can be explained by two effects. Traces of impurities present in the materials may not participate in the oxygen storage-related processes, but also, if the equilibrium is not reached in the measurement time (e.g. in the considered cases 30 min on isothermal reduction), the recorded changes will not reflect the possible maximum ones. However, reduction processes taking longer than 30 min are rather not interesting from a point of view of application.

Interesting behavior was registered for $BaGdMn_2O_{5+\delta}$ and $BaSmMn_2O_{5+\delta}$ oxides. These two compounds exhibit higher than theoretical OSC measured during non-isothermal reduction/oxidation runs ($BaGdMn_2O_{5+\delta}$ also during isothermal measurements). Change of δ exceeding 1 mol per mol of the material likely indicates formation of additional oxygen vacancies in the Ba-related sublattice on reduction.

As shown in Figs. 6.16a and c, some decrease of the reduction time was observed for all materials on cycling. More details about this effect are presented in Figs. 6.18a and b, where comparison of time needed for 95% and 99% of the total change of weight of the considered material to occur is given as a function of cycle number. A significant drop between values on the first and second cycle can be noticed, which are followed by a steady decrease of the characteristics for all compounds. As already mentioned, this is most probably due to activation of the surface of the powders. For the 5th reduction of $BaGdMn_2O_6$ oxide, the rate of the oxygen release, as defined in work [186], reached very high value of 1.6 wt.%·min^{-1}, very interesting from the point of view of application.

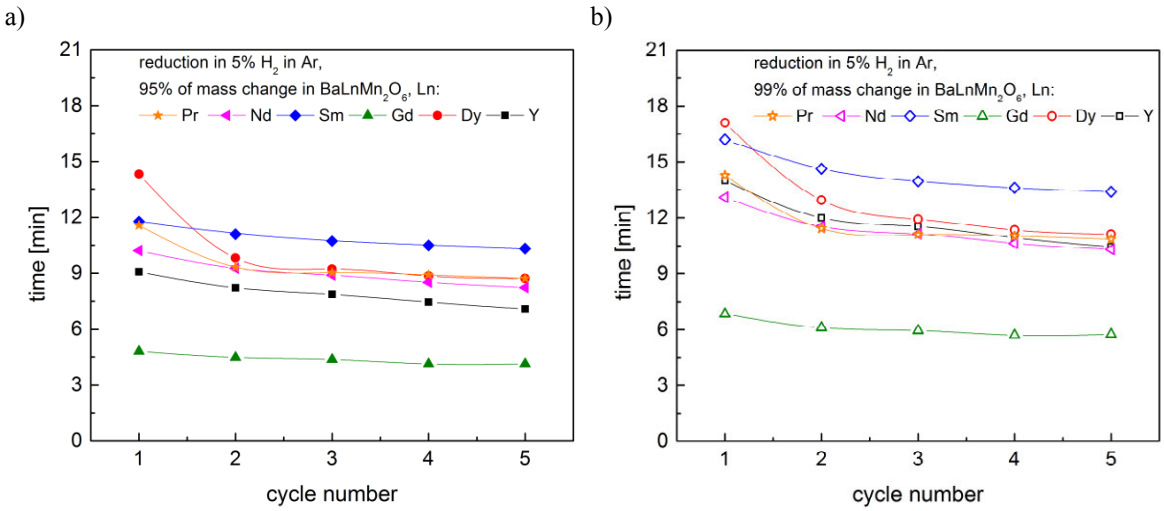

Fig. 6.18. Isothermal reduction in 5 vol.% H_2 in Ar at 500 °C of $BaLnMn_2O_6$ (Ln: Pr, Nd, Sm, Gd, Dy and Y) depending on the cycle number with presented time of the reduction for a) 95% of the total mass changes and b) 99% of the mass changes.

As documented above, the reduction process of $BaLnMn_2O_6$ is much slower, limiting performance of the material on cycling, and therefore optimization of the reduction speed seems the most important challenge considering OSMs from the studied group. First important factor affecting the properties is of course the chemical composition, but also grain size and powders morphology are expected to play an important role in the speed of the considered process [186]. An influence of the sintering method on reduction process was evaluated for $BaNdMn_2O_{5+\delta}$ and $BaYMn_2O_{5+\delta}$ obtained by the described two synthesis methods (see chapter 5.2, and Figs. 6.12 and 6.13). The results concerning reduction time are presented in Fig. 6.19. It is clear, that the reduction of materials obtained by the solid state reaction and having larger grains (marked as II) is significantly slower.

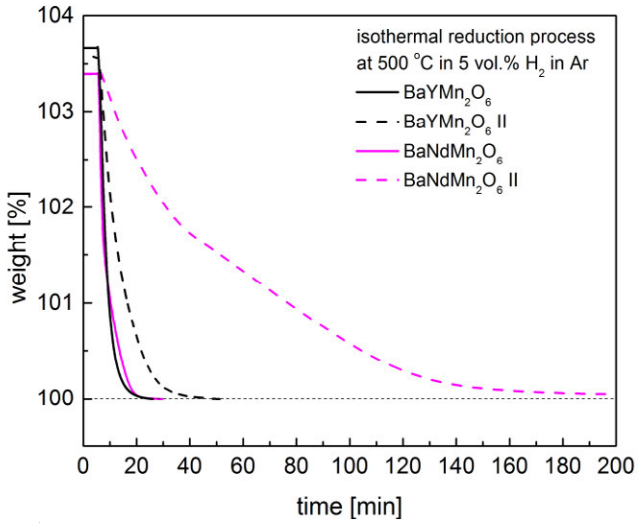

Fig. 6.19. Comparison of 1st reduction at 500 °C in 5 vol.% H_2 in Ar of $BaNdMn_2O_{5+\delta}$ and $BaYMn_2O_{5+\delta}$ materials obtained by two different synthesis procedures.

6.5. Results of XPS studies

As X-ray photoelectron spectroscopy (XPS) technique allows to measure changes of the chemical surrounding and oxidation state of the elements, such studies are of interest for the considered $BaYMn_2O_{5+\delta}$ oxides, since the removed oxygen (preferably from the Y-related sublattice [7]) leaves the vacancy and 2 electrons which are trapped on Mn cations (28, 29):

$$O_O^X \rightarrow V_O^{\bullet\bullet} + 2e' + 1/2\ O_2 \tag{28}$$

$$Ba_{Ba}^X + Y_Y^X + 2Mn_{Mn}^X + 6O_O^X \rightarrow Ba_{Ba}^X + Y_Y^X + 2Mn_{Mn}^{'} + 5O_O^X + V_O^{\bullet\bullet} + 1/2\,O_2 \tag{29}$$

Overall, the manganese changes its oxidation state from average +3.5 down to +2.5 (30). In both reduced and oxidized species, considering the oxidation state, there are two different manganese cations ($Mn_{(1)}$ and $Mn_{(2)}$) present (31). The possible change of the oxidation state of manganese according to [187], can be described as follows:

$$BaYMn_2^{3.5+}O_6 \rightarrow BaYMn_2^{2.5+}O_5 + 1/2\,O_2 \tag{30}$$

$$\downarrow$$

$$Mn_{(1)}^{3+}Mn_{(2)}^{4+} \rightarrow Mn_{(1)}^{2+}Mn_{(2)}^{3+} \tag{31}$$

This can be supported by a rather low electrical conductivity of the reduced material at room temperature ($\sigma \approx 10^{-4}$ S·cm^{-1}, see chapter 7.5), while for the oxidized material it is increased over 3 orders of magnitude. However, Mn^{3+} present in both oxidized and reduced materials (and of course in partially oxidized $BaYMn_2^{3+}O_{5.5}$ phase) is known from its tendency for disproportion into Mn^{2+} and Mn^{4+}, so some deviation may occur. More information can be also found in [158].

Recorded spectra for selected four materials (Ln: Pr, Sm, Gd, Y), in reduced and oxidized state, are depicted in Figs. 6.20a-d. Selected regions of the spectra, corresponding to the vicinity of oxygen 1s- and manganese 2p-related peaks are shown in Figs. 6.21a and b respectively. Changes of O 1s spectra seem to be complex, most likely due to possible influence of present on the surface CO_2 and H_2O molecules or other contaminations.

Nevertheless, multi-peak refinement was conducted for the data from 526-540 eV range (repeated scan of higher resolution) and the results are presented in Fig. 6.22a-h.

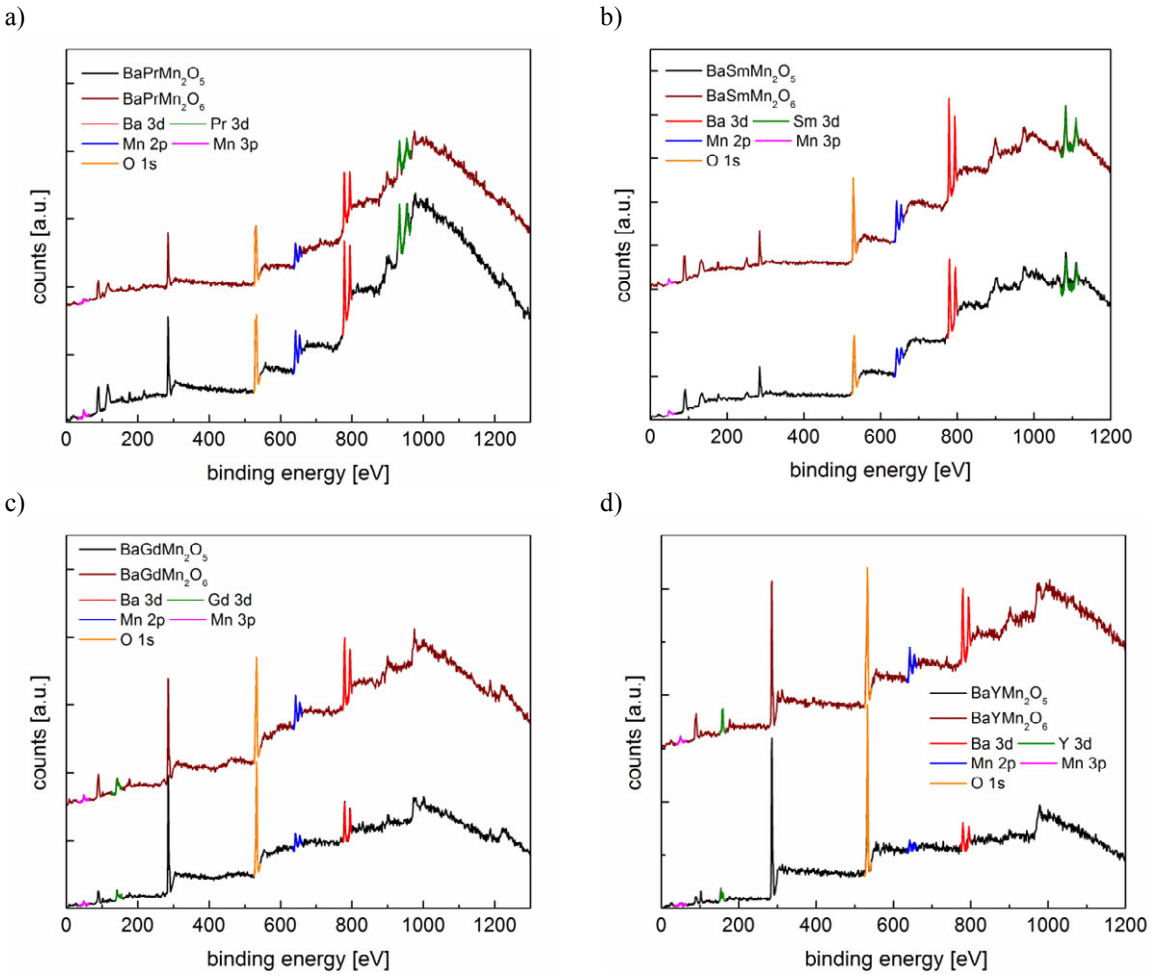

Fig. 6.20. XPS spectra for a) $BaPrMn_2O_5$ and $BaPrMn_2O_6$, c) $BaGdMn_2O_5$ and $BaGdMn_2O_6$, d) $BaYMn_2O_5$ and $BaYMn_2O_6$.

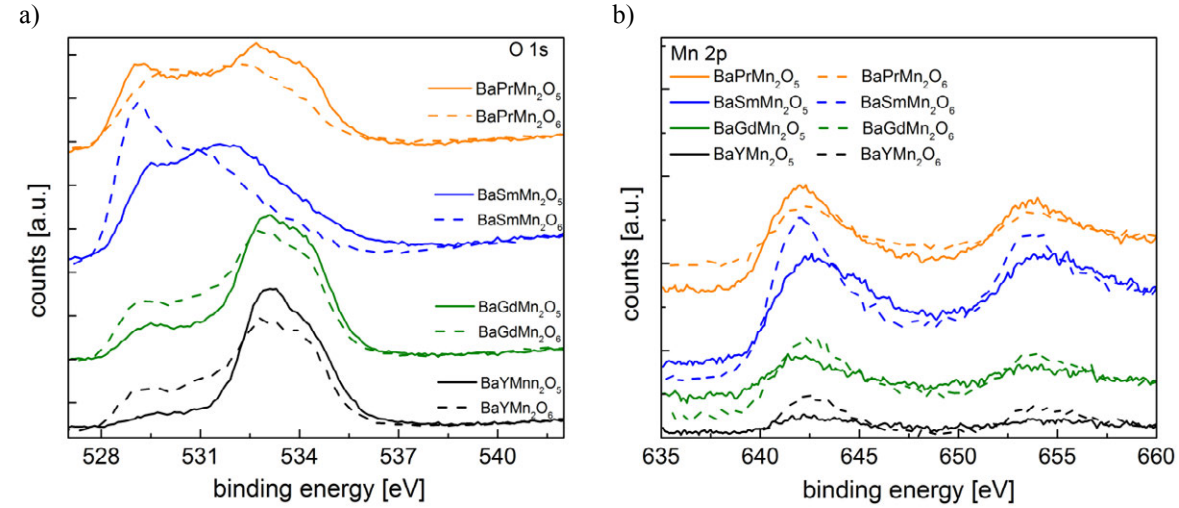

Fig. 6.21. XPS spectra for $BaLnMn_2O_5$ and $BaLnMn_2O_6$, Ln: Pr, Sm, Gd, Y, a) O 1s and b) Mn 2p.

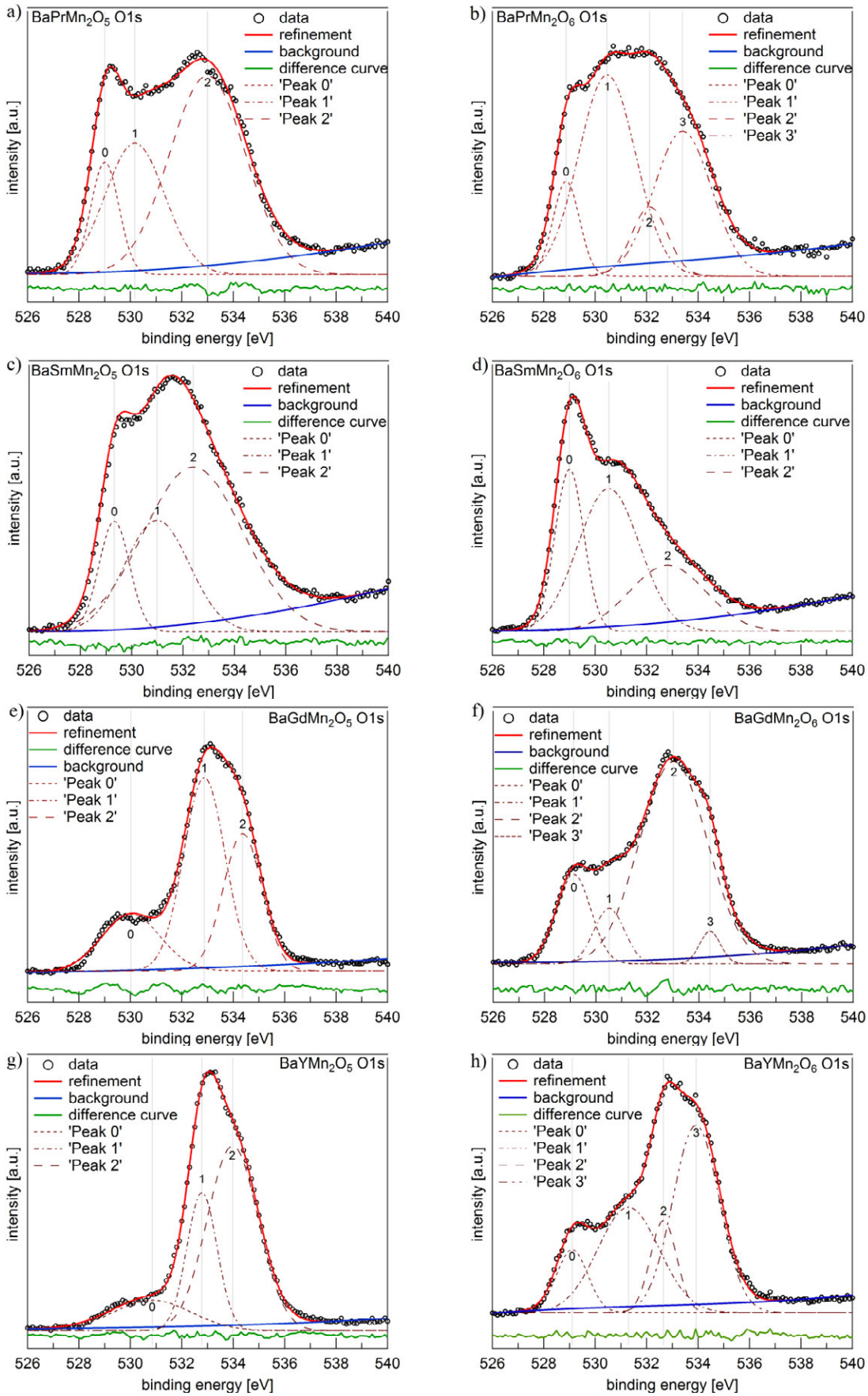

Fig. 6.22. XPS analysis, O 1s spectra with refinement for a) $BaPrMn_2O_5$, b) $BaPrMn_2O_6$, c) $BaSmMn_2O_5$, d) $BaSmMn_2O_6$, e) $BaGdMn_2O_5$, f) $BaGdMn_2O_6$, g) $BaYMn_2O_5$ and h) $BaYMn_2O_6$.

General tendency of shift of the energy towards lower energies can be observed comparing all reduced and oxidized materials. What is more, in the case of all investigated compounds, beside Sm-containing sample, materials in the oxidized form show additional 4th component in relation to the reduced materials 3-component spectra. The exact values of the refinement of O 1s spectra for considered oxides are gathered in Tab. 6.4. It can be seen that for the reduced compounds, binding energy of the refined 'peak 0' increases with the decrease of the size of the Ln ionic radii, and the full width at half maximum (FWHM) decreases.

Tab. 6.4. Results of the refinements of O 1s photoelectron spectra for considered reduced $BaLnMn_2O_5$ and oxidized $BaLnMn_2O_6$ materials.

peak number for refinement of O 1s spectra	location [eV]	FWHM	location [eV]	FWHM
	$BaPrMn_2O_5$		$BaPrMn_2O_6$	
0	529.01(2)	1.29(6)	528.87(2)	1.21(7)
1	530.17(11)	2.73(14)	530.46(8)	2.61(22)
2	533.00(5)	3.48(9)	532.12(7)	1.64(24)
3			533.40(15)	2.65(17)
	$BaSmMn_2O_5$		$BaSmMn_2O_6$	
0	529.32(1)	1.41(7)	528.99(1)	1.32(3)
1	530.99(18)	2.96(60)	530.52(7)	2.82(13)
2	532.40(126)	4.55(95)	532.82(25)	3.50(25)
	$BaGdMn_2O_5$		$BaGdMn_2O_6$	
0	530.02(5)	2.68(15)	529.13(4)	1.57(7)
1	532.87(6)	1.90(10)	530.51(5)	1.40(9)
2	534.36(8)	1.77(9)	533.01(1)	3.12(3)
3			534.43(2)	0.96(6)
	$BaYMn_2O_5$		$BaYMn_2O_6$	
0	530.85(14)	3.58(34)	529.10(5)	1.42(10)
1	532.78(1)	1.38(5)	531.29(15)	2.81(61)
2	533.98(6)	2.33(7)	532.65(2)	1.20(10)
3			533.92(4)	2.13(5)

Exact interpretation of the measured XPS spectra is hindered due to very alike values of the binding energy for certain compounds (see Tab. 6.5 and 6.6), and for some of the cases, significant error of the fitting.

In the case of Mn 2p-related peaks, no clear tendency can be distinguished, which can be correlated with presence of Mn^{4+}, Mn^{3+} or Mn^{2+} states (MnO_2, Mn_2O_3 Mn_3O_4 and MnO references [188]). What is more, as it is depicted in Fig. 6.23, possible binding energies for different compounds containing manganese having different oxidation state impose, making interpretation challenging. For Mn 3p spectra, good refinement can be obtained assuming just one peak approximation, and the tendency, beside Sm-containing

sample shows shift of the peaks towards higher energies for the oxidized samples in relation to the reduced analogues. The precise refinement data are gathered in Tab. 6.7 for Mn 2p and Tab. 6.8 for Mn 3p spectra.

It seems that difficulties of interpretation of the obtained XPS results can be directly related to the surface-only sensitivity of this technique, with penetration depth on the order of 10 nm. The depth profile measurement would be recommended to determine the chemical environment of manganese on the surface where it might be influenced by surface defects and possible contaminations.

Tab. 6.5. Binding energy for oxygen-containing materials [189].

chemical formula	binding energy [eV]
BaO	530.20
MnO	529.90
Mn_2O_3	529.90
Mn_2O_3	530.00
MnO_2	530.00

Tab. 6.6. Binding energy for manganese-containing materials [189].

chemical formula	binding energy [eV]
MnO	653.40
Mn_2O_3	653.40
Mn_2O_3	653.70
MnO_2	653.80
MnO_2	653.90

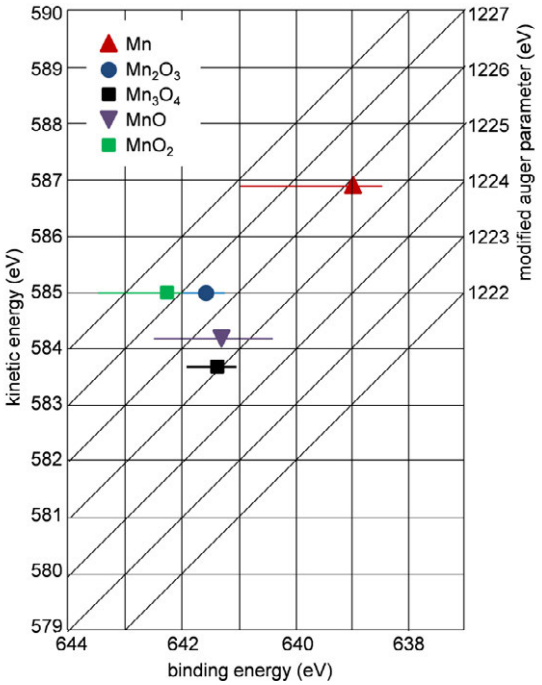

Fig. 6.23. Wagner plot for manganese-containing materials [189].

Tab. 6.7. Results of the refinement of Mn 2p photoelectron spectra for considered reduced $BaLnMn_2O_5$ and oxidized $BaLnMn_2O_6$ materials.

peak number for refinement of Mn 2p spectra	location [eV]	FWHM	location [eV]	FWHM
	$BaPrMn_2O_5$		$BaPrMn_2O_6$	
0	642.29(3)	4.21(11)	642.52(3)	4.45(11)
1	653.79(6)	3.24(19)	653.92(6)	3.10(18)
	$BaSmMn_2O_5$		$BaSmMn_2O_6$	
0	642.88(4)	5.35(15)	642.26(2)	3.95(9)
1	654.30(7)	3.61(24)	653.68(5)	2.98(15)
	$BaGdMn_2O_5$		$BaGdMn_2O_6$	
0	642.28(5)	4.76(20)	642.65(3)	4.39(13)
1	653.55(13)	2.75(40)	654.03(7)	3.56(23)
	$BaYMn_2O_5$		$BaYMn_2O_6$	
0	642.79(8)	4.92(33)	642.70(3)	4.27(13)
1	654.43(20)	3.41(63)	654.15(8)	3.30(25)

Tab. 6.8. Results of the refinement of Mn 3p photoelectron spectra for considered reduced $BaLnMn_2O_5$ and oxidized $BaLnMn_2O_6$ materials.

peak number for refinement of Mn 3p spectra	location [eV]	FWHM	location [eV]	FWHM
	$BaPrMn_2O_5$		$BaPrMn_2O_6$	
0	46.60(4)	4.04(10)	49.70(4)	3.04(20)
	$BaSmMn_2O_5$		$BaSmMn_2O_6$	
0	50.31(34)	6.62(94)	49.12(14)	3.84(43)
	$BaGdMn_2O_5$		$BaGdMn_2O_6$	
0	49.49(6)	3.91(15)	49.90(4)	4.27(12)
	$BaYMn_2O_5$		$BaYMn_2O_6$	
0	49.85(12)	4.08(35)	50.00(6)	4.49(17)

Chapter 6 summary

As documented above, it was possible to successfully synthesize A-site cation ordered $BaLnMn_2O_{5+\delta}$ (Ln: Pr, Nd, Sm, Gd, Dy and Y) materials and characterize their structural properties in the reduced and the oxidized forms. In situ XRD measurements at high temperatures allowed to observe ongoing oxidation process for the exemplary $BaNdMn_2O_5$ II sample. The high temperature neutron diffraction studies under hydrogen-containing atmosphere allowed to elaborate model of the reduction process of $BaLnMn_2O_{5+\delta}$ oxides. The reduction proceeds initially with formation of two-phase $BaLnMn_2O_6$-$BaLnMn_2O_{5.5}$ system, and then two-phase $BaLnMn_2O_{5.5}$-$BaLnMn_2O_5$ mixture, with only relative wt. ratio of respective phases changing during the process. Also, reduction process was investigated on selected $BaLnMn_2O_6$ (Ln: Pr, Sm, Gd, Y) oxides during measurements under vacuum conditions (~ 100 Pa). These studies revealed capability of $BaPrMn_2O_6$ to release 1 mol of oxygen per mol of the compound when heated up to 600 °C, which seems to be very interesting from the viewpoint of application. Systematic, thermogravimetric studies were conducted for all considered samples, which showed reversible change of δ between reduced $BaLnMn_2O_5$ and oxidized $BaLnMn_2O_6$ occurring at moderated temperatures during change of the atmosphere between air and 5 vol.% H_2 in Ar. These studies confirmed excellent oxygen storage-related properties of $BaLnMn_2O_{5+\delta}$. It can be also concluded that both, chemical composition and morphology of the powders are of importance and influence oxygen storage in the studied materials. Also, it seems that surface of the materials differs considerably from the bulk, and is likely highly defected.

7. Properties of $BaErMn_2O_{5+\delta}$ oxides

This chapter is devoted to characterization of properties of $BaErMn_2O_5$ and $BaErMn_2O_6$ compounds, were successfully synthesized by the author of the thesis. Until now, family of cation-ordered $BaLnMn_2O_{5+\delta}$ oxides was known for Ln: La-Ho lanthanides and Y. The Er^{3+} cation is the smallest one successfully introduced and forming layered type of Ba-Er arrangement. Majority of the presented here structural properties at room temperature and at high temperatures recorded during *in situ* XRD studies, microstructural studies, oxygen storage-related properties, as well as data regarding electrical conductivity and Seebeck coefficient were reported in work [165].

7.1. Crystal structure of $BaErMn_2O_5$ and $BaErMn_2O_6$ oxides at room temperature

For successful synthesis of $BaErMn_2O_{5+\delta}$ the described in chapter 5.2 sol-gel method was used with the same initial steps, however, the main synthesis step was performed at 1200 °C for 8 h in 5N Ar atmosphere with a flow of gas of about 100 $cm^3 \cdot min^{-1}$. Room temperature XRD measurements, performed after such synthesis indicated formation of the A-site ordered phase for $BaErMn_2O_{5+\delta}$. Nevertheless, the material was contaminated by some amount of impurities. In further step, after heating up to 500 °C with a rate of 5 °$\cdot min^{-1}$, the series of oxidation and reduction cycles (in 5 vol.% H_2 in Ar), followed by a fast cooling to room temperature in air resulted in significant reduction of intensity of the unidentified XRD reflections. The estimated purity of such the obtained $BaErMn_2O_5$ was found to exceed 95%. The oxidation to $BaErMn_2O_6$ phase was conducted on heating in air up to 500 °C of the reduced material. It should be mentioned that all other attempts to synthesize $BaErMn_2O_{5+\delta}$ (at different temperatures and/or in different oxygen partial pressures) were unsuccessful.

XRD data for the reduced $BaErMn_2O_5$ and the oxidized $BaErMn_2O_6$ compounds, together with Rietveld refinements considering two possible space groups for both materials, are shown in Figs. 7.1a and b.

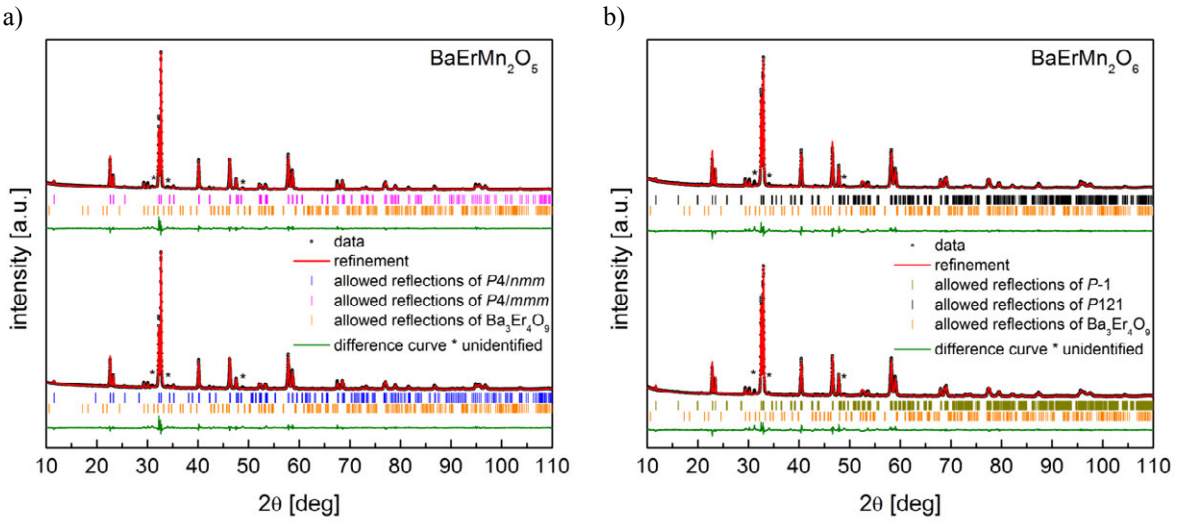

Fig. 7.1. Diffraction data with Rietveld analysis for a) $BaErMn_2O_5$ b) $BaErMn_2O_6$ samples recorded at room temperature. Notice two different space groups selected for the refinements.

Structural parameters obtained by Rietveld analysis for $BaErMn_2O_5$ and $BaErMn_2O_6$ are gathered in Tab. 7.1. The registered diffractogram for reduced $BaErMn_2O_5$ oxide can be successfully refined using either higher symmetry tetragonal *P*4/*mmm* space group or lower symmetrical *P*4/*nmm* space group, which was reported to give a good refinement for the reference $BaYMn_2O_5$ oxide [5, 161]. Refinement statistics for these two cases vary insignificantly. However, considering possibility of a long-range charge ordering in Mn-sublattice it is worth mentioning that in the case of *P*4/*mmm* space group, there is only a single available position for Mn cations refined as (1/2, 1/2, 0.266), while for *P*4/*nmm* symmetry there are two sites available for manganese cations, refined as (1/4, 1/4, 0.277) and (1/4, 1/4, -0.251), which can be, using reference data for $BaYMn_2O_5$ [187], ascribed to presence of Mn^{3+} and Mn^{2+} respectively. Because of a relatively low electrical conductivity of the studied material at room temperature (see chapter 7.5), implying rather presence of localized charges, selection of lower-symmetry *P*4/*nmm* space group seems to more accurate to describe crystal structure of $BaErMn_2O_5$.

Ordering in barium-erbium sublattice seems well-preserved, since there was no improvement of the refinement statistics with an assumption of a partial mixing of Ba^{2+} and Er^{3+} cations. As stated before, some impurities were detected in the obtained material. The main secondary phase (amount not exceeding 3 wt.%) was identified as $Ba_3Er_4O_9$.

In the case of the oxidized $BaErMn_2O_6$ material, lower symmetry implementation for the refinement seems to be justified, taking into account a slight, but evident splitting of most of the recorded peaks. Similarly to $BaErMn_2O_5$ oxide, two different space groups, monoclinic *P*121 and triclinic *P*-1, were selected for Rietveld analysis, and both allowed to

obtain good fits with comparable refinement statistics. In the literature there is no definitive agreement about choice of the space group for the reference $BaYMn_2O_6$ oxide, having only slightly larger Y^{3+} cations [7, 184, 185]. The material was reported to be monoclinic, but precise neutron diffraction studies suggested presence of triclinic *P*-1 symmetry [184]. This is also supported by author's results presented in Tab. 6.1. Due to the mentioned similarity of the ionic radii of Y^{3+} and Er^{3+}, as well as expected (extrapolated from electronic phase diagram, Fig. 4.14) charge-ordered character of interaction between manganese cations, it seems that choice of the lower-symmetry *P*-1 space group is reasonable. Nevertheless, the triclinic distortion is rather small, with only β angle differing significantly from 90 deg (Tab. 7.1). Similarly as in the case of the reduced sample, in the oxidized $BaErMn_2O_6$ layered Ba-Er ordering is present, and also, there are small amounts of secondary phases present, with < 3 wt.% of $Ba_3Er_4O_9$.

Tab. 7.1. Structural parameters of $BaErMn_2O_5$ and $BaErMn_2O_6$ oxides [165].

chemical composition	$BaErMn_2O_5$		$BaErMn_2O_6$	
phase composition	> 95 wt.% of main phase < 5 wt.% of secondary phases identified $Ba_3Er_4O_9$ < 3 wt.%		> 95 wt.% of main phase < 5 wt.% of secondary phases identified $Ba_3Er_4O_9$ < 3 wt.%	
space group	*P*4/*nmm*	*P*4/*mmm*	*P*-1	*P*121
a [Å]	5.5424(1)	3.9191(1)	5.5206(1)	5.5204(1)
α [deg]			90.01(1)	
b [Å]			5.5147(1)	5.5148(1)
β [deg]			90.29(1)	90.29(1)
c [Å]	7.6422(1)	7.6422(1)	7.6100(1)	
γ [deg]			89.92(1)	7.6099(1)
V [Å^3]	234.76(1)	117.38(1)	231.68(1)	231.67(1)
R_{wp} [%]	4.93	4.97	4.63	4.61
χ^2	8.38	8.52	6.10	6.10

Worth mentioning is a decrease of the unit cell volume of $BaErMn_2O_6$ comparing to the $BaErMn_2O_5$, which is smallest among all $BaLnMn_2O_{5+\delta}$ (Fig. 6.3). As it was described in chapter 6.1, for this effect combination of the following factors is responsible: a decrease of average radius of manganese cations after oxidation, correlated to an increase of average oxidation state from +2.5 to +3.5; a decrease of ionic radius with a decrease of coordination number and weaker bonding, due to a lack of oxygen in erbium layer.

Normalizing unit cell parameter to a_p, c/a ratio for $BaErMn_2O_5$ is equal to 0.9750, while for $BaErMn_2O_6$ material c/a equals 0.9745 and c/b = 0.9758, proving rather uniform shrinkage/elongation of the material upon oxidation/reduction.

7.2. In situ structural measurements

Diffractograms recorded during heating in air of $BaErMn_2O_5$ sample (regular one hour scans measured every 25 °C up to 500 °C), as well as on cooling down to room temperature are gathered in Fig. 7.2a. For a clear presentation, selected angular range was chosen, and the described results for characteristic temperatures are marked in color. Temperature dependence of normalized unit cell parameters and volume, together with calculated thermal expansion coefficient are depicted in Fig. 7.2b. For the refinements, *P*4/*nmm* space group was chosen for the reduced material during heating up to 300 °C, while the oxidized compound was refined with *P*4/*mmm* space group, starting from 325 °C up to 500 °C. Description of structural changes occurring upon heating and cooling of the sample is given below.

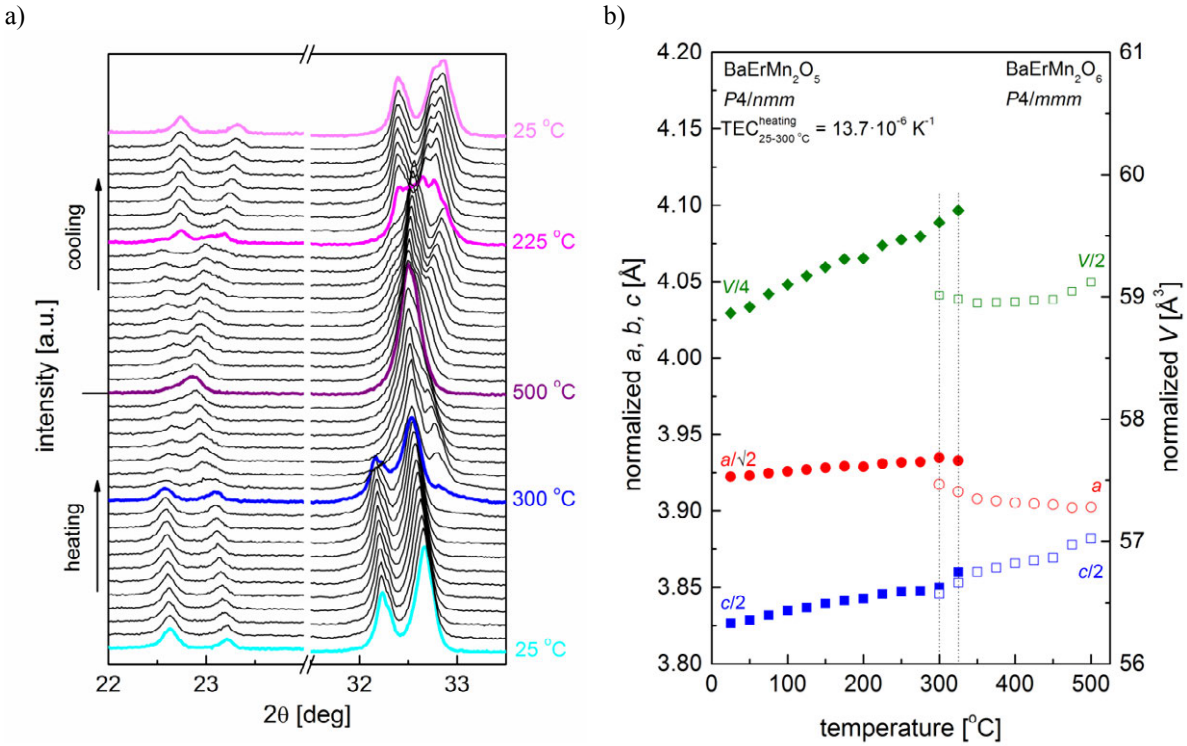

Fig. 7.2. a) XRD data for $BaErMn_2O_5$ recorded during heating up to 500 °C in air and cooling down to RT, b) respective temperature dependence of the normalized unit cell parameters and volume, together with calculated thermal expansion coefficient. Data in Fig. 7.2a published also in [165].

Starting from room temperature (Fig. 7.2a, marked in light blue) up to 275 °C there are no structural changes occurring in the material, except for shifting of the peaks towards lower angles, which can be associated with thermal expansion. At 300 °C, which is marked in blue, a small satellite peak (~ 32.8 deg) appears on the right side of the main (112)

reflection, and already at 325 °C significant increase of the intensity of mentioned peak occurs. At the same temperatures (200) reflection (~ 32.2 deg), which is located on the left side of the main peak is vanishing. Because in similar temperature range, as shown in section below in chapter 7.4, oxidation of $BaErMn_2O_5$ takes place, the observed structural changes might be attributed to formation of the oxidized $BaErMn_2O_6$. However, there is no evidence of formation of partially oxidized phase (i.e. $BaErMn_2O_{5.5}$), which was observed for the Y-containing compound [7]. In 300-325 °C range the structural data were refined with two phases: the initial O_5-type one, and the oxidized O_6 phase, having *P*4/*mmm* symmetry and significantly smaller normalized unit cell volume. During further increase of temperature, it seems that tetragonal structure of the oxidized material relaxes towards cubic symmetry, as can be seen for the diffractogram recorded at 500 °C (purple color), which seems cubic-like.

On cooling of the material down to 375 °C structural distortion starts to re-appear, corresponding well to the changes occurring during heating. However, below this temperature, an additional left side shoulder of the main peak (~ 32.4 deg) appears, and at 225 °C (pink color) an ongoing phase transition is clearly visible. While above this temperature it was not possible to unambiguously determine the structural distortion, below 200 °C and down to room temperature the ordered $BaErMn_2O_6$ phase can be characterized by triclinic symmetry with *P*-1 space group (light pink color).

7.3. Microstructure of $BaErMn_2O_{5+\delta}$ powders

SEM micrographs for the oxidized and the reduced $BaErMn_2O_{5+\delta}$ powders are presented in Figs. 7.3a and b. As can be seen, oxidation and reduction processes have no visible effect on the microstructure, which is practically identical for $BaErMn_2O_5$ and $BaErMn_2O_6$. Majority of the visible particles possess size on the order of few micrometers. For these materials crystallite size was also determined from XRD data using Scherrer's equation, and was found to be of about 100-135 nm. This is much smaller, comparing to the particle size visible on SEM micrographs, and indicates that the grains are actually composed of many aggregated crystallites.

a) $BaErMn_2O_5$ b) $BaErMn_2O_6$

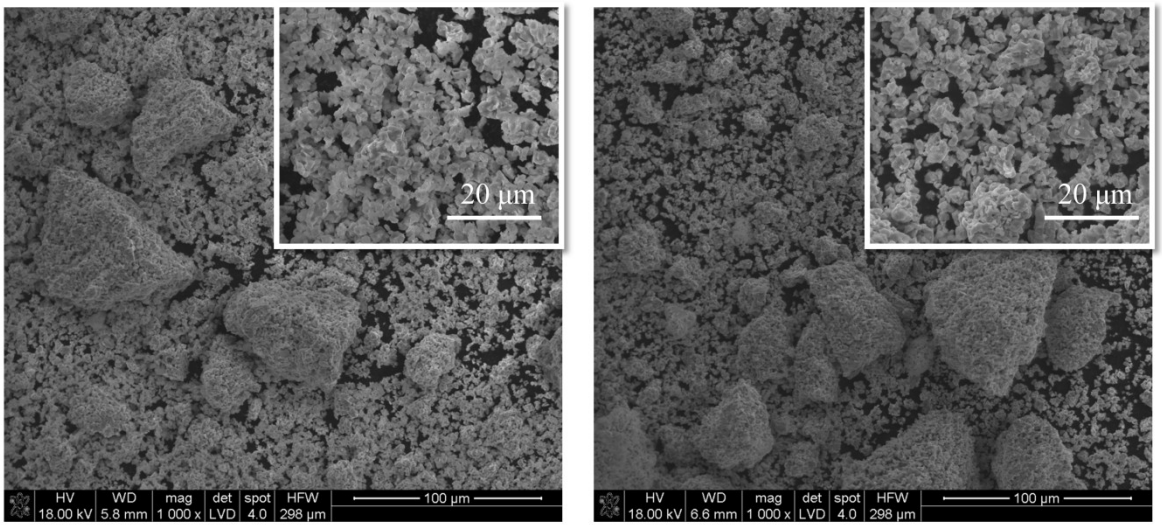

Fig. 7.3. SEM micrographs for: a) $BaErMn_2O_5$ and b) $BaErMn_2O_6$.

7.4. Oxygen storage properties

Results of TG measurements of weight dependence on temperature recorded during non-isothermal studies of oxidation of $BaErMn_2O_5$ and reduction of $BaErMn_2O_6$ materials are depicted in Fig. 7.4a. Comparing with $BaLnMn_2O_{5+\delta}$ series (Figs. 6.12a-f), material containing erbium exhibits the highest characteristic temperature of oxidation (including Y-containing sample), fitting well with a tendency of increasing of this temperature with decrease of the ionic radii of the lanthanides. Interestingly, the characteristic temperature of reduction (355 °C) is lower than the oxidation one, and is the lowest in the studied series of $BaLnMn_2O_{5+\delta}$.

In Fig. 7.4b kinetics of 1st, 2nd and 5th isothermal reduction of $BaErMn_2O_6$ in 5 vol.% H_2 in Ar atmosphere, together with oxidation of $BaErMn_2O_5$ performed in air at 500 °C, are presented. Similarly to other studied compounds, oxidation process takes only seconds, while the reduction is much longer, taking up to 10 minutes. As can be seen, a significant increase of reduction speed was recorded between 1st and 2nd cycle, while the consecutive reductions were only slightly faster. What is of importance, during reduction/oxidation cycles OSC of the compound was preserved.

Important parameters regarding oxygen storage-related properties, such as theoretical and measured reversible oxygen storage capacity, as well as determined temperatures and time needed for oxidation and reduction of the material are presented in Tab. 7.2.

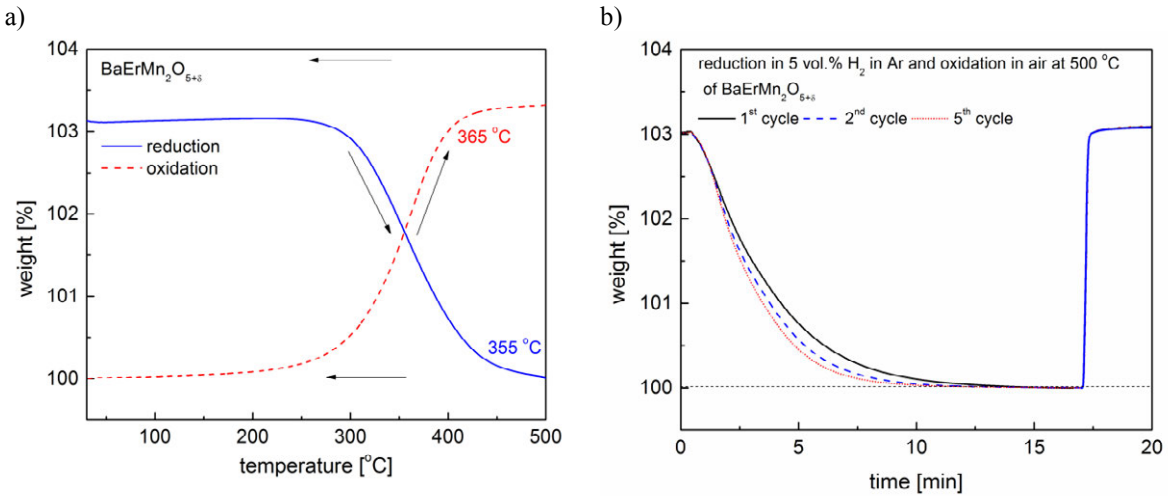

Fig. 7.4. a) Non-isothermal oxidation and reduction cycle and b) Isothermal reduction in 5 vol.% H_2 in Ar and oxidation in synthetic air at 500 °C of $BaErMn_2O_{5+\delta}$. Data published in [165].

Tab. 7.2. Oxygen storage properties of $BaErMn_2O_{5+\delta}$. Some data from [165].

theoretical change of weight in relation to $BaErMn_2O_5$ [wt.%]	3.24
average change of weight on oxidation/reduction cycles [wt.%]	3.10
average change of weight on non-isothermal oxidation/reduction [wt.%]	3.17
characteristic temperature of reduction [°C]	355
temperature of oxidation [°C]	365
time of reduction (99% of total mass change, 5th reduction) [min]	10
time of reduction (95% of total mass change, 5th reduction) [min]	6.5
time of oxidation (99% of total mass change, 5th oxidation) [s]	90
time of oxidation (95% of total mass change, 5th oxidation) [s]	20

7.5. Electrical conductivity and Seebeck coefficient of $BaErMn_2O_{5+\delta}$

For electrical conductivity studies, four-probe DC method was implemented. The sample was of a cuboid shape. Initial measurements of reduced $BaErMn_2O_5$ material were conducted in 5 vol.% H_2 in Ar atmosphere in temperature range between RT and 600 °C, with heating and cooling rate equal to ~ 1.5 °·min^{-1}. Measurements upon oxidation were conducted similarly, but in synthetic air atmosphere and up to 800 °C. Additional studies of changes of the behavior for the reduced $BaErMn_2O_5$ while the material was heated in air were also performed. Measurements of Seebeck coefficient were carried out at the same time. Results of the studies are gathered in Figs. 7.5a and b.

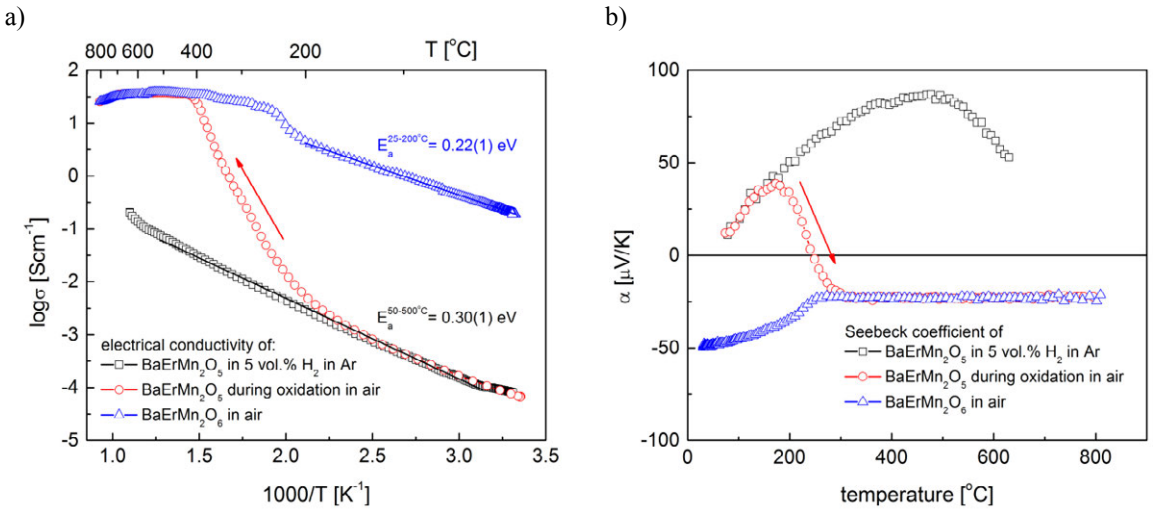

Fig. 7.5. a) Electrical conductivity and b) Seebeck coefficient of $BaErMn_2O_{5+\delta}$ as a function of temperature in different atmospheres. Data published in [165].

Value of the electrical conductivity σ for the reduced material at room temperature is on the order of 10^{-4} $S \cdot cm^{-1}$. With an increase of temperature (in 50-500 °C range) material exhibits activated character of the conductivity with an activation energy E_a = 0.30(1) eV. From Seebeck coefficient studies it can be seen that the reduced material exhibits positive value of α in whole temperature range, indicating electronic holes as main charge carriers. This is unexpected, considering Brouwer diagram presented in Fig. 4.7. Therefore, it seems that in the case of 1:1 mixed Mn^{2+}/Mn^{3+} states, mobility of the charge carriers plays a decisive role concerning sign of the Seebeck coefficient, i.e. holes are dominant. These holes might be associated with electronic configuration of manganese cations on +3 oxidation state.

During measurement of σ and α upon heating of $BaErMn_2O_5$ in air, a substantial increase of the electrical conductivity was observed at temperatures above 200 °C. Corresponding change of sign of Seebeck coefficient was also registered above 250 °C. Both effects indicate the ongoing oxidation of the material.

The oxidized $BaErMn_2O_6$ sample possesses significantly higher electrical conductivity in comparison with the reduced $BaErMn_2O_5$, and at room temperature σ equals almost to 0.2 $S \cdot cm^{-1}$. In vicinity of 225 °C, a further increase of values of σ can be observed, and this effect can be related to the phase transition from charge/orbital-ordered state to paramagnetic metal PM phase. When analyzing the phase diagram for $BaLnMn_2O_6$ [157, 158], the measured temperature of transition corresponds well with the expected value, and is the highest (~ 225 °C) in the considered series of materials. This result is consistent with the phase transition recorded during high temperature *in situ* XRD

measurements (Fig. 7.2). The highest conductivity value was obtained for $BaErMn_2O_6$ material in the vicinity of 500 °C and is almost equal to 40 $S \cdot cm^{-1}$. In the case of oxidized material, in the whole temperature range negative sign of Seebeck coefficient was measured, indicating electrons as the main charge carrier. What is more, below 250 °C, absolute values of α increase with a decreasing temperature, but during further heating Seebeck coefficient is almost independent on temperature.

Chapter 7 summary

Using soft chemistry-type method it was possible for the first time to successfully synthesize cation-ordered $BaErMn_2O_{5+\delta}$ material, and after further reduction and oxidation cycles, $BaErMn_2O_5$ and $BaErMn_2O_6$ compounds with purity exciding 95% were obtained. The materials were characterized in terms of their crystal structure at room temperature, with refined P4/nmm space group for the reduced, and P-1 space group for the oxidized compound. High temperature in situ XRD studies revealed complex behavior during heating of $BaErMn_2O_5$ from RT up to 500 °C, with the oxidation process of the material occurring at around 300 °C, and a phase transition in the vicinity of 225 °C visible on cooling for $BaErMn_2O_6$. Oxygen storage-related properties of $BaErMn_2O_5$-$BaErMn_2O_6$ system were investigated, and were shown to be similar to other studied $BaLnMn_2O_{5+\delta}$. Electrical conductivity of the reduced $BaErMn_2O_5$ is relatively low and shows activated character on temperature. On the other hand, the oxidized $BaErMn_2O_6$ exhibits much higher conductivity with a phase transition in the vicinity of 225 °C. Seebeck coefficient is positive for $BaErMn_2O_5$ and negative for $BaErMn_2O_6$ indicating substantial changes in the electronic structure of materials caused by changes of the oxygen content.

8. Properties of $BaY_{1-x}Ln_xMn_2O_{5+\delta}$ (Ln: Pr, Sm, Gd) oxides

While substitution of Y^{3+} by Ln^{3+} cations in $BaLnMn_2O_{5+\delta}$, as proven in previous chapters 6 and 7, causes a decrease of the measured oxygen storage capacity, it was also shown that it may help with improving other important factors, like for instance speed of reduction (e.g. as documented for $BaGdMn_2O_{5+\delta}$, Tab. 6.3). Consequently, partially substituted samples with general formula of $BaY_{1-x}Ln_xMn_2O_{5+\delta}$ ($0 < x < 1$) seem of interest regarding their oxygen storage-related properties. Also, until now no literature data were available concerning structural properties of reduced or oxidized $BaY_{1-x}Ln_xMn_2O_{5+\delta}$.

In this chapter results of investigations of three oxide systems: $BaY_{1-x}Pr_xMn_2O_{5+\delta}$, $BaY_{1-x}Sm_xMn_2O_{5+\delta}$ and $BaY_{1-x}Gd_xMn_2O_{5+\delta}$ are shown. Similarly to previous studies, crystal structure and oxygen storage properties of these materials are reported in details. The main objective was a search for the optimized chemical composition, which would deliver high OSC and fast reduction rate. Considering choice of the introduced lanthanides, one bigger Pr^{3+} and two intermediate Sm^{3+} and Gd^{3+} cations were selected, as differing considerably from yttrium.

8.1. Partial substitution of Pr into $BaY_{1-x}Pr_xMn_2O_{5+\delta}$ ($0 < x < 1$) system

Introduction of much bigger Pr^{3+} into Y^{3+} sublattice of $BaY_{1-x}Pr_xMn_2O_{5+\delta}$ is interesting from a point of view of crystal structure, as well as oxygen storage-related properties. As documented in chapter 6, $BaPrMn_2O_6$ can release oxygen at elevated temperatures in ~ 100 Pa vacuum conditions (Tab. 6.2) and possesses one of the lowest characteristic temperatures of oxidation (Tab. 6.3), while the Y-containing material possesses the highest OSC. Also, the reduction process for $BaYMn_2O_6$ is single step-like (Fig. 6.16), while for $BaPrMn_2O_6$ it has evident two steps, with formation of the intermediate $O_{5.5}$ phase. Properties of $BaY_{1-x}Pr_xMn_2O_{5+\delta}$ for $x = 0.25$, 0.5 and 0.75 are given below.

Part of the results presented in the following subchapters was previously published by author of this thesis in work [181].

8.1.1. Crystal structure of $BaY_{1-x}Pr_xMn_2O_5$ and $BaY_{1-x}Pr_xMn_2O_6$ oxides at room temperature

Structural data measured for both, the reduced $BaY_{1-x}Pr_xMn_2O_5$ and the oxidized $BaY_{1-x}Pr_xMn_2O_6$ samples, together with the Rietveld refinement are presented in Figs. 8.1a-d, while the refined structural parameters are gathered in Tab. 8.1.

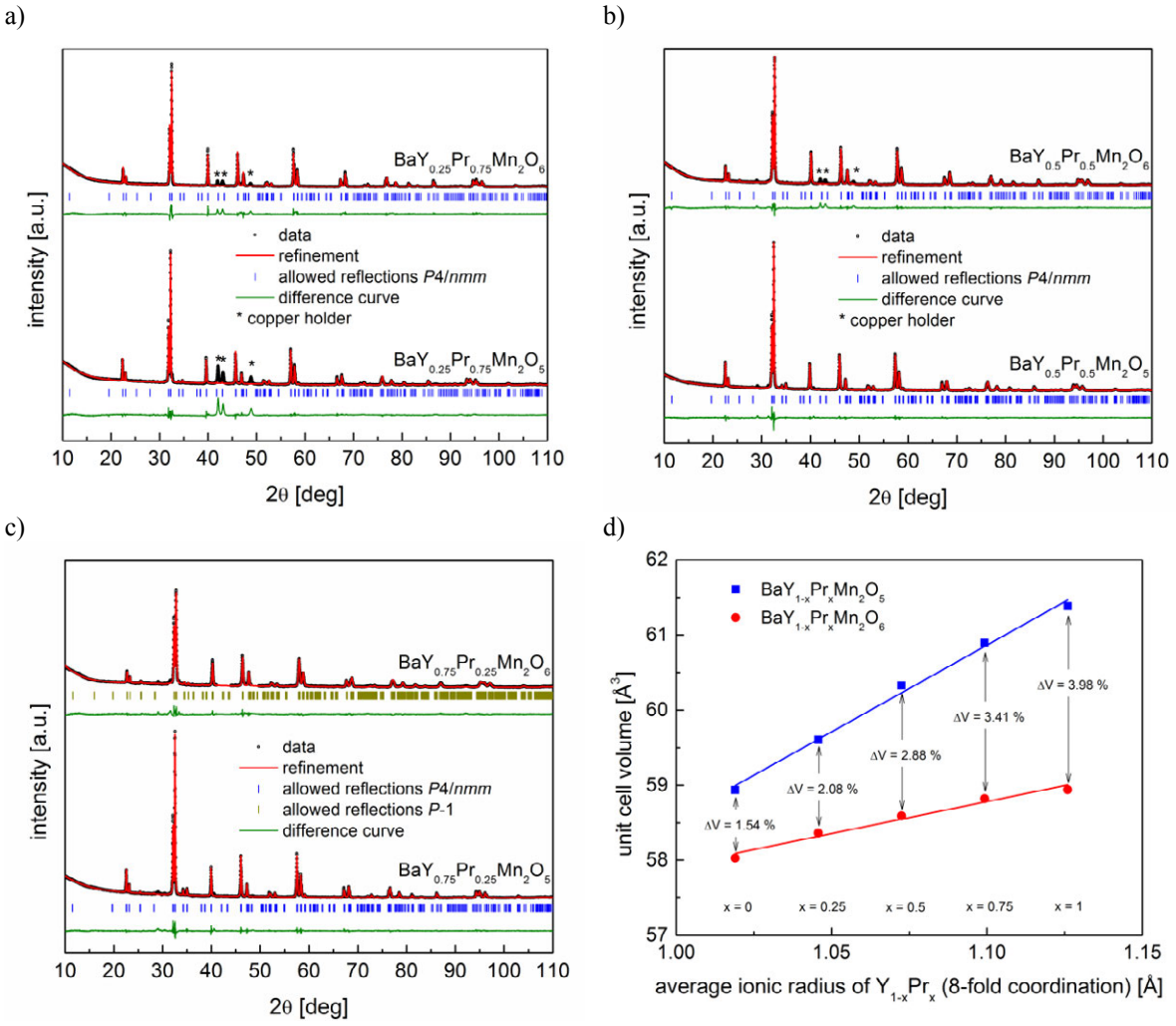

Fig. 8.1. Diffractograms with Rietveld analysis for: a) $BaY_{0.25}Pr_{0.75}Mn_2O_{5+\delta}$, b) $BaY_{0.5}Pr_{0.5}Mn_2O_{5+\delta}$, c) $BaY_{0.75}Pr_{0.25}Mn_2O_{5+\delta}$ samples in oxidized and reduced states at room temperature, and d) normalized unit cell volume of $BaY_{1-x}Pr_xMn_2O_5$ and $BaY_{1-x}Pr_xMn_2O_6$ as a function of average $Y_{1-x}Pr_x$ ionic radius. Copper holder reflections are visible in several scans.

All of the synthesized samples were identified as single phase, with no significant amount of secondary phases present. For structural analyses of the reduced materials tetragonal *P*4/*nmm* space group was applied, giving good quality refinements. For oxidized materials, different space groups were chosen, based on the available literature data [7, 15, 157, 158, 185, 190, 191].

Tab. 8.1. Structural parameters of reduced and oxidized $BaY_{1-x}Pr_xMn_2O_{5+\delta}$ oxides [181].

chemical composition	space group	a [Å] b [Å] α [deg] β [deg]	c [Å] γ [deg]	V [Å^3]	relative increase of V after reduction [%]	χ^2	R_{wp} [%]	t_S
$BaY_{0.25}Pr_{0.75}Mn_2O_5$	*P*4/*nmm*	5.6107(2)	7.7374(3)	243.58(2)	3.41	7.05	5.2	0.980
$BaY_{0.25}Pr_{0.75}Mn_2O_6$	*P*4/*nmm*	5.5441(1)	7.6545(1)	235.28(1)		6.92	5.7	0.985
$BaY_{0.5}Pr_{0.5}Mn_2O_5$	*P*4/*nmm*	5.5931(1)	7.7142(1)	241.32(1)	2.88	3.43	3.4	0.975
$BaY_{0.5}Pr_{0.5}Mn_2O_6$	*P*4/*nmm*	5.5421(1)	7.6304(1)	234.37(1)		8.51	5.2	0.980
$BaY_{0.75}Pr_{0.25}Mn_2O_5$	*P*4/*nmm*	5.5708(1)	7.6825(1)	238.42(1)	2.08	5.04	3.5	0.970
$BaY_{0.75}Pr_{0.25}Mn_2O_6$	*P*-1	5.5337(1) 5.5317(1) 90.01(1) 90.22(1)	7.6263(1) 89.90(1)	233.45(1)		5.85	4.0	0.975

Contrary to $BaPrMn_2O_6$, for which the refinement was conducted assuming tetragonal *P*4/*mmm* symmetry (Tab. 6.4), for $BaY_{0.25}Pr_{0.75}Mn_2O_6$ and $BaY_{0.5}Pr_{0.5}Mn_2O_6$ compounds good refinements were obtained assuming the same *P*4/*nmm* space group as in the case of the reduced material. This suggests that apart from the changing oxygen content, there is no structural transformation present upon oxidation. However, at high temperatures, above the expected transition to paramagnetic metal phase (Fig. 4.14) the expected symmetry is *P*4/*mmm*. At room temperature, with the increase of yttrium content up to 0.75 for $BaY_{0.75}Pr_{0.25}Mn_2O_6$ material, there is an evident split of main XRD reflections, suggesting decrease of the crystal's symmetry. Similar behavior was observed and discussed for $BaYMn_2O_6$ (chapter 6.1). Good refinements of the structural data were obtained assuming either monoclinic *P*121 [190] or triclinic *P*-1 [184] space group. However, choice of the triclinic symmetry is more probable, as suggested by better refinement statistics (R_{wp} = 4.0%, while for the monoclinic it was considerably higher, 4.5%), but also due to structural characteristics presented for $BaYMn_2O_6$ using precise neutron diffraction studies [184]. It should be mentioned that no improvement of refinement statistics was obtained assuming partial mixing between the Ba^{2+} and Y^{3+} or Pr^{3+} cations, suggesting that the layered-type of cation ordering is well-preserved in whole series.

In addition to the discussed space group selection and refined structural parameters (Tab. 8.1), the relative increase of unit cell volume after reduction of the compounds was calculated. Graphical representation of a dependence of unit cell volume as a function of the average radius of $Y_{1-x}Pr_x$ (taken for 8-fold coordination, as previously explained in chapter 6.1) is depicted in Fig. 8.1d. As can be seen, for both series, $BaY_{1-x}Pr_xMn_2O_5$ and

$BaY_{1-x}Pr_xMn_2O_6$ the dependence is linear, suggesting formation of solid solution, and resembles the one obtained for $BaLnMn_2O_{5+\delta}$ (Fig. 6.3).

Calculations of the normalized ratio of $c/(\sqrt{2}a)$ (as well as $c/(\sqrt{2}b)$ in the case of *P*-1 space group) give very similar values for all considered compounds, on order of 0.974-0.976. The only exception is $BaPrMn_2O_6$, for which $c/(2a)$ was estimated to be 0.993. While initially it could be assumed as originating from a partial mixing of Ba^{2+} and Pr^{3+} cations, it was not supported by Rietveld refinements. Another, more probable explanation is that the effect originates from magnetic properties of $BaPrMn_2O_6$, for which transformation near RT from a low-temperature A-type antiferromagnetic phase into ferromagnetic phase is associated with a major increase of the normalized c/a ratio [191].

8.1.2. Oxygen storage properties

Similarly as described in chapter 6, oxygen storage-related properties of the synthesized $BaY_{1-x}Pr_xMn_2O_{5+\delta}$ were measured. Weight changes recorded upon oxidation of the reduced $BaY_{1-x}Pr_xMn_2O_5$ materials, while heating in air up to 500 °C, are presented in Fig. 8.2a. Dependence of the characteristic temperature of oxidation on the praseodymium content is depicted in Fig. 8.2b. As visible in the graph, there is no linear dependence in the series, with all Pr-containing materials oxidizing at much lower temperatures. In addition, only for $BaYMn_2O_5$ oxide the onset of the oxidation process is above 150 °C, while for compounds having the intermediate compositions it occurs at lower temperatures.

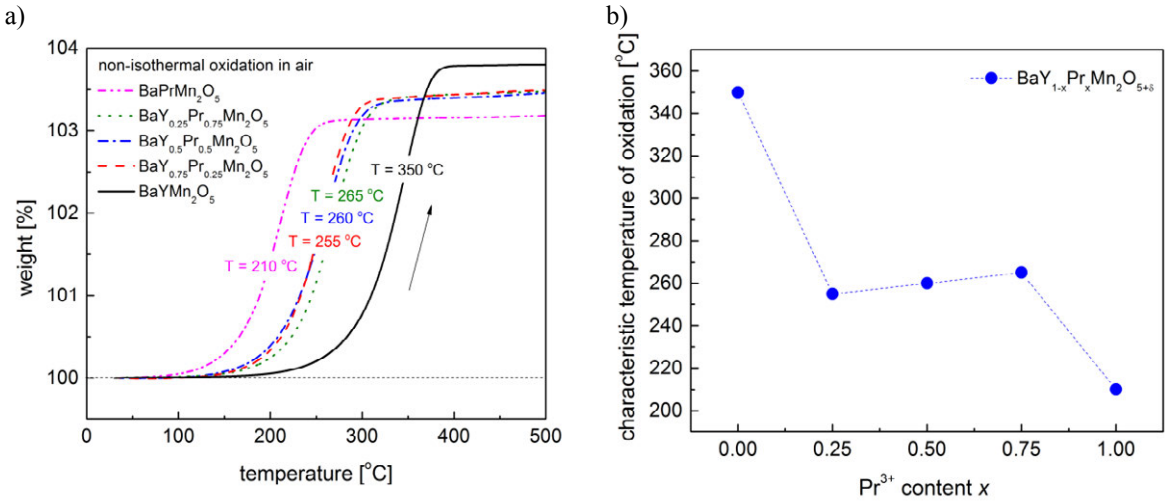

Fig. 8.2. a) Non-isothermal oxidation of $BaY_{1-x}Pr_xMn_2O_5$ materials in air, b) the characteristic temperature of the oxidation process as a function of Pr^{3+} content.

Isothermal reduction and oxidation curves for the investigated $BaY_{1-x}Pr_xMn_2O_{5+\delta}$ materials are shown in Figs. 8.3a and b. Data were collected in 500 °C during rapid change of the atmosphere from air to 5 vol.% H_2 in Ar and then back to air, on 5th reduction/ oxidation cycle. Concerning the reduction rate at 500 °C one may notice different behavior of Pr-rich materials (x = 1 and 0.75), with visible two stages of the process, comparing to the rest of the samples, for which the reduction curves show no inflection in the middle part. This is in good agreement with results presented in Fig. 6.16, suggesting that during such reduction of $BaLnMn_2O_6$ with larger Ln^{3+} cations (or mixture of cations), there is a stronger tendency for the $O_{5.5}$-type phase to appear.

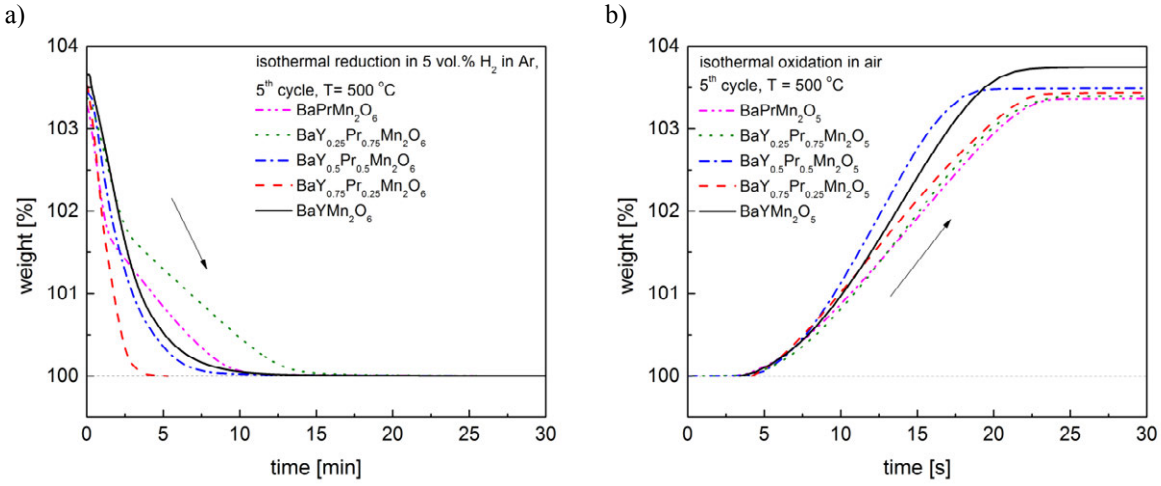

Fig. 8.3. TG data of isothermal a) reduction in 5 vol.% H_2 in Ar, and b) oxidation in synthetic air at 500 °C of $BaY_{1-x}Pr_xMn_2O_{5+\delta}$ materials.

Interestingly, the fastest reduction speed was recorded for $BaY_{0.75}Pr_{0.25}Mn_2O_6$ compound, for which during fifth reduction process 99% of total weight changes occurred in 3.7 minutes. This is one of the best results obtained so far in the literature, significantly better than the reported in Tab. 6.3 result for $BaGdMn_2O_6$. This result may be understood on a basis of a general behavior visible during reduction of $BaLnMn_2O_6$ (Figs. 6.12 and 6.13). The materials, for which the reduction curve shows inflection reduce much slower, with the second part of the curve limiting the performance. It is related to the mentioned formation of the oxygen vacancy-ordered $BaLnMn_2O_{5.5}$ phase, for which (like in the case of the mentioned previously $Ba_2In_2O_5$ brownmillerite [152]), ordered vacancies hinder oxygen transport in the bulk. The considered $BaY_{0.75}Pr_{0.25}Mn_2O_6$ shows single step-like reduction, but also, due to presence of heavier Pr^{3+} cations, the reduction process may be facilitated (Fig. 6.16).

The most important factors from the viewpoint of application of OSMs, including the measured oxygen storage capacity (taken as average of values recorded on reduction and oxidation), characteristic temperature of oxidation and also time of isothermal reduction and oxidation at 500 °C (for 99 % of total weight changes), are gathered in Tab. 8.2. The practical values of oxygen storage capacity in $BaY_{1-x}Pr_xMn_2O_{5+\delta}$ series exhibit the same dependence as the theoretical OSC, i.e., decrease with an increasing amount of the substituted praseodymium. For all of the studied materials, the measured mass change on reduction and oxidation cycles corresponds to δ changes on the order of 0.95.

Tab. 8.2. Oxygen storage properties of the considered $BaY_{1-x}Pr_xMn_2O_{5+\delta}$ materials. Some results presented also in work [181].

chemical composition	theoretical capacity [wt.%]	measured capacity (5^{th} cycle at 500 °C) [wt.%]	characteristic temperature of oxidation [°C]	time of reduction (99% of total mass change, 5^{th} cycle) [min]	time of oxidation (99% of total mass change, 5^{th} cycle) [s]
$BaY_{0.25}Pr_{0.75}Mn_2O_{5+\delta}$	3.52	3.35	265	15.2	26
$BaY_{0.5}Pr_{0.5}Mn_2O_{5+\delta}$	3.62	3.44	260	8.9	24
$BaY_{0.75}Pr_{0.25}Mn_2O_{5+\delta}$	3.73	3.54	255	3.7	25

8.1.3. Cycling performance of $BaY_{0.75}Pr_{0.25}Mn_2O_{5+\delta}$

$BaY_{0.75}Pr_{0.25}Mn_2O_{5+\delta}$ material, showing the best results in terms of reduction speed and also good reversible OSC, exceeding 3.54 wt.% was selected for further evaluation during consecutive 50 reduction/oxidation cycles. As can be seen in Fig. 8.4, the compound shows excellent cycling stability.

During performance test, calculated changes of the oxygen content remain practically the same in all 50 cycles, indicating high reversibility of the reduction/oxidation processes. After the initial cycles, rate of reduction decreases down to ~ 2.9 min for 99% of total weight changes in the 10^{th} cycle (2.5-2.6 min calculating for 95% of the total changes), and remains unchanged in the following 40 cycles. Comparing the presented data for $BaY_{0.75}Pr_{0.25}Mn_2O_{5+\delta}$ with results obtained for the optimized $BaYMn_2O_{5+\delta}$ (synthesized at 900 °C to obtain high specific surface material) [186], the oxygen release rate defined as slope at 50% of the weight change is nearly identical, and equals to 1.5 wt.%·min^{-1}.

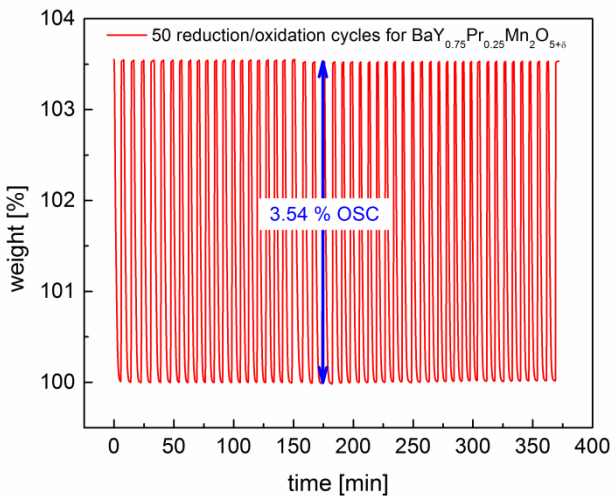

Fig. 8.4. Reversibility of weight changes of $BaY_{0.75}Pr_{0.25}Mn_2O_{5+\delta}$ during 50 reduction/oxidation cycles [181].

Similarly to the microstructure of $BaLnMn_2O_{5+\delta}$ (Ln: Y, Nd) materials presented in chapter 6.3, the considered $BaY_{0.75}Pr_{0.25}Mn_2O_6$ powder, obtained using soft chemistry method, exhibits porous-like structure of agglomerates, as depicted in Fig. 8.5a. After the mentioned 50 cycles, comparing to the initial material, no substantial changes of morphology of the powder could be observed, further supporting good stability and reversibility of the oxygen intake and release processes.

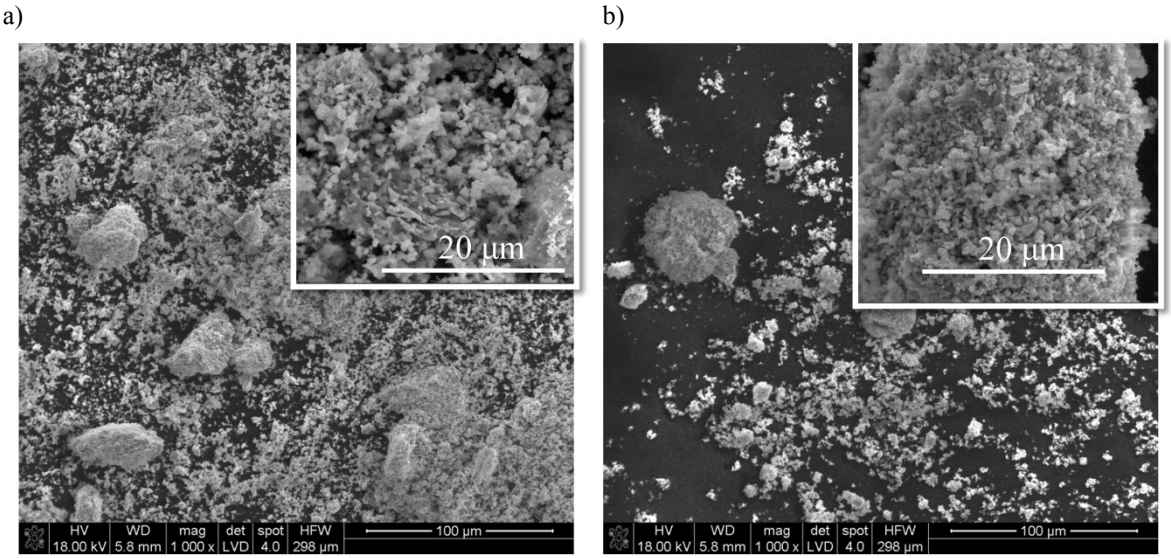

Fig. 8.5. SEM micrographs for: a) initial $BaY_{0.75}Pr_{0.25}Mn_2O_6$ sample, and b) $BaY_{0.75}Pr_{0.25}Mn_2O_6$ material after 50 cycles of reduction and oxidation processes.

8.2. Partial substitution of Sm into $BaY_{1-x}Sm_xMn_2O_{5+\delta}$ ($0 < x < 1$) system

Possibility of formation of $BaY_{1-x}Sm_xMn_2O_{5+\delta}$ ($0 < x < 1$) oxides was also studied, concerning crystal structure of the materials and their oxygen storage-related properties. While rather small changes of the crystal structure can be expected in such series, due to more comparable ionic radii of Y^{3+} and Sm^{3+}, also, relative increase of the unit cell volume after reduction of these materials should be smaller. In addition, change of the doping level should result in decrease of the characteristic temperature of oxidation, as well as modify character of the reduction curve.

Part of the results presented below was previously published by author of this thesis in work [182].

8.2.1. Crystal structure of $BaY_{1-x}Sm_xMn_2O_5$ and $BaY_{1-x}Sm_xMn_2O_6$ oxides at room temperature

Structural data obtained for $BaY_{1-x}Sm_xMn_2O_5$ and $BaY_{1-x}Sm_xMn_2O_6$ oxides together with Rietveld refinements are presented in Figs. 8.6a-d. Structural parameters of the materials are gathered in Tab. 8.3. All of the samples were identified as single phase, with no significant amount of impurities, and expected formation of layered Ba-$Y_{1-x}Sm_x$ cation ordering. For structural analysis of all reduced samples tetragonal *P*4/*nmm* space group was selected, which resulted in good quality refinements. For the oxidized samples, depending on the composition, either *P*4/*nmm* or triclinic *P*-1 space groups were chosen.

As expected from smaller radius of Sm^{3+}, comparing to Pr^{3+}, in the series of oxidized $BaY_{1-x}Sm_xMn_2O_6$ the triclinic structural distortion is present in a wider range of chemical compositions, i.e. for $x \leq 0.5$ (Tab. 8.3). However, degree of this distortion is very small for $BaY_{0.5}Sm_{0.5}Mn_2O_6$, for which worsen refinement statistics were obtained assuming tetragonal *P*4/*nmm* space group (R_{wp} = 5.1% for tetragonal space group and 4.5% for triclinic space group). Similarly like in the case of $BaY_{1-x}Sm_xMn_2O_{5+\delta}$ no improvement of the Rietveld refinements was observed assuming mixing of A-site cations, which suggests that layered-type of arrangement of Ba-$Y_{1-x}Sm_x$ cations is maintained.

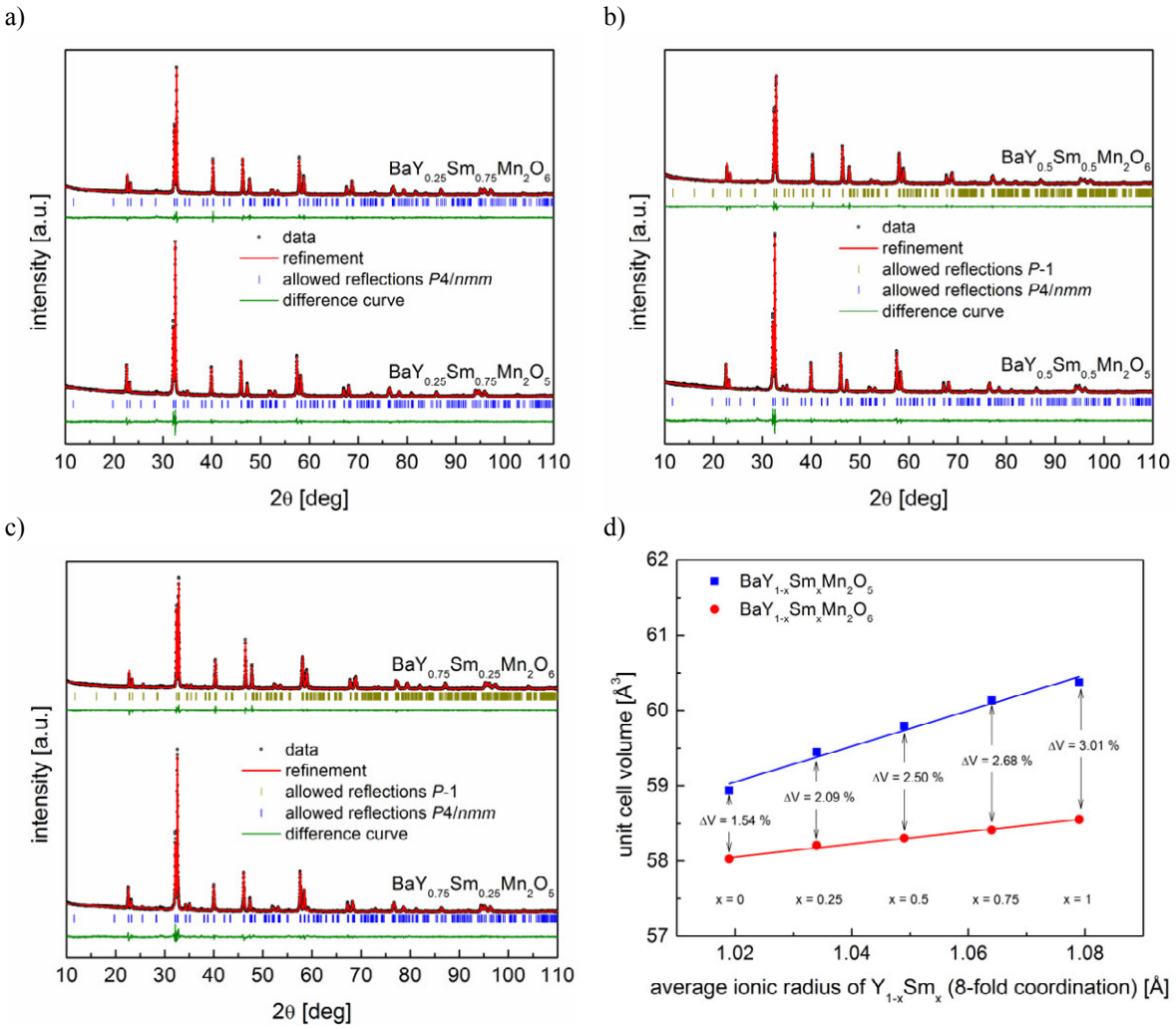

Fig. 8.6. Diffractograms with Rietveld analysis for: a) $BaY_{0.25}Sm_{0.75}Mn_2O_{5+\delta}$, b) $BaY_{0.5}Sm_{0.5}Mn_2O_{5+\delta}$, c) $BaY_{0.75}Sm_{0.25}Mn_2O_{5+\delta}$ samples in oxidized and reduced states at room temperature, and d) unit cell volume of $BaY_{1-x}Sm_xMn_2O_5$ and $BaY_{1-x}Sm_xMn_2O_6$ as a function of average $Y_{1-x}Sm_x$ ionic radius.

In addition to the structural data, relative increase of unit cell volume after reduction was calculated for all studied materials. Graphical representation of this parameter as a function of average radius of $Y_{1-x}Sm_x$ (taken for 8-fold coordination as previously) is depicted in Fig. 8.6d. The observed behavior is expected, with almost linearly decreasing change of the unit cell volume upon reduction/oxidation, which is due to much weaker dependence of V on the average $Y_{1-x}Sm_x$ ionic radius (i.e. chemical composition) in the reduced materials. The explanation for this effect was already discussed in chapter 6.1 (see for comparison Fig. 6.3 and 8.1d).

Tab. 8.3. Structural parameters of reduced and oxidized $BaY_{1-x}Sm_xMn_2O_{5+\delta}$ oxides [182].

chemical composition	space group	a [Å] b [Å] α [deg] β [deg]	c [Å] γ [deg]	V [Å^3]	relative increase of V after reduction [%]	χ^2	R_{wp} [%]	t_S
$BaY_{0.25}Sm_{0.75}Mn_2O_5$	*P*4/*nmm*	5.5885(1)	7.7014(1)	240.53(1)	2.68	1.34	4.3	0.974
$BaY_{0.25}Sm_{0.75}Mn_2O_6$	*P*4/*nmm*	5.5388(1)	7.6162(1)	233.65(1)		1.26	4.4	0.977
$BaY_{0.5}Sm_{0.5}Mn_2O_5$	*P*4/*nmm*	5.5776(1)	7.6884(1)	239.18(1)	2.50	1.75	4.4	0.971
$BaY_{0.5}Sm_{0.5}Mn_2O_6$	*P*-1	5.5333(1) 5.5341(1) 89.80(1) 90.01(1)	7.6158(1) 89.97(1)	233.21(1)		1.34	4.5	0.974
$BaY_{0.75}Sm_{0.25}Mn_2O_5$	*P*4/*nmm*	5.5670(1)	7.6727(1)	237.79(1)	2.09	2.32	5.5	0.968
$BaY_{0.75}Sm_{0.25}Mn_2O_6$	*P*-1	5.5312(1) 5.5280(1) 90.00(1) 90.27(1)	7.6145(1) 89.97(1)	232.82(1)		1.34	4.4	0.972

8.2.2. Oxygen storage properties

Results concerning weight change recorded upon oxidation of $BaY_{1-x}Sm_xMn_2O_5$ materials while heating in air up to 500 °C are presented in Fig. 8.7a. Dependence of the characteristic temperature of oxidation on the chemical composition in the series is shown in Fig. 8.7b. For the studied materials there is a linear dependence visible, with materials having higher amounts of introduced Sm^{3+} cations oxidizing at significantly lower temperatures.

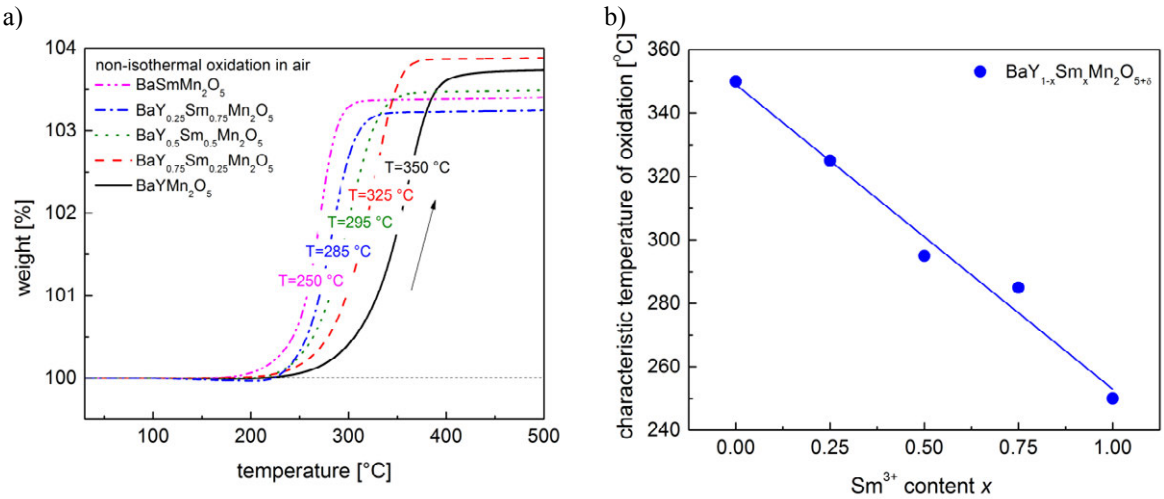

Fig. 8.7. a) Non-isothermal oxidation of $BaY_{1-x}Sm_xMn_2O_5$ materials in air, b) the characteristic temperature of the oxidation process as a function of Sm^{3+} content.

Reduction and oxidation runs of investigated $BaY_{1-x}Sm_xMn_2O_{5+\delta}$ materials are shown in Figs. 8.8a and b. Similarly like in other conducted studies, data were collected at 500 °C during rapid change of atmosphere from oxidizing (air) to reducing (5 vol.% H_2 in Ar), and then back to oxidizing conditions. Results presented concern 5th reduction/ oxidation cycle. As can be observed in Fig. 8.8a, an inflection of the reduction curve, visible for the parent $BaSmMn_2O_6$ oxide, is hardly visible for $BaY_{0.25}Sm_{0.75}Mn_2O_6$, and completely disappears for samples with $x \leq 0.5$. This confirms behavior recorded for $BaSmMn_2O_6$ (Fig. 6.16) and Pr-containing materials (Fig. 8.3).

In the studied series, the fastest reduction was registered for $BaY_{0.5}Sm_{0.5}Mn_2O_6$, however, the reduction time is only slightly shorter, comparing to other samples (Tab. 8.4). When comparing reduction and oxidation processes, like in the case of all previously reported data, the oxidation is much faster, which can be connected to the exothermic character of this reaction.

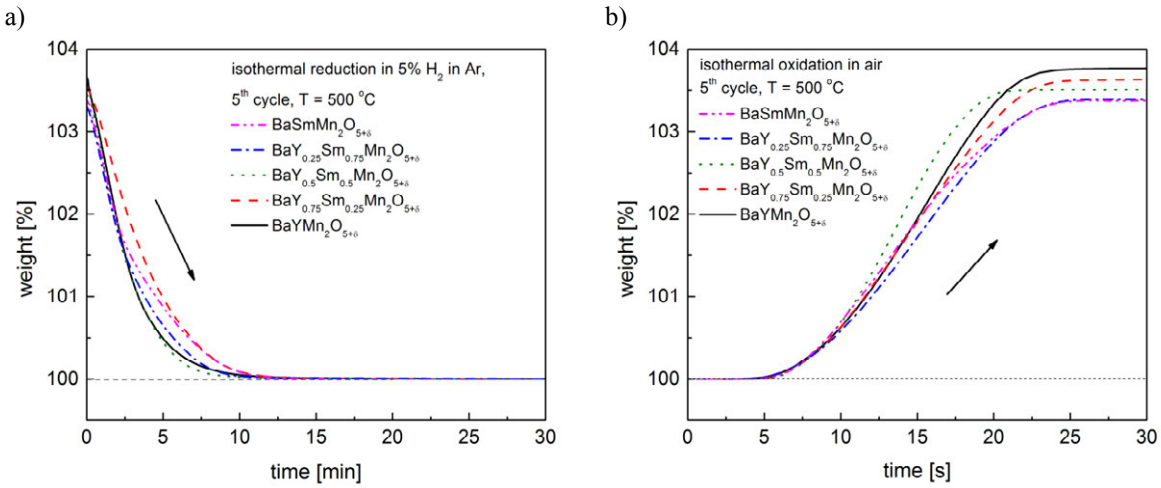

Fig. 8.8. TG data of isothermal a) reduction in 5 vol.% H_2 in Ar, and b) oxidation in synthetic air at 500 °C of $BaY_{1-x}Sm_xMn_2O_{5+\delta}$ materials.

The measured OSC, values of the characteristic temperature of oxidation, as well as reduction and oxidation times are gathered in Tab. 8.4. As expected, the measured oxygen storage capacity in $BaY_{1-x}Sm_xMn_2O_{5+\delta}$ series exhibits the same dependence as the theoretical one: OSC decreases with the increasing amount of the introduced samarium, which results from an increase of the molar mass of the compounds. The recorded changes of the oxygen nonstoichiometry in partially substituted compounds are exceeding 0.99.

Tab. 8.4. Oxygen storage properties of the considered $BaY_{1-x}Sm_xMn_2O_{5+\delta}$ materials. Some results presented also in work [182].

chemical composition	theoretical capacity [wt.%]	measured capacity (5^{th} cycle at 500 °C) [wt.%]	characteristic temperature of oxidation [°C]	time of reduction (99% of total mass change, 5^{th} cycle) [min]	time of oxidation (99% of total mass change, 5^{th} cycle) [s]
$BaY_{0.25}Sm_{0.75}Mn_2O_{5+\delta}$	3.46	3.43	285	10.1	24
$BaY_{0.5}Sm_{0.5}Mn_2O_{5+\delta}$	3.58	3.56	295	9.9	20
$BaY_{0.75}Sm_{0.25}Mn_2O_{5+\delta}$	3.71	3.68	325	11.6	21

8.3. Partial substitution of Gd into $BaY_{1-x}Gd_xMn_2O_{5+\delta}$ ($0 < x < 1$) system

The fastest reduction speed recorded for $BaGdMn_2O_6$ (among all the studied $BaLnMn_2O_6$, Tab. 6.3) leads to a supposition that some improvement of the oxygen storage-related properties may be obtained in a series of substituted $BaY_{1-x}Gd_xMn_2O_{5+\delta}$. Furthermore, comparing to $BaLnMn_2O_{5+\delta}$, presence of gadolinium lowers not only the characteristic temperature of oxidation, but also the temperature of reduction process (Tab. 6.3). In this chapter, results of structural studies together with characterization of oxygen storage performance are included for the considered Gd-containing materials.

Part of the results presented below was previously published by author of this thesis in work [6].

8.3.1. Crystal structure of $BaY_{1-x}Gd_xMn_2O_5$ and $BaY_{1-x}Gd_xMn_2O_6$ oxides at room temperature

Structural data obtained for both, the reduced $BaY_{1-x}Gd_xMn_2O_5$ and the oxidized $BaY_{1-x}Gd_xMn_2O_6$ materials, together with Rietveld refinements, are presented in Figs. 8.9a-d, while the obtained structural parameters are gathered in Tab. 8.5. All of the samples were identified as single phase, with no significant amount of secondary phases. For structural analyses of all the reduced samples tetragonal *P*4/*nmm* space group was applied, yielding good refinement statistics ($R_{wp} \leq 4.9\%$). Following the observed trend about the oxidized and substituted $BaY_{1-x}Ln_xMn_2O_6$ (Ln: Pr, Sm) compounds, in the case of Gd-containing samples, the triclinic distortion is present in even wider chemical composition range, including also $BaY_{0.25}Gd_{0.75}Mn_2O_6$. For this compound, however, the distortion is rather minimal. While the magnitude of the distortion is not high, it is visible in a form of splitting of several peaks, including presence of a left shoulder of the most

intensive peak (~ 32 deg). Like in the case of previously described two systems, layered-type of arrangement of smaller $Y_{1-x}Gd_x$ and much bigger Ba^{2+} cations is well-preserved.

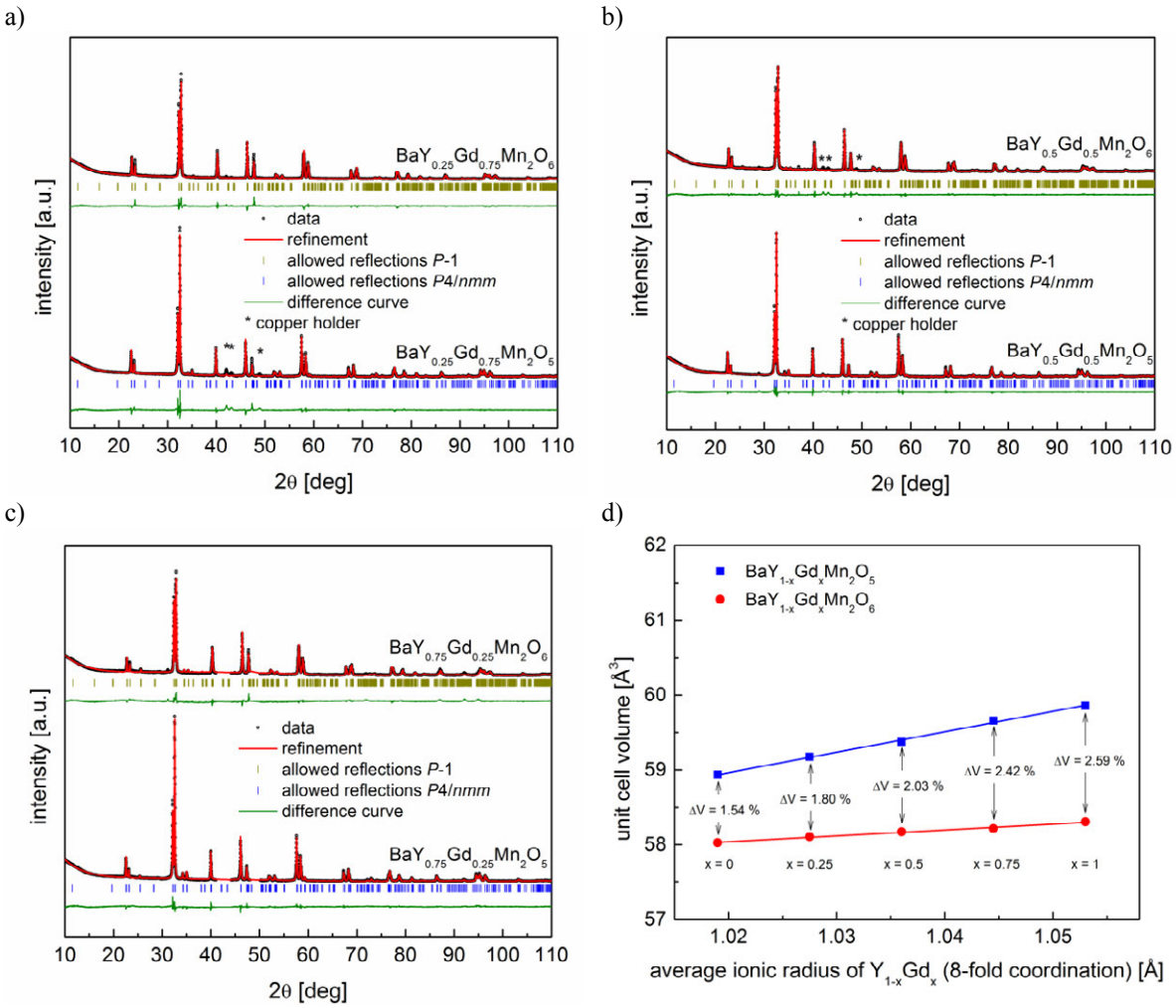

Fig. 8.9. Diffractograms with Rietveld analysis for: a) $BaY_{0.25}Gd_{0.75}Mn_2O_{5+\delta}$, b) $BaY_{0.5}Gd_{0.5}Mn_2O_{5+\delta}$, c) $BaY_{0.75}Gd_{0.25}Mn_2O_{5+\delta}$ samples in oxidized and reduced states at room temperature, and d) unit cell volume of $BaY_{1-x}Gd_xMn_2O_5$ and $BaY_{1-x}Gd_xMn_2O_6$ as a function of average $Y_{1-x}Gd_x$ ionic radius.

In addition to the structural data, relative increase of V after reduction was also calculated, as shown in Fig. 8.9d. Also in the case of this series of materials, a linear dependence of the normalized volume as a function of average radius of $Y_{1-x}Gd_x$ (taken for 8-fold coordination) was observed, with higher slope visible for the reduced materials.

Tab. 8.5. Structural parameters of reduced and oxidized $BaY_{1-x}Gd_xMn_2O_{5+\delta}$ oxides [6].

chemical composition	space group	a [Å] b [Å] α [deg] β [deg]	c [Å] γ [deg]	V [Å^3]	relative increase of V after reduction [%]	χ^2	R_{wp} [%]	t_S
$BaY_{0.25}Gd_{0.75}Mn_2O_5$	*P*4/*nmm*	5.5746(1)	7.6789(1)	238.63(1)	2.45	8.26	4.6	0.970
$BaY_{0.25}Gd_{0.75}Mn_2O_6$	*P*-1	5.5313(1) 5.5314(1) 90.01(1) 90.24(1)	7.6130(6) 89.96(1)	232.86(1)		5.20	3.7	0.973
$BaY_{0.5}Gd_{0.5}Mn_2O_5$	*P*4/*nmm*	5.5642(1)	7.6711(1)	237.50(1)	2.03	3.63	3.1	0.969
$BaY_{0.5}Gd_{0.5}Mn_2O_6$	*P*-1	5.5290(1) 5.5273(1) 90.01(1) 90.29(1)	7.6142(1) 89.97(1)	232.69(1)		4.09	3.3	0.971
$BaY_{0.75}Gd_{0.25}Mn_2O_5$	*P*4/*nmm*	5.5577(1)	7.6632(2)	236.70(2)	1.80	4.06	4.9	0.967
$BaY_{0.75}Gd_{0.25}Mn_2O_6$	*P*-1	5.5271(5) 5.5240(5) 90.00(2) 90.30(1)	7.6130(6) 89.95(1)	232.43(4)		7.16	5.9	0.970

8.3.2. Oxygen storage properties

Oxygen storage related-properties of $BaY_{1-x}Gd_xMn_2O_{5+\delta}$ are shown in Figs. 8.10 and 8.11. As can be seen, dependence of the characteristic temperature of oxidation is not following exactly level of chemical substitution, but materials with higher Gd content oxidize at significantly lower temperatures, with onset of the process occurring above 150 °C.

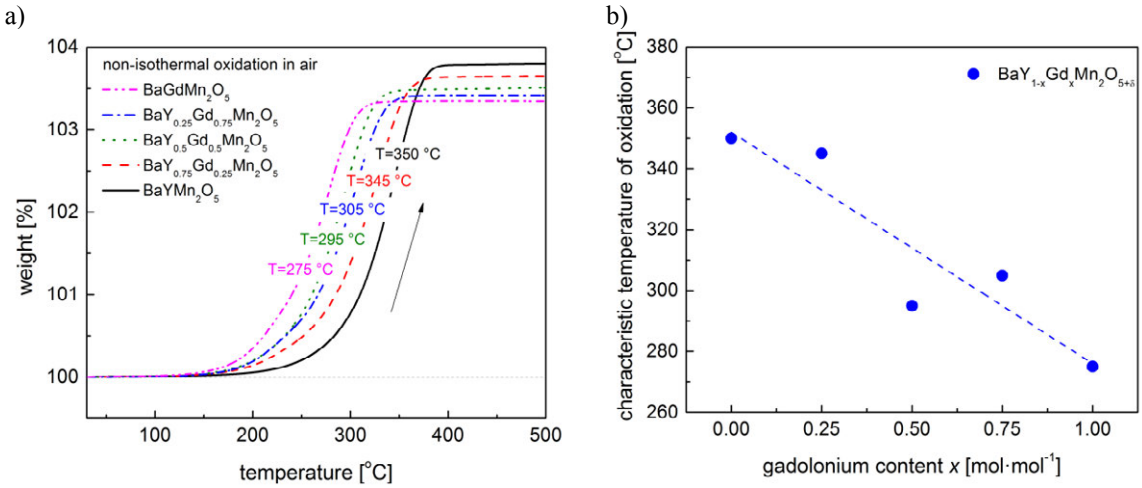

Fig. 8.10. a) Non-isothermal oxidation of $BaY_{1-x}Gd_xMn_2O_5$ materials in air, b) the characteristic temperature of the oxidation process as a function of Gd^{3+} content.

The recorded at 500 °C isothermal reduction curves (Fig. 8.11a) show single step-type process for all materials, with very similar behavior visible for all samples with gadolinium content x ≤ 0.75. Like it was observed previously, the reduction process is much faster than the oxidation for all the considered materials.

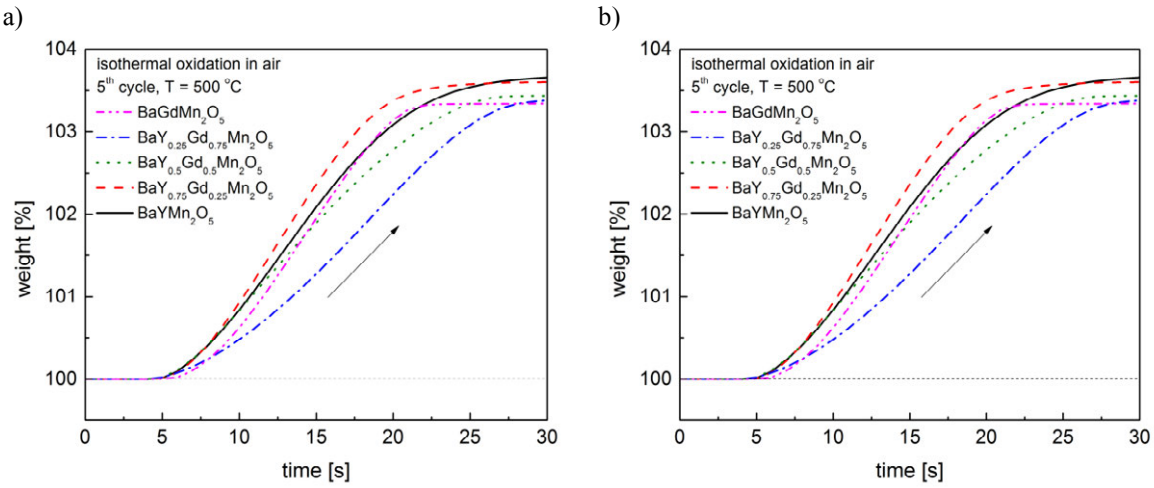

Fig. 8.11. TG data of isothermal a) reduction in 5 vol.% H_2 in Ar, and b) oxidation in synthetic air at 500 °C of $BaY_{1-x}Gd_xMn_2O_{5+\delta}$ materials.

The most important factors from the viewpoint of application of oxygen storage materials, including theoretical oxygen storage capacity, the actual, measured capacity (taken as average values on reduction and oxidation at one cycle), the characteristic temperature of oxidation and also time of isothermal reduction and oxidation at 500 °C are gathered in Tab. 8.6. The measured OSC in $BaY_{1-x}Gd_xMn_2O_{5+\delta}$ series exhibit the same dependence as the theoretical one, it decreases with the increasing level of substituted gadolinium. For all of the studied materials, the measured mass change on reduction and oxidation cycles corresponds to δ changes exceeding 0.97.

Tab. 8.6. Oxygen storage properties of the considered $BaY_{1-x}Gd_xMn_2O_{5+\delta}$ materials. Some results presented also in work [6].

chemical composition	theoretical capacity [wt.%]	measured capacity (5^{th} cycle at 500 °C) [wt.%]	characteristic temperature of oxidation [°C]	time of reduction (99% of total mass change, 5^{th} cycle) [min]	time of oxidation (99% of total mass change, 5^{th} cycle) [s]
$BaY_{0.25}Gd_{0.75}Mn_2O_{5+\delta}$	3.43	3.40	305	9.5	26
$BaY_{0.5}Gd_{0.5}Mn_2O_{5+\delta}$	3.55	3.45	295	10.7	25
$BaY_{0.75}Gd_{0.25}Mn_2O_{5+\delta}$	3.69	3.64	345	9.8	20

8.3.3. Ionic transport in $BaY_{1-x}Gd_xMn_2O_{5+\delta}$

As documented in the Methodology section (chapter 5.5), using reduction time dependence on the temperature presented in Arrhenius-type coordinates, it is possible to evaluate the activation energy of the oxygen transport. In order to do so, isothermal reduction process for all of the considered $BaY_{1-x}Gd_xMn_2O_{5+\delta}$ materials were studied in 400-600 °C temperature range. Results of the measurements are shown in Figs. 8.12a and b.

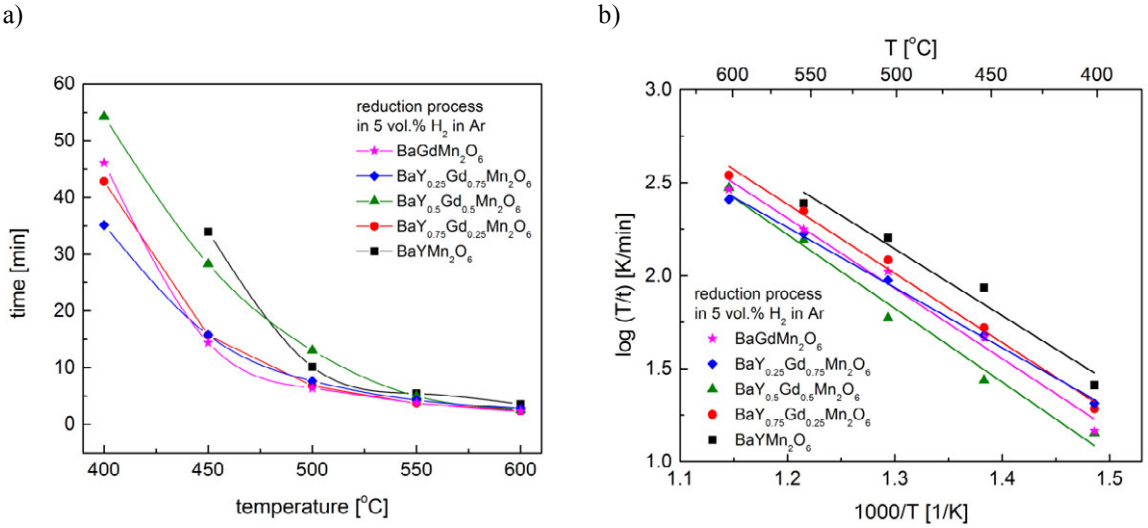

Fig. 8.12. a) Reduction time of the samples as a function of temperature in 400-600 °C temperature range, with b) data presented in Arrhenius-type coordinates.

The reduction time data are also given in Tab. 8.7, with the calculated value of the activation energy. The obtained values are generally similar, being in 0.71-0.88 eV range. The obtained values may be related to the energy barrier of migration of the oxygen ions in the bulk. For more details about estimation of E_a using different assumptions, please see Methodology section.

Tab. 8.7. Time of reduction of the considered $BaY_{1-x}Gd_xMn_2O_{5+\delta}$ materials.

chemical composition	time of reduction [min] at respective temperature calculated for 95% change of total weight change					E_a [eV]
	400 °C	450 °C	500 °C	550 °C	600 °C	
$BaGdMn_2O_{5+\delta}$	46.1	14.4	6.4	3.8	2.3	0.82
$BaY_{0.25}Gd_{0.75}Mn_2O_{5+\delta}$	35.1	15.2	7.7	4.3	2.8	0.71
$BaY_{0.5}Gd_{0.5}Mn_2O_{5+\delta}$	54.3	28.3	13.1	5.0	2.6	0.85
$BaY_{0.75}Gd_{0.25}Mn_2O_{5+\delta}$	42.8	15.7	6.8	3.7	2.4	0.80
$BaYMn_2O_{5+\delta}$	86.5[a]	33.9	10.2	5.5	3.6	0.88

[a]Measurement was stopped due to prolonged time. The value given represents ~ 80% level of reduction.

Corresponding to the reduction time, the recorded oxygen storage capacity values for all studied compounds are gathered in Tab. 8.8. It should be pointed out that the measured OSC exceeds 3.2 wt.% in all of the cases, even at a very low temperature of 400 °C. Analyzing the results, a clear tendency of an increase of OSC with the increase of temperature is visible. What is more, in some of the cases measured OSC exceeds the theoretical value. This effect was already explained, as resulting from additional reduction of the material, with final oxygen content lower than 5.

Tab. 8.8. Oxygen storage capacity for $BaY_{1-x}Gd_xMn_2O_{5+\delta}$ samples at various temperatures.

chemical composition	measured OSC at respective temperatures [wt.%] calculated for 95% change of total weight change					theoretical OSC [wt.%]
	400 °C	450 °C	500 °C	550 °C	600 °C	
$BaGdMn_2O_{5+\delta}$	3.22	3.31	3.33	3.34	3.33	3.30
$BaY_{0.25}Gd_{0.75}Mn_2O_{5+\delta}$	3.30	3.43	3.44	3.46	3.48	3.42
$BaY_{0.5}Gd_{0.5}Mn_2O_{5+\delta}$	3.39	3.50	3.54	3.54	3.53	3.55
$BaY_{0.75}Gd_{0.25}Mn_2O_{5+\delta}$	3.42	3.58	3.60	3.62	3.63	3.69
$BaYMn_2O_{5+\delta}$		3.56	3.61	3.67	3.72	3.85

Chapter 8 summary

The presented results of structural measurements for series of the reduced and the oxidized $BaY_{1-x}Ln_xMn_2O_{5+\delta}$ (Ln: Pr, Sm and Gd, $0 < x < 1$) showed formation of solid solutions in whole chemical composition range, as well as presence of the expected layered-type cation ordering of Ba-$Y_{1-x}Ln_x$. All the reduced materials exhibit tetragonal symmetry with P4/nmm space group at room temperature, which suggest presence of rock salt-type ordering of Mn^{2+} and Mn^{3+} cations. For the corresponding oxidized compounds structural distortion was found to depend on the amount of introduced Pr^{3+}, Sm^{3+} or Gd^{3+} cations, with the widest range of triclinic distortion observed for $BaY_{1-x}Gd_xMn_2O_6$ oxides ($x \leq 0.75$) for the smallest (among studied materials) Gd^{3+} cations present. A significant increase of the unit cell volume upon reduction was measured for all the compounds, matching well the behavior observed for $BaLnMn_2O_{5+\delta}$. Much smaller changes of the unit cell volume as a function of the chemical composition, recorded for the oxidized samples, are also in accordance to the data obtained for $BaLnMn_2O_6$. Oxygen storage-related properties of the substituted $BaY_{1-x}Ln_xMn_2O_{5+\delta}$ were found to depend on the chemical composition. It should be emphasized that because of the similar microstructure of all materials obtained by soft chemistry method, it was possible to elucidate the influence of

the chemical composition on the performance of materials directly. The best reduction characteristics were observed for materials having single step-like reduction curve. This can be interpreted as due to a decreased tendency of formation of the anion-ordered structure of $BaY_{1-x}Ln_xMn_2O_{5.5}$, in which oxygen movement in the bulk may be hindered. While the reversible oxygen storage capacity decreases for samples with yttrium substituted by heavier cations, these materials starts to oxidize at lower temperatures, and some of them exhibit improved reduction behavior. Among the studied materials, oxide with $BaY_{0.75}Pr_{0.25}Mn_2O_{5+\delta}$ composition was found to be the best performing, as the time needed for 99% of its weight change on reduction in 5 vol.% H_2 in Ar at 500 °C decreased from the initial 3.7 min down to about 2.9 min in the 50^{th} reduction/oxidation cycle. Also, excellent stability and reversibility during these 50 cycles was observed. In addition, measurements of the reduction time dependence on temperature allowed to calculate the activation energy of the oxygen transport, which was found to be in 0.71-0.88 eV range.

9. Properties of $Ba_{0.9}Sr_{0.1}Y_{1-x}Ln_xMn_2O_{5+\delta}$ (Ln: Pr, Sm, Gd) oxides

Motivation for a work, which results are gathered in this chapter, was a search for Mn-containing OSM materials, based on the cation-ordered $BaLnMn_2O_{5+\delta}$ and exhibiting improved OSC. As presented in the previous three chapters, the practical, reversible oxygen storage capacity reflects the value of the theoretical one. Consequently, introduction of lighter Sr^{2+} at Ba^{2+} position seems of interest, as it should allow to obtain materials with higher OSC. However, until now there are no reports concerning possibility of such substitution.

Part of the results presented in the following chapters was previously published by author of this thesis in works [192, 193].

9.1. Crystal structure of $Ba_{0.9}Sr_{0.1}Y_{1-x}Ln_xMn_2O_5$ and $Ba_{0.9}Sr_{0.1}Y_{1-x}Ln_xMn_2O_6$ oxides at room temperature

Initially, introduction of Sr^{2+} cations at barium site was checked for various $BaLnMn_2O_{5+\delta}$ and $BaY_{1-x}Ln_xMn_2O_{5+\delta}$ oxides. Even with modifications of the synthesis conditions, it was yielding rather discouraging results, as the materials could not be obtained as single phase ones, with significant amount of secondary phases present. The same problems were faced with trials concerning Ca^{2+} cations. The obtained structural results (not shown here) indicated that the maximum level of substitution of Ba^{2+} by Sr^{2+} is on the order of 10%, while for calcium is practically negligible.

After the initial trials, $Ba_{0.9}Sr_{0.1}YMn_2O_{5+\delta}$, $Ba_{0.9}Sr_{0.1}SmMn_2O_{5+\delta}$, as well as materials having both substitutions, i.e. $Ba_{0.9}Sr_{0.1}Y_{0.75}Pr_{0.25}Mn_2O_{5+\delta}$, $Ba_{0.9}Sr_{0.1}Y_{0.75}Sm_{0.25}Mn_2O_{5+\delta}$, $Ba_{0.9}Sr_{0.1}Y_{0.5}Sm_{0.5}Mn_2O_{5+\delta}$ and $Ba_{0.9}Sr_{0.1}Y_{0.75}Gd_{0.25}Mn_2O_{5+\delta}$ were selected for further studies, due to relatively small amount of secondary phases present. Similarly as in previous chapters, the materials after reduction and oxidation processes were investigated in terms of their crystal structure using XRD method (Figs. 9.1a-f). Relative increase of unit cell volume V after reduction was also calculated, as shown in Fig. 9.2. The obtained data were refined using Rietveld analysis, which results are gathered in Tab. 9.1.

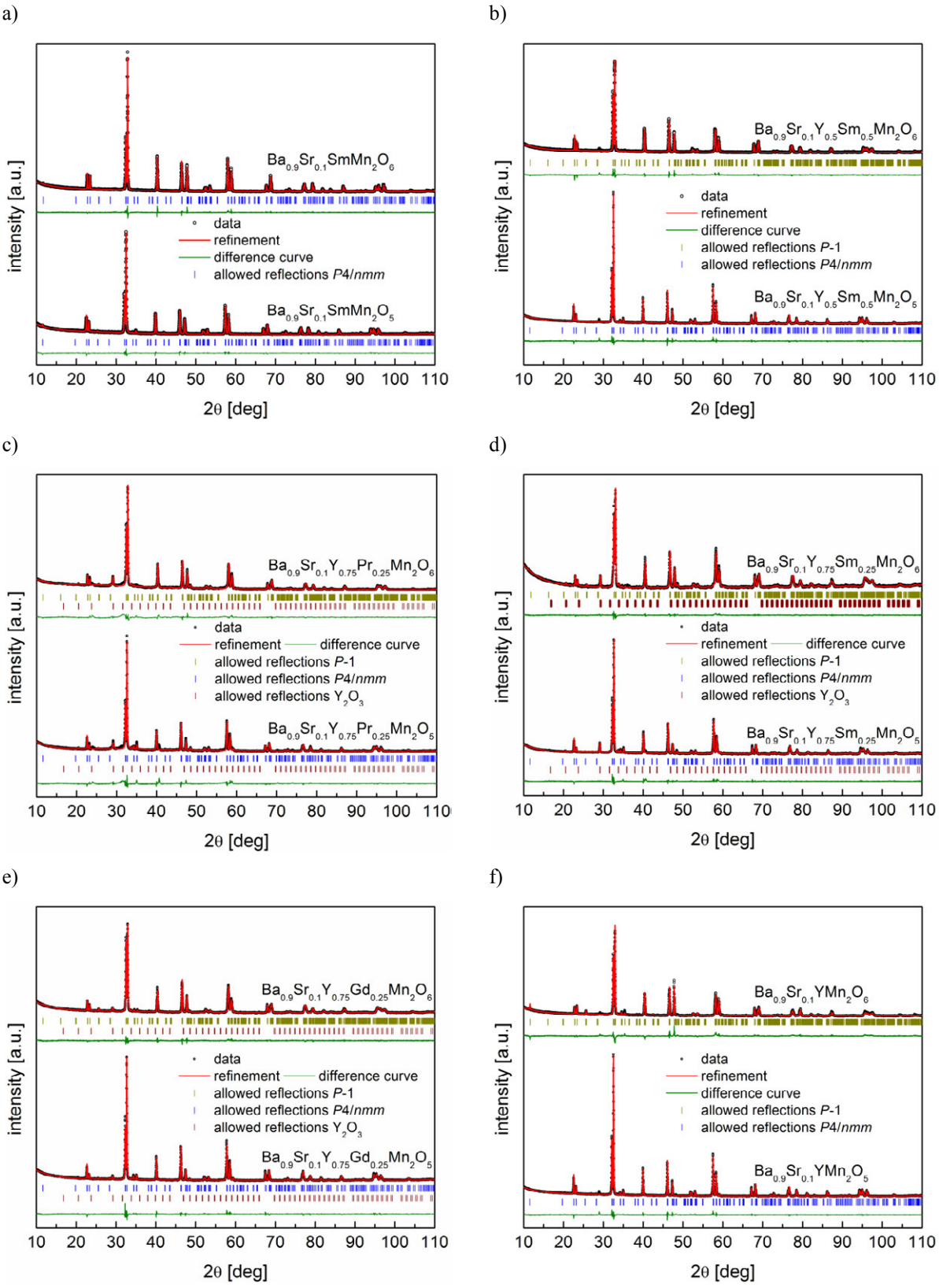

Fig. 9.1. Diffractograms with Rietveld analysis for: a) $Ba_{0.9}Sr_{0.1}SmMn_2O_{5+\delta}$, b) $Ba_{0.9}Sr_{0.1}Y_{0.5}Sm_{0.5}Mn_2O_{5+\delta}$ c) $Ba_{0.9}Sr_{0.1}Y_{0.75}Pr_{0.25}Mn_2O_{5+\delta}$, d) $Ba_{0.9}Sr_{0.1}Y_{0.75}Sm_{0.25}Mn_2O_{5+\delta}$, e) $Ba_{0.9}Sr_{0.1}Y_{0.75}Gd_{0.25}Mn_2O_{5+\delta}$ and f) $Ba_{0.9}Sr_{0.1}YMn_2O_{5+\delta}$, samples in oxidized and reduced state at room temperature.

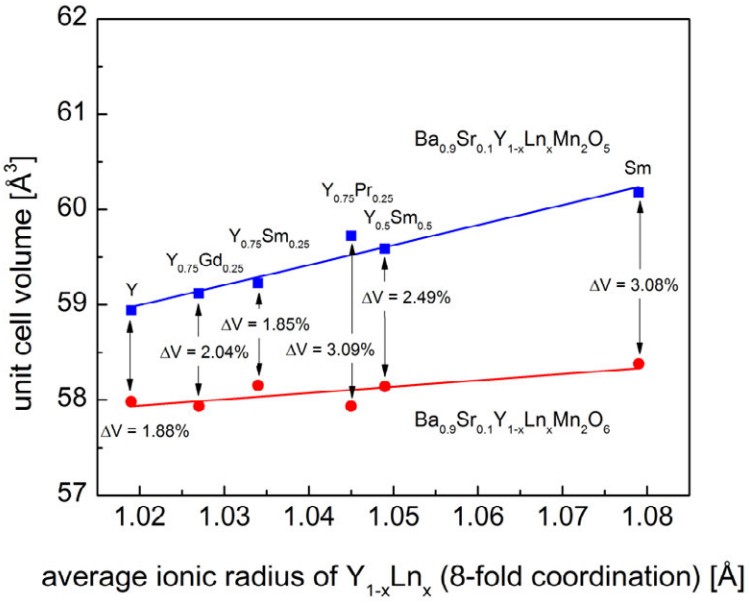

Fig. 9.2. Unit cell volume of $Ba_{0.9}Sr_{0.1}Y_{1-x}Ln_xMn_2O_5$ and $Ba_{0.9}Sr_{0.1}Y_{1-x}Ln_xMn_2O_6$ oxides as a function of average ionic radius of $Y_{1-x}Ln_x$.

Relatively good refinements were obtained assuming tetragonal *P4/nmm* space group for all of the reduced compounds, as could be expected analyzing results for other studied materials. However, presence of unreacted Y_2O_3 was also detected in some of the samples (reduced and oxidized), as indicated in Tab. 9.1. For the oxidized materials triclinic *P*-1 space group was selected and refined with the only exception for $Ba_{0.9}Sr_{0.1}SmMn_2O_6$ oxide, for which no distortion was detected, and the structure could be refined with higher-symmetry *P4/nmm* space group. This is expected trend, concerning data for $BaY_{1-x}Sm_xMn_2O_{5+\delta}$ series (Tabs. 6.1 and 8.3). In all of the considered in this chapter perovskites the layered-type cation ordering in the A-sublattice is maintained.

It should be stated that taking into account presence of the secondary phase (Y_2O_3), which may hinder oxygen storage-related performance, possibility of introduction of only a small amount of strontium to the materials does not open big chances for improvement of the materials. The contamination is expected to lower OSC of $Ba_{0.9}Sr_{0.1}Y_{1-x}Ln_xMn_2O_{5+\delta}$.

In addition, it was found that while the same effect of a substantial increase of the unit cell volume occurs on reduction (Fig. 9.2), the observed dependence deviates somewhat from the very linear behavior found for other studied Mn-containing materials. Nevertheless, also in this case the dependence of V as a function of average ionic radius of $Y_{1-x}Ln_x$ is more pronounced for the reduced materials, comparing to the oxidized ones.

Tab. 9.1. Structural parameters of reduced and oxidized $Ba_{0.9}Sr_{0.1}Y_{1-x}Ln_xMn_2O_{5+\delta}$ oxides with Sr substitution in Ba sublattice. Data presented in [192, 193].

chemical composition	space group	a [Å] b [Å] α [deg] β [deg]	c [Å] γ [deg]	V [Å^3]	relative increase of V after reduction	χ^2	R_{wp} [%]	t_S
$Ba_{0.9}Sr_{0.1}SmMn_2O_5$	*P*4/*nmm*	5.5889(1)	7.7062(1)	240.71(1)	3.08	2.24	2.90	0.973
$Ba_{0.9}Sr_{0.1}SmMn_2O_6$	*P*4/*nmm*	5.5356(1)	7.6205(1)	233.52(1)		2.70	3.10	0.976
$Ba_{0.9}Sr_{0.1}Y_{0.5}Sm_{0.5}Mn_2O_5$	*P*4/*nmm*	5.5702(1)	7.6823(1)	238.36(1)	2.49	3.89	3.59	0.981
$Ba_{0.9}Sr_{0.1}Y_{0.5}Sm_{0.5}Mn_2O_6$	*P*-1	5.5260(1) 5.5279(1) 90.00(1) 90.21(1)	7.6136(1) 90.04(1)	232.57(1)		4.18	3.71	0.971
$Ba_{0.9}Sr_{0.1}Y_{0.75}Pr_{0.25}Mn_2O_5$ ~ 10 wt.% of Y_2O_3	*P*4/*nmm*	5.5735(1)	7.6901(1)	238.89(1)	3.09	7.52	4.80	0.968
$Ba_{0.9}Sr_{0.1}Y_{0.75}Pr_{0.25}Mn_2O_6$ ~ 10 wt.% of Y_2O_3	*P*-1	5.5290(1) 5.5285(1) 90.01(1) 90.18(1)	7.6157(1) 90.12(1)	231.74(1)		5.29	3.77	0.972
$Ba_{0.9}Sr_{0.1}Y_{0.75}Sm_{0.25}Mn_2O_5$ ~ 7 wt.% of Y_2O_3	*P*4/*nmm*	5.5566(1)	7.6729(1)	236.91(1)	1.85	3.40	3.23	0.965
$Ba_{0.9}Sr_{0.1}Y_{0.75}Sm_{0.25}Mn_2O_6$ ~ 7 wt.% of Y_2O_3	*P*-1	5.5235(1) 5.5229(1) 90.29(1) 90.13(1)	7.6253(1) 89.97(1)	232.61(1)		2.86	3.28	0.969
$Ba_{0.9}Sr_{0.1}Y_{0.75}Gd_{0.25}Mn_2O_5$ ~ 4 wt.% of Y_2O_3	*P*4/*nmm*	5.5530(1)	7.6689(1)	236.47(1)	2.04	2.53	2.89	0.964
$Ba_{0.9}Sr_{0.1}Y_{0.75}Gd_{0.25}Mn_2O_6$ ~ 4 wt.% of Y_2O_3	*P*-1	5.5167(1) 5.5158(1) 89.98(1) 90.31(1)	7.6157(1) 90.12(1)	231.74(1)		1.80	2.35	0.967
$Ba_{0.9}Sr_{0.1}YMn_2O_5$	*P*4/*nmm*	5.5486(1) 5.5486(1)	7.6577(1)	235.76(1)	1.88	4.13	3.56	0.963
$Ba_{0.9}Sr_{0.1}YMn_2O_6$	*P*-1	5.5141(1) 5.5123(1) 89.98(1) 90.31(1)	7.6127(1) 90.12(1)	231.39(1)		3.47	3.26	0.966

9.2. Microstructure of $Ba_{0.9}Sr_{0.1}Y_{1-x}Ln_xMn_2O_{5+\delta}$ powders

As could be expected from the structural results, presence of the secondary Y_2O_3 phase was confirmed during SEM observations. Exemplary micrographs recorded for the reduced and the oxidized $Ba_{0.9}Sr_{0.1}Y_{0.75}Pr_{0.25}Mn_2O_{5+\delta}$ are shown in Figs. 9.3a and b. The secondary phase was confirmed by EDX studies, and is visible in a form of additional precipitates, which are attached to the grains of the main phase.

a) $Ba_{0.9}Sr_{0.1}Y_{0.75}Pr_{0.25}Mn_2O_5$ b) $Ba_{0.9}Sr_{0.1}Y_{0.75}Pr_{0.25}Mn_2O_6$

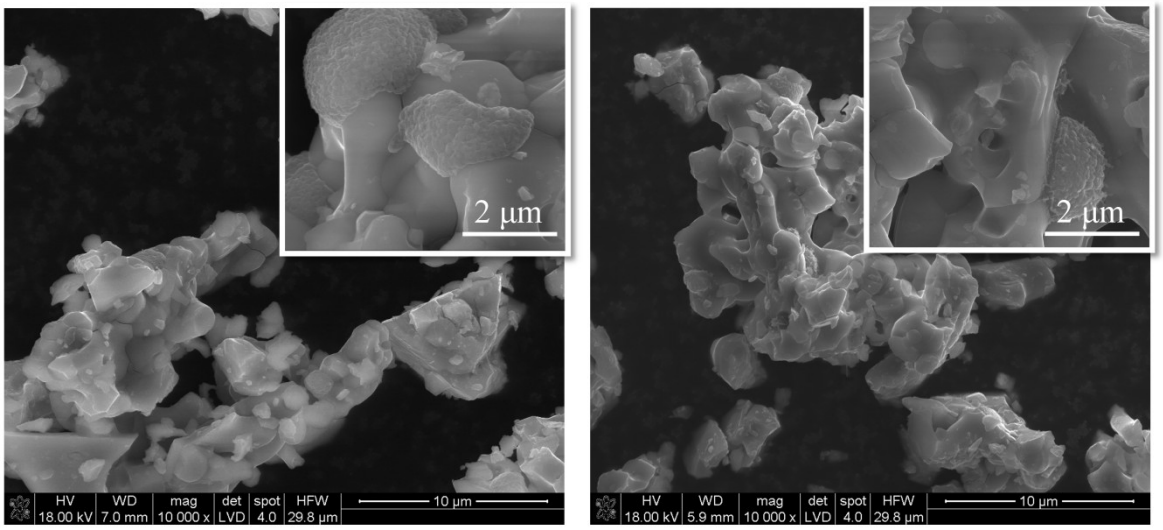

Fig. 9.3. SEM micrographs for a) the reduced and b) the oxidized $Ba_{0.9}Sr_{0.1}Y_{0.75}Pr_{0.25}Mn_2O_{5+\delta}$.

9.3. Oxygen storage properties

Behavior of the oxidized materials during reduction in 5 vol.% H_2 in Ar, as well as the reduced materials in air atmosphere while the temperature was increased up to 500 °C was investigated similarly like for other considered in this work OSMs, and the results are depicted in Figs. 9.3a and b. In terms of the reduction process, $Ba_{0.9}Sr_{0.1}SmMn_2O_6$ exhibits characteristic inflection of the curve, approximately in the middle of the reached capacity, similar to the one observed for sample without strontium substitution (Fig. 6.16c). Curve recorded for $Ba_{0.9}Sr_{0.1}Y_{0.5}Sm_{0.5}Mn_2O_6$ is also inflected, but surprisingly, the slope increases in the second part of reduction. This is unexpected behavior, which origin is unknown. In addition, this is the only compound in the studied series, which is fully reduced before reaching 500 °C.

Oxidation process, however, for all studied compounds starts at different temperature, and based on the performance, two groups of materials can be selected. In the first one that includes $Ba_{0.9}Sr_{0.1}SmMn_2O_{5+\delta}$, $Ba_{0.9}Sr_{0.1}Y_{0.75}Gd_{0.25}Mn_2O_{5+\delta}$ as well as $Ba_{0.9}Sr_{0.1}YMn_2O_{5+\delta}$, the oxidation occurs in one sharp step. In the second group, at higher temperatures (above the main weight increase) further oxidation takes place. Unfortunately, there is clear dependence observed regarding temperatures of oxidation or reduction on the chemical substitution or average ionic radius of $Y_{1-x}Ln_x$.

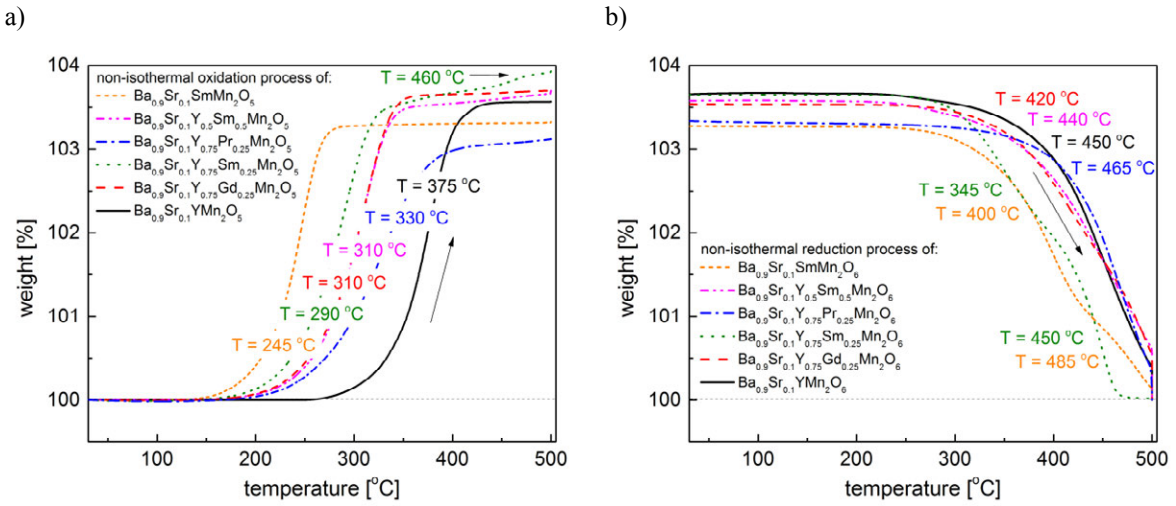

Fig. 9.4. Non-isothermal a) reduction and b) oxidation of $Ba_{0.9}Sr_{0.1}Y_{1-x}Ln_xMn_2O_{5+\delta}$. Data from [192, 193].

Isothermal studies of reduction and oxidation speed were conducted at 500 °C, and results of the experiments are presented in Figs. 9.5a and b, respectively. All of the considered materials exhibit fast speed of oxidation, but rather low speed of reduction, lower than the reference $BaYMn_2O_{5+\delta}$ oxide. The only exception is material with $Ba_{0.9}Sr_{0.1}Y_{0.75}Sm_{0.25}Mn_2O_{5+\delta}$ composition, for which the initial part of the reduction curve is very steep, and while some inflection is visible in the second part, a decrease of the reduction speed in this range is not so high. As OSC of this material is also relatively high, it was selected for more throughout evaluation concerning the cycling performance, as presented in chapter below. Systematic comparison of the measured oxygen storage properties is given in Tab. 9.2.

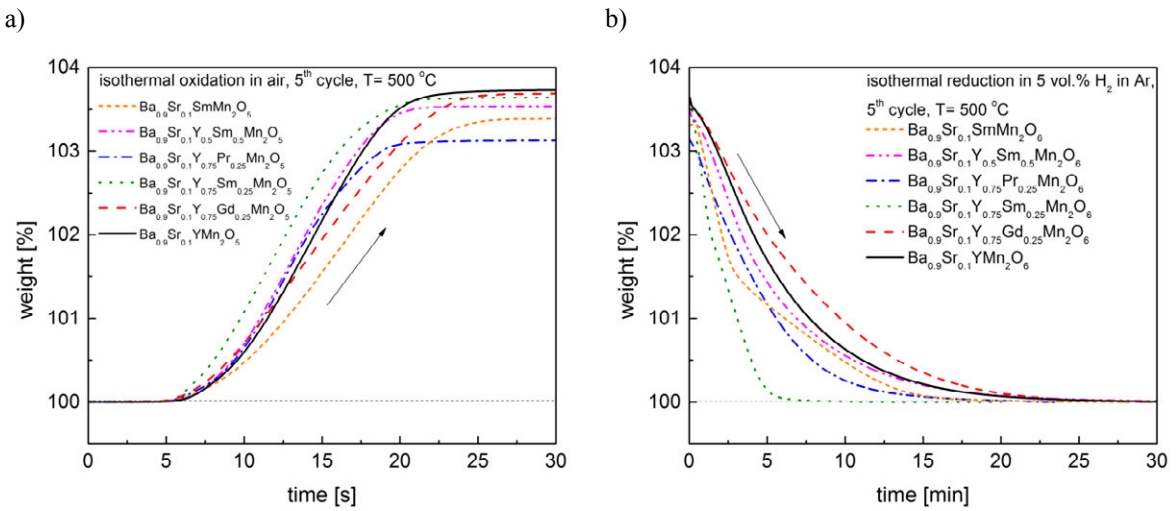

Fig. 9.5. Isothermal a) reduction in 5 vol.% H_2 in Ar and b) oxidation in synthetic air at 500 °C of the evaluated $Ba_{0.9}Sr_{0.1}Y_{1-x}Ln_xMn_2O_{5+\delta}$ materials. Despite longer total time for the samples, oxidation data shown in selected range, to keep it consistent with previous figures. Some data from [192, 193].

Tab. 9.2. Oxygen storage properties of the considered $Ba_{0.9}Sr_{0.1}Y_{1-x}Ln_xMn_2O_{5+\delta}$ materials.

chemical composition	theoretical OSC [wt.%]	measured OSC (5^{th} cycle at 500 °C) [wt.%]	characteristic temperature of oxidation [°C]	characteristic temperature of reduction [°C]	time of reduction (99% of total mass change, 5^{th} cycle) [min]	time of oxidation (99% of total mass change, 5^{th} cycle) [s]
$Ba_{0.9}Sr_{0.1}SmMn_2O_{5+\delta}$	3.39	3.43	245	400, 485	17.5	42
$Ba_{0.9}Sr_{0.1}Y_{0.5}Sm_{0.5}Mn_2O_{5+\delta}$	3.62	5.62	310	440	24.1	250
$Ba_{0.9}Sr_{0.1}Y_{0.75}Pr_{0.25}Mn_2O_{5+\delta}$	3.77	3.23	330	465	17.8	320
$Ba_{0.9}Sr_{0.1}Y_{0.75}Sm_{0.25}Mn_2O_{5+\delta}$	3.75	3.72	290, 460	345, 485	6.4	83
$Ba_{0.9}Sr_{0.1}Y_{0.75}Gd_{0.25}Mn_2O_{5+\delta}$	3.74	3.72	310	420	23.7	43
$Ba_{0.9}Sr_{0.1}YMn_2O_{5+\delta}$	3.89	3.78	375	450	22.9	38

It can be stated that while some improvement of the OSC was attained (e.g. for $Ba_{0.9}Sr_{0.1}YMn_2O_{5+\delta}$), unfortunately, introduction of Sr^{2+} cations worsens the oxygen storage-related properties of the materials.

9.4. Cycling performance of $Ba_{0.9}Sr_{0.1}Y_{0.75}Sm_{0.25}Mn_2O_{5+\delta}$

Reduction/oxidation performance tests of 20 consecutive cycles were conducted for $Ba_{0.9}Sr_{0.1}Y_{0.75}Sm_{0.25}Mn_2O_5$, as presented in Fig. 9.6a. The studies revealed that stability of the material in working conditions is good, and after some decreas of the measured OSC in the first few cycles, the material stabilizes in terms of the oxygen storage capacity. It is worth to emphasize that the speed of reduction increases during consecutive cycles. In this particular case, between first and twentieth cycle, the reduction is accelerated by about two minutes. Interestingly, the effect mainly arises from diminishing inflection in the second part of the reduction curve (Fig. 9.6b).

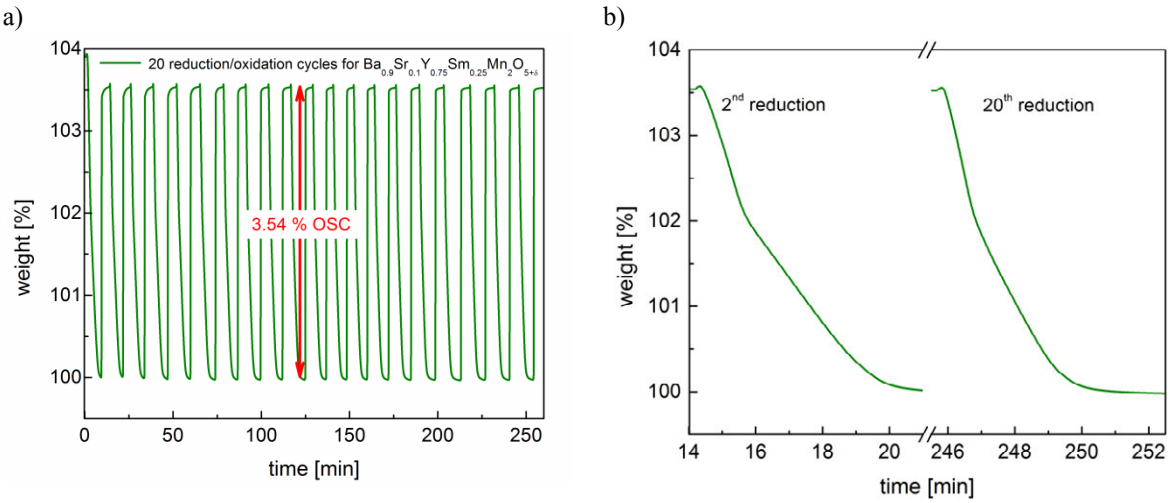

Fig. 9.6. a) Reversibility of weight changes of $Ba_{0.9}Sr_{0.1}Y_{0.75}Sm_{0.25}O_{5+\delta}$ during 20 reduction/oxidation cycles, b) data for 2nd and 20th reduction. Published in [192].

9.5. Ionic transport in selected $Ba_{0.9}Sr_{0.1}Y_{1-x}Ln_xMn_2O_{5+\delta}$

In a similar way as presented in chapter 8.3.3, for further investigations, measurements of the reduction kinetics were conducted in 400-600 °C temperature range. The results are presented directly in Fig. 9.7a, and in Arrhenius-type coordinates in Fig. 9.7b. Systematic data with the calculated activation energy of the ionic transport are given in Tab. 9.3.

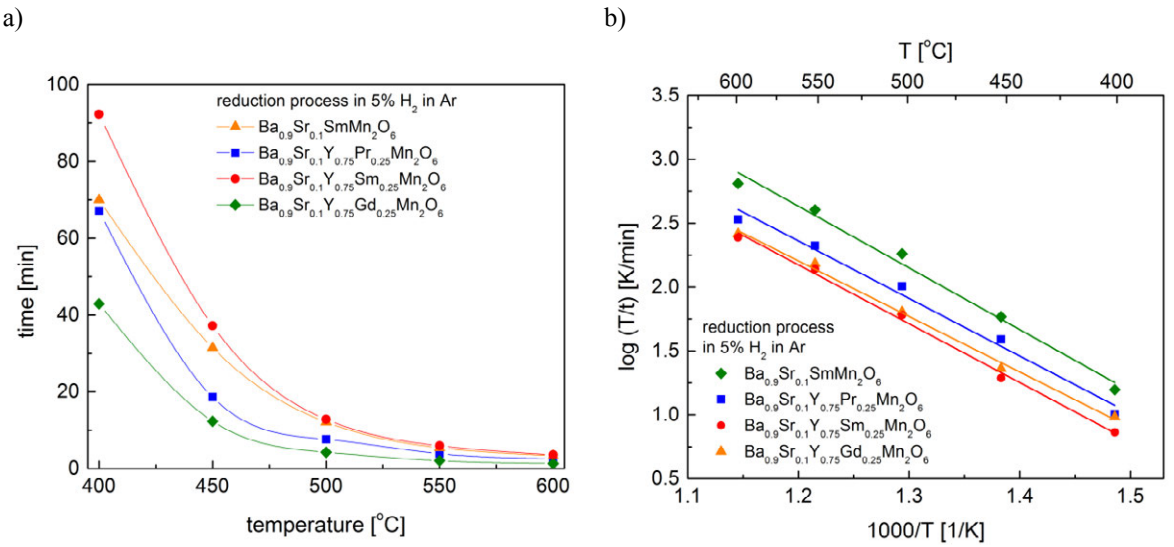

Fig. 9.7. Reduction time of the samples as a function of temperature in 400-600 °C temperature range, with b) data presented in Arrhenius-type coordinates.

Tab. 9.3. Time of reduction of the considered $Ba_{0.9}Sr_{0.1}LnMn_2O_{5+\delta}$.

chemical composition	time of reduction [min] at respective temperature calculated for 95% change of total weight change					E_a [eV]
	400 °C	450 °C	500 °C	550 °C	600 °C	
$Ba_{0.9}Sr_{0.1}SmMn_2O_{5+\delta}$	70.0	31.5	12.1	5.4	3.3	0.73
$Ba_{0.9}Sr_{0.1}Y_{0.75}Pr_{0.25}Mn_2O_{5+\delta}$	67.2	18.6	7.6	3.9	2.6	0.76
$Ba_{0.9}Sr_{0.1}Y_{0.75}Sm_{0.25}Mn_2O_{5+\delta}$	42.9	12.4	4.3	2.0	1.4	0.82
$Ba_{0.9}Sr_{0.1}Y_{0.75}Gd_{0.25}Mn_2O_{5+\delta}$	92.3	37.2	12.8	6.0	3.6	0.78

As can be seen in Tab. 9.3, the calculated activation energy is similar (0.73-0.82 eV), comparing to the values obtained for $BaY_{1-x}Gd_xMn_2O_{5+\delta}$ series (Tab. 8.7).

Nevertheless, with an increase of the temperature, the measured oxygen storage capacity was found to also increase (Tab. 9.4), and in some of the cases even above the theoretical limit. However, it this case a possible explanation is that the effect originates also from a partial decomposition of the material, and not only from the excessive reduction (below oxygen content equal 5). Such assumption is supported by a general weight change decrease visible on the TG curves in the following cycles, not reaching the initial values.

Tab. 9.4. Oxygen storage capacity for considered $Ba_{0.9}Sr_{0.1}LnMn_2O_{5+\delta}$ at various temperatures.

chemical composition	measured capacity [wt.%] at respective temperatures calculated for 95% change of total weight change					theoretical OSC [wt.%]
	400 °C	450 °C	500 °C	550 °C	600 °C	
$Ba_{0.9}Sr_{0.1}SmMn_2O_{5+\delta}$	3.25	3.36	3.38	3.39	3.47	3.39
$Ba_{0.9}Sr_{0.1}Y_{0.75}Pr_{0.25}Mn_2O_{5+\delta}$	3.18	3.26	3.31	3.37	3.41	3.77
$Ba_{0.9}Sr_{0.1}Y_{0.75}Sm_{0.25}Mn_2O_{5+\delta}$	3.70	3.75	3.75	3.80	3.83	3.75
$Ba_{0.9}Sr_{0.1}Y_{0.75}Gd_{0.25}Mn_2O_{5+\delta}$	3.05	3.57	3.60	3.62	3.62	3.74

Chapter 9 summary

It was found that the synthesis process in the case of many samples with strontium introduced at the Ba^{2+} site is very difficult, mainly due to a narrow range of formation of solid solutions, on the order on 0.1 mol per mol of the compound. The materials are mainly contaminated by presence of Y_2O_3 secondary phase. However, it was possible to synthesize single phase cation-ordered $Ba_{0.9}Sr_{0.1}Y_{0.5}Sm_{0.5}Mn_2O_{5+\delta}$. When considering oxygen storage-related properties, strontium substituted materials exhibit no clear dependence of any of the parameters on the chemical composition, and while some improvement of the OSC may be achieved, the reduction kinetics of the samples are rather slow. Nevertheless, relatively good performance was observed for $Ba_{0.9}Sr_{0.1}Y_{0.75}Sm_{0.25}Mn_2O_{5+\delta}$ compound.

10. Properties of Co- and Fe-containing perovskite-type oxides

The described results for series of manganese-containing materials (chapters 6-9) showed possibility of enhancement of the oxygen storage-related properties of $BaLnMn_2O_{5+\delta}$-type of compounds, but mainly in terms of the reduction speed and characteristic temperature of oxidation or reduction. At the same time, the attempted trials concerning improvement of the oxygen storage capacity were not successful, and the OSC was found to be restricted by the theoretical capacity of $BaYMn_2O_{5+\delta}$ oxide (3.85 wt.%), as substitution of lighter strontium in Ba-sublattice is problematic. Motivation of the presented in this chapter work was to investigate properties of the alternative group of oxides, which may allow to cross 4 wt.% barrier of the practical, reversible OSC. Part of the results presented below, concerning properties of selected Co- and Fe-containing perovskites was previously published by author of this thesis in work [194].

10.1. Crystal structure of reduced and oxidized Co- and Fe-containing perovskite-type oxides at room temperature

Selected, synthesized materials with $La_{0.6}Sr_{0.4}Co_{0.8}Fe_{0.2}O_{3-\delta}$, $La_{0.5}Sr_{0.5}Co_{0.5}Fe_{0.5}O_{3-\delta}$, $Sm_{0.5}Sr_{0.5}Co_{0.5}Fe_{0.5}O_{3-\delta}$, $La_{0.5}Ba_{0.5}Co_{0.5}Fe_{0.5}O_{3-\delta}$ and $Sm_{0.5}Ba_{0.5}Co_{0.5}Fe_{0.5}O_{3-\delta}$ chemical composition after oxidation and reduction were analyzed in terms of their crystal structure using Rietveld method. The recorded diffractograms with the refinements for the oxidized and the reduced materials are presented in Figs. 10.1a-e. The obtained during fitting structural parameters are gathered in Tab. 10.1.

In the case of the oxidized $La_{0.6}Sr_{0.4}Co_{0.8}Fe_{0.2}O_3$ and $La_{0.5}Sr_{0.5}Co_{0.5}Fe_{0.5}O_3$, using literature data from neutron diffraction studies [195], monoclinic $I12/c1$ space group was chosen for the refinement. As it was expected, unit cell volume, when normalized to the simple perovskite one (divided by 8 in this case) is very similar for both compounds. When reduced in 5 vol.% H_2 in Ar at 500 °C, both materials transform into brownmillerite-type phase (Fig. 4.11), which is highly unstable even at room temperature in the air atmosphere, and the materials start to slowly oxidize, resulting in a formation of two phase mixture of reduced brownmillerite-type and oxidized perovskite-type phases.

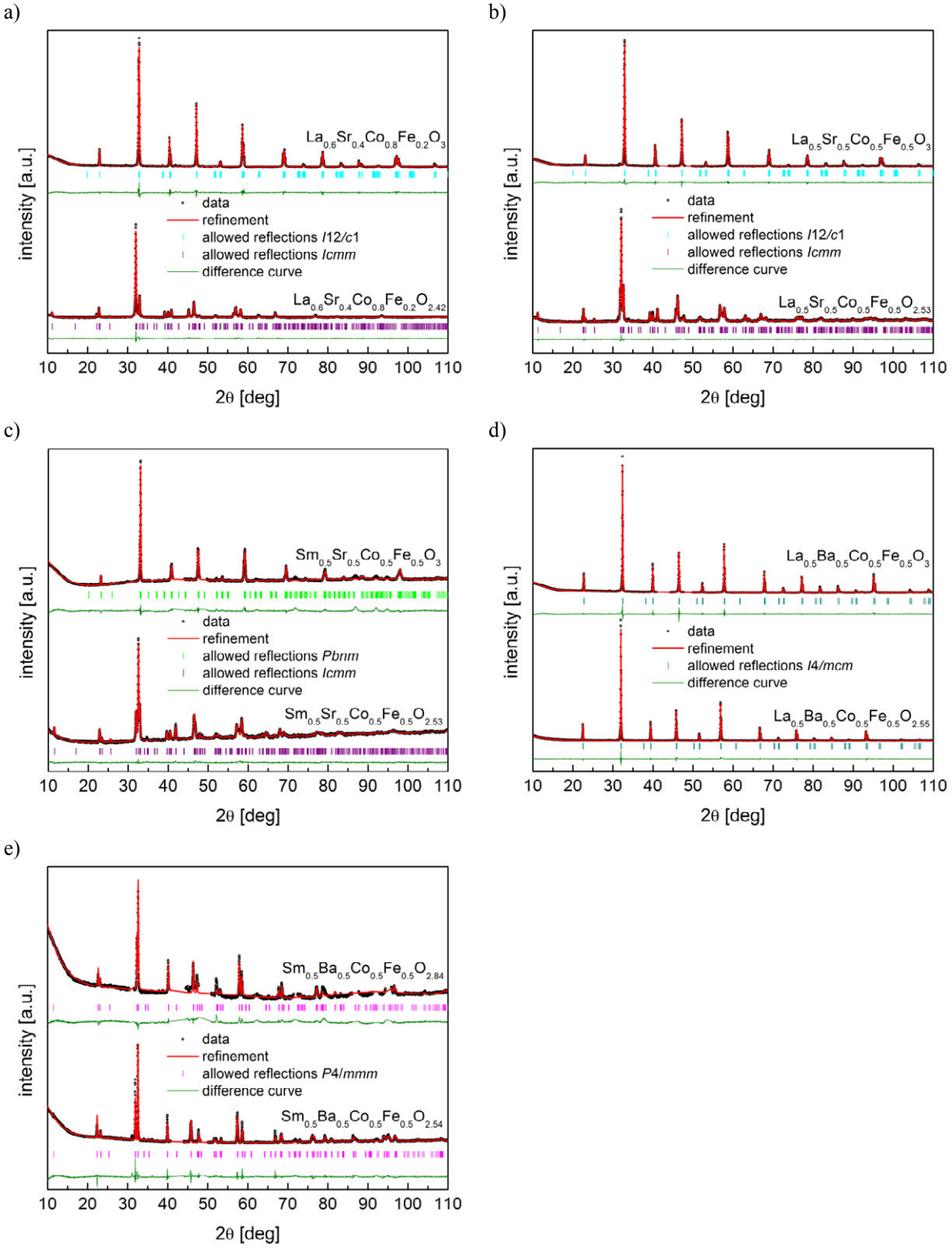

Fig. 10.1. Diffractograms with Rietveld analysis for a) $La_{0.6}Sr_{0.4}Co_{0.8}Fe_{0.2}O_{3-\delta}$, b) $La_{0.5}Sr_{0.5}Co_{0.5}Fe_{0.5}O_{3-\delta}$, c) $Sm_{0.5}Sr_{0.5}Co_{0.5}Fe_{0.5}O_{3-\delta}$, d) $La_{0.5}Ba_{0.5}Co_{0.5}Fe_{0.5}O_{3-\delta}$ and e) $Sm_{0.5}Ba_{0.5}Co_{0.5}Fe_{0.5}O_{3-\delta}$ samples in oxidized and reduced forms recorded at room temperature. Angular range with holder-related peaks was excluded for some of the materials.

Tab. 10.1. Structural parameters of reduced and oxidized Fe- and Co-containing perovskite-type oxides. Data from [194].

chemical composition	space group	a [Å] b [Å] β [deg]	c [Å]	normalized V [Å^3]	R_{wp} [%]	χ^2	relative increase of V after reduction [%]
$La_{0.6}Sr_{0.4}Co_{0.8}Fe_{0.2}O_{2.42}$[c]	*Icmm*	5.6157(2) 16.0644(5)	5.4491(1)	61.45(1)[d]	1.73	2.08	8.0
$La_{0.6}Sr_{0.4}Co_{0.8}Fe_{0.2}O_3$[a]	*I*12/*c*1	5.4158(1) 5.4382(1) 90.30(1)	7.6815(1)	56.56(1)	2.21	3.59	
$La_{0.5}Sr_{0.5}Co_{0.5}Fe_{0.5}O_{2.53}$[c]	*Icmm*	5.6225(1) 15.9060(4)	5.5048(1)	61.78(1)[d]	6.70	0.83	7.5
$La_{0.5}Sr_{0.5}Co_{0.5}Fe_{0.5}O_3$[a]	*I*12/*c*1	5.4393(1) 5.4523(1) 90.25(1)	7.7084(1)	57.15(1)	1.95	2.81	
$Sm_{0.5}Sr_{0.5}Co_{0.5}Fe_{0.5}O_{2.53}$[c]	*Icmm*	5.6293(2) 15.5820(7)	5.4648(2)	59.92(1)[d]	1.59	1.44	6.9
$Sm_{0.5}Sr_{0.5}Co_{0.5}Fe_{0.5}O_3$[a]	*Pbnm*	5.3948(1) 5.4254(1)	7.6275(1)	55.81(1)	3.00	5.99	
$La_{0.5}Ba_{0.5}Co_{0.5}Fe_{0.5}O_{2.55}$[c]	*I*4/*mcm*	5.6163(1)	7.9384(2)	62.60(1)	2.73	2.77	4.9
$La_{0.5}Ba_{0.5}Co_{0.5}Fe_{0.5}O_3$[a]	*I*4/*mcm*	5.5238(1)	7.8086(1)	59.56(1)	3.54	6.28	
$Sm_{0.5}Ba_{0.5}Co_{0.5}Fe_{0.5}O_{2.54}$[c]	*P*4/*mmm*	3.9489(1)	7.6035(2)	59.28(1)	4.58	6.43	1.3
$Sm_{0.5}Ba_{0.5}Co_{0.5}Fe_{0.5}O_{2.84}$[a]	*P*4/*mmm*	3.9069(2)	7.6627(5)	58.48(1)	8.04	7.38	

[a]Oxygen stoichiometry data from [196]. [b]Small amount (~ 8 wt.%) of rhombohedral *R*-3*c* phase was detected. [c]Data calculated from TG measurements. [d]Unit cell volume was divided by 8.

In the case of $Sm_{0.5}Sr_{0.5}Co_{0.5}Fe_{0.5}O_{3-\delta}$ compound, reduced material exhibits brownmillerite-type *Icmm* structure and transforms into orthorhombic *Pbnm* upon oxidation, resulting in a change of the unit cell volume of 6.9%. Regarding $La_{0.5}Ba_{0.5}Co_{0.5}Fe_{0.5}O_{3-\delta}$ composition, it can be well refined assuming tetragonal *I*4/*mcm* space group for both, reduced and oxidized compounds, indicating no phase transition upon oxidation, while the unit cell volume changes about 4.9%. No phase transition upon oxidation is also likely in the case of $Sm_{0.5}Ba_{0.5}Co_{0.5}Fe_{0.5}O_{3-\delta}$, due to presence of the same space group (*P*4/*mmm*) for reduced and oxidized compounds. Interestingly, structure of this material exhibits the same layered-type of Ba^{2+} and Sm^{3+} cation ordering, as it was observed in the studied $BaLnMn_2O_{5+\delta}$ (chapters 6-9). Large difference ionic radii of samarium and barium seems to be the main factor responsible for such the ordering. At the same time there is not structural or charge ordering in the Co-Fe sublattice, and the materials possesses aristotype *P*4/*mmm* symmetry. To keep it consistent within this chapter, although $AA'B_2O_{5+\delta}$ notation is more appropriate for this compound, notation typical for

the disordered perovskite-type materials is used. It is worth mentioning, that the oxygen change, calculated using data from thermogravimetric experiments, is quite low for this material, being equal to 0.3 (or 0.6 per double perovskite formula unit). On the other hand it can be much higher, and for example for $La_{0.6}Sr_{0.4}Co_{0.8}Fe_{0.2}O_{3-\delta}$ can exceed 0.55 (or 1.1 per double perovskite formula unit, see Tab. 10.1). This behavior is different comparing to the studied manganese-containing oxides, and may originate from difference of the intrinsic properties of manganese, iron and cobalt elements, which prefer different oxidation states, while present in the oxides. For example, presence of high amounts of Co^{4+} and Fe^{4+} cations is not very common in most of the perovskite-type oxides, and even if so, very high oxygen partial pressure or electrochemical intercalation of the oxygen into the materials are required for all Co and Fe to adopt +4 oxidation state [195]. On the other hand, Mn^{4+} oxidation state is well known and is often observed.

It seems that crystal structure of the considered materials also plays an important role regarding oxygen storage capacity, with the ordered structure hindering the incorporation of the oxygen up to the fully oxidized state. At the same time, the disordered structure of other studied in this chapter perovskites, which allows for statistical formation of the oxygen vacancies, seems more suitable for Fe- and Co-containing perovskites from the point of view of the oxygen storage.

10.2. In situ structural measurements

High temperature XRD studies, due to the fact, that oxidation process occurs very fast in elevated temperatures, were conducted as very fast scans, of only about 1 minute long and consequently, the angular range was limited down to 20-60 deg. Figs. 10.2-10.5 presents in part “a” structural evolution of the reduced compounds during oxidation in air and in part “b” behavior of the oxidized sample during heating in air. Data are shown for selected angular range (31.5-33.5 deg).

While heating of the reduced $La_{0.6}Sr_{0.4}Co_{0.8}Fe_{0.2}O_{2.42}$ in air, firstly only a slight shift of the main reflection into lower angles occurs, and it can be associated with thermal expansion only. In the temperature range of 100 °C up to ~ 200 °C, position of the peak remains almost the same. The average thermal expansion of the material is very low, with $TEC_{25\text{-}200°C} = 3.8 \cdot 10^{-6}\ K^{-1}$, which may be connected with a partial oxidation of the

brownmillerite phase already ongoing. With further increase of the temperature, oxidation takes place and is visible on the Fig. 10.2a as a disappearance of the brownmillerite-related peak, and at the same time, as an appearance of the reflection associated with the perovskite-type phase. In the vicinity of the transition temperature intensity of visible peaks is low, showing that the ongoing oxidation affects crystal structure of the material, lowering structural coherence length. In this region, for the XRD data refinements presence of two phases (reduced *Icma* and oxidized *I*12/*c*1 phase) was assumed. In the temperature range of 230-275 °C additional oxidation of the perovskite phase likely takes place. Data of the temperature behavior of the oxidized $La_{0.6}Sr_{0.4}Co_{0.8}Fe_{0.2}O_3$ is presented in Fig. 10.2b, showing only a slight shift of the main reflection towards lower angles, which is associated with thermal expansion of the material. If results for both of the cases are compared at the temperature of 300 °C, it can be noticed that the diffractograms are almost the same, which indicates that the starting $La_{0.6}Sr_{0.4}Co_{0.8}Fe_{0.2}O_{2.42}$ material is fully oxidized at this temperature, and the actual oxygen content in the material is equal to 3.

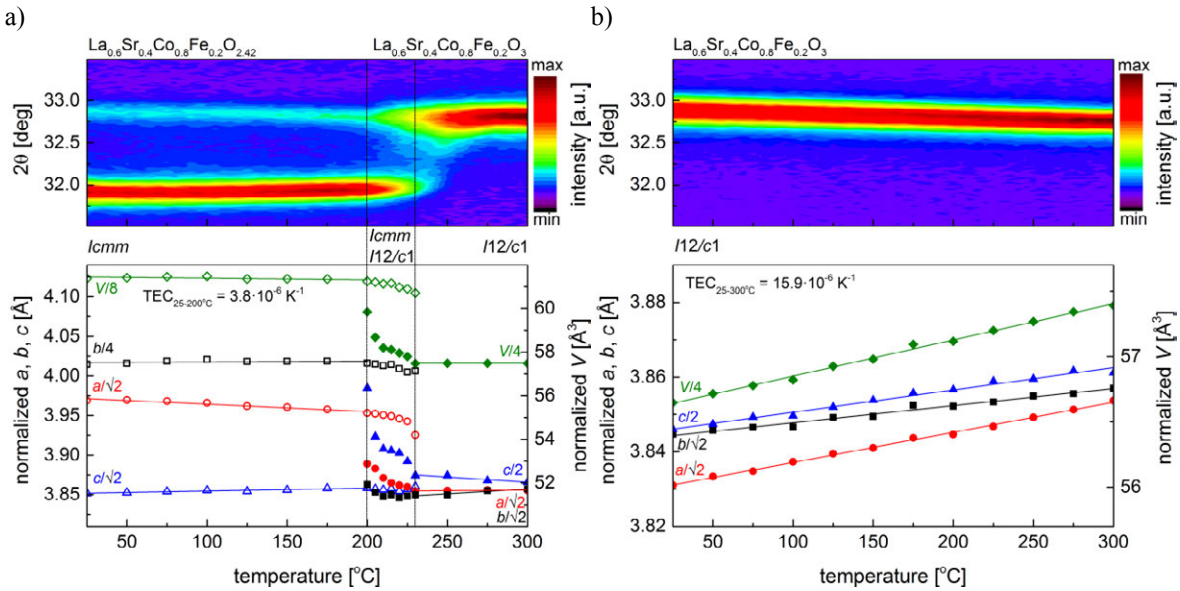

Fig. 10.2. Structural evolution and temperature dependence of normalized unit cell parameters and volume, together with calculated thermal expansion coefficients for a) reduced $La_{0.6}Sr_{0.4}Co_{0.8}Fe_{0.2}O_{2.42}$ and b) oxidized $La_{0.6}Sr_{0.4}Co_{0.8}Fe_{0.2}O_3$ sample during heating in air. Data shown for selected angular range.

Similar behavior was observed for the reduced $La_{0.5}Sr_{0.5}Co_{0.5}Fe_{0.5}O_{2.53}$ (Fig. 10.3a). At low temperatures no changes apart from thermal expansion are recorded, then, a partial oxidation takes place, and in the intermediate region, with low intensity of the peaks, brownmillerite-perovskite transformation occurs. Finally, strong shift of the main peak of the perovskite-type phase in temperature range of 125-190 °C takes place, which can be

linked to the oxidation of the perovskite phase. At higher temperatures only thermal expansion-related shift of the peaks towards lower angles is visible. Temperature dependence of the normalized unit cell parameters and volume (also in the two-phase range), together with calculated thermal expansion coefficient are also presented in Fig. 10.3a.

Equivalent data for the oxidized $La_{0.5}Sr_{0.5}Co_{0.5}Fe_{0.5}O_3$ are presented in Fig. 10.3b, and the obtained results are the same like for the described above $La_{0.6}Sr_{0.4}Co_{0.8}Fe_{0.2}O_3$ oxide. What is more, thermal expansion coefficients of oxidized $La_{0.5}Sr_{0.5}Co_{0.5}Fe_{0.5}O_3$ and $La_{0.6}Sr_{0.4}Co_{0.8}Fe_{0.2}O_3$ materials are alike.

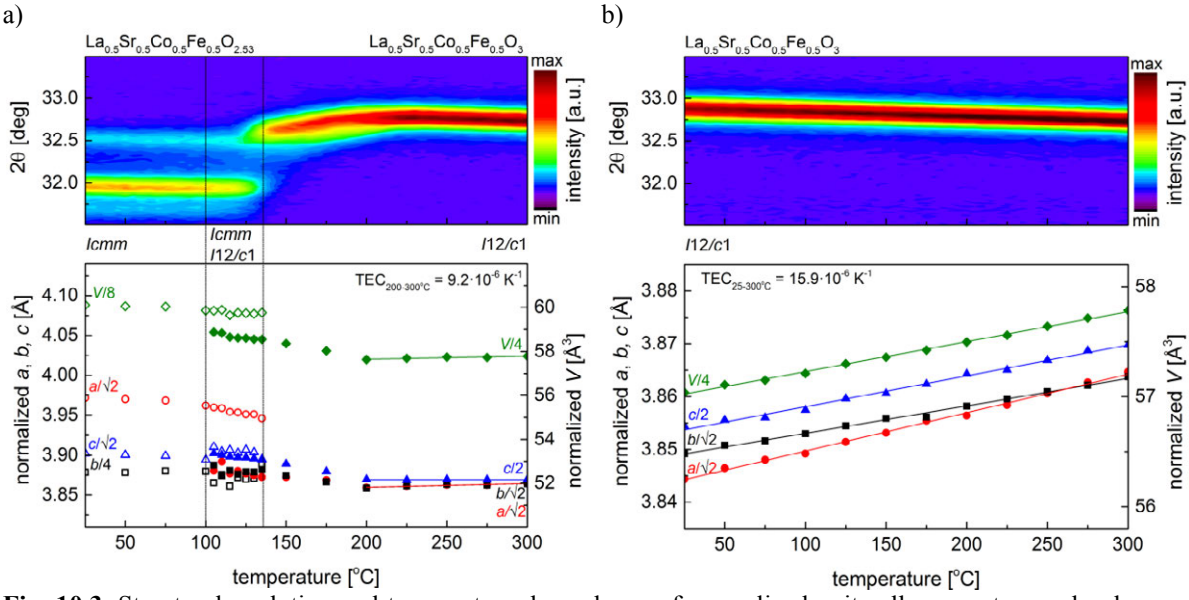

Fig. 10.3. Structural evolution and temperature dependence of normalized unit cell parameters and volume, together with calculated thermal expansion coefficients for a) reduced $La_{0.5}Sr_{0.5}Co_{0.5}Fe_{0.5}O_{2.53}$ and b) oxidized $La_{0.5}Sr_{0.5}Co_{0.5}Fe_{0.5}O_3$ sample during heating in air. Data shown for selected angular range.

In the case of $Sm_{0.5}Sr_{0.5}Co_{0.5}Fe_{0.5}O_{3-\delta}$ (Figs. 10.4a and b) the observed changes are of the same nature as described above for $La_{0.5}Sr_{0.5}Co_{0.5}Fe_{0.5}O_{3-\delta}$ and $La_{0.6}Sr_{0.4}Co_{0.8}Fe_{0.2}O_{3-\delta}$ oxides, and at 300 °C the sample can be considered as fully oxidized.

For barium-containing material (Figs. 10.5a and b), $La_{0.5}Ba_{0.5}Co_{0.5}Fe_{0.5}O_{3-\delta}$, there is no evidence of a phase transition occurring upon oxidation, and the space group remains the same (*I*4/*mcm*). Above 190 °C main peak shifts towards higher angles, and at the same time its intensity decreases in a region where the oxidation takes place, indicating shorter structural coherence length.

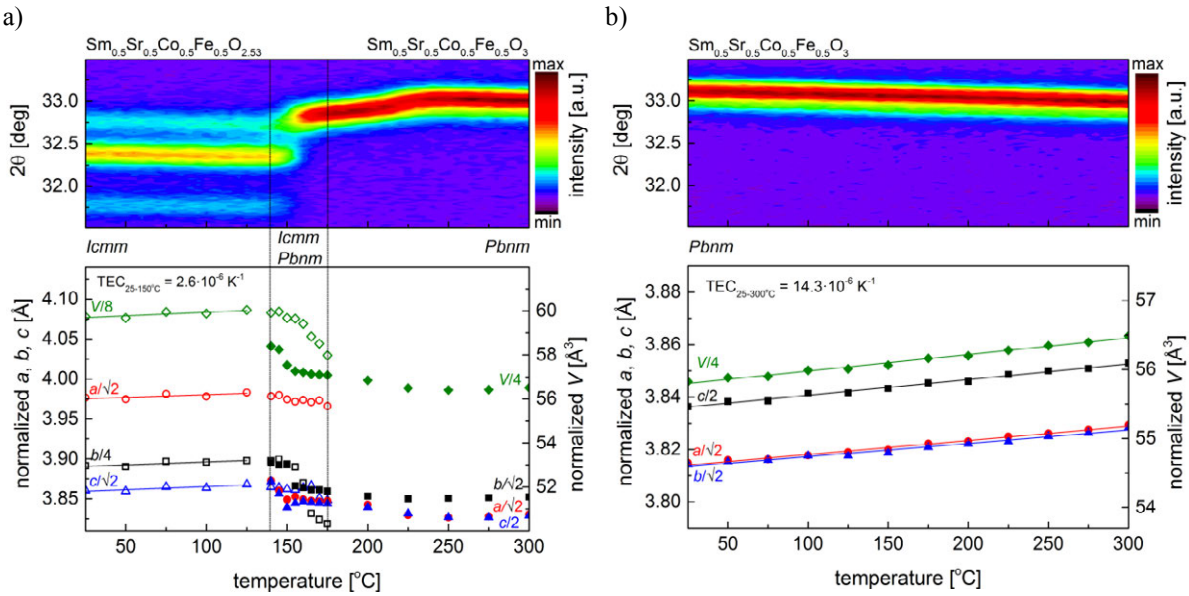

Fig. 10.4. Structural evolution and temperature dependence of normalized unit cell parameters and volume, together with calculated thermal expansion coefficients for a) reduced $Sm_{0.5}Sr_{0.5}Co_{0.5}Fe_{0.5}O_{2.53}$ and b) oxidized $Sm_{0.5}Sr_{0.5}Co_{0.5}Fe_{0.5}O_3$ sample during heating in air. Data shown for selected angular range.

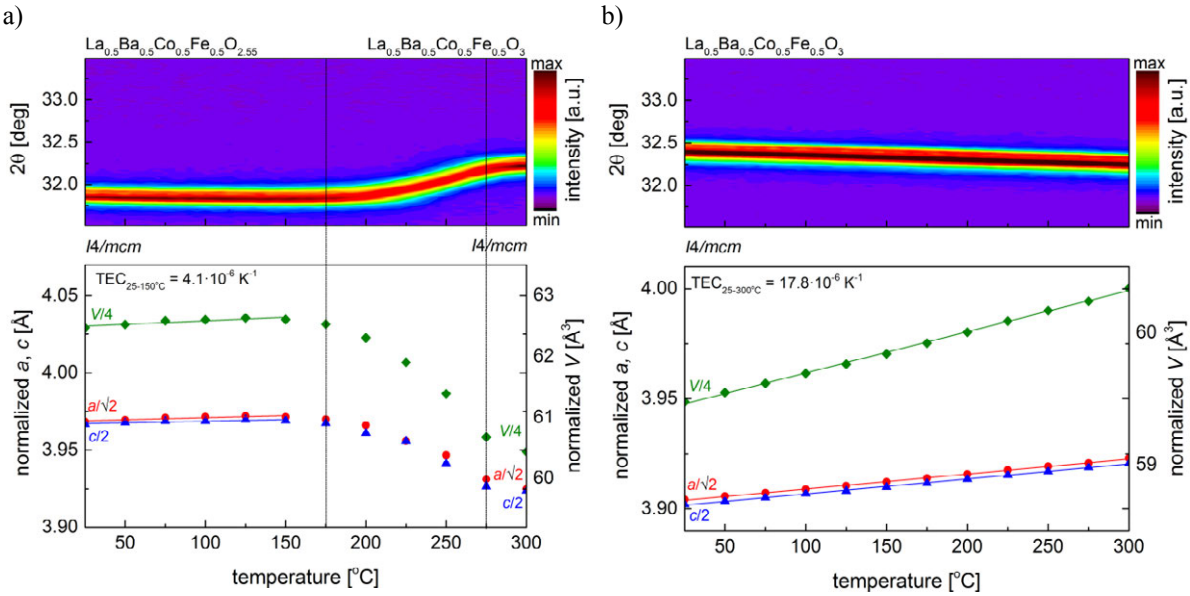

Fig. 10.5. Structural evolution and temperature dependence of normalized unit cell parameters and volume, together with calculated thermal expansion coefficients for a) reduced $La_{0.5}Ba_{0.5}Co_{0.5}Fe_{0.5}O_{2.55}$ and b) oxidized $La_{0.5}Ba_{0.5}Co_{0.5}Fe_{0.5}O_3$ sample during heating in air. Data shown for selected angular range.

Another Ba-containing material, $Sm_{0.5}Ba_{0.5}Co_{0.5}Fe_{0.5}O_{2.54}$, also does not exhibit phase transition upon oxidation, with cation-ordered structure and *P4/mmm* space group in the reduced and the oxidized material. This compound oxidizes above 230 °C (Fig. 10.6a). Its unit cell volume changes are much smaller than for the other considered oxides, and position of the main peak changes only slightly while oxidation process proceeds. However, the c/a ratio, is changing significantly upon oxidation (Tab. 10.1).

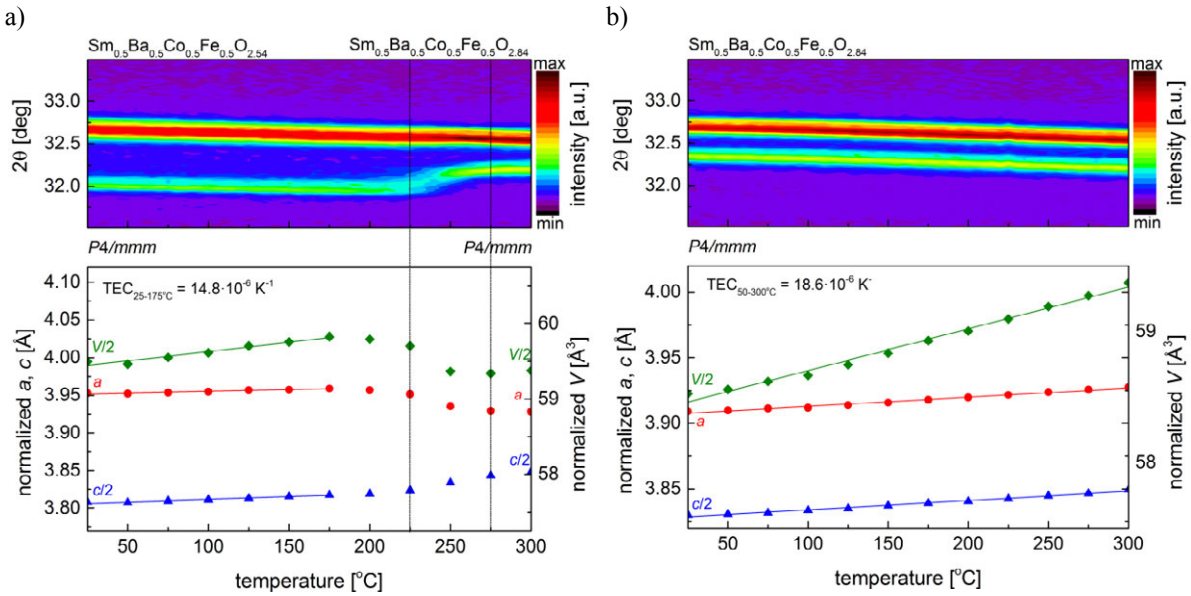

Fig. 10.6. Structural evolution and temperature dependence of normalized unit cell parameters and volume, together with calculated thermal expansion coefficients for a) reduced $Sm_{0.5}Ba_{0.5}Co_{0.5}Fe_{0.5}O_{2.54}$ and b) oxidized $Sm_{0.5}Ba_{0.5}Co_{0.5}Fe_{0.5}O_3$ sample during heating in air. Data shown for selected angular range.

The presented and discussed above unique high-temperature *in situ* studies allowed to directly observe structural changes that occurs during oxidation of the reduced Co- and Fe- containing perovskite-type materials.

10.3. Microstructure of powders

Exemplary SEM micrographs for $La_{0.5}Sr_{0.5}Co_{0.5}Fe_{0.}5O_3$ are presented in Fig. 10.7. This is typical microstructure of the studied in this series oxides. The grains are much rougher and bigger, comparing to the ones shown for $BaLnMn_2O_{5+\delta}$ (e.g. Figs. 6.9a and b).

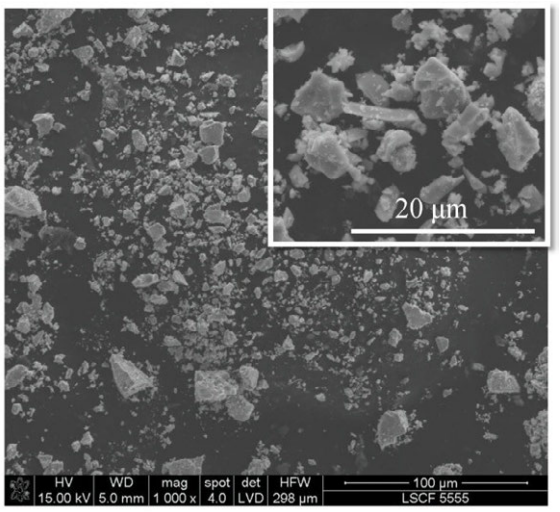

Fig. 10.7. SEM micrographs for $La_{0.5}Sr_{0.5}Co_{0.5}Fe_{0.5}O_3$.

10.4. Oxygen storage properties

Results of non-isothermal measurements of a weight change for all considered samples, conducted in 5 vol.% H_2 in Ar for reduction process and in air for oxidation process during increase of the temperature up to 500 °C, are presented in Figs. 10.8a-e.

In the case of $La_{0.6}Sr_{0.4}Co_{0.8}Fe_{0.2}O_{2.42}$, $La_{0.5}Sr_{0.5}Co_{0.5}Fe_{0.5}O_{2.53}$ as well as $Sm_{0.5}Sr_{0.5}Co_{0.5}Fe_{0.5}O_{2.53}$ materials that exhibit brownmillerite-type structure, oxidation process occurs in three stages. Initially, sudden increase of the oxygen content, in very low temperatures, below 60 °C, 45 °C and 90 °C, respectively, occurs, which can be associated with phase transition into the perovskite-type phase. Irregular behavior of the temperature (pointed with small arrows on Figs. 10.8a-c) originates from heat generated during the oxidation, influencing the TG apparatus that was not able to maintain required 5 $°\cdot min^{-1}$ heating speed. Afterwards, a slower increase of weight of the samples was recorded and is likely related to the oxidation of the perovskite-type phase, however, described curves show some inflection in this region. At the highest considered temperatures, a decrease of weight of the samples was registered, and is mostly visible for $Sm_{0.5}Sr_{0.5}Co_{0.5}Fe_{0.5}O_{3-\delta}$ compound. In the case of $La_{0.5}Ba_{0.5}Co_{0.5}Fe_{0.5}O_{2.55}$ and $Sm_{0.5}Ba_{0.5}Co_{0.5}Fe_{0.5}O_{2.54}$ oxidation process occurs in a less rapid way. Again, after reaching the maximum, increase of the temperature up to 500 °C results in a slight decrease of the weight of the samples.

When comparing data obtained during XRD studies with thermogravimetric tests, an obvious discrepancy of the recorded temperatures of the ongoing processes is visible. This, however, can be easily explained by different experimental conditions. Particularly, during TG measurements, constant flow of gas of 100 $cm^3\cdot min^{-1}$ was provided near the sample of a small mass (~50 mg), supplying needed oxygen for the oxidation. During XRD studies, about 2-3 times bigger amount of the material, being compacted on a holder, was used, with no gas flow through the oven-chamber. In addition, because the oxidation process of the brownmillerite phase is highly exothermic, the onset temperature of the oxidation was found to be dependent on the amount of sample used for the measurements, as well as on the way of distribution of the powder on the holder.

Behavior registered on the TG reduction process is quite similar for all of the samples, with a rather smooth curves of the weight decrease, except for $La_{0.6}Sr_{0.4}Co_{0.8}Fe_{0.2}O_{3-\delta}$, for which there is evident inflection visible.

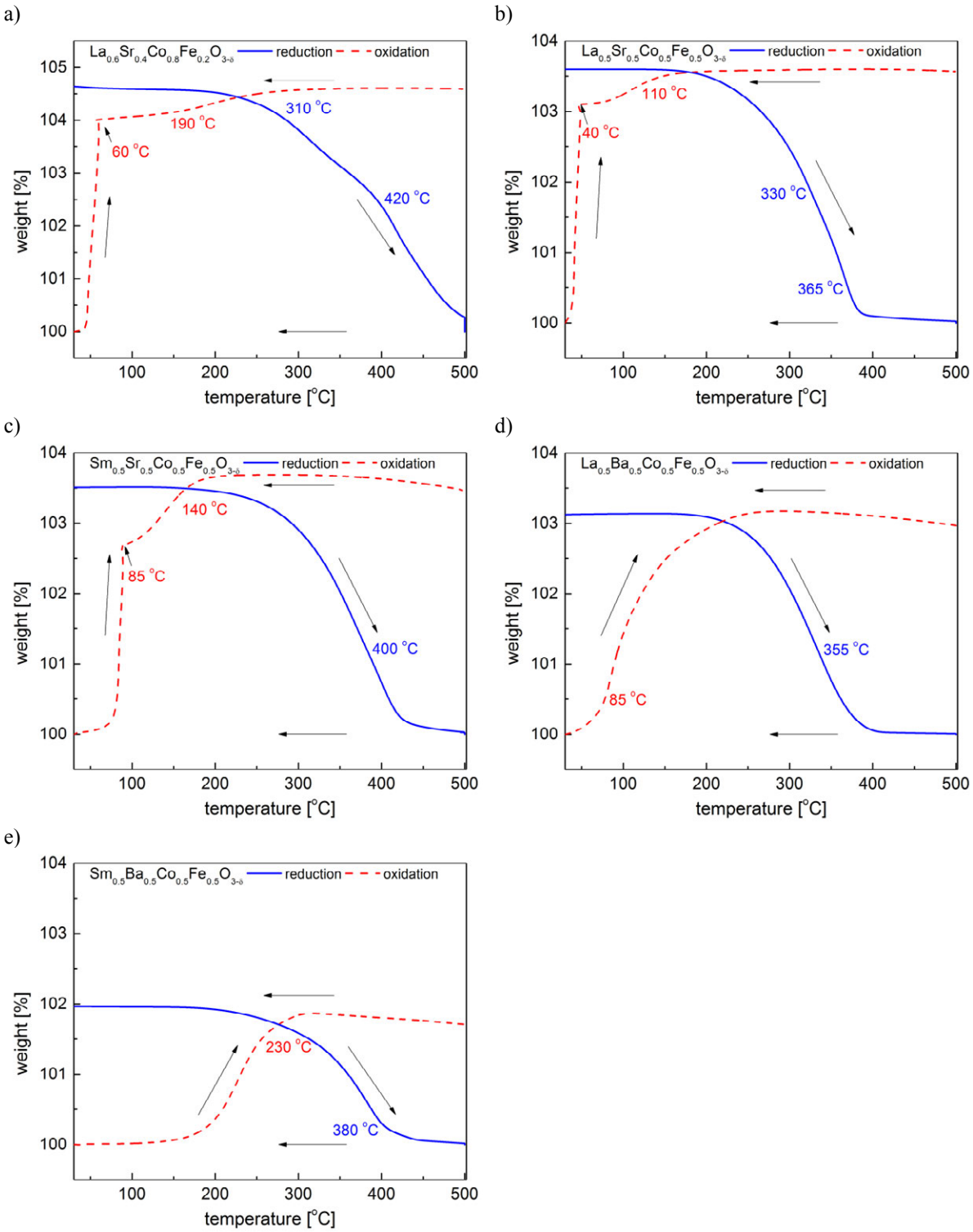

Fig. 10.8. Non-isothermal oxidation and reduction cycles recorded for a) $La_{0.6}Sr_{0.4}Co_{0.8}Fe_{0.2}O_{3-\delta}$, b) $La_{0.5}Sr_{0.5}Co_{0.5}Fe_{0.5}O_{3-\delta}$, c) $Sm_{0.5}Sr_{0.5}Co_{0.5}Fe_{0.5}O_{3-\delta}$, d) $La_{0.5}Ba_{0.5}Co_{0.5}Fe_{0.5}O_{3-\delta}$, and e) $Sm_{0.5}Ba_{0.5}Co_{0.5}Fe_{0.5}O_{3-\delta}$.

Isothermal measurements of reduction and oxidation of the considered Fe- and Co-containing materials are presented in Figs. 10.9a and b, respectively. It is clearly visible that the reduction process is significantly slower than the oxidation, which is in similarity with results obtained for $BaY_{1-x}Ln_xMn_2O_{5+\delta}$ and $Ba_{0.9}Sr_{0.1}Y_{1-x}Ln_xMn_2O_{5+\delta}$ materials

presented in chapters 6-9 of this work. This phenomenon can be also explained as due to an exothermic nature of the oxidation [5]. The slowest reduction rate was registered for the material with the highest measured OSC, $La_{0.6}Sr_{0.4}Co_{0.8}Fe_{0.2}O_{3-\delta}$, and the fastest one for $La_{0.5}Ba_{0.5}Co_{0.5}Fe_{0.5}O_{3-\delta}$, for which 95% of the weigh decrease occurs after 2.6 min.

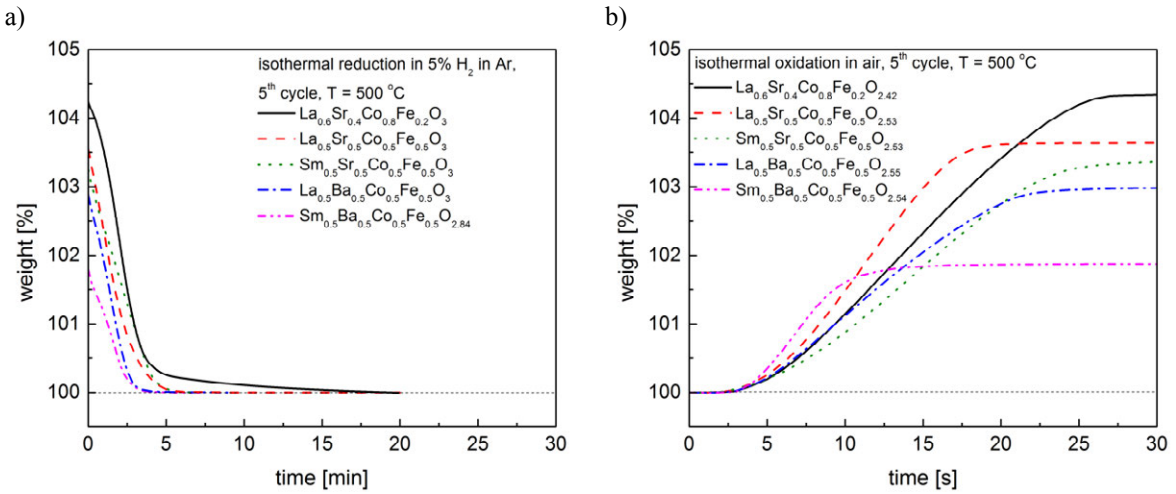

Fig. 10.9. TG data of isothermal a) reduction in 5 vol.% H_2 in Ar, and b) oxidation in synthetic air at 500 °C of $La_{0.6}Sr_{0.4}Co_{0.8}Fe_{0.2}O_{3-\delta}$, $La_{0.5}Sr_{0.5}Co_{0.5}Fe_{0.5}O_{3-\delta}$, $Sm_{0.5}Sr_{0.5}Co_{0.5}Fe_{0.5}O_{3-\delta}$, $La_{0.5}Ba_{0.5}Co_{0.5}Fe_{0.5}O_{3-\delta}$, and $Sm_{0.5}Ba_{0.5}Co_{0.5}Fe_{0.5}O_{3-\delta}$ materials.

Oxygen storage-related properties including theoretical OSC, which was calculated based on the oxygen content changes between reduced and oxidized materials with changes of $\delta = 0.5$ (and 0.6 for $La_{0.6}Sr_{0.4}Co_{0.8}Fe_{0.2}O_{3-\delta}$, assuming presence of cobalt on +2 and iron on +3 oxidation states in the reduced compound), measured OSC, characteristic temperature of oxidation, and also time of reduction and oxidation of the samples during isothermal measurements at 500 °C, are gathered in Tab. 10.2.

Tab. 10.2. Oxygen storage properties of the considered materials. Some results presented also in work [194].

chemical composition	theoretical capacity [wt.%]	measured capacity (5^{th} cycle at 500 °C) [wt.%]	characteristic temperature of oxidation [°C]	characteristic temperature of reduction [°C]	time of reduction (99% of total mass change, 5^{th} cycle) [min]	time of oxidation (99% of total mass change, 5^{th} cycle) [s]
$La_{0.6}Sr_{0.4}Co_{0.8}Fe_{0.2}O_{3-\delta}$	4.27	4.30	60[a], 190	310, 420	14.6	24
$La_{0.5}Sr_{0.5}Co_{0.5}Fe_{0.5}O_{3-\delta}$	3.80	3.60	40[a], 110	330, 365	5.2	18
$Sm_{0.5}Sr_{0.5}Co_{0.5}Fe_{0.5}O_{3-\delta}$	3.57	3.36	85[a], 140	300	5.3	32
$La_{0.5}Ba_{0.5}Co_{0.5}Fe_{0.5}O_{3-\delta}$	3.29	2.95	85	335	3.6	26
$Sm_{0.5}Ba_{0.5}Co_{0.5}Fe_{0.5}O_{3-\delta}$	3.21	1.85	230	380	3.8	56

[a]Temperature of sudden weight increase, however, not to the full capacity.

10.5. Cycling performance of $La_{0.5}Sr_{0.5}Co_{0.5}Fe_{0.5}O_{3-\delta}$

When comparing all considered in this chapter materials, and previously presented data in terms of OSC and reduction speed for Mn-containing materials, $La_{0.5}Sr_{0.5}Co_{0.5}Fe_{0.5}O_{3-\delta}$ oxide can be selected as the most promising one. Performance of this material recorded during first 20 consecutive cycles at 500 °C is shown in Fig. 10.10. Unfortunately, a slight decrease of the reduction speed and also in oxygen storage capacity was observed, indicating limited stability of the material at this temperature. For comparison, manganese-containing oxides exhibit perfect stability in the same working conditions as shown (Fig. 8.4). For further clarification, after performance tests, structure of the oxidized $La_{0.5}Sr_{0.5}Co_{0.5}Fe_{0.5}O_3$ was tested, showing preservation of the initial monoclinic *I*12/*c*1 structure (with only slightly different unit cell parameters), but with presence of a small amount (~ 8 wt.%) contamination of perovskite-type rhombohedral *R*-3*c* phase. This indicates possible ongoing modification of the chemical composition of the main phase during reduction and oxidation cycles.

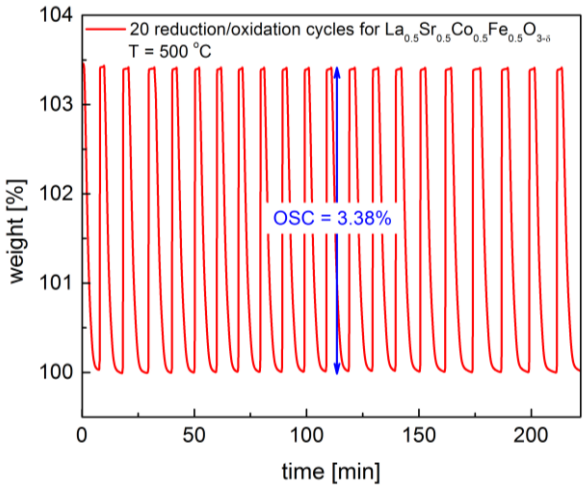

Fig. 10.10. Reversibility of weight changes of $La_{0.5}Sr_{0.5}Co_{0.5}Fe_{0.5}O_{3-\delta}$ during 20 reduction/oxidation cycles at 500 °C [194].

10.6. Ionic transport in Co- and Fe-containing perovskite-type oxides

Additional isothermal measurements of reduction speed were conducted in the temperature range of 400-600 °C, and the results are depicted in Fig. 10.11a, as well as

presented in the Arrhenius-type coordinate system in Fig. 10.11b. As expected, with the increase of the temperature, time required for the reduction to proceed in 95% decreases in an exponential manner. Different behavior at highest temperatures was recorded for $La_{0.6}Sr_{0.4}Co_{0.8}Fe_{0.2}O_{3-\delta}$, and it may be explained as associated to a partial decomposition of the material, which already takes place in the vicinity of 500 °C.

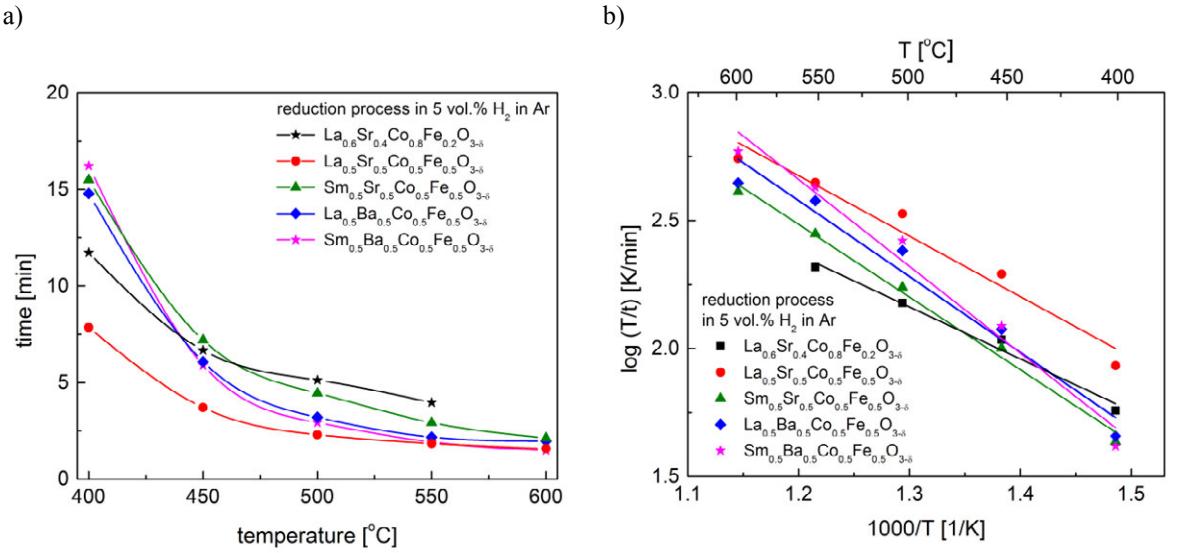

Fig. 10.11. a) Reduction time of the samples as a function of temperature in 400-600 °C temperature range, with b) data presented in Arrhenius-type coordinates. Some data from [194].

It must be stated that at lower temperatures the full available capacity was not reached in every case, due to slow reduction kinetics. The highest reversible OSC was registered for most of the materials at 500 °C. Unfortunately, at higher temperatures (550 °C and 600 °C) the measured capacity decreases, which may be associated with an increasing deviation from the oxygen stoichiometry in the oxidized phases in air [196].

Time required for 95% of a weight change for considered materials depending on the temperature is presented in Tab. 10.3, together with the calculated activation energy of the process. Associated, measured and theoretical OSC data are gathered in Tab. 10.4.

Tab. 10.3. Time of reduction of the considered materials. Some data from [194].

chemical composition	time of reduction [min] at respective temperature calculated for 95% change of total weight change					E_a [eV]
	400 °C	450 °C	500 °C	550 °C	600 °C	
$La_{0.6}Sr_{0.4}Co_{0.8}Fe_{0.2}O_{3-\delta}$	11.7	6.7	5.1	4.0	-	0.28
$La_{0.5}Sr_{0.5}Co_{0.5}Fe_{0.5}O_{3-\delta}$	7.9	3.7	2.3	1.9	1.6	0.33
$Sm_{0.5}Sr_{0.5}Co_{0.5}Fe_{0.5}O_{3-\delta}$	15.5	7.2	4.5	2.9	2.1	0.44
$La_{0.5}Ba_{0.5}Co_{0.5}Fe_{0.5}O_{3-\delta}$	14.8	6.1	3.2	2.2	2.0	0.45
$Sm_{0.5}Ba_{0.5}Co_{0.5}Fe_{0.5}O_{3-\delta}$	16.2	5.9	2.9	1.9	1.5	0.54

Tab. 10.4. Oxygen storage capacity of the studied perovskite-type oxides. Some data from [194].

chemical composition	measured OSC at respective temperatures [wt.%] calculated for 95% change of total weight change					theoretical OSC [wt.%]
	400 °C	450 °C	500 °C	550 °C	600 °C	
$La_{0.6}Sr_{0.4}Co_{0.8}Fe_{0.2}O_{3-\delta}$	3.99	4.08	4.20[a]	4.32[a]	-	4.27
$La_{0.5}Sr_{0.5}Co_{0.5}Fe_{0.5}O_{3-\delta}$	3.45	3.46	3.61	3.41	3.38	3.80
$Sm_{0.5}Sr_{0.5}Co_{0.5}Fe_{0.5}O_{3-\delta}$	3.39	3.33	3.37	3.14	3.02	3.57
$La_{0.5}Ba_{0.5}Co_{0.5}Fe_{0.5}O_{3-\delta}$	3.02	2.96	2.97	2.81	2.74	3.29
$Sm_{0.5}Ba_{0.5}Co_{0.5}Fe_{0.5}O_{3-\delta}$	1.92	1.88	1.89	1.74	1.69	3.21

[a]Starts to decompose.

Unfortunately, as documented, upon reduction at temperatures around and higher than 500 °C, $La_{0.6}Sr_{0.4}Co_{0.8}Fe_{0.2}O_{3-\delta}$ with the highest OSC begins to decompose, which is visible as an increase of the measured capacity and increase of time needed for reduction in the following cycles. However, the recorded OSC for this material, even at 450 °C, is equal to 4.08%, and is significantly higher than the theoretical OSC for $BaYMn_2O_{5+\delta}$ (3.85 wt.%). What is more, activation energy calculated for $BaYMn_2O_{5+\delta}$ as to 0.88 eV is significantly higher than in the case of all compounds discussed in this chapter.

Chapter 10 summary

Crystal structure and oxygen storage-related properties of selected Fe- and Co-containing perovskite-type materials were evaluated. It was found that the reduced $La_{0.6}Sr_{0.4}Co_{0.8}Fe_{0.2}O_{2.42}$, $La_{0.5}Sr_{0.5}Co_{0.5}Fe_{0.5}O_{2.53}$ and $Sm_{0.5}Sr_{0.5}Co_{0.5}Fe_{0.5}O_{2.53}$ possess brownmillerite-type structure, which upon oxidation transforms into perovskite-type structure. In the case of $La_{0.5}Ba_{0.5}Co_{0.5}Fe_{0.5}O_{2.55}$ and $Sm_{0.5}Ba_{0.5}Co_{0.5}Fe_{0.5}O_{2.54}$ there is no phase transition occurring during oxidation process. Interestingly, $Sm_{0.5}Ba_{0.5}Co_{0.5}Fe_{0.5}O_{3-\delta}$ sample exhibits the same, layered-type order of Sm-Ba cations, like the one present in the studied Mn-containing materials. Investigation of the oxygen storage-related properties revealed that the reduction process is significantly slower than the oxidation one. For $La_{0.6}Sr_{0.4}Co_{0.8}Fe_{0.2}O_{3-\delta}$, the measured, reversible oxygen storage capacity can exceed 4 wt.% already at 450 °C. Unfortunately, this material starts to decompose at 500 °C and above. Promising results were registered for $La_{0.5}Sr_{0.5}Co_{0.5}Fe_{0.5}O_{3-\delta}$ compound, that is characterized by a very fast reduction speed, with 3.43 wt.% capacity delivered in 2.3 min at 500 °C. But also, due to stability issues on reduction, a worsening of the properties on cycling was observed. It seems that the main disadvantage of the considered materials originates from their insufficient stability in reducing atmospheres, and also lack of stability of a reduced compounds in the air atmosphere, even in ambient conditions.

11. Conclusions and recommendations

The performed systematic studies of novel oxygen storage materials having perovskite-based structure were presented in chapters 6-10 of this thesis. On the basis of the collected experimental results and provided discussion, the following conclusions can be drawn:

- Soft chemistry sol-gel method can be successfully used for preparation of single phase $BaLnMn_2O_{5+\delta}$ (Ln: Pr, Nd, Sm, Gd, Dy, Er and Y) and $BaY_{1-x}Ln_xMn_2O_5$ (Ln: Pr, Sm and Gr) materials, as well as relatively pure $Ba_{0.9}Sr_{0.1}Y_{0.75}Ln_{0.25}Mn_2O_{5+\delta}$ (Ln: Pr, Sm and Gd) oxides. The method is also suitable for synthesis of Fe- and Co-containing perovskites having $La_{0.6}Sr_{0.4}Co_{0.8}Fe_{0.2}O_{3-\delta}$, $La_{0.5}Sr_{0.5}Co_{0.5}Fe_{0.5}O_{3-\delta}$, $Sm_{0.5}Sr_{0.5}Co_{0.5}Fe_{0.5}O_{3-\delta}$, $La_{0.5}Ba_{0.5}Co_{0.5}Fe_{0.5}O_{3-\delta}$ and $Sm_{0.5}Ba_{0.5}Co_{0.5}Fe_{0.5}O_{3-\delta}$ formula.

- Formation of A-site layered-type cation-ordered structure was confirmed by Rietveld refinements of XRD data for the reduced and the oxidized $BaLnMn_2O_{5+\delta}$ (Ln: Pr, Nd, Sm, Gd, Dy and Y) compounds. Possibility of formation of solid solution was proven for substituted samples with Pr^{3+}, Sm^{3+} and Gd^{3+} cations introduced into Y-sublattice in the materials with general formula of $BaY_{1-x}Ln_xMn_2O_5$ (Ln: Pr, Sm and Gr). Double substitution in Y- and Ba-sublattice at the same time, studied for $Ba_{0.9}Sr_{0.1}Y_{0.75}Ln_{0.25}Mn_2O_{5+\delta}$ (Ln: Pr, Sm and Gd) samples, was also proven to be successful, however, some amount (not exceeding 10 wt.%) of the secondary Y_2O_3 was detected. Substitution of bigger amount of strontium into Ba-sublattice was found to be impossible, showing rather narrow range of formation of such solid solutions. This greatly limits possibility of enhancement of the oxygen storage capacity of Mn-containing $BaLnMn_2O_{5+\delta}$-type oxides by synthesis of materials with lower molar mass.

- Structural refinements performed at the room temperature for the reduced Mn-containing materials indicated that their crystal structure can be successfully refined assuming tetragonal symmetry with *P*4/*nmm* space group. In this space group there are two crystallographic positions for manganese cations, which strongly suggests presence of charge ordering of Mn^{2+} and Mn^{3+}, confirming literature data.

More complicated behavior was found for the oxidized compounds. In the case of the samples with substitution in the Y-sublattice, lowering of the symmetry from aristotype *P*4/*mmm* (for $BaPrMn_2O_6$, $r_{Pr^{3+}}$ = 1.126 Å) through *P*4/*nmm* (from $BaY_{0.25}Pr_{0.75}Mn_2O_6$, $r_{average}$ = 1.099 Å, down to $BaGdMn_2O_6$, $r_{Gd^{3+}}$ = 1.053 Å, with border case for $BaY_{0.5}Sm_{0.5}Mn_2O_6$, $r_{average}$ = 1.049 Å, which can be well-refined using tetragonal or triclinic symmetry) down to *P*-1 symmetry (from $BaY_{0.75}Pr_{0.25}Mn_2O_6$, $r_{average}$ = 1.046 Å, to $BaYMn_2O_6$, $r_{Y^{3+}}$ = 1.019 Å and $BaErMn_2O_{5+\delta}$ $r_{Er^{3+}}$= 1.004 Å) was observed with decreasing average $Y_{1-x}Ln_x$ ionic radius. The dependence is presented in Fig. 11.1. The oxidized materials with strontium substitution in Ba-sublattice exhibit analogous dependence, but shifted, due to influence of smaller Sr^{2+} cations.

Considering studied Fe- and Co-containing perovskites, existence of brownmillerite-type phase was confirmed for the reduced $La_{0.6}Sr_{0.4}Co_{0.2}Fe_{0.8}O_{2.42}$, $La_{0.5}Sr_{0.5}Co_{0.5}Fe_{0.5}O_{2.53}$ and $Sm_{0.5}Sr_{0.5}Co_{0.5}Fe_{0.5}O_{2.53}$ oxides (*Icmm* space group). Upon oxidation these materials transform to perovskite-type phase, *I*12/*c*1 for the first two compounds and *Pbnm* for the Sm-containing oxide. On the contrary, $La_{0.5}Ba_{0.5}Co_{0.5}Fe_{0.5}O_{3-\delta}$ and A-site cation-ordered $Sm_{0.5}Ba_{0.5}Co_{0.5}Fe_{0.5}O_{3-\delta}$ possess the same crystal structure in reduced and oxidized forms (*I*4/*mcm* and *P*4/*mmm*, respectively).

- New perovskite type materials, $BaErMn_2O_5$ and $BaErMn_2O_6$, having the smallest lanthanide cation substituted into Y-sublattice, were successfully obtained for the first time, with sol-gel method yielding > 95 wt.% purity of the considered compounds. Also, layered-type of A-site cation arrangement was found to be maintained in both, reduced and oxidized samples, with the *P*4/*nmm* and *P*-1 space groups, respectively.

- A large decrease of the unit cell volume of all studied oxides was found to occur during oxidation of the reduced compounds, with much bigger changes recorded during oxidation of the brownmillerite-type materials (changes up to 8% for $La_{0.6}Sr_{0.4}Co_{0.2}Fe_{0.8}O_{2.42}$), comparing to Mn-containing cation-ordered oxides (up to 4% for $BaPrMn_2O_5$). The smallest change of V of all investigated in this work materials was recorded for $BaErMn_2O_5$, and is equal to 1.3%. Unit cell volume was

found to be linearly dependent on the average radius of A' cations for both, the reduced and the oxidized compounds.

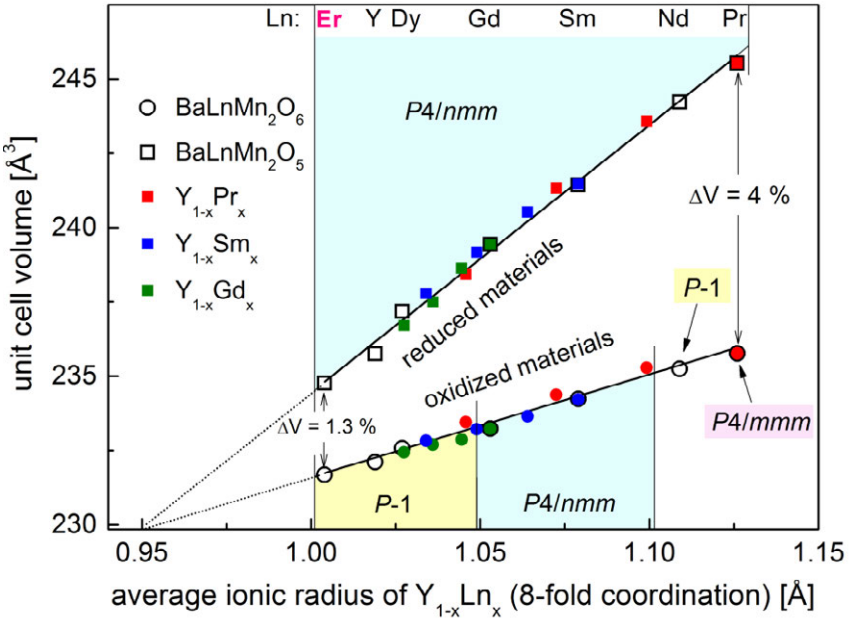

Fig. 11.1. Dependence of the unit cell volume on average ionic radius of $Y_{1-x}Ln_x$ together with assigned space groups used for the refinement for both, reduced and oxidized $BaY_{1-x}Ln_xMn_2O_{5+\delta}$.

- Precise *in situ* high temperature XRD measurements (1 h scans) allowed to directly observe the ongoing structural changes during oxidation in air and reduction under low vacuum of selected $BaLnMn_2O_{5+\delta}$ materials. Existence of the vacancy-ordered $BaLnMn_2O_{5.5}$ *Icma* phase was registered for Pr-, Gd- and Y- containing samples. $BaPrMn_2O_6$ material was found to release 1 mol of oxygen when heated up to 600 °C under ~ 100 Pa vacuum. It seems to be interesting from the viewpoint of application.

- High temperature *in situ* neutron diffraction measurements conducted in 5 vol.% H_2 in Ar revealed presence of step-like character of the reduction process, with initial two-phase system of $BaLnMn_2O_6$ and $BaLnMn_2O_{5.5}$ (Ln: Pr, Nd, Y), in which phase proportion was changing towards partially reduced ($\delta = 0.5$) oxide with time, during isothermal measurements at 300 °C (100% of *Icma* $BaLnMn_2O_{5.5}$ phase after ~ 6 h at 300 °C). The parameters of the oxidized phase are only slightly changing during this transformation, supporting two-phase-type behavior. In the second step, with a further increase of the temperature up to 400 °C, analogous mixture of two phases, $BaLnMn_2O_{5.5}$ and fully reduced $BaLnMn_2O_5$ was registered with weight ratio shifting towards reduced *P*4/*mmm* phase with time. In all of the cases, fully reduced

materials were obtained after ~ 3 hours at 400 °C. Model of the ongoing structural changes, related to the oxygen release from materials during such reduction process, is depicted in Fig. 11.2.

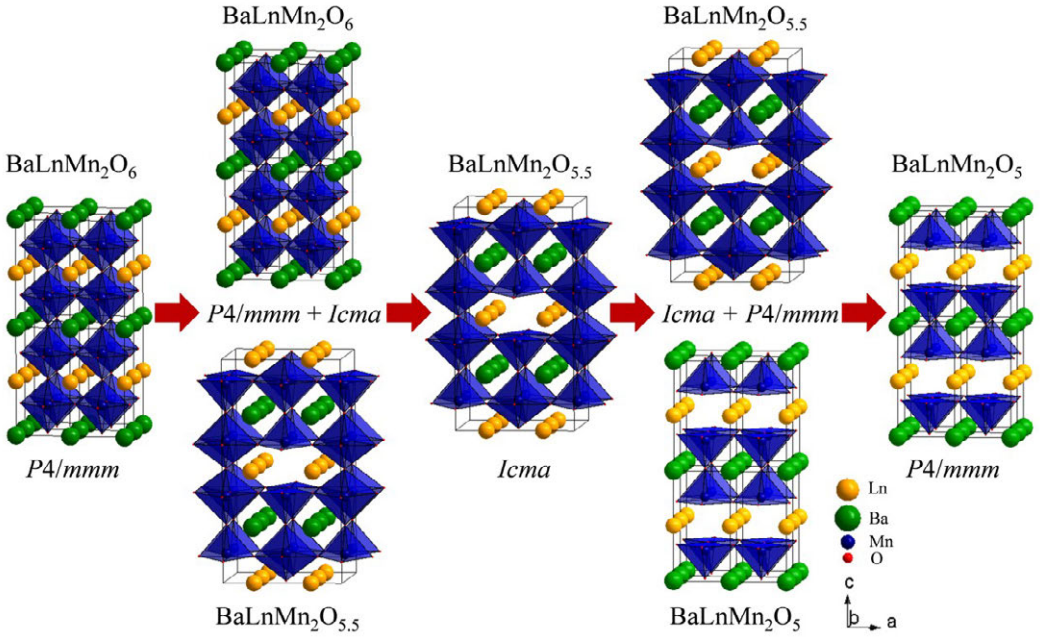

Fig. 11.2. Model of the structural changes of $BaLnMn_2O_{5+\delta}$ materials during ongoing reduction process. Radii of ions not to scale.

The conducted *in situ* XRD studies revealed complex behavior during oxidation of $BaErMn_2O_5$ occurring at around 300 °C and cooling to the room temperature, There is no evidence of formation of the partially oxidized $BaErMn_2O_{5.5}$ during this process. The oxidized $BaErMn_2O_6$ shows a structural phase transition at about 225 °C, corresponding well with changes of the electrical conductivity.

Rapid *in situ* high temperature XRD studies (1 min per scan) performed for Co- and Fe- containing materials studied in this work, which were conducted on heating every 5 °C, allowed to observe ongoing structural changes related to the oxidation.

- Microstructure of the obtained in sol-gel method materials was found to be alike for reduced and oxidized compounds, with porous-like structure and majority of grains being few-micrometer in size. As crystallite size determined from Scherrer's equation is much smaller, this indicates that all grains consists of many crystallites. Specific surface area was determined to be in 1.0-2.5 $m^2 \cdot g^{-1}$ range for all Mn-containing samples. In the case of materials obtained from solid state reaction method, the grains were found to be significantly bigger and well-crystallized.

- Systematic investigations of the oxygen storage-related properties revealed practically complete and reversible changes between reduced $BaLnMn_2O_5$ and oxidized $BaLnMn_2O_6$ (Ln: Pr, Nd, Sm, Gd, Dy, Er and Y, change of $\delta \approx 1$), which occur at moderate temperatures (300-500 °C) during changes of the oxygen partial pressure (air, 5 vol.% H_2 in Ar). For all the materials, the theoretical and measured reversible OSC was proven to be dependent on the substituted Ln^{3+} cation, and decrease with an increase of its mass. However, in all of the cases OSC exceeds 3 wt.%, with the highest values recorded for the reference $BaYMn_2O_{5+\delta}$ oxide, equal to 3.71 wt.% out of theoretical 3.85 wt.%, and for $Ba_{0.9}Sr_{0.1}YMn_2O_{5+\delta}$ material, 3.73 wt.% from the theoretical one equal 3.89 wt.%). Analogously, both theoretical and measured OSC of partially substituted $BaY_{1-x}Ln_xMn_2O_{5+\delta}$ (Ln: Pr, Gd, Sm) samples was found to decrease with an increase of Ln content, however, all the materials show almost theoretical change of δ between the reduced and the oxidized state, as well as high OSC, above 3.35 wt.%.

  Among Fe- and Co- containing oxides, $La_{0.6}Sr_{0.4}Co_{0.8}Fe_{0.2}O_{3-\delta}$ possesses the highest OSC among all studied in this work compounds, exceeding 4 wt.% (out of theoretical 4.27 wt.%), however, the material decomposes at 500 °C and above, and therefore its practical application seems to be limited, also due to slower kinetics at lower temperatures. Graphical summary of the results described above can be found in at Fig. 11.3.

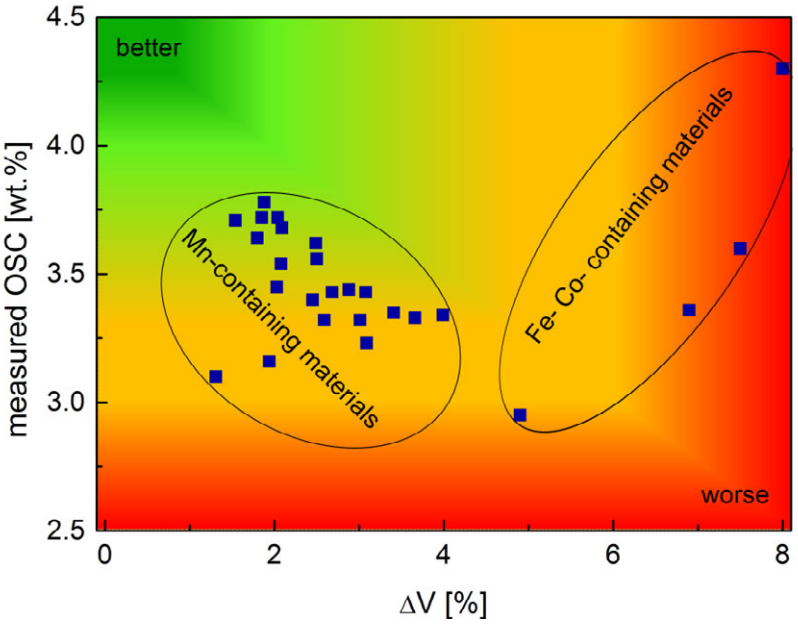

Fig. 11.3. Dependence of the measured oxygen storage capacity on change of the unit cell volume during oxidation for Mn- and Fe-, Co-containing groups of materials.

- Characteristic temperature of the oxidation process was found to be strongly dependent on size of substituted cations in Y-sublattice, and in the case of singly substituted materials, the lowest value of 210 °C was recorded for $BaPrMn_2O_5$ oxide. This trend is graphically presented in Fig. 11.4. Doubly substituted materials, however, do not fully follow this dependence

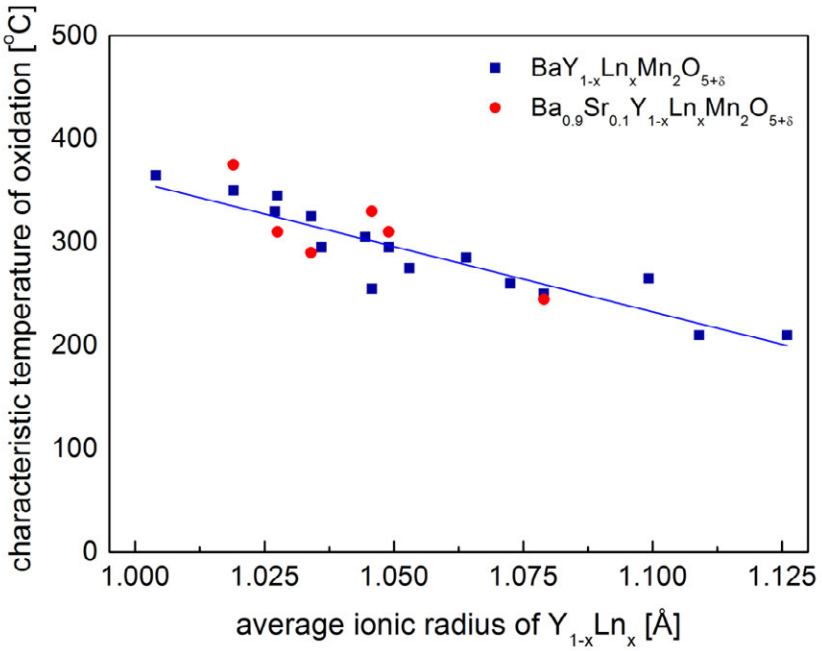

Fig. 11.4. Dependence of the characteristic temperature of oxidation on average ionic radius of $Y_{1-x}Ln_x$ for $BaY_{1-x}Ln_xMn_2O_{5+\delta}$ and $Ba_{0.9}Sr_{0.1}Y_{1-x}Ln_xMn_2O_{5+\delta}$.

In the case of materials that exhibit brownmillerite-type structure, oxidation process occurs in three stages with a first sudden increase of the oxygen content, at rather low temperatures (45-90 °C), associated with a phase transition into perovskite-type structure, followed by the oxidation of the perovskite-type phase, and then at the highest temperatures by a decrease of the oxygen content. The brownmillerite phase was found not to be fully stable in ambient conditions. In addition, because the oxidation process is highly exothermic, the onset temperature of the oxidation was discovered to be dependent on the amount of material used for the measurements, and also on the way of distribution of the powder on the holder.

- Isothermal studies concerning oxygen storage-related properties of the reduction and the oxidation processes revealed that in the case of all studied compounds reduction is endothermic and occurs much slower than the oxidation, which is exothermic. The

reduction is therefore the limiting process in terms of cycling performance. Also, for all studied materials, an improvement of the reduction speed was noticed in the consecutive cycles, with the greatest progress between the first and the second cycle.

- Synthesis method, resulting in different morphology of the obtained samples was proven to have a great impact on the reduction speed. The applied modified soft chemistry method seems to be appropriate for synthesis of the OSMs, yielding powders with porous-like morphology of the secondary particles, which exhibit faster reduction rate, comparing to the materials with the same chemical composition, but obtained using solid state reaction method.

- Among studied double perovskite materials, $BaY_{0.75}Pr_{0.25}Mn_2O_{5+\delta}$ oxides was found to be the best performing, and showed excellent stability and reversibility in the measured 50 reduction/oxidation cycles with the reduction time needed for 99% of a weight change on the order of 2.9 min, which is a great enhancement in comparison with ~ 10.9 min, registered for the reference $BaYMn_2O_{5+\delta}$ material obtained by the same method.

  For $La_{0.5}Sr_{0.5}Co_{0.5}Fe_{0.5}O_{3-\delta}$ oxide, a very fast reduction kinetics were measured (with 3.43 wt.% capacity delivered in 2.3 minutes at 500 °C), however, for this material the reduction speed decreases with the following cycles. It seems that the main reason for this behavior comes from insufficient stability in reducing atmospheres. Considering this, despite higher OSC in relation to the studied $BaLnMn_2O_{5+\delta}$-type materials, application of Fe- and Co-containing perovskites as OSMs seems to be limited to lower temperatures (< 500 °C).

- A systematic investigation performed for all $BaLnMn_2O_{5+\delta}$ allowed to conclude that both chemical composition and powder morphology are determining the kinetics of the reduction process. From the practical point of view, the limiting part of the reduction process may be associated with presence of the two-step-like reduction curve (presence of inflection in the middle of the available capacity), with the second part being significantly slower. Considering crystal structure, this effect arises from formation of the oxygen vacancy ordered $BaLnMn_2O_{5.5}$-type phase, which was observed for materials with bigger Ln^{3+} (or average $Y_{1-x}Ln_x$) radius. The described relationship is depicted in Fig.11.5 below.

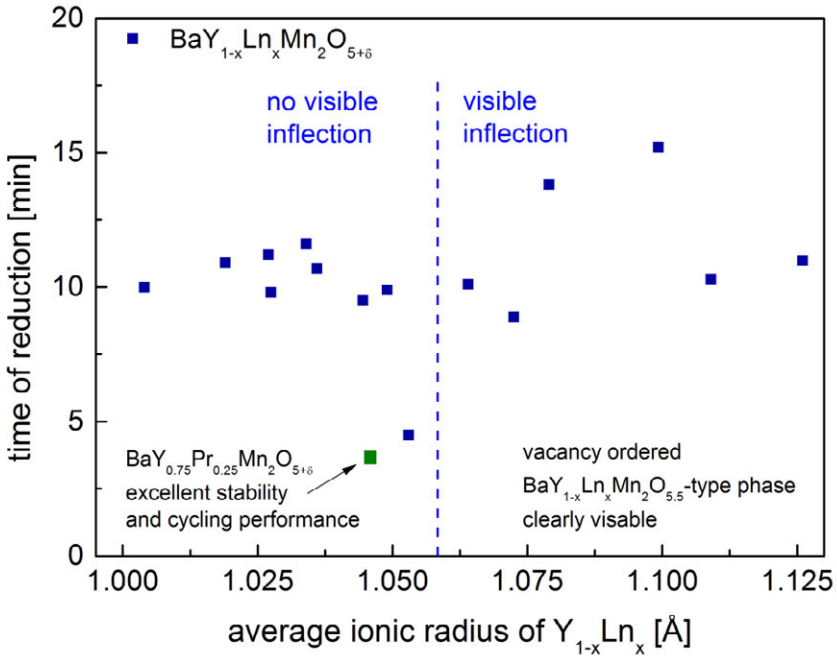

Fig. 11.5. Dependence of the time needed for 95% of total weight change (recorded for 5th cycle) on average ionic radius of $Y_{1-x}Ln_x$ for $BaY_{1-x}Ln_xMn_2O_{5+\delta}$.

- In addition, a method that allows for investigation of activation energy of the ionic transport in the oxygen storage materials was elaborated and used. In the proposed calculations, the obtained value of the activation energy can be related with the oxygen diffusion in the bulk of the studied materials in the last part of the reduction process. Among studied materials similar values were recorded for Mn-containing samples (0.71-0.88 eV), while for Co- and Fe-containing materials significantly lower values of E_a were measured (0.28-0.45 eV). Comparison of the activation energy values for considered groups of materials, as a function of the unit cell volume change on reduction, is depicted in Fig. 11.6. The observed behavior may be attributed to the crystal structure of the materials, but also to the different nature and strength of tendency of formation of the oxygen vacancy-ordered phases.

- Interpretation of the recorded XPS spectra was hindered, however, it seems that surface of the synthesized compounds differ considerably from the bulk, with presence of significant amount of defects.

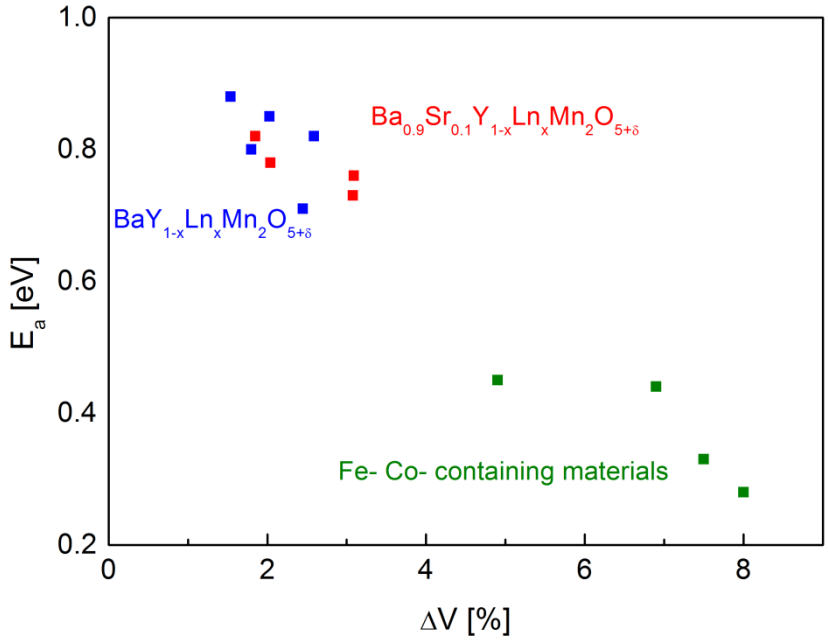

Fig. 11.6. Dependence of activation energy of the reduction process on the change of unit cell volume upon reduction/oxidation for considered $BaY_{1-x}Ln_xMn_2O_{5+\delta}$ and $Ba_{0.9}Sr_{0.1}Y_{1-x}Ln_xMn_2O_{5+\delta}$ and Fe- and Co- containing materials.

- Concerning the Er-containing sample, the reduced $BaErMn_2O_5$ shows activated character of the electrical conductivity dependence on temperature, with E_a = 0.30(1) eV in 50-500 °C range, and with σ value at RT on the order of 10^{-4} S·cm^{-1}. The oxidized $BaErMn_2O_6$ possesses much higher electrical conductivity, almost 0.2 S·cm^{-1} at room temperature, and 40 S·cm^{-1} near 500 °C. At about 225 °C structural and (likely) magnetic phase transitions occur for this material, which can be associated with about tenfold increase of the electrical conductivity. Temperature of this transition is the highest among the ones recorded for $BaLnMn_2O_{5+\delta}$ group of oxides. Sign of Seebeck coefficient is positive for $BaErMn_2O_5$ and negative for $BaErMn_2O_6$, indicating substantial changes in electronic structure, as caused by changing oxygen content.

- As a recommendation for the further studies of OSMs it can be stated that the presented in this work results show possibility of further improvements of the oxygen storage-related properties of $BaLnMn_2O_{5+\delta}$-type materials, but the research should be rather focused on modification of morphology of the powders, than optimization of the chemical composition. More details with initial results of such improvement of the materials are given in Appendix C.

Appendix A

Structural studies of selected $BaLnMn_2O_{5+\delta}$ using synchrotron radiation

As mentioned in the results and discussion section of this work, in literature there is no general agreement regarding selection of the space group suitable for refinement of $BaLnMn_2O_{5+\delta}$, especially the oxidized materials with smaller Ln^{3+} cation introduced [A1-A6]. While good quality XRD data were collected using Panalytical Empyrean diffractometer (see chapter 6.1), and allowed to refine the structural parameters, in addition to the presented results, selected compound were also studied using precise, high-energy, high-resolution synchrotron X-ray powder technique available at 11-BM station at Argonne's Advanced Photon Source (Argonne National Laboratory, Illinois, USA).

The recorded data together with Rietveld refinement for $BaLnMn_2O_5$ and $BaLnMn_2O_6$ (Ln: Sm, Gd and Y) oxides are presented in Figs. A1a-f. The presented results of refinements (Tab. A1) are essentially the same comparing to the standard XRD data (Tab. 6.1). This strongly indicates that in both cases selection of the appropriate crystal structure and space group was correct, as well as that the refined unit cell parameters, volume and other structural factors are properly evaluated. Nevertheless, the precise synchrotron data allowed to notice several additional effects. Despite preferential orientation-related correction included, intensity of (200) reflection could not be refined very well for all samples. Also, some of the peaks showed noticeable asymmetry and broadening. This can be correlated with presence of the internal strain originating from the synthesis technique, i.e. reduction and oxidation at 500 °C. In other words, crystal lattice of the materials likely did not fully relax after accommodation or removal of 1 mole of the oxygen. No significant amount of the secondary phases was detected, with $BaMnO_3$ and $YMnO_3$ minor impurities visible for the Y-containing materials. Also, no improvement of the refinements was achieved assuming partial mixing between Ba and Ln cations, indicating that the layered arrangement of the cations is well-maintained. Interestingly, in the case of $BaGdMn_2O_6$ material, an additional peak was observed in the vicinity of 1.5 deg (not seen in other materials), which could be successfully refined assuming additional doubling of the unit cell along *c*-axis ($4a_p$ in this direction). As can be seen in Fig. A1d inset, the Le Bail-type refinement indicated possibility of presence of such the structure, however, it was not possible to establish partial coordinates of all the atoms in such a large unit cell.

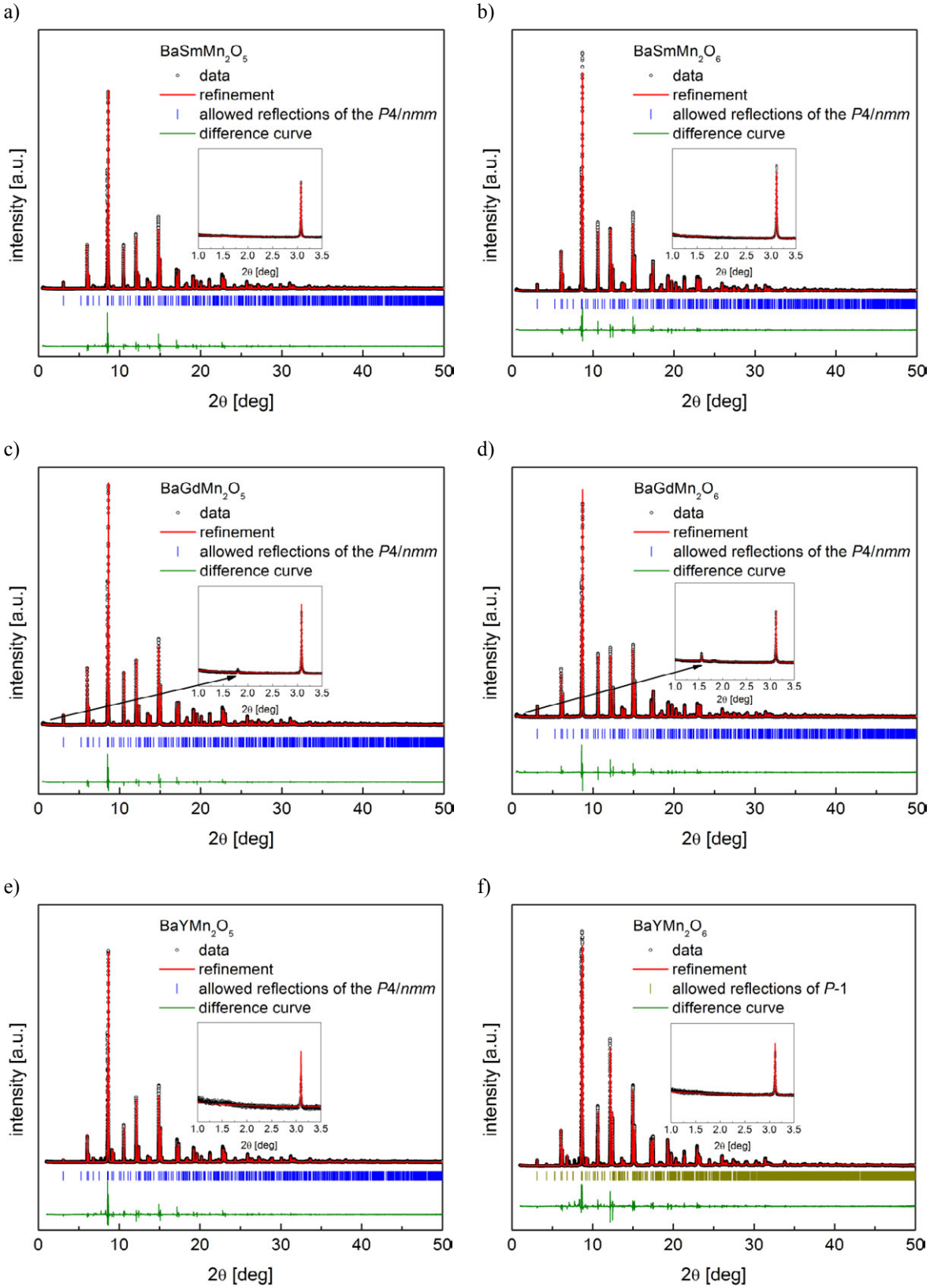

Fig. A1. X-ray synchrotron data with Rietveld refinement for studied a) $BaSmMn_2O_5$, b) $BaSmMn_2O_6$, c) $BaGdMn_2O_5$, d) $BaGdMn_2O_6$, e) $BaYMn_2O_5$ and f) $BaYMn_2O_6$.

Tab. A1. Structural parameters of the considered $BaLnMn_2O_{5+\delta}$ at the room temperature.

composition	space group	a [Å] b [Å]	c [Å] β [deg]	V [Å^3]	Mn(1)[b] x y z	Mn(2)[b] x y z	O(1)[b] x y z	O(2)[b] x y z	O(3)[b] x y z	χ^2
$BaSmMn_2O_5$	*P*4/*nmm*	5.5929(1)	7.7127(1)	241.25(1)	0.25 0.25 0.271	0.25 0.25 -0.254(1)	0.489(1) 0.489(1) 0.311(1)	0.25 0.25 0.013(1)		11.97
$BaSmMn_2O_6$	*P*4/*nmm*	5.5405(1)	7.6300(1)	234.22(1)	0.25 0.25 0.259(1)	0.25 0.25 -0.249(1)	0.515 0.515 0.274	0.25 0.25 0.013(1)	0.25 0.25 0.483(1)	13.96
$BaGdMn_2O_5$	*P*4/*nmm*	5.5797(1)	7.6862(1)	239.30(1)	0.25 0.25 0.254(1)	0.25 0.25 -0.272(1)	0.509(1) 0.509(1) 0.313(1)	0.25 0.25 -0.007(1)		4.01
$BaGdMn_2O_6$	*P*4/*nmm*	5.5346(1)	7.6110(1)	233.14(1)	0.25 0.25 0.248(1)	0.25 0.25 -0.260(1)	0.514(1) 0.514(1) 0.279(1)	0.25 0.25 0.005(1)	0.25 0.25 0.489(2)	6.68
$BaYMn_2O_5$	*P*4/*nmm*	5.5489(1)	7.6588(1)	235.82(1)	0.25 0.25 0.276(1)	0.25 0.25 -0.254(1)	0.505(1) 0.505(1) 0.318(1)	0.25 0.25 0.000(1)		9.27
$BaYMn_2O_6$	*P*-1	5.5230(1) 5.5181(1)	7.6125(1) 90.30(1)[a]	231.99(1)	0.256(1) 0.257(1) 0.258(1)	0.256(1) 0.246(1) -0.259(1)	[c]	[c]	[c]	9.44

[a]The remaining α and γ angles are ≈ 90 deg. [b]Fractional coordinates in the unit cell. [c]Due to lower symmetry, fractional coordinates of the oxygens are not given.

Appendix B

Structural studies of selected $BaLnMn_2O_{5+\delta}$ using neutron diffraction

Free neutrons are produced in either fission or spallation processes. Free neutrons obtained in a nuclear reactor are extracted from a moderator block, and directed to experimental instruments. Monochromator and filters are used to separate neutrons of a desired wavelength from thermal spectrum. The low-energy neutrons are then scattered on individual nuclei and atomic structures. Because value of scattering length of the neutron-nucleus system is specific and varies not only on elements, but also isotopes, neutron diffraction allows for structural investigation of the materials [A7].

The E9 apparatus was chosen out of all instruments (Fig. B1) available in Helmholz Zentrum Berlin, due to its low-length wavelength, which enables inspection of a broad *d*-range. The schematic diagram of the E9 instrument is presented in Fig. B2. The experiment was allocated for 7 days of a beam time.

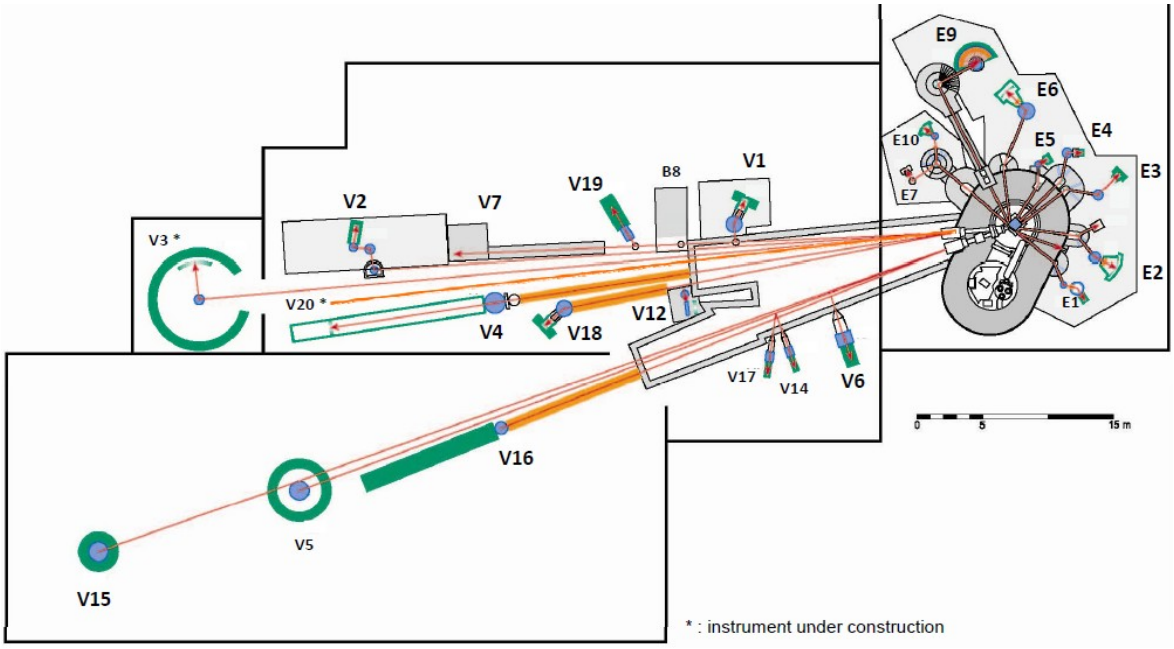

Fig. B1. Neutron instruments and reactor Barr II in HZB. Instruments provided with thermal neutrons (E) and instruments provided with cold neutrons (V) [A8].

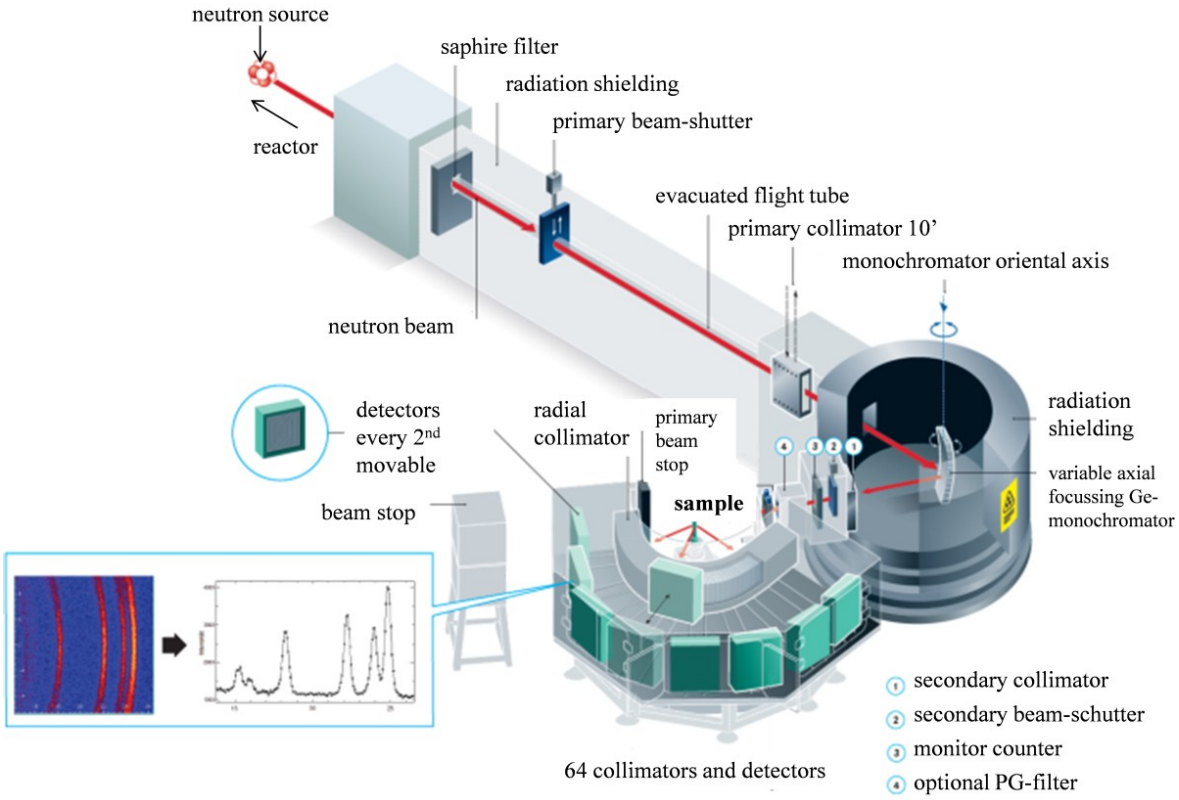

Fig. B2. Schema of E9 instrument in HZB. Based on [A8].

Neutron diffraction measurements were conducted on oxidized samples, isothermally as a 12 consecutive scans (unless technical problems occurred) at every temperature, starting from 200 °C up to 500 °C every 100 °C in atmosphere of 5 vol.% H_2 in Ar. Gathered data together with refined structural parameters and graphical interpretation of the crystal structures are presented in Figs. B3-B5 for praseodymium-, neodymium- and yttrium-containing samples, respectively.

At temperature of 200 °C similar behavior was observed for all three investigated samples, with the structure remaining unchanged with the time, and no indication of significant oxygen release. For scans recorded at this temperature, in all of the cases Rietveld refinement was conducted assuming *P*4/*mmm* space group, with single manganese position available. The structural parameters of every following refinement together with refinement accuracy parameters are presented in Tabs. B1, B6 and B11 respectively in the order of the size of substituted Ln cation.

With an increase of the temperature up to 300 °C recorded structural changes indicate the oxygen release proceeds initially with formation of two-phase $BaLnMn_2O_6$-$BaLnMn_2O_{5.5}$ system, and then with the further increase of temperature up to 400 °C two-phase $BaLnMn_2O_{5.5}$-$BaLnMn_2O_5$ mixture, with only relative wt. ratio of respective phases

changing during the process (and leading to the final $BaLnMn_2O_5$ material). For the detailed description of the process please see Chapter 6.2.2 at the main section of the thesis. Structural parameters calculated for the individual consecutive measurements recorded at 300 °C together with phase composition and refinement accuracy parameters are gathered in Tabs. B2, B7 and B12 respectively and analogously for the results from 400 °C in Tabs. B4, B9 and B14. Additionally, for the last measurement from 300 °C, which in the case of every sample showed 100% of *Icma* partially reduced $BaLnMn_2O_{5.5}$ phase, atomic coordinates and isotropic thermal parameters were calculated and are presented in Tabs. B3, B8 and B13 respectively. Those particular refinements were used to create of the graphical representation of *Icma* structures presented on the Figs. B3-B5.

Further increase of temperature, up to 500 °C revealed presence of only the reduced (O_5) *P*4/*mmm* phase, which was registered for all studied compounds. The precise refinement parameters are presented in Tabs. B5, B10 and B15.

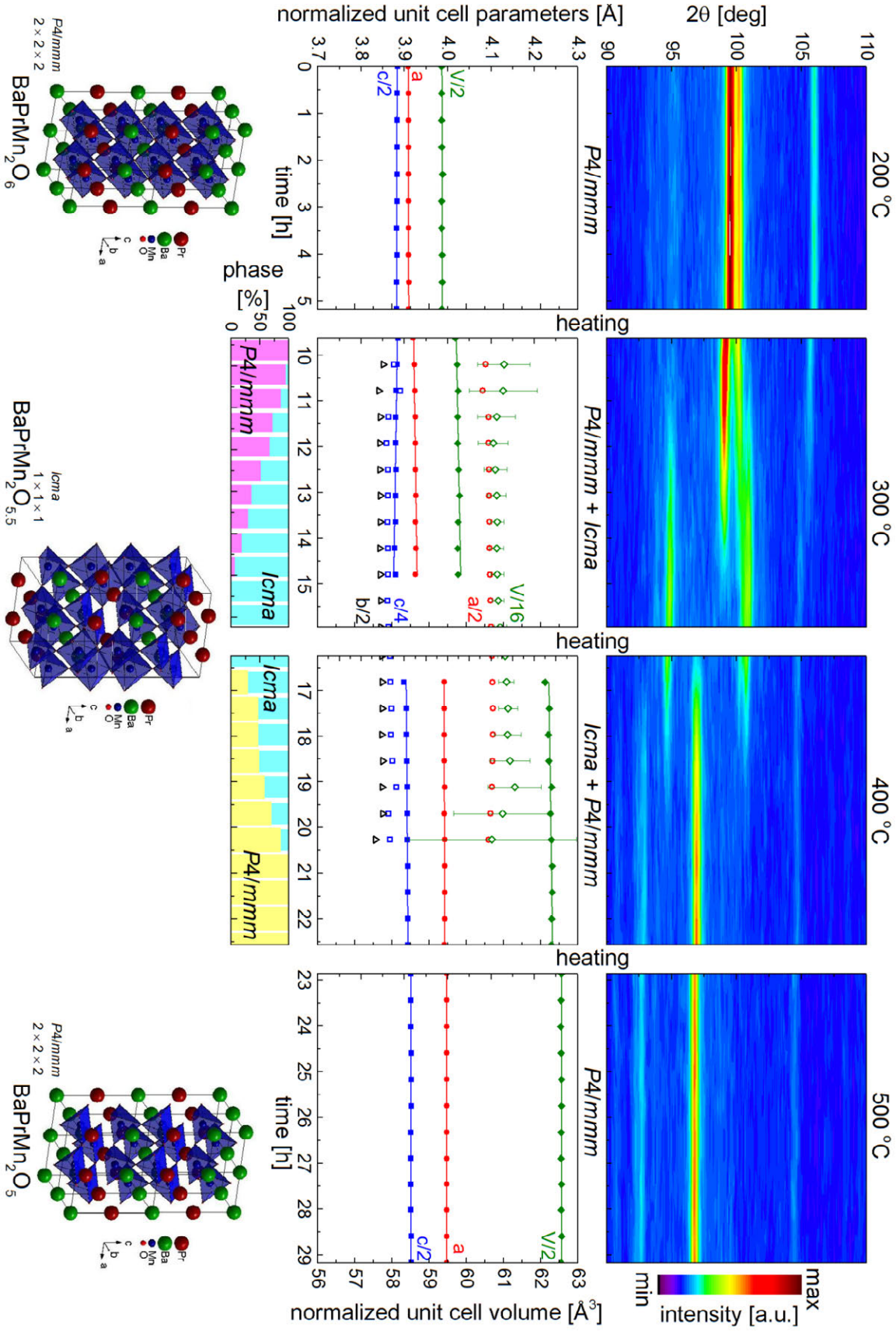

Fig. B3. Structural evolution of oxidized $BaPrMn_2O_6$ sample during heating in 5 vol.% H_2 in Ar. Intensity data shown for selected angular range (main peaks). Corresponding temperature dependence of normalized unit cell parameters and volume data, together with the unit cells for oxidized (*P*4/*mmm*) $BaPrMn_2O_6$, partially reduced (*Icma*) $BaPrMn_2O_{5.5}$, and fully reduced (*P*4/*mmm*) $BaPrMn_2O_5$ are given.

Tab. B1. Structural parameters of $BaPrMn_2O_6$ materials at 200 °C at constant 5 vol.% H_2 in Ar flow.

$BaPrMn_2O_6$ (*P4/mmm*) 200 °C					
	a [Å]	c [Å]	V [Å^3]	χ^2	R_{wp} [%]
1	3.9091(1)	7.7676(5)	118.70(1)	1.513	9.11
2	3.9095(1)	7.7660(5)	118.70(1)	1.213	8.16
3	3.9095(1)	7.7656(5)	118.69(1)	1.227	8.21
4	3.9096(1)	7.7659(5)	118.70(1)	1.176	8.01
5	3.9101(1)	7.7667(5)	118.75(1)	1.090	7.73
6	3.9096(1)	7.7653(5)	118.69(1)	1.189	8.08
7	3.9098(1)	7.7644(5)	118.69(1)	1.133	7.87
8	3.9100(1)	7.7655(5)	118.72(1)	1.141	7.91
9	3.9104(1)	7.7651(5)	118.74(1)	1.141	7.90
10	3.9102(2)	7.7638(6)	118.71(1)	1.207	8.14
11	3.9091(1)	7.7676(5)	118.70(1)	1.513	9.11
12	3.9095(1)	7.7660(5)	118.70(1)	1.213	8.16

Tab. B2. Structural parameters of $BaPrMn_2O_{5+\delta}$ materials at 300 °C at constant 5 vol.% H_2 in Ar flow.

$BaPrMn_2O_{5+\delta}$ ($BaPrMn_2O_6$ *P4/mmm* + $BaPrMn_2O_{5.5}$ *Icma*) at 300 °C										
	a [Å]	c [Å]	V [Å^3]	*P4/mmm* [%]	a [Å]	b [Å]	c [Å]	V [Å^3]	χ^2	R_{wp} [%]
1	3.9203(1)	7.7706(5)	119.42(1)	100					1.237	8.24
2	3.9231(1)	7.7664(6)	119.53(1)	94.5	8.1759(50)	7.7034(22)	15.5024(41)	976.38(71)	1.300	8.39
3	3.9247(2)	7.7628(6)	119.57(1)	86.6	8.1619(44)	7.6850(36)	15.5620(96)	976.11(92)	1.477	8.91
4	3.9253(2)	7.7601(7)	119.56(2)	71.6	8.1892(22)	7.6902(20)	15.4531(55)	973.18(50)	1.258	8.23
5	3.9252(2)	7.7596(8)	119.55(2)	67.0	8.1891(18)	7.6875(16)	15.4360(45)	971.75(41)	1.323	8.44
6	3.9256(2)	7.7616(10)	119.61(2)	51.5	8.1899(13)	7.6890(12)	15.4470(34)	972.73(31)	1.318	8.43
7	3.9269(3)	7.7590(12)	119.65(3)	35.3	8.1911(11)	7.6917(10)	15.4489(27)	973.34(25)	1.184	7.98
8	3.9255(4)	7.7603(16)	119.58(3)	29.3	8.1936(8)	7.6912(7)	15.4467(20)	973.43(18)	1.064	7.56
9	3.9265(7)	7.7550(29)	119.56(6)	18.0	8.1923(8)	7.6894(8)	15.4488(21)	973.18(19)	1.251	8.20
10	3.9258(11)	7.7599(50)	119.59(10)	6.4	8.1949(8)	7.6907(7)	15.4478(18)	973.59(17)	1.295	8.33
11				0	8.1971(7)	7.6933(6)	15.4441(16)	973.95(16)	1.162	7.95
12				0	8.1997(7)	7.6935(7)	15.4530(17)	974.84(16)	1.175	7.99

Tab. B3. Atomic coordinates and isotropic thermal parameters calculated for $BaPrMn_2O_{5.5}$ (*Icma* space group) for 12th consecutive neutron measurement at 300 °C.

$BaPrMn_2O_{5.5}$ at 300°C *Icma* space group				
	x	y	z	U_{iso}
Ba1	0.244(7)	0	0.253(4)	0.030(34)
Pr1	0.266(4)	0	0.001(8)	0.060(53)
Mn1	0	0.25	0.118(1)	0.020(21)
Mn2	0	25	0.374(1)	0.020(21)
O1	0.232(1)	0.244(5)	0.103(1)	0.044(10)
O2	0	0.25	0.250(2)	0.044(10)
O3	-0.006(9)	0	0.098(1)	0.044(10)
O4	-0.006(8)	0	0.385(1)	0.044(10)
O5	0	0.25	0.5	0.044(10)

Tab. B4. Structural parameters of $BaPrMn_2O_{5+\delta}$ materials at 400 °C at constant 5 vol.% H_2 in Ar flow.

$BaPrMn_2O_{5+\delta}$ ($BaPrMn_2O_{5.5}$ *Icma* + $BaPrMn_2O_5$ *P*4/*mmm*) at 400 °C										
	a [Å]	c [Å]	V [Å^3]	*P*4/*mmm* [%]	a [Å]	b [Å]	c [Å]	V [Å^3]	χ^2	R_{wp} [%]
1				0.0	8.2047(9)	7.6979(8)	15.4673(20)	976.89(19)	1.365	8.59
2	3.9918(5)	7.7988(18)	124.27(4)	29.7	8.2062(9)	7.6998(8)	15.4696(22)	977.45(20)	1.133	7.82
3	3.9925(3)	7.8094(10)	124.48(2)	47.7	8.2080(12)	7.6994(10)	15.4786(28)	978.19(26)	1.044	7.52
4	3.9917(3)	7.8092(9)	124.43(2)	47.5	8.2084(17)	7.6982(15)	15.4772(38)	978.00(36)	1.207	8.09
5	3.9919(2)	7.8112(7)	124.48(2)	48.8	8.2063(26)	7.7026(20)	15.4884(59)	979.02(54)	1.108	7.75
6	3.9933(2)	7.8148(7)	124.62(2)	58.0	8.2052(34)	7.7005(33)	15.5257(67)	980.98(72)	1.239	8.2
7	3.9926(2)	7.8137(6)	124.56(2)	70.0	8.1964(66)	7.7028(63)	15.4558(109)	975.81(132)	1.131	7.83
8	3.9931(2)	7.8146(6)	124.60(1)	86.4	8.1885(107)	7.6677(122)	15.4694(177)	971.28(227)	1.101	7.73
9	3.9933(2)	7.8158(6)	124.64(1)	100					1.096	7.78
10	3.9932(2)	7.8165(6)	124.64(1)	100					1.163	8.03
11	3.9932(2)	7.8154(5)	124.62(1)	100					1.070	7.69
12	3.9926(2)	7.8156(6)	124.59(1)	100					1.226	8.22

Tab. B5. Structural parameters of $BaPrMn_2O_5$ materials at 500 °C at constant 5 vol.% H_2 in Ar flow.

$BaPrMn_2O_5$ (*P*4/*mmm*) 500 °C					
	a [Å]	c [Å]	V [Å^3]	χ^2	R_{wp} [%]
1	3.9977(2)	7.8304(6)	125.14(1)	1.194	8.12
2	3.9973(2)	7.8304(6)	125.12(1)	1.175	8.07
3	3.9973(2)	7.8296(6)	125.11(1)	1.208	8.17
4	3.9975(2)	7.8308(6)	125.14(1)	1.298	8.48
5	3.9975(2)	7.8312(6)	125.15(1)	1.105	7.81
6	3.9973(2)	7.8322(6)	125.15(1)	1.099	7.79
7	3.9974(2)	7.8306(6)	125.13(1)	1.074	7.71
8	3.9973(2)	7.8306(6)	125.12(1)	1.097	7.79
9	3.9978(2)	7.8300(6)	125.14(1)	1.166	8.03
10	3.9977(2)	7.8298(6)	125.13(1)	1.170	8.04
11	3.9977(2)	7.8315(6)	125.16(1)	1.188	8.11
12	3.9973(2)	7.8310(6)	125.13(1)	1.322	8.54

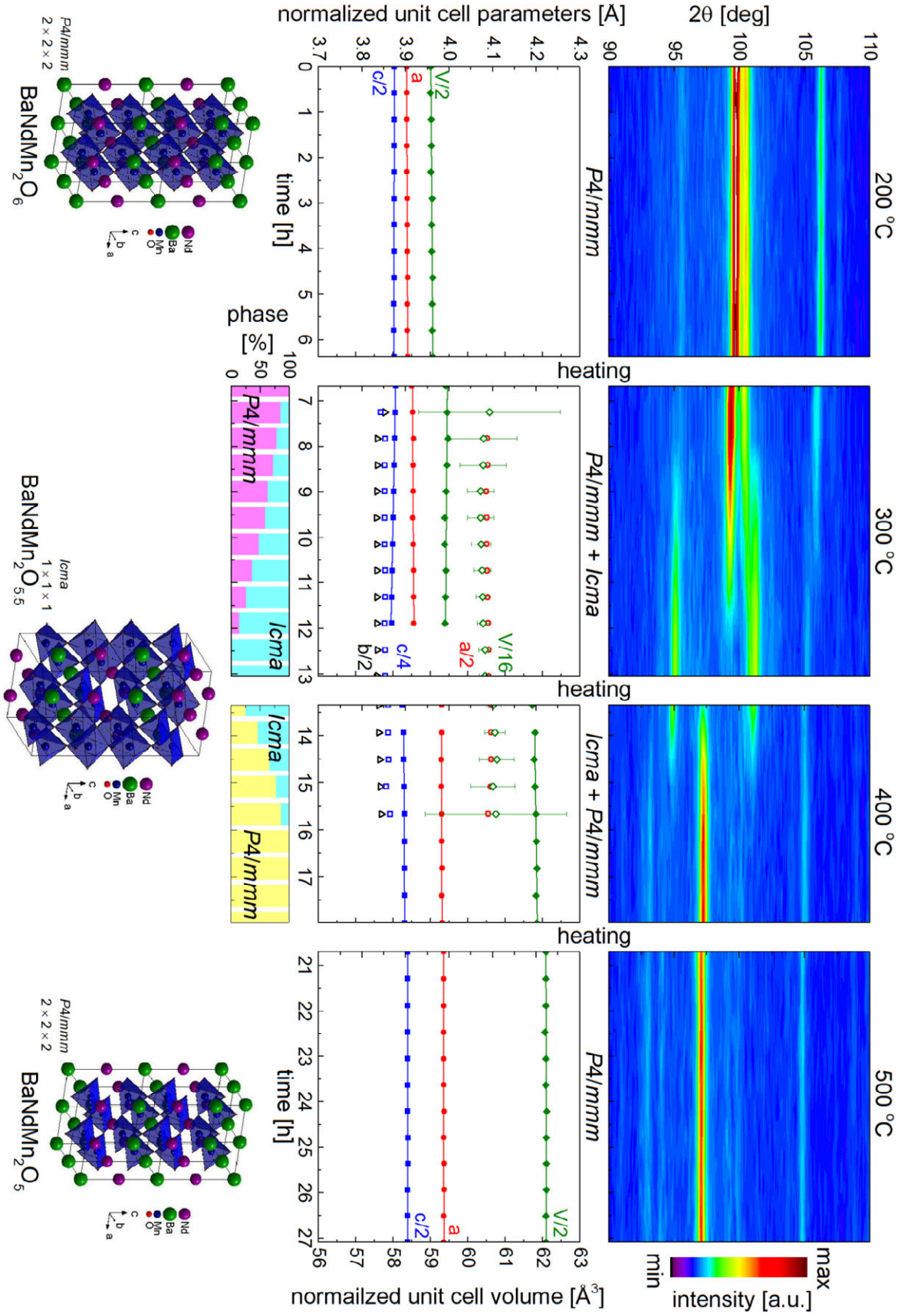

Fig. B4. Structural evolution of oxidized $BaNdMn_2O_6$ sample during heating in 5 vol.% H_2 in Ar. Intensity data shown for selected angular range (main peaks). Corresponding temperature dependence of normalized unit cell parameters and volume data, together with the unit cells for oxidized (*P*4/*mmm*) $BaNdMn_2O_6$, partially reduced (*Icma*) $BaNdMn_2O_{5.5}$, and fully reduced (*P*4/*mmm*) $BaNdMn_2O_5$ are given.

Tab. B6. Structural parameters of $BaNdMn_2O_6$ materials at 200 °C at constant 5 vol.% H_2 in Ar flow.

$BaNdMn_2O_6$ (*P*4/*mmm*) 200 °C					
	a [Å]	c [Å]	V [Å^3]	χ^2	R_{wp} [%]
1	3.9029(1)	7.7491(1)	118.04(1)	1.798	9.59
2	3.9027(1)	7.7490(5)	118.03(1)	1.425	8.50
3	3.9034(1)	7.7480(5)	118.06(1)	1.260	7.97
4	3.9034(1)	7.7491(5)	118.07(1)	1.376	8.32
5	3.9034(1)	7.7479(5)	118.05(1)	1.341	8.23
6	3.9041(1)	7.7494(5)	118.12(1)	1.368	8.31
7	3.9041(1)	7.7478(5)	118.09(1)	1.357	8.26
8	3.9040(1)	7.7477(5)	118.09(1)	1.393	8.37
9	3.9047(1)	7.7480(5)	118.13(1)	1.273	8.01
10	3.9046(1)	7.7468(5)	118.11(1)	1.452	8.55
11	3.9046(1)	7.7467(5)	118.11(1)	1.449	8.54
12	3.9053(1)	7.7472(5)	118.15(1)	1.266	7.98

Tab. B7. Structural parameters of $BaNdMn_2O_{5+\delta}$ materials at 300 °C at constant 5 vol.% H_2 in Ar flow.

$BaNdMn_2O_{5+\delta}$ ($BaNdMn_2O_6$ *P*4/*mmm* + $BaNdMn_2O_{5.5}$ *Icma*) at 300 °C										
	a [Å]	c [Å]	V [Å^3]	*P*4/*mmm* [%]	a [Å]	b [Å]	c [Å]	V [Å^3]	χ^2	R_{wp} [%]
1	3.9147(1)	3.8779(5)	118.86(1)	100					1.328	8.18
2	3.9167(1)	3.8759(5)	118.92(1)	84.9	8.1853(95)	7.7062(84)	15.3702(179)	969.51(190)	1.375	8.24
3	3.9182(1)	3.8749(6)	118.97(1)	78.1	8.1743(20)	7.6734(17)	15.4148(100)	966.89(89)	1.399	8.32
4	3.9174(2)	3.8739(7)	118.90(1)	72.0	8.1772(28)	7.6727(26)	15.4083(68)	966.73(62)	1.436	8.41
5	3.9175(2)	3.8727(8)	118.87(2)	62.7	8.1710(16)	7.6697(15)	15.4092(41)	965.69(36)	1.190	7.65
6	3.9169(2)	3.8714(10)	118.79(2)	58.3	8.1737(16)	7.6675(15)	15.4089(40)	965.70(36)	1.462	8.54
7	3.9171(3)	3.8709(12)	118.79(3)	47.0	8.1737(12)	7.6698(11)	15.4082(29)	965.94(26)	1.406	8.33
8	3.9186(3)	3.8700(14)	118.85(3)	35.4	8.1746(10)	7.6699(10)	15.4132(25)	966.38(23)	1.324	8.07
9	3.9192(6)	3.8680(24)	118.83(5)	25.4	8.1776(8)	7.6698(8)	15.4119(24)	966.64(18)	1.287	7.96
10	3.9186(10)	3.8684(43)	118.80(9)	13.6	8.1795(7)	7.6703(6)	15.4086(17)	966.73(16)	1.172	7.58
11				0	8.1820(8)	7.6721(7)	15.4136()18	967.55(17)	1.567	8.78
12				0	8.1815(7)	7.6728(6)	15.4122(17)	967.50(15)	1.399	8.31

Tab. B8. Atomic coordinates and isotropic thermal parameters calculated for $BaNdMn_2O_{5.5}$ (*Icma* space group) for 9th consecutive neutron measurement at 300 °C.

$BaNdMn_2O_{5.5}$ at 300°C *Icma* space group				
	x	y	z	U_{iso}
Ba1	0.252(19)	0	0.250(3)	0.020(34)
Y1	0.260(3)	0	0.000(3)	0.035(27)
Mn1	0.25	0	0.119(2)	0.021(26)
Mn2	0	0.25	0.377(2)	0.021(26)
O1	0.230(2)	0.250(5)	0.107(7)	0.035(10)
O2	0	0.25	0.249(2)	0.035(10)
O3	0.000(4)	0	0.096(1)	0.035(10)
O4	-0.002(2)	0	0.384(1)	0.035(10)

Tab. B9. Structural parameters of $BaNdMn_2O_{5+\delta}$ materials at 400 °C at constant 5 vol.% H_2 in Ar flow.

$BaNdMn_2O_{5+\delta}$ ($BaNdMn_2O_{5.5}$ *Icma* + $BaNdMn_2O_5$ *P4/mmm*) at 400 °C										
	a [Å]	c [Å]	V [Å^3]	*P4/mmm* [%]	a [Å]	b [Å]	c [Å]	V [Å^3]	χ^2	R_{wp} [%]
1	3.9828(7)	7.7845(32)	123.49(7)	24.7	8.1936(9)	7.6795(7)	15.4384(21)	971.23(19)	1.668	9.10
2	3.9836(3)	7.7905(13)	123.63(3)	45.7	8.1939(12)	7.6798(11)	15.4422(31)	971.74(28)	1.286	7.95
3	3.9825(2)	7.7920(8)	123.58(2)	65.9	8.1939(22)	7.6841(19)	15.4466(56)	972.56(47)	1.314	8.03
4	3.9824(2)	7.7940(6)	123.61(1)	76.8	8.1899(27)	7.6861(24)	15.4238(67)	970.91(59)	1.216	7.50
5	3.9830(2)	7.7955(6)	123.67(1)	85.4	8.1791(95)	7.6902(83)	15.4575(178)	972.26(190)	1.578	8.82
6	3.9835(1)	7.7946(5)	123.69(1)	100.0					1.210	7.65
7	3.9840(1)	7.7956(5)	123.74(1)	100.0					1.324	8.15
8	3.9833(2)	7.7948(6)	123.68(1)	100.0					1.504	8.68
9	3.9837(2)	7.7962(5)	123.73(1)	100.0					1.431	8.47

Tab. B10. Structural parameters of $BaNdMn_2O_5$ materials at 500 °C at constant 5 vol.% H_2 in Ar flow.

$BaNdMn_2O_5$ (*P4/mmm*) 500 °C					
	a [Å]	c [Å]	V [Å^3]	χ^2	R_{wp} [%]
1	3.9881(2)	7.8097(3)	124.21(1)	1.289	8.06
2	3.9880(2)	7.8097(6)	124.21(1)	1.375	8.33
3	3.9878(1)	7.8102(5)	124.20(1)	1.177	7.71
4	3.9871(2)	7.8101(6)	124.16(1)	1.325	8.17
5	3.9879(2)	7.8100(5)	124.21(1)	1.356	8.26
6	3.9878(1)	7.8098(5)	124.20(1)	1.205	7.79
7	3.9886(1)	7.8101(5)	124.25(1)	1.389	8.37
8	3.9880(2)	7.8104(6)	124.22(1)	1.353	8.24
9	3.9883(2)	7.8106(6)	124.24(1)	1.442	8.54
10	3.9883(1)	7.8103(5)	124.24(1)	1.196	7.76
11	3.9880(1)	7.8100(5)	124.21(1)	1.269	7.98
12	3.9881(2)	7.8096(6)	124.21(1)	1.383	8.33

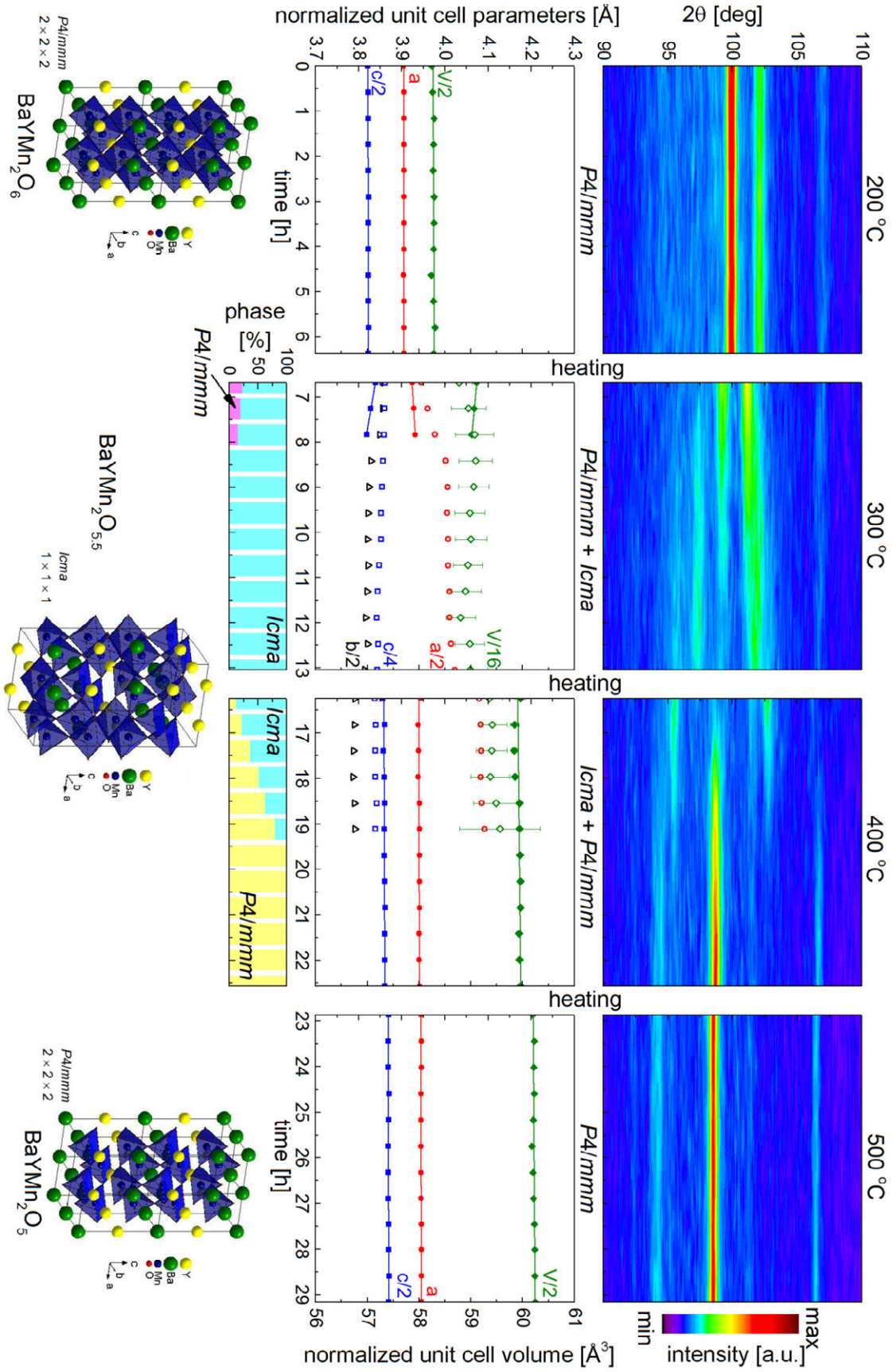

Fig. B5. Structural evolution of oxidized $BaYMn_2O_6$ sample during heating in 5 vol.% H_2 in Ar. Intensity data shown for selected angular range (main peaks). Corresponding temperature dependence of normalized unit cell parameters and volume data, together with the unit cells for oxidized (*P*4/*mmm*) $BaYMn_2O_6$, partially reduced (*Icma*) $BaYMn_2O_{5.5}$, and fully reduced (*P*4/*mmm*) $BaYMn_2O_5$ are given.

Tab. B11. Structural parameters of $BaYMn_2O_6$ materials at 200 °C at constant 5 vol.% H_2 in Ar flow.

$BaYMn_2O_6$ (*P*4/*mmm*) 200 °C					
	a [Å]	c [Å]	V [Å^3]	χ^2	R_{wp} [%]
1	3.9044(2)	7.6425(9)	116.51(2)	1.531	9.20
2	3.9047(2)	7.6436(9)	116.54(2)	1.384	8.73
3	3.9053(2)	7.6450(9)	116.60(2)	1.394	8.76
4	3.9049(3)	7.6450(11)	116.58(2)	1.431	8.86
5	3.9047(2)	7.6446(9)	116.56(2)	1.486	9.03
6	3.9052(2)	7.6457(9)	116.60(2)	1.481	9.02
7	3.9052(2)	7.6450(10)	116.59(2)	1.593	9.35
8	3.9050(2)	7.6455(9)	116.59(2)	1.496	9.07
9	3.9039(2)	7.6433(9)	116.49(2)	1.548	9.23
10	3.9050(2)	7.6446(10)	116.57(2)	1.455	8.94
11	3.9056(2)	7.6467(9)	116.64(2)	1.285	8.39
12	3.9050(2)	7.6454(9)	116.59(2)	1.513	9.11

Tab. B12. Structural parameters of $BaYMn_2O_{5+\delta}$ materials at 300 °C at constant 5 vol.% H_2 in Ar flow.

$BaYMn_2O_{5+\delta}$ ($BaYMn_2O_6$ *P*4/*mmm* + $BaYMn_2O_{5.5}$ *Icma*) at 300 °C										
	a [Å]	c [Å]	V [Å^3]	*P*4/*mmm* [%]	a [Å]	b [Å]	c [Å]	V [Å^3]	χ^2	R_{wp} [%]
1	3.9240(6)	7.6792(29)	118.24(6)	22.4	7.8910(13)	7.7175(11)	15.4430(26)	940.46(26)	1.323	8.45
2	3.9282(7)	7.6562(29)	118.14(6)	18.9	7.9203(18)	7.7138(14)	15.4410(33)	943.38(33)	1.473	8.93
3	3.9314(8)	7.6381(32)	118.05(7)	15.0	7.9536(20)	7.7001(18)	15.4345(39)	945.26(37)	1.452	8.85
4					8.0037(17)	7.6594(14)	15.4249(32)	945.59(32)	1.795	9.87
5					8.0130(14)	7.6505(13)	15.4157(29)	945.03(29)	1.658	9.49
6					8.0101(16)	7.6461(14)	15.4099(32)	943.80(29)	1.511	9.06
7					8.0157(17)	7.6434(15)	15.4106(34)	944.17(31)	1.464	8.90
8					8.0157(15)	7.6458(13)	15.3902(30)	943.22(28)	1.473	8.91
9					8.0216(17)	7.6400(15)	15.3787(34)	942.48(31)	1.598	9.34
10					8.0212(15)	7.6343(14)	15.3663(30)	940.98(29)	1.448	8.83
11					8.0282(16)	7.6430(13)	15.3811(31)	943.78(29)	1.298	8.39
12					8.0464(20)	7.6306(17)	15.3745(40)	943.97(34)	1.258	8.23

Tab. B13. Atomic coordinates and isotropic thermal parameters calculated for $BaYMn_2O_{5.5}$ (*Icma* space group) for 12th consecutive neutron measurement at 300 °C.

	x	y	z	U_{iso}
Ba1	0.283(3)	0	0.231(1)	0.00414(4)
Y1	0.255(4)	0	0.004 (2)	0.06273(5)
Mn1	0	0.25	0.120(2)	0.01299(4)
Mn2	0	0.25	0.375(3)	0.01299(4)
O1	0.232(3)	0.260(4)	0.102(1)	0.05093(20)
O2	0	0.25	0.259(3)	0.05093(20)
O3	0.028(5)	0	0.107(2)	0.05093(20)
O4	0.006(6)	0	0.397(2)	0.05093(20)
O5	0	0.25	0.5	0.05093(20)

Tab. B14. Structural parameters of $BaYMn_2O_{5+\delta}$ materials at 400 °C at constant 5 vol.% H_2 in Ar flow.

$BaYMn_2O_{5+\delta}$ ($BaYMn_2O_{5.5}$ *Icma* + $BaYMn_2O_5$ *P4/mmm*) at 400 °C										
	a [Å]	c [Å]	V [Å^3]	*P4/mmm* [%]	a [Å]	b [Å]	c [Å]	V [Å^3]	χ^2	R_{wp} [%]
1	3.9433(12)	7.7128(44)	119.93(10)	11.9	8.1598(13)	7.5843(10)	15.3486(26)	949.87(25)	1.284	8.31
2	3.9378(10)	7.7207(39)	119.72(9)	21.7	8.1656(14)	7.5814(11)	15.3588(28)	950.81(28)	1.155	7.89
3	3.9390(6)	7.7147(23)	119.70(5)	36.5	8.1693(16)	7.5784(13)	15.3535(33)	950.54(30)	1.114	7.72
4	3.9382(4)	7.7192(17)	119.72(4)	51.3	8.1668(19)	7.5765(15)	15.3557(17)	950.14(38)	1.177	7.96
5	3.9409(3)	7.7203(11)	119.90(2)	62.3	8.1699(24)	7.5830(17)	15.3663(48)	951.98(43)	1.106	7.72
6	3.9409(3)	7.7200(10)	119.90(2)	79.1	8.1840(44)	7.5855(31)	15.3540(73)	953.18(78)	1.244	8.19
7	3.9414(3)	7.7191(10)	119.92(2)	100					1.350	8.60
8	3.9411(2)	7.7213(9)	119.93(2)	100					1.234	8.21
9	3.9409(3)	7.7230(9)	119.94(2)	100					1.294	8.40
10	3.9404(2)	7.7203(8)	119.87(2)	100					1.199	8.10
11	3.9406(2)	7.7218(8)	119.91(2)	100					1.303	8.46
12	3.9411()	7.7218(8)	119.94(2)	100					1.353	8.62

Tab. B15. Structural parameters of $BaYMn_2O_5$ materials at 500 °C at constant 5 vol.% H_2 in Ar flow.

$BaYMn_2O_5$ (*P4/mmm*) 500 °C					
	a [Å]	c [Å]	V [Å^3]	χ^2	R_{wp} [%]
1	3.9446(2)	7.7386(7)	120.41(2)	1.174	8.05
2	3.9457(2)	7.7381(8)	120.47(2)	1.178	8.08
3	3.9453(2)	7.7381(7)	120.45(2)	1.226	8.24
4	3.9451(2)	7.7404(7)	120.47(2)	1.258	8.35
5	3.9447(2)	7.7394(7)	120.43(2)	1.175	8.08
6	3.9443(2)	7.7373(7)	120.37(2)	1.253	8.33
7	3.9451(2)	7.7369(7)	120.42(2)	1.298	8.52
8	3.9452(2)	7.7377(7)	120.44(2)	1.199	8.20
9	3.9455(2)	7.7395(7)	120.48(2)	1.208	8.20
10	3.9455(2)	7.7396(7)	120.48(2)	1.183	8.12
11	3.9453(2)	7.7415(7)	120.50(2)	1.141	7.96
12	3.9459(2)	7.7395(7)	120.51(2)	1.183	8.13

Appendix C

Method of manufacturing of highly-efficient oxygen storage materials

Subject of this appendix is a patent application resulting from Polish-Japanese cooperation. The application is entitled "*Method of manufacturing of highly-efficient oxygen storage materials*" and arose from collaboration of the authors: Konrad Świerczek (contribution 30%), Alicja Klimkowicz (contribution 25%), Akito Takasaki (contribution 25%), Kun Zheng (contribution 10%), Tetsuya Yamazaki (contribution 10%). The application is registered in Polish Patent Office under WIPO ST 10/C: PL414043 and the European Patent Office application number EP15186419.6.

The invention concerns oxygen storage materials with a double-perovskite type structure and a general formula $BaY_{1-x}Ln_xMn_2O_{5+\delta}$ (Ln: Ce, Pr, Nd, Pm, Sm, Eu, Gd, Tb, Dy, Ho, Er, Tm, Yb, Lu and Y) and method of treatment resulting in an increase of oxygen storage capacity of the material and faster oxygen release speed. In order to evaluate enhancement of the proposed solution thermogravimetric (TG) studies were performed concerning the oxidation and the reduction properties, as well as X-ray diffraction studies of two exemplary materials: $BaPrMn_2O_{5+\delta}$ and $BaSmMn_2O_{5+\delta}$.

In general, double perovskite-type oxides may be synthesized using different suitable sintering routes, e.g. soft chemistry method or solid state reaction method, as it was described in chapter 5 of this thesis. After sintering pellets were thoroughly ground and sieved through 100μm sieve. Then in the case of Pr-containing material the high energy milling process was carried out in a planetary ball mill, with the rotary speed of 500 rpm in air for 15 min, with the milling chamber interior made of ZrO_2, maintaining the weight ratio of balls to material of 100:1. The Sm-containing sample was milled for 15 min in the rotary vibrating ball mill, in ZrO_2 chamber and with the 875 cpm (cycles per minute) speed, in air and at room temperature. After milling the samples were heated up to 500 °C in thermogravimetric (TG) apparatus with the heating rate of 10°/min and subjected to the activation process involving five consecutive, isothermal oxidation/reduction cycles, in the rapidly changing gas atmosphere between 5 vol.% of H_2 in Ar (during the reduction) and synthetic air (during the oxidation).

For a purpose of comparison, some data already presented in chapter 6 of non-milled $BaPrMn_2O_{5+\delta}$ and $BaSmMn_2O_{5+\delta}$ samples were repeated.

As prepared samples were investigated in terms of their crystal structure using X-ray powder diffraction (XRD), and the obtained diffraction patterns are shown in Fig. C1a and b for the reduced $BaPrMn_2O_5$ and $BaSmMn_2O_5$ materials respectively, before and after milling. As observed by the broadening and overlapping of the X-ray reflexes, an ongoing process of cation mixing between Ba and Pr sites occur (merge of the main X-ray reflections in vicinity of 32 deg). Also, for both milled sample presence of small amount of ZrO_2 was detected.

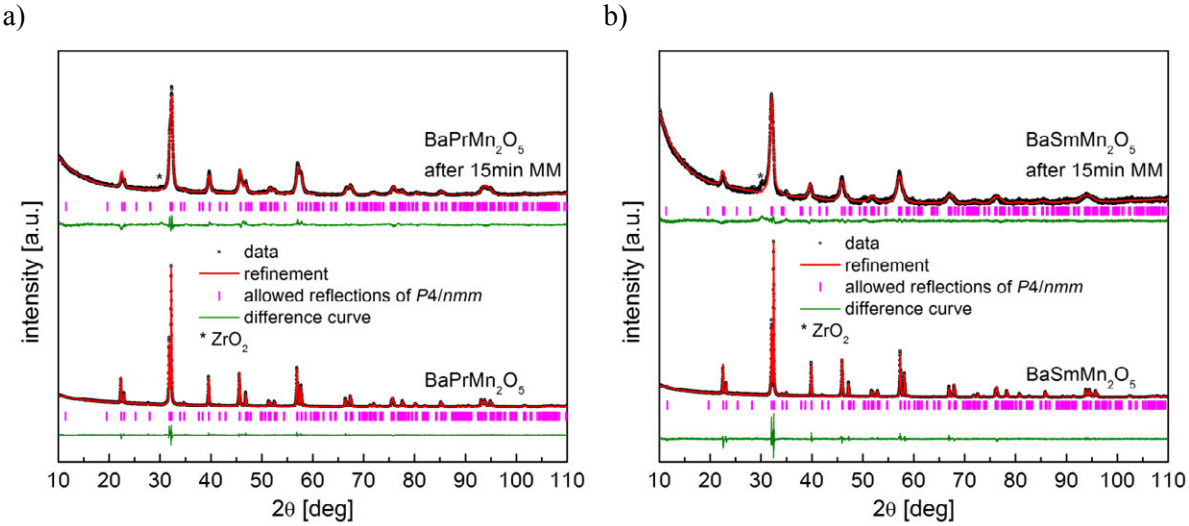

Fig. C1. Diffractograms with Rietveld analyses for a) $BaPrMn_2O_5$ and b) $BaSmMn_2O_5$ materials in initial state and after high energy milling for 15 min.

When comparing the structural a and c parameters for samples after milling presented in Tab. C1 to the ones of non-milled samples (Tab. 6.1), lowering of a/c ratio was observed, indicating partial transformation from tetragonal structure ($a \neq c$, ordered material) to cubic one ($a = c$, disordered structure). Size of the crystallite calculated out of the Scherrer equation shows expected significant decreases of the size of grains after milling process.

Tab. C1. Structural parameters of reduced and oxidized samples after high energy mechanical milling (MM) treatment for 15 min and crystallite size calculated for samples before and after milling.

chemical composition	space group	a [Å]	c [Å]	V [Å^3]	χ^2	R_{wp} [%]	d before MM[Å]	d after MM [Å]
$BaPrMn_2O_5$	*P4/nmm*	5.6197(1)	7.7806(3)	245.72(2)	2.165	3.29	105	18
$BaPrMn_2O_6$	*P4/mmm*	3.9071(1)	7.7480(3)	118.28(1)	2.768	3.65	99	19
$BaSmMn_2O_5$	*P4/nmm*	5.6008(8)	7.8296(20)	245.61(9)	1.920	3.10	144	21
$BaSmMn_2O_6$	*P4/nmm*	5.5425(3)	7.7466(7)	237.97(3)	1.919	3.14	137	21

Fig. C2 shows the non-isothermal reduction process recorded under the atmosphere of 5 vol.% H_2 in Ar, as a function of temperature starting from TR up to 500 °C. Although a slight decrease of the OSC can be observed for the material after milling, reduction curve smoothened significantly. Nonetheless, on the derivative curve two minimums are still observed. The characteristic temperature of the reduction process was lowered by milling from 380/485 °C down to 340/410 °C.

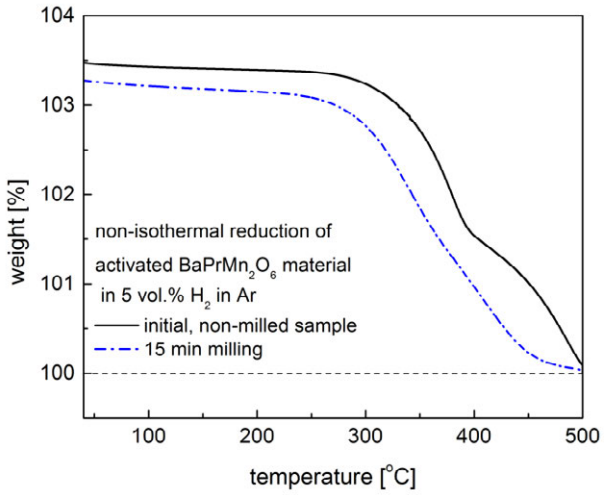

Fig. C2. TG curves corresponding to the oxygen release from $BaPrMn_2O_6$ samples taken in 5 vol.% of H_2 atmosphere for initial material and after high energy milling, during heating from the RT to 500 °C.

For the oxidized materials (initial and after milling treatment) the isothermal reduction was performed under the atmosphere of 5 vol.% H_2 in Ar, and analogous oxidation process was registered in air atmosphere at a temperature of 500 °C. The results are presented in Fig. C3a and b for $BaPrMn_2O_{5+\delta}$, and C3c and d for $BaSmMn_2O_{5+\delta}$, respectively. The measured OSC decreases for the milled for 15 min $BaPrMn_2O_{5+\delta}$ sample, and equals to 2.9 wt.%, however, on the contrary, for $BaSmMn_2O_{5+\delta}$ sample subjected for 15 min milling OSC increases, and equals 3.6 wt.%. It is worth mentioning that these values exceed OSC of the commercial OSM materials from ceria-zirconia (CeO_2-ZrO_2) ceria-lanthana (CeO_2-Ln_2O_3) systems. Furthermore, as can be seen both, the reduction and oxidation processes occur significantly faster for the milled samples, as comparing with the non-milled ones. The reduction process can be compared by using either direct time needed for 95% of the total weight change or by comparison of reduction rate parameter r defined by Motohashi [A9] as a speed of a weight change calculated for 50% of the total capacity. In the case of milled samples, r parameter increases considerably, and while for $BaSmMn_2O_{5+\delta}$ equals to 0.5 for the initial sample, for the sample milled for 15 min it

reaches 4.4. Furthermore, smoothing of the reduction curve is clearly visible for materials after milling treatment, and the reduction process exhibits single-step character, with no inflection in vicinity of the half of total weight change.

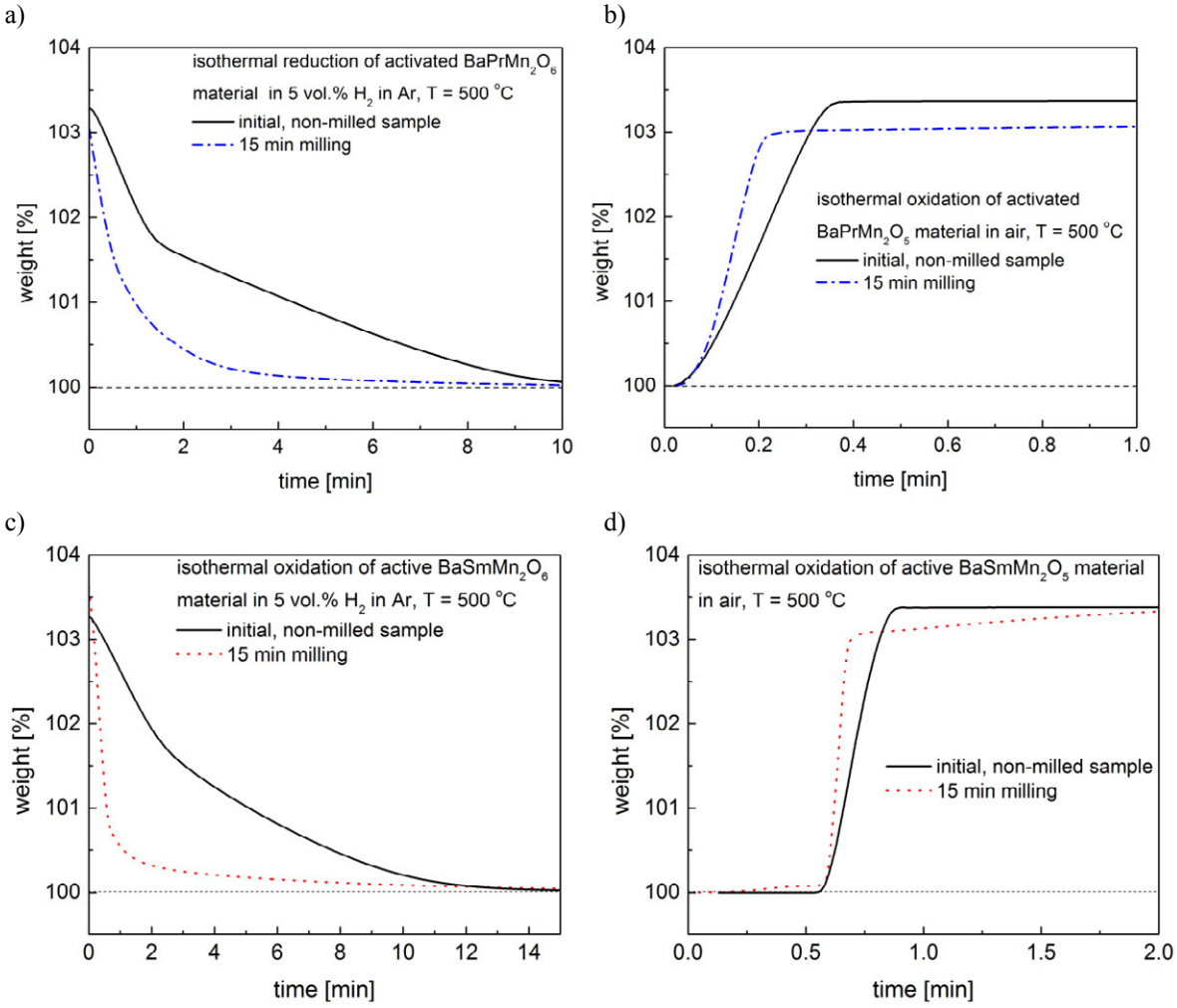

Fig. C3. Isothermal reduction in 5 vol.% H2 in Ar of a) $BaPrMn_2O_6$ and c) $BaSmMn_2O_6$. Isothermal oxidation of b) $BaPrMn_2O_5$ and d) $BaSmMn_2O_5$ in synthetic air at 500 °C.

Oxygen storage-related parameters calculated on the basis of the performed TG analyses are gathered in Tab. C2.

Tab. C2. Oxygen storage properties of considered $BaPrMn_2O_{5+\delta}$ and $BaSmMn_2O_{5+\delta}$ materials before and after MM.

chemical composition	milling time	oxygen storage capacity (OSC) at 500 °C [wt.%] / [μmol O·g^{-1}]	characteristic temperature of reduction (linear approximation in the range of the largest change) [°C]	time of reduction at 500 °C (95% of a total weight change) [min]	reduction rate parameter r [wt.%·min^{-1}]
$BaPrMn_2O_{5+\delta}$	0	3.3 / 2050	310	8.3	1.0
$BaPrMn_2O_{5+\delta}$	15	2.9 / 1800	240	3.4	2.9
$BaSmMn_2O_{5+\delta}$	0	3.3 / 2050	330	8.7	0.5
$BaSmMn_2O_{5+\delta}$	15	3.6 / 2250	220	2.7	4.4

The obtained data show that the process of high energy milling of perovskite-type oxygen storage materials of the general $BaLnMn_2O_{5+\delta}$ formula provides improvement of the oxidation/reduction properties of these materials, in particular, decrease in reduction temperature and shortening of the reduction time as well as increase of the reduction rate parameter, thereby extending the temperature range of reversible oxygen absorption/release. The high energy milling process, conducted in air for 15 min, provides partial mixing in the Ba-Ln sublattice in $BaLnMn_2O_{5+\delta}$ and allows for activation of the surface of the perovskite-based material that improve the reversible oxygen absorption/release properties of this group of oxides.

Appendix D

Flameless oxidation of methane with $BaYMn_2O_6$ used as catalyst and oxygen carrier

$BaYMn_2O_6$ oxide was shown in literature [A10] to possess substantial catalytic activity towards methane combustion. In order to further evaluate this property, a custom-made setup for studies of catalytic-related properties was constructed at the Department of Hydrogen Energy, Faculty of Energy and Fuels, AGH University of Science and Technology. The construction and presented studies were performed in collaboration with M.Sc. Tomasz Rząsa.

Schematic representation of the constructed apparatus is presented in Fig. D1. The main part of the setup is a micro-reactor, built using quartz U-tube and containing active material embedded in quartz powder. Type and amount of gas supplied to the system can be adjusted using mass flow controllers, and in the case of gas mixture usage, respective gases are mixed in the mixer. Small amount of the exhaust gas is directed to a quadruple mass spectrometer (Pfeiffer Vacuum Thermostar GSD 301) to analyze its composition.

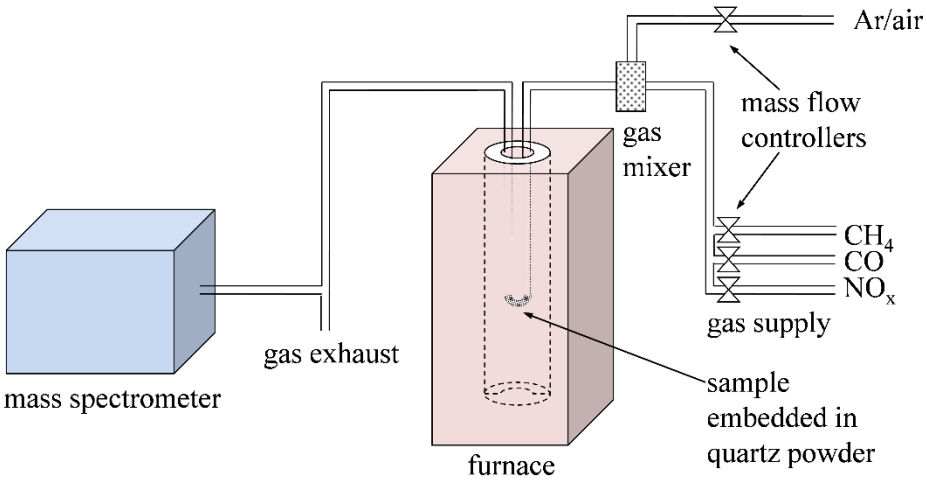

Fig. D1. Schematics of a custom-made setup for studies of methane combustion in oxygen-free conditions.

For the conducted preliminary studies, $BaYMn_2O_6$ material was mixed with quartz powder (0.25 g $BaYMn_2O_6$ with 2.68 g of silica rough powder), and placed into the quartz U-tube. The measurements were performed at three temperatures: 500 °C, 550 °C and 600 °C (autocatalysis of CH_4 initiates at ~ 700 °C [A10]). During heating to a predetermined temperature, the sample remained in an inert atmosphere (pure argon) for

a long time (few hours) in order to stabilize and purify the gas system from traces of contaminations. Then, the mixture of 10 vol.% CH_4 in Ar was directed into the micro-reactor with a flow of about 50 $cm^3 \cdot min^{-1}$. After closing the methane mixture flow, the system was flushed with argon for remove the residual CH_4. During the described above steps, simultaneous recording of the composition of the exhaust gases was carried out on the quadruple mass spectrometer using Quadstar software. Results gathered during the experiment (i.e. ionic current values, which can be associated with CH_4 and CO_2 molecules) are presented in Fig. D2. As can be seen, with switching of the gas from Ar to 10 vol.% CH_4 in Ar a corresponding increase of signals associated with methane and carbon dioxide occurs. It is worth mentioning that after Ar purge and another switching to CH_4-containing atmosphere, the respective maxima of ionic current are much higher, which is likely due to the ongoing reduction of the active material, which when reduced, becomes catalytically inactive. It can be stated that the combustion of CH_4 in oxygen-free conditions most likely proceeds according to Mars-van Krevelen mechanism (Fig. 2.1).

Furthermore, taking maxima of the second cycle as reference point, it can be stated that difference between the second maximum and the first one divided by the second maximum represents the minimum percentage of the CH_4, which at that point underwent the conversion according to the reaction above. This value can be estimated as about 14% at 550 °C and 32% at 600 °C. Please notice, however, that the presented calculations are rather of qualitative character, since based on preliminary data. Also, similarly like discussed in work [A10], no optimization of the material was done (e.g. increase of a specific surface area), so, citing: "the catalytic activity could be drastically enhanced as the surface area of the $BaYMn_2O_{5+\delta}$ product is accordingly increased".

Assuming total conversion of the methane, the respective chemical reaction can be written as (A1):

$$4BaYMn_2O_6 + CH_4 \rightarrow 4BaYMn_2O_5 + CO_2 + 2H_2O \qquad (A1)$$

It should be also stated that while with the ongoing reduction of the active $BaYMn_2O_6$ the catalytic activity of the material will diminish, using unique property of $BaYMn_2O_5$ to fully re-oxidize, the catalytic activity of the material can be restored. What is more, the reported flameless conversion of CH_4 with $BaYMn_2O_6$ used as the oxygen carrier and catalyst and extends results published by Motohashi [A10] for a case of a lack of oxygen in the gas atmosphere.

The discussed above studies concern conversion of methane, however, the constructed setup allows also for studies of catalytic activity of the materials in relation to NO_x or CO gases.

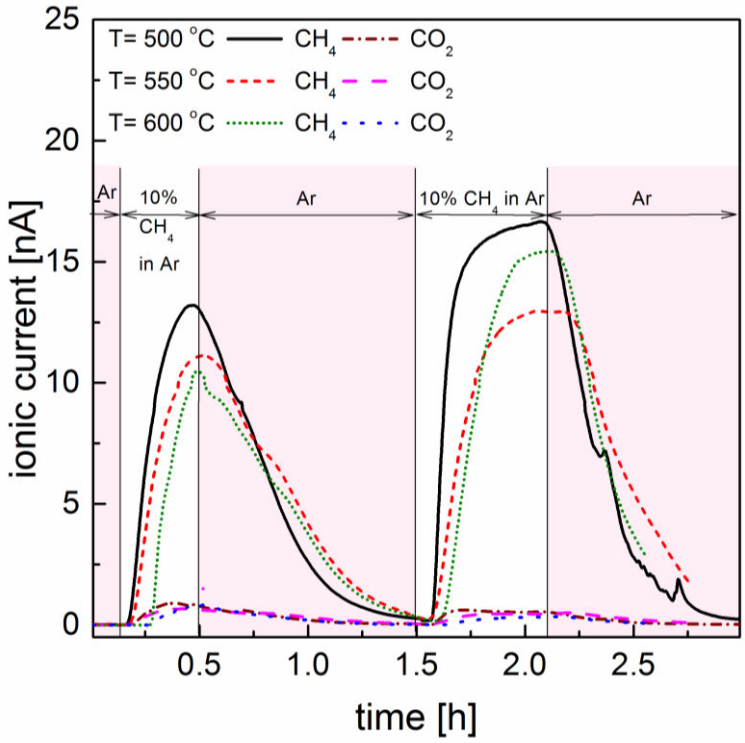

Fig. D2. Mass spectrometer signals data recorded in the anaerobic methane combustion experiment.

References

[1] Asia-Pacific to Continue to Lead Global Industrial Gases Market in 2018: Transparency Market Research, Albany, NY (PRWEB) February 16, 2015, http://www.transparencymarketresearch.com/pressrelease/industrial-gases-market.htm, accessed on 13th of July 2015

[2] D. Wawrzyńczak, D. Bukalak, Inżynieria i Ochrona Środowiska 15(3) (2012) 277-286

[3] J. da Costa, S. Smart, J. Motuzas, S. Liu, D. Zhang, State of Art (SOTA) Report on Dense Ceramic Membranes for Oxygen Separation from Air, http://www.anlecrd.com.au/_literature_139177/SOTA_report_on_dense_ceramic_membranes_for_oxygen_separation_from_air_-_UQ, accessed on 13th of July 2015

[4] D. Ruthven, S. Farooq, K. Knaebel, "*Pressure Swing Adsorption*", VCH, New York; 1993

[5] T. Motohashi, T. Ueda, Y. Masubuchi, M. Takiguchi, T. Setoyama, K. Oshima, S. Kikkawa, Chem. Mater. 22 (2010) 3192-3196

[6] A. Klimkowicz, K. Zheng, G. Fiołka, K. Świerczek, Chemik 2013 67(12) 1202-1205

[7] M. Karppinen, H. Okamoto, H. Fjellvåg, T. Motohashi, H. Yamauchi, J. Solid State Chem. 177 (2004) 2122-2128

[8] D.N. Tsinoglou, G.C. Koltsakis, J.C. Peyton Jones, Ind. Eng. Chem. Res. 41 (2002) 1152-1165

[9] M. Machida, K. Kawamura, K. Ito, K. Ikeue, Chem. Mater. 17 (2005) 1487-1492

[10] A. Trovarelli, "*Catalysis by ceria and related materials*", Imperial College Press, London, 2002

[11] Z. Yang, Y.S. Lin, Y. Zeng, Ind. Eng. Chem. Res. 41 (2002) 2775-2784

[12] D.J.L. Brett, A. Atkinson, N.P. Brandon, S.J. Skinner, Chem. Soc. Rev. 37 (2008) 1568-1578

[13] A.A. Taskin, Y. Ando, Phys. Rev. Lett. 98 (2007) 207201 1-4

[14] I.O. Troyanchuk, S.V. Trukhanov, G. Szymczak, Crystallog. Rep. 47(4) (2002) 658-665

[15] S.V. Trukhanov, I.O. Troyanchuk, M. Hervieu, H. Szymczak, K. Bärner, Phys. Rev. B 66 (2002) 184424 1-10

[16] T. Nakajiama, H. Kageyama, Y. Ueda, Physica B 329-333 (2003) 844-845

[17] R.D. Shannon, Acta Cryst. A 32 (1976) 751-767

[18] Oxygen global market report, 26 Jan 2007 | By gasworld http://www.gasworld.com/oxygen-global-market-report/1277.article, accessed on 22nd of February 2015

[19] Medical Gases Market By Product (Oxygen, Nitrogen, Helium, Laser Gas, Lung Gas, Aerobic, Anaerobic Mixtures, Helium Oxygen Gas Mixtures, Medical Air, Carbon Dioxide-Oxygen, Laser Gas, Lung Gas, Ethylene Oxide), By Equipment (Manifolds, Outlets, Medical Air Compressors, Masks) Analysis And Segment Forecasts To 2020, Published: May 2014 | ISBN Code: 978-1-68038-125-2 http://www.grandviewresearch.com/industry-analysis/medical-gases-market, accessed on 22nd of February 2015

[20] CTA refrigeration industrial, Presentation about Oxymat system: http://www.ctarefrigeracion.com/descargas/pdf_oxymat/Folleto%20Generadores%20de%20O2%20Medical.pdf , accessed on 22nd of February 2015

[21] S.T. O'Connor, "*Liquid Air and the Liquefaction of Gases, Theory, History, Biography, Practical Applications*", Manufacture - Primary Source Edition, BiblioLife, 2014

[22] Linde Group, History and technological process. Cryogenic air separation: http://www.linde-engineering.com/internet.global.lindeengineering.global/en/images/AS.B1EN%201113%20-%20%26AA_History_.layout19_4353.pdf, accessed on 22nd of February 2015

[23] R.F. Barron, K.D. Timmerhaus," *Advances in Cryogenic Engineering*", Springer Science+Business Media, New York, 1972, 20-36

[24] R.F. Barron, "*Cryogenic Systems*", McGraw-Hill, New York, 1966, 75-177

[25] Liquid Air, an introduction to liquid air: http://liquidair.org.uk/full-report/report-chapter-two, accessed on 11th of August 2015

[26] D.R. Vinson, Comput. Chem. Eng. 30 (2006) 1436-1446

[27] R. Agrawal, D.M. Herron, Encyclopedia of Separation Science, vol. 5, Academic Press, San Diego, 2000, 1895-1910

[28] D. Finlayson, A.J. Sharp, GB365092 A, "*Improvements in or relating to the treatment of gaseous mixtures for the purpose of separating them into their components or enriching them with respect to one or more of their components*", 1932

[29] P.R. Nelson: Master thesis, "*Oxygen From Air By Pressure Swing Adsorption*", 1993

[30] J. Smolarek, H.R. Schaub, J.B. Fassbaugh, T.M. Aaron, US 005658371 A, "*Single bed pressure swing adsorption process for recovery of oxygen from air*", 1997

[31] S. Sircar, T. Naheiri, J.R. Fischer, US 006146447 A, "*Oxygen generation process and system using single adsorber and single blower*", 2000

[32] J. Smolarek, H.R Schaub, US 005656068 A, "*Large capacity vacuum pressure swing adsorption process and system*", 1997

[33] D.M. Stuart, J.R. Coates, US 5989315 A, "*Vacuum swing adsorption to separate oxygen-enriched gas stream from air where vacuum is drawn by flow of pressurized steam raised by heat evolved from combustion using some of the separated oxygen*", 1998

[34] Xebec webpage: http://www.xebecinc.com/technology-what-is-psa.php, accessed on 22nd of February 2015

[35] Carlos A. Grande, ISRN Chemical Engineering 2012 (2012) 982934 1-13

[36] K.S. Knaebel, "*Adsorbent Selection*", Adsorption Research Inc. Dublin, Ohio 43016

[37] J.M. Zelinski, L. Kattle, "*Physical Characterization: Surface Area and Porosity*", 2013, http://www.intertek.com/knowledge-education/whitepapers/, accessed on 22nd of February 2015

[38] M.W. Ackley, S.U. Rege, H. Saxena, Micropor. Mesopor. Mat. 61 (2003) 25-42

[39] R.T. Yang, "*Adsorbents. Fundamentals and Applications*", John Wiley & Sons, New Jersey, NJ, USA, 2003

[40] Sam Gas Projects page http://www.samgasplants.com/psa-oxygen-gas-plant.html, accessed on 22nd of February 2015

[41] S. Giddey, F.T. Ciacchi, S.P.S. Badwal, J. Membrane Sci. 346 (1) (2010) 227-232

[42] M. Ulbricht, Polymer 47 (2006) 2217-2262

[43] A. Basile, S.P. Nunes, "*Advanced membrane science and technology for sustainable energy and environmental applications*", Woodhead Publishing Limited, 2011

[44] R.W. Baker, "*Membrane Technology and Applications*", John Wiley and Sons Ltd. 2012

[45] S. Smart, J.C. Diniz da Costa, S. Baumann, W.A. Meulenberg, "*Oxygen transport membranes: dense ceramic membranes for power plant applications*", in: A. Basile, S.P. Nunes "*Advance membrane science and technology for sustainable energy and environmental applications*", Woodhead Publishing Ltd, Cambridge, 2011, 255-294

[46] J. Sunarsoa, S. Baumannb, J.M. Serrac, W.A. Meulenbergb, S. Liua, Y.S. Lind, J.C. Diniz da Costa, J. Membrane Sci. 320 (2008) 13-41

[47] K. Li, "*Ceramic Membranes for Separation and Reaction",* John Wiley & Sons Ltd, London, 2006

[48] A.R. Smith, J. Klosek, Fuel Process. Technol. 70(2) (2001) 115-134

[49] W.F. Castle, Int. J. Refrig. 25(1) (2002) 158-172

[50] DOE/NETL, "*Cost and Performance Baseline for Fossil Energy Plants*", Vol. 3a, Low Rank Coal to Electricity: IGCC Cases, 2011

[51] DOE/NETL, *Pulverised coal oxycombustion power plants*, Vol 1: Bituminous coal to electricity, 2008

[52] S.L. Matson, W.J. Ward, S.G. Kimura, W.R. Browall, J. Membr. Sci. 29(1) (1986) 79-96

[53] B.D. Bhide, S.A. Stern, J. Membr. Sci. 62(1) (1991) 37-58

[54] A. Meriläinen, A. Seppälä, P. Kauranen, Appl. Energ. 94 (2012) 285-294

[55] J.G. Jee, M.B. Kim, C.H. Lee, Chem. Eng. Sci. 60 (2005) 869-882

[56] Air Products webpage http://www.airproducts.com/~/media/Files/PDF/company/safetygram-6.pdf, accessed on 1st of August 2015

[57] Air Products webpage http://www.airproducts.com/products/Gases/supply-options/bulk-deliveries-and-storage-systems/typical-bulk-liquid-storage-systems.aspx accessed on 1st of August 2015

[58] A. Züttel, A. Borgschulte, L. Schlapbach, "*Hydrogen as a Future Energy Carrier*", WILEY-VCH, 2008

[59] Praxair webpage http://www.praxair.com/gases/buy-liquid-oxygen-or-compressed-oxygen-gas, accessed on 9th of July 2015

[60] L. Karvonen, M. Valkeapaa, R.-S. Liu, J.M. Chen, H. Yamauchi, M. Karppinen, Chem. Mater. 22 (2010) 70-76

[61] R. Le Toquin, W. Paulus, A. Cousson, C. Prestipino, C. Lamberti, J. Am. Chem. Soc. 128 (40) (2006) 13161-13174

[62] P. Bezdicka, A. Wattiaux, J.C. Grenier, M. Pouchard, P. Hagenmuller, Z. Anorg. Allg. Chem. 619 (1993) 7-12

[63] S.B. Adler, Chem. Rev. 104 (2004) 4791-4843

[64] A. Lebon, P. Adler, C. Bernhard, A.V. Boris, A.V. Pimenov, A. Maljuk, C.T. Lin, C. Ulrich, B. Keimer, Phys. Rev. Lett. 92 (2004) 037202 1-4

[65] K. Jeamjumnunja, W. Gong, T. Makarenko, A.J. Jacobson, J. Sol. State Chem. 230 (2015) 397-403

[66] Y. Nagai, T. Yamamoto, T. Tanaka, S. Yoshida, T. Nonaka, T. Okamoto, A. Suda, M. Sugiura, Catal. Today 74 (2002) 225-234

[67] M. Karppinen, H. Yamauchi, S. Otani, T. Fujita, T. Motohashi, Y.-H. Huang, M. Valkeapää, H. Fjellvåg, Chem. Mater. 18 (2006) 490-494

[68] S. Remsen, B. Dabrowski, Chem. Mater. 23 (2011) 3818-3827

[69] T. Motohashi, Y. Hirano, Y. Masubuchi, K. Oshima, T. Setoyama, S. Kikkawa, Chem. Mater. 25 (2013) 372-377

[70] M. Hervieu, A. Guesdon, J. Bourgeois, E. Elkaïm, M. Poienar, F. Damay, J. Rouquette, A. Maignan, C. Martin, Nat. Mater. 13 (2013) 74-80

[71] T. Motohashi, T. Takahashi, M. Kimura, Y. Masubuchi, S. Kikkawa, Y. Kubota, Y. Kobayashi, H. Kegeyama, M. Takata, S. Kitagawa, R. Matsuda, J. Phys. Chem. C, 119 (5) (2015) 2356-2363

[72] P. Atkins, J. de Paula, "*Atkins' Physical Chemistry*", Oxford University Press, Oxford, 2002

[73] C.T. Herbschleb: Doctoral thesis, „*ReactorSTM : imaging catalysts under realistic conditions*" Leiden University, 2011

[74] J.A. Alonso, M.J. Martínez-Lope, M.T. Casais, J.L. MacManus-Discroll, P.S.I.P.N. de Silva, L.F. Cohen, M.T. Fernández-Díaz, J. Mater. Chem. 7 (1997) 2139-2144

[75] A. Mineshige, J. Izutsu, M. Nakamura, K. Nigaki, M. Kobune, S. Fujii, M. Inaba, Z. Ogumi, T. Yao, Electrochem. 68 (2000) 515-518

[76] D. Mantzavinos, A. Hartley, I.S. Metcalfe, M. Sahibzada, Solid State Ionics 134 (2000) 103-109

[77] R.A. Cox-Galhotra, S. McIntosh, Solid State Ionics 181 (2010) 1429-1436

[78] J.A. Lane, S.J. Benson, D. Waller, J.A. Kilner, Solid State Ionics 121 (1999) 201-208

[79] R.A. De Souza, J.A. Kilner, J.F. Walker, Mater. Lett. 43 (2000) 43-52

[80] E. Bucher, A. Egger, P. Ried, W. Sitte, P. Holtappels, Solid State Ionics 179 (2008) 1032-1035

[81] Y.A. Mastrikov, M.M. Kuklja, E.A. Kotomin, J. Maier, Energy Environ. Sci. 3 (2010) 1544-1550

[82] Y.A. Mastrikov, R. Merkle, E. Heifets, E.A. Kotomin, J. Maier, J. Phys. Chem. C, 114 (2010) 3017-3027

[83] E. Kotomin, R. Merkle, J. Maier, poster presentation "*Atomistic modelling of oxygen incorporation into (La,Sr)MnO_3 solid oxide fuel cell cathode*" available at Max

Planck Institutes webpage: http://www.fkf.mpg.de/de accessed on 21st of August 2015

[84] R. Merkle, J. Maier, Angew. Chem. Int. Ed. 47 (2008) 2-23

[85] J . Maier, J. Jamnik, M. Leonhardt, Solid State Ionics 129 (2000) 25-32

[86] V.V. Kharton, A.V. Kovalevsky, A.P. Viskup, J.R. Jurado, F.M. Figueiredo, E.N. Naumovich, J.R. Frade, J. Solid State Chem. 156 (2001) 437-444

[87] A. Lebon, P. Adler, C. Bernhard, A.V. Boris, A.V. Pimenov, A. Maljuk, C.T. Lin, C. Ulrich, B. Keimer, Phys. Rev. Lett. 92 (2004) 037202 1-4

[88] M. Sugiura, Cat. Surv. Asia. 7 (2003) 77-87

[89] M. Machida, K. Kawamura, T. Kawano, D. Zhang, K. Ikeue, J. Mater. Chem. 16 (2006) 3084-3090

[90] K. Ikeue, M. Eto, D. Zhang, T. Kawano, M. Machida, J. Catal. 248 (2007) 46-52

[91] D. Zhang, F. Yoshioka, K. Ikeue, M. Machida, Chem. Mater. 20 (2008) 6697-6703

[92] M. Machida, K. Ikeue, M. Miura, US 8357626 B2, "*Oxygen storage/release material and exhaust gas purifying catalyst comprising the same*", 2013

[93] C. Abughayada, B. Dabrowski, S. Kolesnik, D.E. Brown, O. Chmaissem, Chem. Mater. 27 (18) (2015) 6259-6267

[94] C. Abughayada, B. Dabrowski, S. Remsen, S. Kolesnik, O. Chmaissem, J. Solid State Chem. 217 (2014) 127-135

[95] World Vehicle Population: http://wardsauto.com/ar/world_vehicle_population_110815, accessed on 21st of February 2015

[96] T. Palucka, "*Doing the Impossible*", Invention & Technology 19 (3) 2004, available at http://www.americanheritage.com/ webpage, accessed on 1st of August 2015

[97] S.N.S.A. Bahari, W.A.Y.W. Yusoff, "*Quality Improvement of Three-Way Catalytic Converter (Twc) System*", LAP Lambert Acad. Publ., 2011

[98] J.C. Hilliard, G.S. Springer, "*Fuel Economy: in Road Vehicles Powered by Spark Ignition Engines",* Springer Science & Business Media, 2013

[99] TWC graph, http://www.pakwheels.com/blog/ever-wondered-what-is-the-purpose-of-catalytic-converter-in-your-civic-or-corolla/ accessed on 11th of August 2015

[100] Journal of Laws No. 227, item 2250 – The Regulation of Polish Minister of Infrastructure from 16.12.2003

[101] Gas engines: http://www.blackthorn.net/gas-engines/, accessed on 31st of July 2015

[102] National Academy Press. "*Evaluating Vehicle Emissions Inspection and Maintenance Programs*" 33 (2001) 27-29

[103] D.N. Tsinoglou, G.C. Koltsakis, J.C. Peyton Jones, Ind. Eng. Chem. Res. 41 (2002) 1152-1165

[104] G.C. Koltsakis, I.P. Kandylas, A.M. Stamatelos, Chm. Eng. Corn. 164 (1998) 153-189

[105] T. Shamim, V.C. Medisetty, J. Eng. Gas Turb. Power 125 (2003) 547-554

[106] S. Keav, S.K. Matam, D. Ferri, A. Weidenkaff, Catalysts 4 (2014) 226-255

[107] T. Mattisson, Hindawi Publishing Corporation ISRN Chemical Engineering 2013 (2013) 526375 1-19

[108] A. Abad, T. Mattisson, A. Lyngfelt, M. Rydén, Fuel 85 (2006) 1174-1185

[109] Q. Song, W. Liu, C.D. Bohn, R.N. Harper, E. Sivaniah, S.A. Scott, J.S. Dennis: Energy Environ. Sci., 6 (2013) 288-298

[110] D. Ferri, L. Forni, Appl. Catal. B- Environ. 16 (1998) 119-126

[111] A.N. Zagoruiko, "*New developments in the area of nonstationary and sorption-enhanced catalytic processes*", Novosibirsk, 2011

[112] W. Shelton, D. Keairns *Analysis of Integrated Gasification Fuel Cell Plant Configuration*, 2011 DOE/NETL 2011-148 available on https://www.netl.doe.gov, accessed on 23th of December 2015

[113] A. Lanzini, T.G. Kreutz, E. Martelli, M. Santarelli, Proceedings of ASME turbo expo 2012, GT 2012, Copenaghen (2012) 337-347

[114] D.L. Keairns, R.A. Newby, *Integrated Gasification Fuel Cell (IGFC) Systems* 11th Annual SECA Workshop 2010, Pittsburgh, PA, USA, available on https://www.netl.doe.gov, accessed on 23th of December 2015

[115] JSPS-PAN Joined project Development of IGFC System with Oxygen and Hydrogen Storage Units, 2014-2016

[116] K. Kumar, D. Kumar, Int. J. Res. Sci. Technol. 3(V) (2014) 1-7

[117] G.V. Subba Rao, B.V.R Chowdari, Mater. Res. Soc. 1(1) (2006) 8-14

[118] R. Mitchell, "*Perovskites modern and ancient*", Almaz Press, Thunder Bay, Ontario, 2002

[119] M. Johnsson, P. Lemmens, "*Crystallography and Chemistry of Perovskites, Handbook of Magnetism and Advanced Magnetic Media*", John Wiley & Sons, New York, 2006

[120] K. Świerczek, B. Dabrowski, L. Suescun, S. Kolesnik, J. Solid State Chem. 182(2) (2009) 280-288

[121] B. Dabrowski, O. Chmaissem, J. Mais, S. Kolesnik, J.D. Jorgensen, S. Short, J. Solid State Chem. 170 (1) (2003) 154-164

[122] A.M. Glazer, Acta Crystallog. B 28 (1972) 3384-3392

[123] K. Świerczek, "*Designing of physicochemical properties of oxide cathode materials for IT-SOFC and Li-ion cells*", polish title: "*Projektowanie właściwości fizykochemicznych tlenkowych materiałów katodowych, dla ogniw IT-SOFC Oraz Li-ion*" Ceramika 111, Kraków, 2010

[124] C.J. Howard, H.T. Stokes, Acta Crystallogr. B 54 (1998) 782-789

[125] N.W. Thomas, Acta Crystallogr. B 54 (1989) 337-344

[126] C.N.R. Rao, "*Chemistry of high temperature superconductors*", world Science Publishing Co. Pte. Ltd. Singapore, 1991

[127] H. Geng, J. Lan, A. Mei, Y. Lin, C.W. Nan Electrochim. Acta 56(9) (2011) 3406-3414

[128] Y. Takeda, R. Kanno, T. Takada, O. Yamamoto, M. Takada, Y. Bando, Z. anorg. allg. Chem. 540/541 (1986) 259-270

[129] J.W. Fergus, R. Hui, X. Li, D.P. Wilkinson, J. Zhang, "*Solid Oxide Fuel Cells Materials Properties and Performance*", CRC Press, 2009

[130] J.B. Goodenough, "*Structure and Bonding Series, Localized to Itinerant Electronic Transition in Perovskite Oxides*" Springer, 2001

[131] T. Wolfram, Ş. Ellialtioğlu, "*Electronic and Optical Properties of d-band Perovskites*", Cambridge University Press, 2006

[132] C.N.R. Rao, "*Transition Metal Oxides Structure, Properties, and Synthesis of Ceramic Oxides*", Wiley-VCH, 1998

[133] J.B. Torrance, P. Lacorre, A.I. Nazzal, E.J. Ansaldo, C. Niedermayer, Phys. Rev. B 45 (1992) 8209-8212

[134] E.V. Tsipis, V.V. Kharton, J. Solid State Electrochem. 12 (2008) 1039-1060

[135] E.V. Tsipis, V.V. Kharton, J. Solid State Electrochem. 12 (2008) 1367-1391

[136] W. van Gool, "*Fast Ion Transport in Solids*", North-Holland, 1973

[137] P. Hagenmuller, W. van Gool, "*Solid Electrolytes*", Academic Press, 1978

[138] R.L. Cook, A.F. Sammells, Solid State Ionics 45 (1991) 311-321

[139] A.F. Sammells, R.L. Cook, J.H. White, J.J. Osborne, R.C. MacDuff, Solid State Ionics 52 (1992) 111-123

[140] J.A. Kilner, R.J. Brook, Solid State Ionics 6 (1982) 237-252

[141] M. Mogensen, D. Lybye, N. Bonanos, P.V. Hendriksen, F.W. Poulsen, Solid State Ionics 174 (2004) 279-286

[142] J. Richter, P. Holtappels, T. Graule, T. Nakamura, L.J. Gauckler, Monatsh. Chem. 140 (2009) 985-999

[143] H.U. Anderson, „*Defect chemistry of p-type perovskites*" in F.W. Poulsen, J.J. Bentzen, T. Jacobsen, E. Skou, M.J.L. Østergård, Proceedings of the 14th Risø International Symposium on Materials Science, Risø National Laboratory (1993) 1-18

[144] J. Kanamori, J. Appl. Phys. 31 (1960) 14S-23S

[145] G. King, P.M. Woodward, J. Mater. Chem. 20 (2010) 5785-5796

[146] A.W. Sleight, "*A Study of the Incidence of the Ordered Perovskite Structure*", University of Connecticut, 1963

[147] C.J. Howard, H.T Stokes, Acta Cryst. B 60 (2004) 674-684

[148] C.J. Howard, B.J Kennedy, P.M. Woodward, Acta Crystallogr. B 59 (2003) 463-471

[149] A.A. Colville, S. Geller, Acta Crystallogr. B 27 (1971) 2311-2315

[150] V. Caignaert, N. Nguyen, M. Hervieu, B. Raveau, Mater. Res. Bull. 20 (1985) 479

[151] P. Gallaher, J. MacChesney, D. Buchanan, Chem. Phys. 41(8) (1964) 2429-2434

[152] J.B. Goodenough, J.E. Ruiz-Diaz, Y.S. Zhen, Solid State Ionics 44 (1990) 2l-31

[153] J.H. Kim, L. Mogni, F. Prado, A. Caneiro, J.A. Alonso, A. Manthiram, J. Electrochem. Soc. 156(12) (2009) B1376-B1382

[154] C. Frontera, A. Caneiro, A.E. Carrillo, J. Oró-Solé, and J.L. García-Muñoz, Chem. Mater. 17 (2005) 5439-5445

[155] C. Kuroda, K. Zheng, K. Świerczek, Int. J. of Hydrogen Energ. 38 (2013) 1027-1038

[156] C.N.R. Rao, B. Raveau: "*Colossal Magnetoresistance, Charge Ordering and Related Properties of Manganese Oxides* " World Scientific, Singapore, 1998

[157] T. Nakajima, H. Kageyama, H. Yoshizawa,Y. Ueda, J. Phys. Soc. Jpn. 71(12) (2002) 2843-2846

[158] Y. Ueda, T. Nakajima, J. Phys.: Condens. Matter 16 (2004) S573-S583

[159] R. Mathieu, D. Akahoshi, A. Asamitsu, Y. Tomioka, Y. Tokura, Phys. Rev. Lett. 93 (2004) 227202 1-4

[160] J.P. Chapman, J.P. Attfield, M. Molgg, C.M. Friend, T.P. Beales, Angew. Chem., Int. Ed. Engl. 35 (1996) 2482-2484

[161] F. Millange, V. Caignaert, B. Domenges, B. Raveau, E. Suard, Chem. Mater. 10 (1998) 1974-1983

[162] D. Ávila-Brande, G. King, E. Urones-Garrote, Subakti, A. Llobet, S. García- Martín, Adv. Funct. Mater. 24 (2014) 2510-2517

[163] V. Caignaert, F. Millange, B. Domengès, B. Raveau, Chem.Mater. 11 (1999) 930-938

[164] S. Sengodan, S. Choi, A. Jun, T.H. Shin,Y.-W. Ju, H.Y. Jeong, J. Shin, J.T.S. Irvine, G. Kim, Nat. Mater. 14(2) (2015) 205-209

[165] K. Świerczek, A. Klimkowicz, K. Zheng, B. Dabrowski, J. Solid State Chem. 203 (2013) 68-73

[166] K. Świerczek, J. Power Sources 196 (2011) 7110-7116

[167] D. Mantzavinos, A. Hartley, I.S. Metcalfe, M. Sahibzada, Solid State Ionics 134 (1-2) (2000) 103-109

[168] A.R. West "*Solid state chemistry and its applications*", second edition, student edition, Wiley, Chichester, UK, 2014

[169] A.C. Larson, R.B. von Dreele, Los Alamos Natl. Lab. Rep. - LAUR, 2004, 86-748

[170] B.H. Toby, J. Appl. Crystallogr. 34 (2001) 210-213

[171] A. Baszczuk, B. Dabrowski, M. Avdeev, Dalton Trans. 44 (2015) 10817-10827

[172] A.J. Dianoux, G.H. Lander, *Neutron data booklet* (2^{nd} edition), Old City Publishing, Incorporated, Philadelphia, 2003

[173] K. Świerczek, B. Dabrowski, L. Suescun, S. Kolesnik, J. Solid State Chem. 182 (2009) 280-288

[174] C. Perca, L. Pinsard-Gaudart, A. Daoud-Aladine, M.T. Fernández-Díaz, J. Rodríguez-Carvajal, Chem. Mater. 17 (2005) 1835-1843

[175] T. Nakajima, H. Kageyama, K. Ohoyama, H. Yoshizawa, Y. Ueda J. Solid State Chem. 177 (2004) 987-999

[176] NIST Center for neutron research webpage, resources: https://www.ncnr.nist.gov/, accessed on 30th of December 2015

[177] HZB webpage, neutron source, instruments Bar II: https://www.helmholtz-berlin.de/, accessed on 30th of December 2015

[178] M. Gilleßen, M. Lumeij, J. George, R. Stoffel, T. Motohashi, S. Kikkawa, R. Dronskowski, Chem. Mater. 24 (2012) 1910-1916

[179] D. Stroud, Phys. Rev. B 12 (1975) 3368-3373

[180] A. Klimkowicz, K. Świerczek, A. Takasaki, J. Molenda, B. Dabrowski, Mat. Res. Bull. 65 (2015) 116-122

[181] A. Klimkowicz, K. Świerczek, K. Zheng, M. Baranowska, A. Takasaki, B. Dabrowski, Solid State Ionics 262 (2014) 354-358

[182] A. Klimkowicz, K. Zheng, G. Fiołka, K. Świerczek, Ceram. Mater. 65 (1) (2013) 92-96

[183] Y. Miyauchi, A. Mitsuru, D. Akahoshi, H. Kuwahara, J. Phys. Soc. Jpn. 80 (2011) 074708 01-03

[184] A.J. Wiliams, J.P. Attfield, Phys. Rev. B 72 (2005) 024436 1-5

[185] T. Nakajima, H. Kageyama, Y. Ueda, J. Phys. Chem. Sol. 63 (2002) 913-916

[186] T. Motohashi, T. Ueda, Y. Masubuchi, S. Kikkawa, J. Ceram. Soc. Jpn. 119(11) (2011) 894-897

[187] F. Millange, E. Suard, V. Caignaert, B. Raveau, Mat. Res. Bull. 34 **(**1999) 1-9

[188] M.C. Biesinger, B.P. Payne, A.P. Grosvenor, L.W.M. Lau, A.R. Gerson, R.St.C. Smart, Appl. Surf. Sci. 257 (2011) 2717-2730

[189] National Institute of Standards and Technology XPS database: http://srdata.nist.gov/xps/Default.aspx, accessed on 31th of December 2015

[190] T. Nakajima, H. Kageyama, M. Ichihara, K. Ohoyama, H. Yoshizawa, Y. Ueda, J. Solid State Chem. 177 (2004) 987-999

[191] T. Nakajima, H. Kageyama, H. Yoshizawa, K. Ohoyama, Y. Ueda, J. Phys. Soc. Jpn. 72(12) (2003) 3237-3242

[192] K. Świerczek, A. Klimkowicz, A. Niemczyk, A. Olszewska, T. Rząsa, J. Molenda, A. Takasaki, Funct. Mater. Lett. 7(6) (2014) 1440004

[193] K. Świerczek, A. Klimkowicz, L. Del Valle, Chapter: „*Technologia magazynowania tlenu w tlenkach perowskitowych*" in „*Paliwa i energia XXI wieku*" Wydawnictwo Naukowe Akapit, 2014

[194] A. Klimkowicz, K. Świerczek, A. Takasaki, B. Dabrowski, Solid State Ionics 257 (2014) 23-28

[195] K. Świerczek, B. Dabrowski, L. Suescun, S. Kolesnik, J. Solid State Chem. 182 (2009) 280-288

[196] K. Świerczek, J. Power Sources 196 (2011) 7110-7116

Appendixes' references

[A1] T. Nakajima, H. Kageyama, Y. Ueda, J. Phys. Chem. Sol. 63 (2002) 913-916

[A2] M. Karppinen, H. Okamoto, H. Fjellvåg, T. Motohashi, H. Yamauchi, J. Solid State Chem. 177 (2004) 2122-2128

[A3] A.J. Williams, J.P. Attfield, Phys. Rev. B 72 (2005) 024436 1-5

[A4] K. Jeamjumnunja, W. Gong, T. Makarenko, A.J. Jacobson, J. Solid State Chem. 230 (2015) 397-403

[A5] T. Nakajima, H. Kageyama, M. Ichihara, K. Ohoyama, H. Yoshizawa, Y. Ueda, J. Solid State Chem. 177 (2004) 987-999

[A6] T. Motohashi, T. Takahashi, M. Kimura, Y. Masubuchi, S. Kikkawa, Y. Kubota, Y. Kobayashi, H. Kageyama, M. Takata, S. Kitagawa, R. Matsuda, J. Phys. Chem. C, 119(5) (2015) 2356-2363

[A7] A.J. Dianoux, G.H. Lander, *Neutron data booklet* (2^{nd} edition), Old City Publishing, Incorporated, Philadelphia, 2003

[A8] HZB webpage, neutron source, instruments Bar II: https://www.helmholtz-berlin.de/, accessed on 30th of December 2015

[A9] T. Motohashi, T. Ueda, Y. Masubuchi, S. Kikkawa, J. Ceram. Soc. Jpn. 119(11) (2011) 894-897

[A10] T. Motohashi, T. Ueda, Y. Masubuchi, M. Takiguchi, T. Setoyama, K. Oshima, S. Kikkawa, Chem. Mater. 22 (2010) 3192-3196

Figure and table captions